Ollscoil na h-Éireann, Corcaigh

Investigation of neoclassical tearing modes on MAST using Thomson scattering

A thesis submitted for the degree of

Doctor of Philosophy

by

Thomas O'Gorman

February 2012

Academic Supervisor: **Dr P. Mc Carthy**

Head of Department: **Prof. John McInerney**

Department of Physics

University College Cork

Contents

Declaration

The thesis submitted is the author’s own work and has not been submitted for another degree, either at University College Cork or elsewhere.

Abstract

The tokamak concept for a commercial nuclear fusion reactor is a promising one. However, a number of issues must be resolved to reach this goal, including effective mitigation of plasma instabilities such as Neoclassical tearing modes (NTMs). Diagnostics systems provide the crucial information required to further understand the physics of such phenomena and a key diagnostic is Thomson scattering (TS), which determines the electron temperature (T_e) and density (n_e) of plasmas. This thesis describes upgrades to the two TS diagnostic systems (ruby and Nd:YAG) on Mega Amp Spherical Tokamak (MAST) , improving their spatial and sampling rates and reducing T_e and n_e errors, and the use of these upgraded systems to study NTMs in greater detail than was previously possible on this machine. Specifically, the contributions of the different stability terms of the modified Rutherford equation (MRE) to the evolution of 2,1 NTMs were investigated using data from the upgraded TS systems and other diagnostics systems on MAST. The upgraded ruby TS system can now resolve 200 points along a 1.4 m chord, the number of points being more than any other current Television TS (TVTS) systems. The uncertainty in T_e and n_e has reduced to $<$ 4% and $<$ 3% for a observation volumes with a radial extent of 7mm in the range of 40 eV - 2 keV and at a density of $n_e = 2 \times 10^{19}$ m^{-3}. The sampling rate is also improved and the system can now measure two images at a separation of 230 μs and be operated in either a double pulse mode (two T_e and n_e profiles measured) or single pulse mode (one T_e and n_e profile and one background light). The upgraded Nd:YAG TS system has a 1 cm spatial resolution and a 240 Hz sampling rate, with lasers now capable of firing in burst mode. Measurements from the two upgraded TS systems were compared and their T_e and n_e profiles agreed well. Following these upgrades, these two TS systems now permit TS measurements of the finite island width stability term on MAST for the first time and measurements of this stability parameter were used in investigations of 2,1 NTM evolution on MAST. The finite island width was determined by fitting a heat transport model to TS measurements of T_e from the upgraded ruby and Nd:YAG systems. In addition, other stability parameters of the MRE were estimated, based on TS, charge exchange recombination spectroscopy and Mirnov coil measurements (and using CHEASE and NCLASS codes) from the same MAST shots. The pressure of the MAST plasma was varied using an external heat source and this enabled a comparison between 2,1 NTM evolution determined using the MRE to that from magnetic measurements of island evolution. A good agreement was found. In addition, these experiments were used to assess the relative contributions of the different MRE stability terms for 2,1 NTMs on MAST, using a fitting approach. The results show that the tokamak curvature stability term is the principal stabilising term and is comparable in magnitude to the principal destabilising term, the bootstrap term. In addition, the finite island width is shown to be a crucial term for determining

the onset threshold of 2,1 NTMs on MAST. In contrast, the ion polarisation term is found not to influence the evolution of these 2,1 NTMs. Finally, to permit a greater number of finite island width measurements and more reliable pressure scan experiments, an FPGA triggering system has been developed and initial tests indicate it operates as designed. This system permits TS measurements to be synchronised with the phase of the rotating island and triggers the TS laser on different points of the NTM evolution. Furthermore, it can change the Z position of the MAST plasma in real-time, which results in a drop in plasma pressure at the location of the island. This permits more reliable pressure scan experiments. The NTM stability term results presented in this thesis represent the first step in such NTM evolution research on MAST and the combination of the improved TS capabilities and the new triggering system will permit the further, more accurate diagnostic measurements required to achieve a greater understanding of these instabilities and potentially lead to effective mitigation techniques.

Acknowledgements

I would like to say thank you to my numerous supervisors, Dr. Sean Prunty, Dr. Michael Walsh, Dr. Graham Naylor and Dr. Paddy Mc Carthy for their advice and support throughout my research. I'm also very grateful to Dr. Rory Scannell for his advice and help throughout my PhD. Also, thanks to Martin Dunstan and Nigel Thomas-Davies for providing lots of help with the practical running of the TS diagnostics.

I would like to thank Dr Keiran Gibson at the University of York for his support and advice about NTMs. I would also like to thank Jack Snape, Billy Huang and Dr Koki Imade at the University of York for their help and discussions about NTMs and FPGAs. Thank you to everyone at Culham Science Centre for making it a fun and interesting place to work over the last few years. I feel fortunate to have had the opportunity to work with so many acomplished scientists during my PhD.

I am grateful to my collaborators in both the Culham Science Centre and the University of York and for allowing me to use their data in my research. Finally, thank you to the Euratom Mobility programme and UCC for their financial support during my PhD.

On a more personal note, thanks to Jenni for her endless help and patience throughout this thesis and to Lana Al-Shami and Scooby for their help with my house move to York and advice on diagrams. Finally thanks to my parents, my sisters and my friends for their support.

Abbreviations

Abbreviation	Description
eV	electron volts
F/#	F/ number (focal ratio)
HeNe	helium neon
Nd:YAG	neodymium doped yttrium aluminium garnet

Acronyms

Acronym	Description
CPLD	complex programmable logic device
CXRS	charge exchange recombination spectrography
ECE	electron cyclotron emission
ECCD	electron cyclotron current drive
EQE	effective quantum efficiency
ELM	edge-localised mode
FPGA	field programmable gate array
FWHM	full width half maximum
HFS	high field side
ITER	International Thermonuclear Experimental Reactor
JET	Joint European Torus
LIDAR	Laser Imaging Detection and Ranging
LFS	low field side
MAST	Mega Ampere Spherical Tokamak
MCF	magnetic confinement
MCP	micro channel plate
MHD	magneto-hydrodynamics
MRE	modified Rutherford equation
MTF	modulated transfer function
MSE	motional stark effect
NTM	neoclassical tearing mode
NBI	neutral beam injector
OD	optical density
PSF	point spread function
QE	quantum efficiency
TS	Thomson scattering
TVTS	Television Thomson scattering
SOL	scrape-off layer
SXR	soft xray

Symbols

Symbol	Description
c	speed of light
ϵ_0	permittivity of a vaccuum
m_0	rest mass of an electron
n_e	electron density
T_e	electron temperature
w_c	critical island width
w_d	finite island width

Chapter 1

Introduction

This chapter briefly introduces fusion as an energy source, before looking at magnetic confinement, the tokamak concept and spherical tokamaks. The challenges faced to achieve a commercial fusion powerplant are then discussed, focusing on the effects of NTMs and the important role of diagnostics in investigating these and other instabilities. Finally, an outline of this thesis is given.

1.1 Nuclear fusion

Nuclear fusion is the method by which the stars produce their energy and controlled fusion on earth represents an ideal energy source as it is both sustainable and environmentally friendly, avoiding the environmental damage and high CO_2 emissions associated with fossil fuels. Deuterium and tritium are used as fuel and these are, respectively, either readily available or can be produced during the reaction. The waste products from fusion have a short half-life and are safe to dispose of within a short timescale. Controlled fusion is therefore a potential solution to meet the ever-increasing world energy demand, which is expected to increase 36% in the best-case scenario by 2035 [1].

During nuclear fusion, two light nuclei are fused to form a new set of elements. As the total mass of the reaction products is less than the total initial mass, this results in the release of energy (according to Einstein's equation ($E = \Delta mc^2$)). Nuclear reactions are governed by the strong nuclear force, which has a range of $\sim$ one fermi (10^{-15} m). However, for distances larger than a few fermi, the repulsive Coulomb force between the two nuclei becomes dominant. For two nuclei to fuse, they must therefore gain sufficient energy to produce a finite probability that they can 'tunnel' through the Coulomb barrier (figure 1.1).

The most promising nuclear fusion reaction is between two different isotopes of hydrogen, deuterium (^2H, 'D') and tritium (^3H, 'T') because it has higher cross-sections at lower temperatures (figure 1.2). This D-T reaction produces a 3.5 MeV alpha particle (^{4}He) and a 15.1 MeV neutron

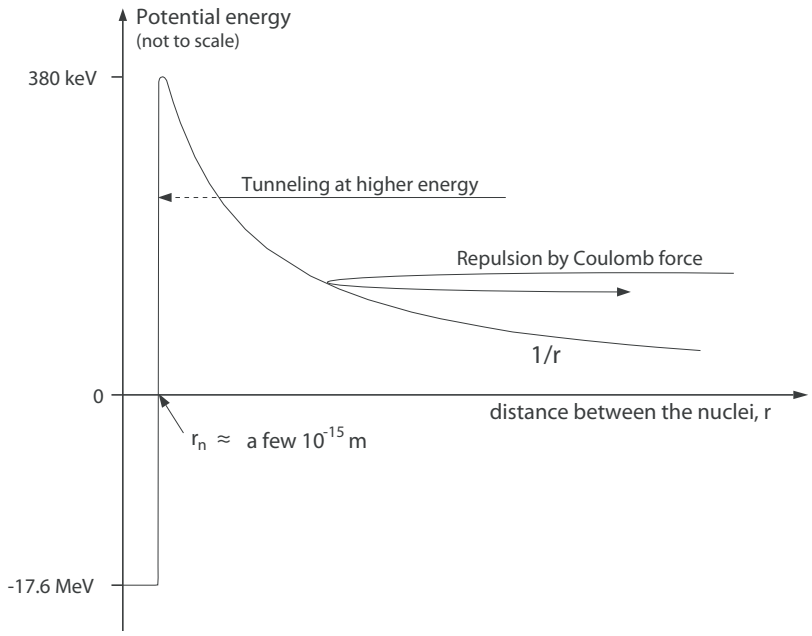

Figure 1.1: The potential energy of two nuclei as a function of the distance between them (r). Once the nuclei gains sufficient energy to permit it to tunnel through the Coulomb barrier, as needed for fusion to occur. Once the nuclei have overcome the Coulomb barrier, the strong nuclear force becomes dominant (r_n is the range of this force). The energies shown are for deuterium and tritium.

(n) and is given by:

$$^2\mathrm{H} + ^3\mathrm{H} \rightarrow \ ^4\mathrm{He}(3.5\ \mathrm{MeV}) + \mathrm{n}(15.1\ \mathrm{MeV}). \tag{1.1}$$

Deuterium is an abundant fuel and occurs with a weight fraction of 3.3×10^{-5} in water. This means that there is sufficient deuterium to produce fusion energy for billions of years. Tritium is more difficult to obtain as it is an unstable radioactive isotope that decays with a half life of 12.3 years:

$$^3\mathrm{H} \rightarrow \ ^3\mathrm{He} + \ \mathrm{e} + \ \bar{\nu} \tag{1.2}$$

However, tritium can be produced as part of a fusion reaction by using the neutrons produced from the D-T reaction and reacting these with a lithium blanket, thus overcoming this problem:

$$\mathrm{n} + \ ^7\mathrm{Li} \rightarrow \ ^4\mathrm{He} + ^3\mathrm{H} + \mathrm{n'} - 2.5\ \mathrm{eV} \tag{1.3}$$

In a controlled nuclear fusion reaction deuterium and tritium are therefore used, and these fuel atoms are in a plasma state (an ionised gas) at the temperatures required for fusion to occur, and the resulting neutrons can be used to generate electricity. Fusion reactions are therefore potentially self-sustaining, as the energy from the alpha particles (^{4}He) produced during the fusion reaction can sustain the D-T reaction and the neutrons produced can also be used to breed tritium (as above). Reaching a self-sustaining state is the aim of controlled fusion and for this to occur the alpha particle heating must be sufficient to maintain the plasma temperature against thermal losses and

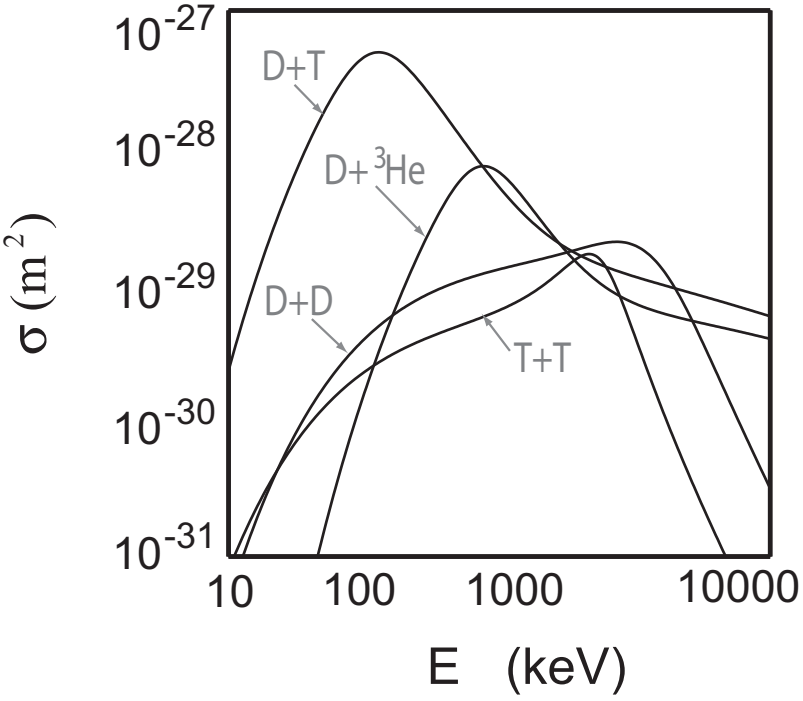

Figure 1.2: The cross-sections (σ) for fusion reactions using different fuels. These fuels are deuterium (D), tritium (T) and helium 3 (^{3}He). The D-T reaction shows the highest σ at lower energies.

the plasma must be kept at a sufficient density by the confinement scheme for a sufficient length of time. This self-sustaining state is called ignition and the requirements of temperature, density and time to achieve this are defined by Lawson's criterion [2] for ignition:

$$n_e T_e \tau_E \geq 5 \times 10^{21} (m^{-3}.keV.s) \tag{1.4}$$

where, n_e is the electron number density, T_e the electron temperature and τ_E the energy confinement time, which is the rate at which the plasma loses energy.

1.2 Magnetically confined fusion

In order to meet Lawson's criteria for ignition, the plasma must be isolated from material surfaces, to prevent both thermal losses and to achieve sufficient confinement time and density. As plasma is an ionised gas which can be contained in a magnetic field, due to the Lorenz force, these fields can be used as a means of confinement. This approach is referred to as magnetic confinement fusion (MCF). Most MCF schemes are toroidal, as this shape prevents end losses and thus maximises confinement time, and a range of these schemes have been developed. These include the stellarator, the reverse field pinch and the tokamak.

The most successful MCF scheme to date is the tokamak. This is a toroidal machine designed to confine a plasma in the shape of a torus (figure 1.3). Toroidal, poloidal and vertical magnetic fields

are used to confine the plasma in a stable equilibrium. The toroidal and vertical fields are produced by magnetic field coils, which are generally placed outside of the vessel, and the poloidal field is generated by the plasma current. The plasma current flows toroidally and can be generated by transformer action (inductive current drive) or by using non-inductive methods. The combination of the vertical, poloidal and toroidal fields produces a complex helical field that achieves a high level of plasma stability. This stability allows longer confinement times, at higher densities, than other MCF schemes.

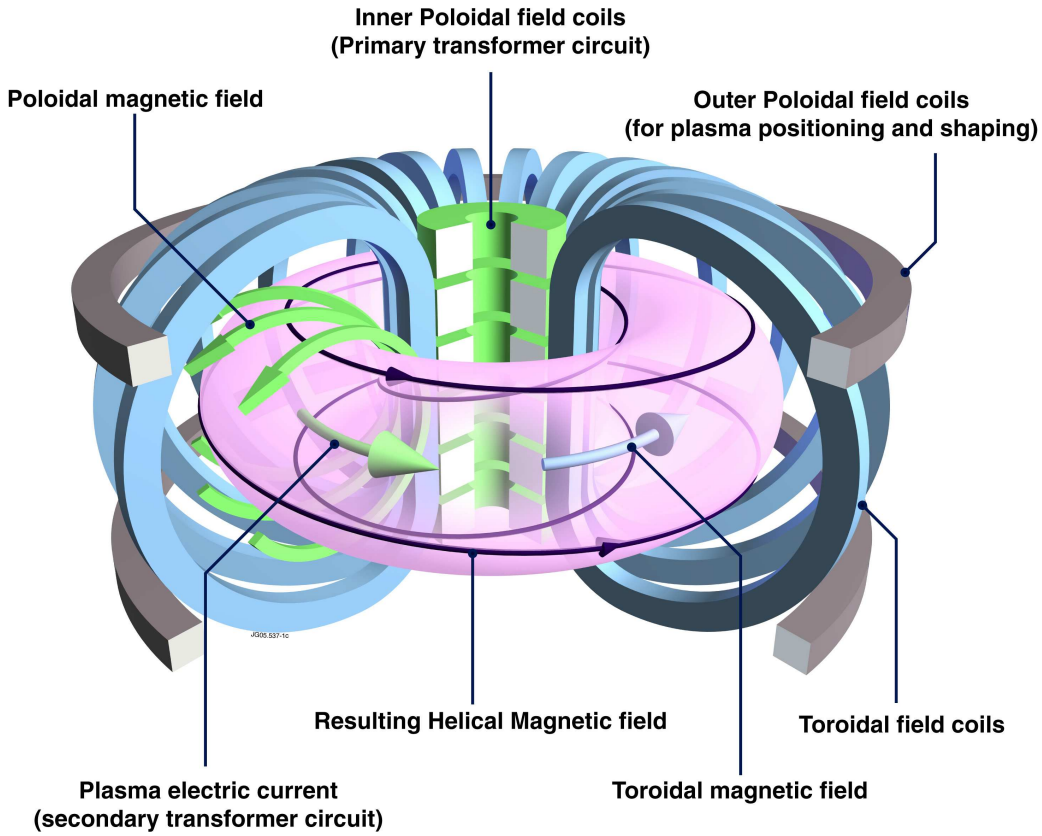

Figure 1.3: Currents and magnetic fields in a tokamak. The plasma is shown in pink and this is surrounded by the toroidal magnetic field coils (blue). A transformer in the centre of the torus (green) is used to generate the plasma current (direction indicated by horizontal green arrow), which in turn generates the poloidal magnetic field (green arrows). The outer poloidal field coils (grey) are used for shaping and positioning the plasma. The helical field line (black line), that results from the combination of the toroidal and poloidal fields is on a rational (q=4) surface in this example. Drawing *jg05-537-1c* obtained from JET drawing office.

The combination of toroidal and poloidal fields in the tokamak produces helical field lines (figure 1.3) which lie on a set of nested 'flux' surfaces. Each field line is characterised by the number of times it travels poloidally (n) and toroidally (m) around the tokamak. The ratio of m to n is given by the safety factor (q), which is an important parameter for stability. On flux surfaces where q is a rational number the field line will travel n times poloidally and m times toroidally

before closing on itself, whereas when q is an irrational number the field-lines will never close on themselves, but instead map out the entire flux surface.

Charged particles in the plasma follow a helical path around these field lines and are therefore, to a first approximation, confined to the flux surfaces. In practice, however, particle drifts occur and lead to particles and energy migrating across flux-surfaces and leaving the core plasma. These drifts are caused by both the curvature of the field lines and instabilities and the challenge is, therefore, to reduce these to minimal levels in order to satisfy Lawsons criterion and achieve ignition. Rational q surfaces are more prone to instabilities, due to the field lines not covering these surfaces ergodically, and this is important for stability analysis.

1.3 Confinement in tokamaks

The energy confinement time (τ_E) in Lawson's criteria equation (equation 1.4) is used to indicate the performance of a tokamak and is given by the ratio of the total plasma energy to the rate of energy loss. τ_E can be easily determined as the total plasma energy can be calculated using equilibrium codes (such as EFIT on MAST) and the power entering the plasma can be determined by the sum of the Ohmic heating from the plasma current and the external heating, from sources such as neutral beam injection (NBI) and electron cyclotron resonance heating (ECRH).

Over the past 50 years, various confinement regimes on tokamaks have emerged. The simplest, and original, regime is Ohmic confinement, where all of the plasma energy comes from Ohmic heating from the plasma current. This regime has very good confinement time (τ_E^O), which is found to scale with the size of the tokamak (aR^2)[3]:

$$\tau_E^O = 0.07 \bar{n_e} a R^2 q_{edge}. \tag{1.5}$$

where τ_E^O is in seconds, $\bar{n_e}$ is the average electron density in 10^{20} m^{-3}, R is the major radius, a is the minor radius and q_{edge} is the safety factor at the edge of the plasma. The scaling of this Ohmic regime led to initial optimism that ignition could be achieved if a large enough tokamak was built. However, as Ohmic heating is the result of plasma resistivity, which reduces with T$_e$, it was found that ignition is not possible without auxiliary heating.

A new confinement regime that includes auxiliary heating was subsequently developed. This is known as low confinement mode ('L-mode'). The energy confinement time (τ_E^L) in this regime is low and is far less than had been predicted from the Ohmic regime results[3]:

$$\tau_E^L = 0.037 \frac{I R^{1.75} \kappa^{0.5}}{P^{0.5} a^{0.37}} \tag{1.6}$$

where I is the plasma current in MA, κ is the elongation of the plasma and P is the applied heating in MW.

An improved confinement regime, known as H-mode or high confinement mode, was discovered on the ASDEX tokamak. It was found that when the power injected is increased above a threshold value, the plasma undergoes a transition from L-mode to H-mode and the energy confinement time is increased by a factor of two [3]. This improvement in τ_E results from the formation of a transport barrier at the edge of the plasma, called the H-mode pedestal. This pedestal is unstable and periodic relaxations in pressure, which release energy from the plasma, are observed. These relaxations are called edge localised modes (ELMs) and the amount of energy they release into the vessel wall is a major concern for future next step devices such as ITER.

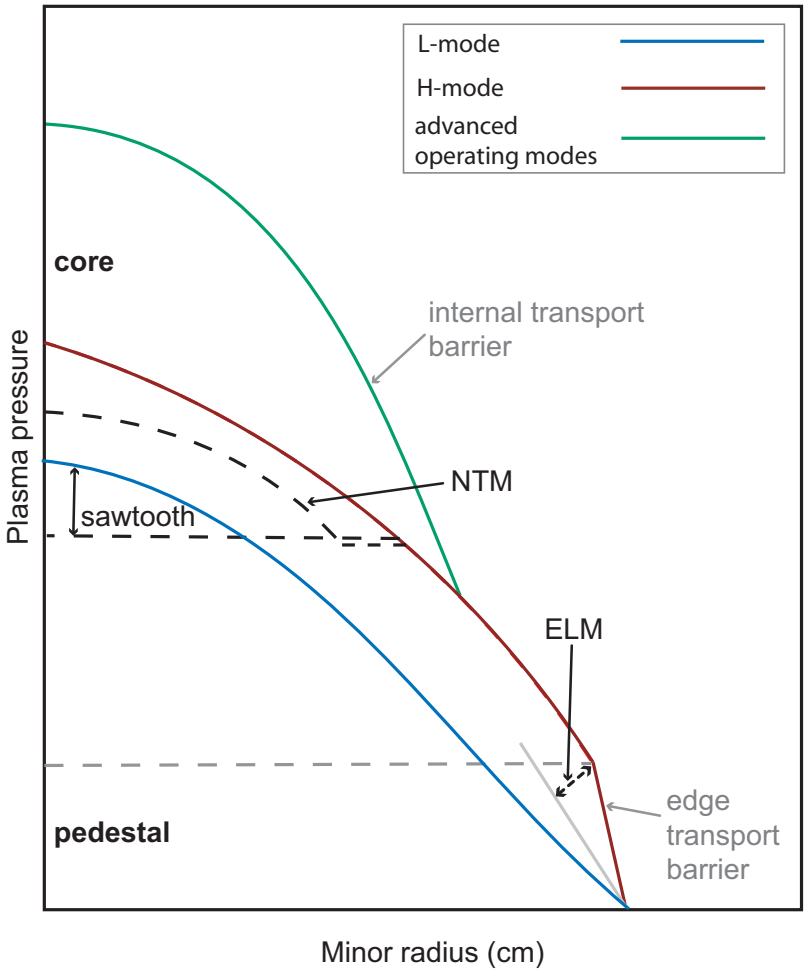

Figure 1.4: The effect of different confinement modes and instabilites on tokamak plasma pressure. This illustrates the improvement in plasma confinement from L-mode (blue line), to H-mode (red line) and the advanced operating modes (green line). The effects of sawteeth, ELM and neoclassical tearing mode instabilities on confinement are also shown (black dotted lines). The height of the edge pedestal is shown as a grey dotted line. Drawing *jg05-537-1c* obtained from JET drawing office.

More advanced confinement regimes have been developed that have further improved confinement compared to the H-mode regime (figure 1.4). Importantly, these regimes are designed to

permit tokamaks to operate in a steady state, which is required for fusion power plants to be more efficient. Steady state is currently not possible because using a transformer to induce the plasma current makes the tokamak a pulsed machine. These regimes focus on using a non-inductive source to generate the toroidal current. This source is called the 'bootstrap' current and is self-generated from gradients in the electron pressure. For these scenarios, an H-mode edge pedestal and internal transport barriers (ITBs) are required. ITBs are created by the suppression of turbulence in the vicinity of rational q surfaces and are associated with non-montonic q profiles (where a q profile is peaked in the centre of the tokamak with a negative core magnetic shear ($s = rq^{-1}dq/dr$)). This type of q profile can be formed by using early auxilliary plasma heating and once the ITB is formed, the q profile can be sustained by the induced 'bootstrap' current. These advanced confinement regimes can greatly improve confinement, but require very accurate control of the plasma parameters and are not yet routinely produced on any tokamak.

1.4 Beta limit

The confinement efficiency of a tokamak can also be expressed in terms of β, which is defined as:

$$\beta = \frac{2\mu_0 p}{B^2} = \frac{plasma\ pressure}{magnetic\ field\ pressure}, \tag{1.7}$$

As generating the toroidal field is the major cost of a potential fusion reactor, it is desirable for the value of β to be as large as possible. However, the maximum value achievable on tokamaks is usually limited by the onset of various types of magnetohydrodynamic (MHD) instability which occur at higher β values. The main β-limiting instability is the kink mode [3] and investigations [4, 5, 6] have shown that the maximum β achievable (β_{max}) before the plasma becomes unstable to these modes can be expressed as:

$$\beta \leq \beta_{max} = 0.72\frac{1+\kappa^2}{2}\epsilon \tag{1.8}$$

where ϵ is the inverse aspect ratio (and $\epsilon = a/R$). β_{max} can therefore be increased by increasing the ϵ or κ of the tokamak. This result led to the development of spherical tokamaks (ST), in which both these quantities are much higher than in conventional tokamaks and thus higher β_{max} values are achieved.

1.5 Spherical tokamaks

The ST concept (figure 1.5) was originally proposed by Peng and Strickler [7] and the first experimental device, the Small Tight Aspect Ratio Tokamak (START), was built at the Culham Laboratory in the early 1990s. This device produced electron temperatures of ~ 100 eV and record β

values of 40% [8], substantially higher than the previous record of 12.6% measured on the large aspect ratio DIII-D machine. As a result, a large number of STs have been built worldwide and include PEGASUS (USA), GLOBUS-M (Russian Federation), ETE (Brazil), TST-2 (Japan) and two larger mega-ampere devices, NSTX (USA) and MAST (UK).

There are many advantages of the STs over conventional tokamaks [9, 10]. In particular, The proximity of the plasma to the central solenoid in an ST allows a more effective use of the toroidal field. Given that generation of this field will be a major expense for future fusion power plants, STs therefore represents a more cost-effective solution and the development of ST power plants (STPP) is one goal of current ST research [11, 12]. This research also focuses on the development of an component test facility (CTF) [13], which is an intermediate step towards a commercial STPP and would permit potential powerplant materials to be tested using high neutron fluxes. Recent work suggests that STs could also be used to burn long half-life nuclear waste from fission reactors [14].

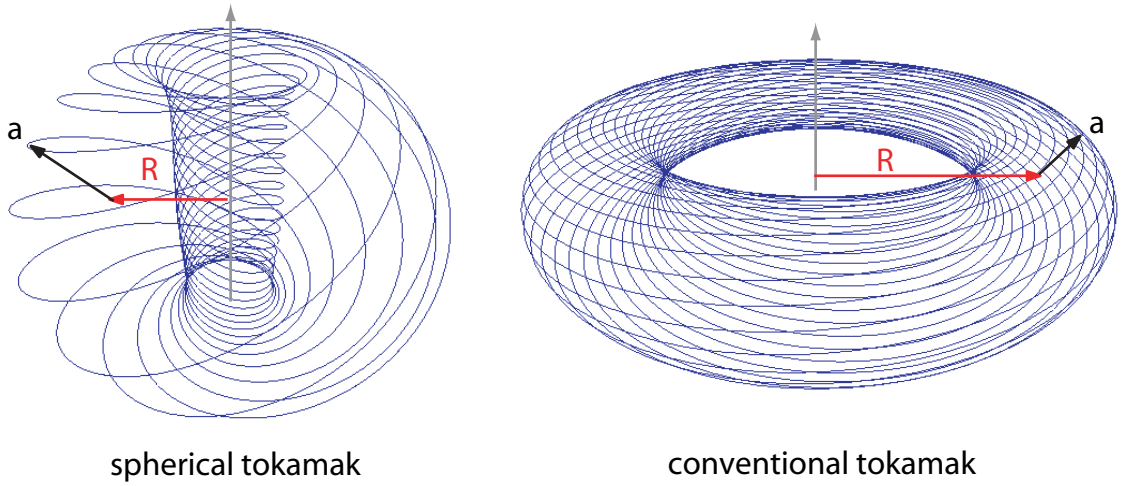

Figure 1.5: Aspect ratios of conventional tokamaks and STs, as indicated by a number of field line traces (blue lines). The major radius (R, red arrow) in STs is smaller than in conventional tokamaks, whereas the minor radius (a, black arrow) is of a comparable value. The resulting small aspect ratio of the ST makes its resemble a cored-out apple in shape, whereas the conventional tokamak resembles a doughnut. Grey arrows indicate the central columns of these tokamaks.

Although the ST concept is less developed than the conventional tokamak concept, a copper coiled ST would provide a lower cost solution for a CTF or STPP. Many of the challenges in developing the ST concept to the commerical powerplant stage are related to the close proximity of both the central solenoid and toroidal field coils to the burning nuclear fusion reaction that will occur in future devices. The limited space on this inboard side reduces the amount of shielding from high energy neutrons that can be applied and thus the lifetime of these components. The limited space also reduces the maximum toroidal field possible. Another challenge for a viable STPP is to generate a sustained toroidal current from the bootstrap current. It has been shown that

for a steady state or long pulse STPP or CTF, the majority of the toroidal current (90%) needs to be provided by the bootstrap current [12], as driving the current by other means would significantly increase their cost. However, this bootstrap current also provides the main drive for neoclassical tearing modes (see details in section 1.7 and in Chapter 5) and a greater understanding of these instabilities is needed. Experiment results from MAST, NSTX and other STs will determine the future and viability of the ST concept. The MAST ST specifically is introduced in chapter 2 as all of the work presented in this thesis has been carried out on this tokamak.

1.6 The Bootstrap Current

The bootstrap current is vital for steady state operation on tokamaks (as briefly discussed in section 1.3) and studies indicate that bootstrap fractions greater that 70% are required for an economically viable fusion reactor [6]. However, current machines typically do not reach this value. The existence of a bootstrap current was first predicted from neoclassical transport theory [15], which includes the effects of toroidicity on the plasma transport.

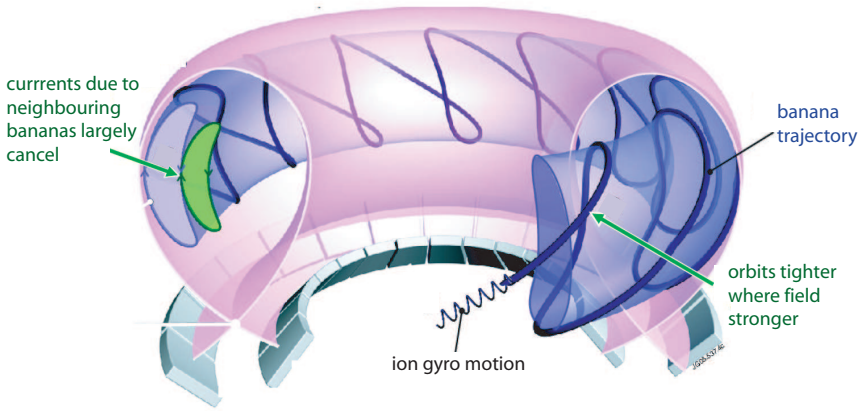

Figure 1.6: Origin of the bootstrap current. The pink surface represents the plasma boundary and the trajectory of the trapped particles (banana trajectory) is shown as a dark blue line. The projection of this trajectory on the poloidal plane has a banana shape (purple banana shape) and is referred to as a banana orbital. A second banana orbital (green banana shape) is shown to illustrate the interaction between two adjacent orbitals, where particles move in opposite direction (see arrows), which produces the bootstrap current if a density gradient exists. Drawing *jg05-537-1c* obtained from JET drawing office.

The bootstrap current arises due to the interaction between passing and trapped particles in the plasma. These particles are defined by how they are affected by the magnetic mirror that forms in the tokamak as a result of the radial gradient of the toroidal magnetic field. As particles follow the helical magnetic field lines they will encounter an increasing magnetic field as they approach the inner wall side of the torus and those with sufficient parallel kinetic energy will overcome the

magnetic mirror effect and become 'passing particles'. These passing particles are then free to follow the helical field lines around the torus. In contrast, particles with insufficient parallel kinetic energy are reflected back to the low field side of the tokamak and are know as 'trapped particles'. The projections of these trapped particle orbits onto the poloidal plane are banana shaped (figure 1.6) and referred to as 'banana orbits'.

On the outer side of each banana orbital, particles are moving in the direction of the toroidal current, whilst on the inner side they are moving against it. At the intersection between two banana orbits, there are therefore particles moving with and against the toroidal current. If both orbitals contain the same number of particles, then there is no net current in this region. However, if a density gradient exists there will be a net banana orbital current drive and this current is transfered from the trapped to the passing particles through collisional coupling. This current now carried by the passing particles is the bootstrap current.

1.7 Neoclassical tearing modes

In addition to the kink mode, a major β-limiting MHD stability is the neoclassical tearing mode (NTM) [16, 17, 18]. A tearing mode is a resistive instability which forms as a magnetic island on rational surfaces inside a tokamak plasma (figure 1.7) and can be classical or neoclassical. Magnetic islands deform the flux surfaces within the tokamak, whereby the temperature profiles are flattened across these islands and this reduces the energy confinement.

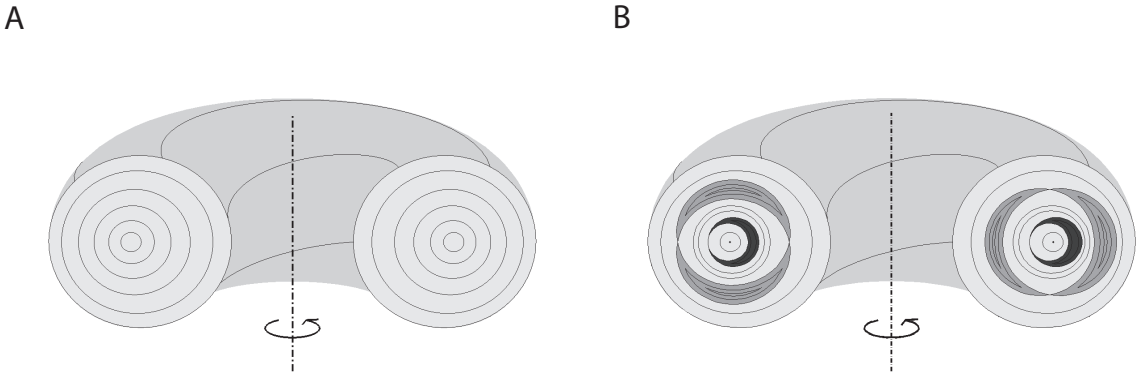

Figure 1.7: Tokamak cross-sections showing the formation of a tearing mode on flux surfaces. A. The flux surfaces (black circles) before the tearing mode forms. B. The deformation of the flux surfaces as a result of two tearing modes, each on a different rational surface. The tearing mode observed in the outer part of the cross section (dark grey shaded region) is a 2,1 and forms on a $q = 2$ surface. The inside tearing mode (light grey shaded) is a 1,1 and forms on a $q = 1$ surface.

In some conditions, a flattening of the pressure across a magnetic island occurs and this leads to a reduction in the bootstrap current at this location, which influences the dynamics of the island

[19]. Where this occurs the instability is referred to as an NTM. In these modes, the missing bootstrap current at this location acts a driving term, which increases the island width until all of the bootstrap current is removed and the island reaches a saturated island size (w_{sat}). A 'hole' in the bootstrap current can be interpreted as a current in the opposite direction that enhances the size of the magnetic island. Saturated magnetic islands can have a radial width as large as 10% of the minor radius (a) and lead to significant reductions in energy confinement time. The effect of saturated NTMs on the energy confinement time (τ_E) can be described using the belt model [20], as given by:

$$\frac{\Delta\tau_E}{\tau_E} = \Delta_\tau \frac{w_{sat}}{a} \tag{1.9}$$

$$\Delta_\tau = 4\frac{r_s^3}{a^3} \tag{1.10}$$

where r_s is the location of the NTM in terms of a. This indicates that NTMs occurring closest to the edge of the plasma will lead to the greatest reduction in τ_E. The most deleterious NTM is the 2,1 NTM, where 2 refers the the poloidal mode number m and 1 to the toroidal mode number n. This type of mode is located on the $q = 2$ rational surface typically at an r/a of ~ 0.8.

In addition to their influence on energy confinement, NTMs can also result in locked mode disruptions of the plasma. These typically occur because magnetic islands rotate with the plasma fluid and induce eddy currents in the tokamak vessel which, in turn, induce a torque which slows the island rotation, thus destablising it. These locked mode disruptions cause the plasma discharge to terminate prematurely and release the plasma energy into the surrounding vessel. NTMs are therefore a major concern for future devices both in terms of confinement and potential damage to the vessel. As a result, a major area of fusion research is investigating the stability and control of these instabilities. NTMs are discussed in greater detail in Chapter 5, section 5.2.

1.7.1 Controlling NTMs

NTMs are likely to be present on future devices, such as the International Thermonuclear Experimental Reactor (ITER) [21, 22] and will need to be controlled. ITER is an important intermediate step towards a commerical tokamak powerplant. This machine is currently being constructed, with its first plasma expected in 2019, and is based on the conventional tokamak design. It will potentially produce 500 MW of power and operate at $Q = 10$, where Q is defined as the fusion power divided by the input heat power and will operate on a number of scenarios, which are designed to produce regimes ranging from the conventional H-mode to advanced operating. To achieve these potential Q values it is important to be able to mitigate NTMs which may cause loss of confinement or disruptions.

A number of different methods to control NTMs have already been developed and are described

in the ITER physics basis [23] and electron cyclotron current drive (ECCD) is the primary tool planned for NTM mitigation on ITER. Up to 20 MW of ECCD power will be injected into the plasma from upper ports and the current induced will both replace the missing bootstrap current and alter $\Delta^{'}$ favourably, in order to stabilise NTMs. Although a number of different experiments on several tokamaks have demonstrated successful NTM stabilisation using this method, a greater understanding of the threshold and onset of these instabilities is still required to determine the exact level of ECCD power needed for effective stabilisation on ITER.

Both the effects of NTMs on the Q and the efficiency of ECCD power in stabilising these (for 2,1 and 3,2 NTMs) has been investigated for the ITER scenario 2 plasma [22]. This was done by simulating effects of an NTM on the predicted Q of this plasma when a range of different ECCD powers were applied to stabilise it (figure 1.8). To include the uncertainty in the predicted performance of this scenario, these simulations were repeated for different H factors, where these factors represent $\pm$ 25% performance variation. The results predict that NTMs can have a significant effect on the values of Q obtained in ITER and that the 2,1 mode will have the greatest effect on plasma performance. It also shows that ECCD can stabilise these modes and improve Q, but the value of Q achieved is still reduced from that of an NTM-free plasma.

The above analysis has not looked at the effects of mode locking, which is an important consideration for ITER due to its potential to cause plasma disruptions. 2,1 NTMs are most likely to lock as they are positioned close to the vessel wall and analysis using ITER-like plasmas in the DIII-D machine [25] suggests that an island width of $\sim$ 5 cm would be a sufficient for a 2,1 NTM, with a rotation frequency of 420 Hz, to lock to the ITER wall. This is much smaller than the predicted w_{sat} for 2,1 NTMs on ITER (24 cm) and therefore locked modes may be a significant problem for ITER operations if 2,1 NTMs are not stabilised before reaching a large width.

As a result of the above findings, investigations of NTMs are being carried out on most tokamaks. In particular, these look to resolve uncertainties about the relative contributions of different stabilising terms to NTM formation and stability. There is currently no full theoretical description of these contributions and NTM evolution. However, large island evolution can be described by resistive MHD theory and small island effects can be modelled using a 2 fluid description or full kinetic theory. The modified Rutherford equation (MRE) [26, 17] uses approximations of the island evolution from these theoretical models to determine the time evolution of NTMs, as a function of these stability terms. A full description of this equation is given in chapter 5. Although the predicted evolution of NTMs determined by the MRE agrees well with experimental measurements on a number of machines, the explicit contributions of the individual stability terms are still uncertain.

In recent years, a number of attempts have been made to measure these stability terms. The main focus to date has been on one stability parameter, the finite island width,this parameter can be

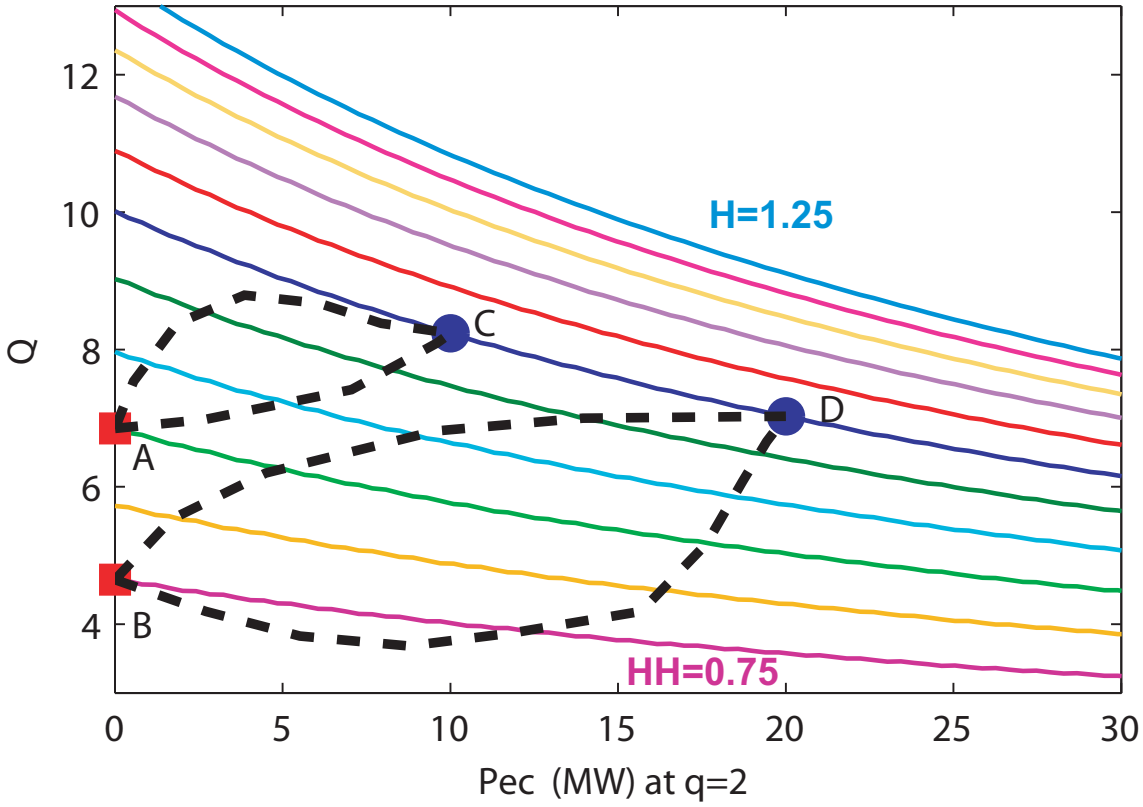

Figure 1.8: The effect of 2,1 and 3,2 NTMs on the values of Q as a function of applied ECCD power. These data were obtained from an estimate of an ITER scenario 2 shot [24]. A number of different coloured lines from blue (H =1.25) to pink (H = 0.75) represent the possible confinement of this scenario. When taking the example of the H=1 case it is observed that if no ECCD is applied, Q values of 4.7 and 6.9 are predicted when 2,1 and 3,2 NTMs are present respectively. In contrast, if the full 20 MW of ECCD power is applied then these Q values increase to 7 and 8.5 respectively. Figure taken from [24]

calculated from the T_e profile around an NTM. The size of this parameter gives the island width, above which the T_e profile is flattened; this flattening results in the bootstrap drive. Experimental measurements of this parameter have been performed on ASDEX [27] and TEXTOR [28] using ECE, but not on MAST or other STs, as ECE systems do not work on these machines. More research is therefore needed, on a wider range of machines, in order to accurately determine both this and other stability terms. These measurements would permit better understanding of the evolution, stability, and therefore mitigation, of NTMs for current and future machines.

1.8 Plasma diagnostics

A large number of plasma diagnostics exist to measure different plasma properties on tokamaks. These diagnostics differ in the types of parameter measured, whether these are measured as absolute values or as relative dependencies and the scale (global or local) on which they are measured. Such

a wide range of measurements are needed to both understand overall plasma behaviour and stability and to examine local properties and phenomena, such as ELMs and NTMs. Examples of diagnostic systems used on the majority of tokamaks include interferometry, soft x-ray, magnetic diagnostics, motional stark effect (MSE), charge exchange recombination spectroscopy (CXRS) and Thomson scattering (TS). This thesis focuses on TS diagnostics, which measure the T_e and n_e of a plasma. The central theme of this thesis is an upgrade of the TS diagnostic systems on the MAST machine. Details of this diagnostic are discussed in detail in chapter 3. One of the principal motivations for the TS upgrade was to study NTMs requiring high radial resolution ($\leq$ 1 cm) and low fractional T_e errors ($\leq$ 5%). Even when these parameters are achieved the sampling of TS systems is low compared to the evolution of NTMs on MAST, so that only a small number of measurements are possible during a plasma discharge. Two important parameters in NTM evolution, the island width and the finite threshold width, have been measured for the first time using a TS system on a spherical tokamak and this has been facilitated by the MAST TS upgrade described. In addition, using MAST CXR, MSE and magnetic diagnostics, additional terms critical to NTM evolution have been estimated.

1.9 Thesis Outline

This thesis focuses on improvements to the TS diagnostic systems on MAST and the use of these upgraded systems to study NTMs in greater detail than was previously possible on this machine. In addition, it considers a triggering system that was developed to enable real-time triggering of TS systems on NTMs. The motivation for this work was to enable more accurate T_e and n_e measurements of a number of plasma phenomona to be made using TS, including NTMs, to contribute to tokamak physics. Publications produced based on this work are listed in appendix C.

In this chapter, a brief introduction is given to nuclear fusion, confinement and tokamaks and some of the challenges for achieving ignition and steady state operation on future tokamak power-plants. In particular, it has been outlined how NTMs are a barrier to this aim and how improved understanding of the factors contributing to NTM evolution is needed for effective mitigation techniques to be developed. Chapter 2 builds upon this introduction, by outlining the components and capabilities of the MAST tokamak. It then provides details of the operational control of MAST and the specific diagnostics and codes that are relevant to the results in this thesis, with the exception of TS (see chapter 3 description). Finally, the programmable hardware devices used to develop the upgraded triggering system are introduced.

Chapters 3 and 4 focus on the upgrades to the TS systems on MAST. Chapter 3 describes TS theory and the two TS MAST diagnostic systems, the ruby and Nd:YAG systems, in some detail. It then presents details of the upgrade to the Nd:YAG system and outlines the new system

capabilities. In addition, other work contributing to TS diagnostic improvements on both MAST and the proposed ITER LIDAR TS system are described. These are a method to reduce systematic errors on the Nd:YAG system, reduction of potential systematic errors in the filter design of the LIDAR system and finally, improvements of TS edge pedestal fitting.

Chapter 4 then describes the upgrade to the ruby TS system on MAST, which was a central part of my PhD. This system was fully upgraded and all components were replaced in order to provide a sub-cm resolution and reduced noise and this chapter outlines the design considerations, hardware specifications and capabilities of the new system. In addition, calibration of this upgraded diagnostic is described and a number of initial TS results are presented.

By improving the TS diagnostics systems on MAST measurements of the finite island width parameter (as described in section 1.7.1 above) are now possible for the first time on MAST. Chapter 5 first introduces the theory of NTMs, including the MRE equation which describes NTM stability. It then presents novel measurements and estimations of MRE stability parameters, based on TS and other diagnostic measurements (and using a number of codes) on MAST. The relative contributions of these stability terms to NTM stability in a MAST plasma are then investigated in a number of beta scan experiments. Finally, the initial results using a new NTM triggering system, designed to synchronise the TS measurements with the rotating island structure, are presented.

Chapter 2

The MAST Machine and Diagnostics

This chapter introduces the Mega Amp Spherical Tokamak (MAST) machine used for all results presented in the following chapters. Firstly, the components, capabilities and operation of MAST are described, with an example shot illustrated (section 2.1). The principal diagnostics systems on MAST, which are relevant to the study of NTMs, are then discussed (section 2.2). Finally, the codes used in the analysis of MAST data for the results in this thesis are summarised (section 2.3).

2.1 MAST

MAST is a spherical tokamak (ST) (see section 1.4) at the Culham Science Centre, which became operational in 1999. It has been designed to further investigate the ST concept following the success of its predecessor, the small tight aspect ratio tokamak (START) [29]. In particular, the MAST programme aims to establish the physics basis for an ST-based test facility (CTF) [13] and to improve understanding of tokamak physics and engineering, in order to improve the design of next stage machines (such as ITER and DEMO) and a potential ST-based fusion power plant (STPP) [12].

2.1.1 MAST design and capabilities

MAST is a medium size tokamak (figure 2.1) and comprises a cylindrical shaped, stainless steel vessel (4 m diameter $\times$ 4.4 m height) that is designed to sustain a high vacuum within its interior. As for other STs, it has a low aspect ratio, which permits high beta operation (see section 1.4). The shape of STs permits improved access compared to conventional tokamaks and on MAST this diagnostic access is via 3 large rings of ports in the vessel.

The toroidal field on MAST is generated by 24 toroidal field coils, located external to the vacuum vessel (figure 2.2A). These coils divide the vessel into 12 sectors and create a toroidal field which has a value of 0.55 T at the major radius (R) and varies strongly across the tokamak,

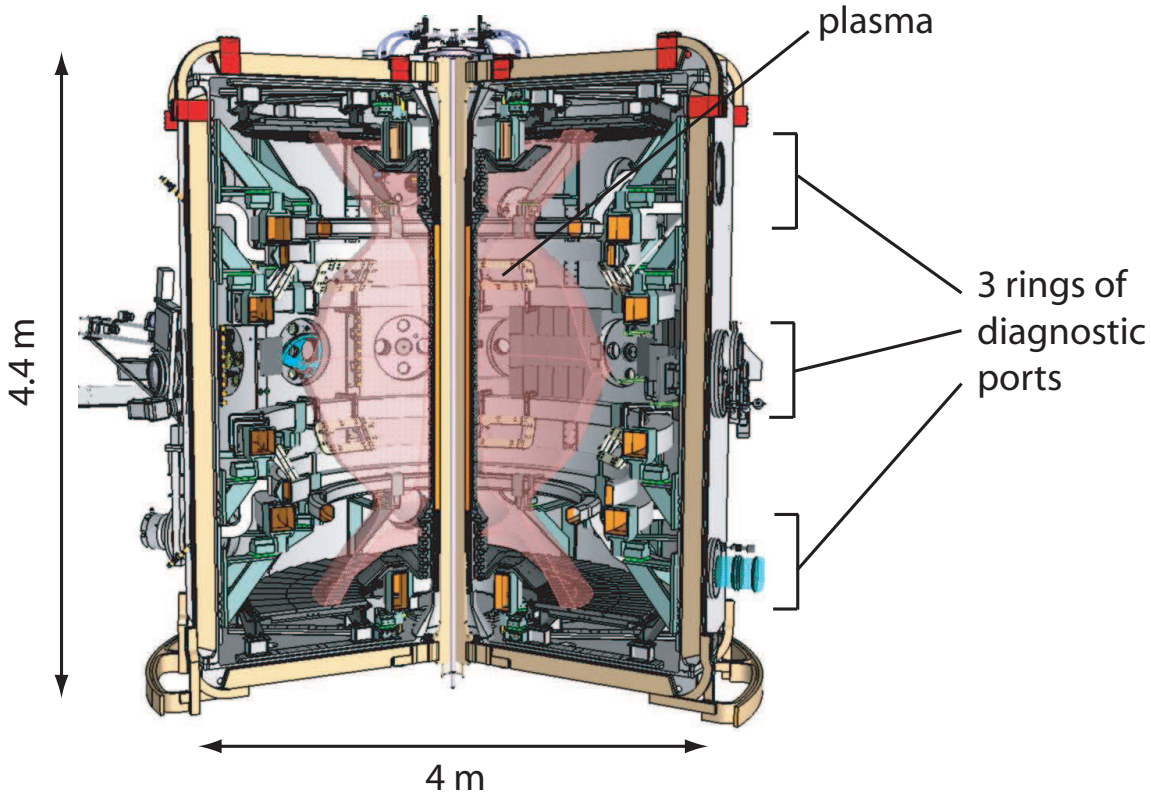

Figure 2.1: Cross-section of the MAST machine, showing the dimensions of the vacuum vessel. Rings of diagnostic ports are indicated and the shape of a typical plasma is shown in pink.

from 2 T at the inboard to 0.25 T at the outboard. Poloidal field coils are located inside the vessel (figure 2.2B) and comprise a central solenoid (P1 coil) and an additional 5 coil pairs (P2-P6 coils). These coils create the poloidal field and are used to give the plasma its shape, provide plasma positional control and also counteract the hoop force, which would otherwise push the plasma to a larger radius. Both the poloidal and toroidal coils are water cooled to dissipate the Joule heating that occurs during their operation. There are additional coils on MAST, including toroidal Alfvén eigenmode coils and ELM coils, which are used for studies of Alfvén eigenmodes and ELM mitigation respectively.

External plasma heating is mainly provided by two neutral beam injectors (NBIs), which have a combined heating power of 5 MW (2.5 MW each). These NBIs can also introduce momentum into the MAST plasma, resulting in a toroidal velocity of ≤ 300 km/s, which may play some role in suppressing turbulence and increasing MHD stability [30, 31].

There is a large range of diagnostics systems on MAST, including TS, charge exchange spectroscopy (CXRS), magnetic coils, soft x-rays (SXR), motional Stark effect (MSE), interferometer, beam emission spectroscopy and a large number of fast cameras. The TS diagnostic system is described in detail in chapter 3 and the remaining diagnostics systems that have been used for NTM

studies (in chapter 5) are outlined in section 2.2.

Parameter	**Value**
Maximum plasma current (MA)	1.5
Major radius, R (m)	0.9
Minor radius, a (m)	0.6
Toroidal field (T)	0.55 (at R)
Maximum shot length (s)	0.7
NBI heating power (MW)	5 (each NBI at 2.5 MW)
Typical core T_e (keV)	0.5-1.5
Typical core n_e (m^{-3})	1-5 x 10^{19}
Typical core velocity (km/s)	300
Plasma volume (m^{-3})	10
Vessel volume (m^{-3})	50
Inverse aspect ratio, ϵ	0.75
Elongation, κ	$1.6 \leq \kappa \leq 2.5$
Triangularity, δ	$\delta \leq 0.5$
Maximum β	15%

Table 2.1: Table to show key MAST parameters. κ and δ are defined in figure 2.3

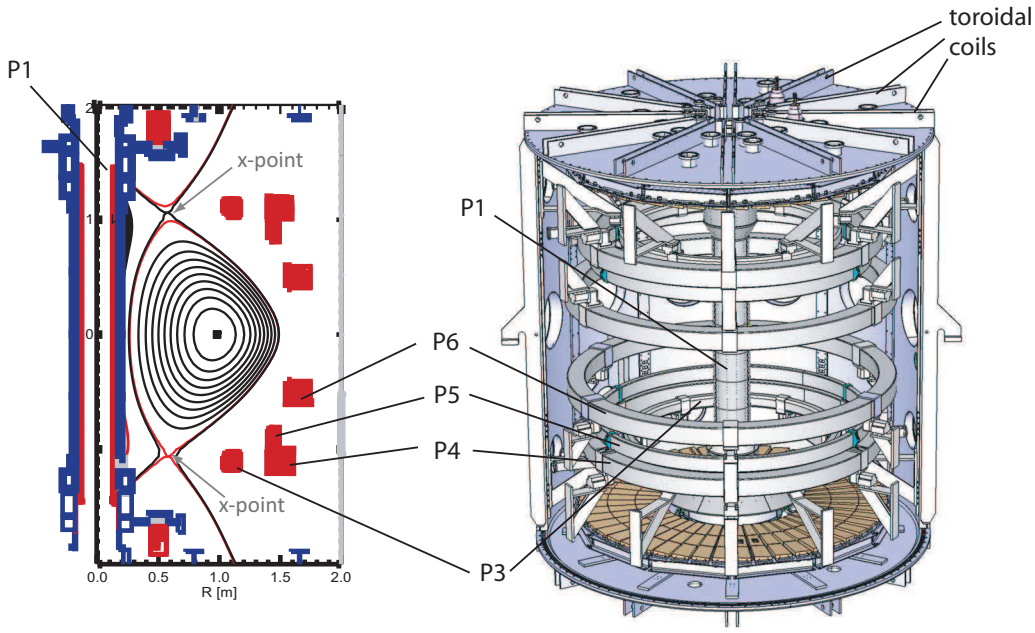

Figure 2.2: The toroidal and poloidal field coils of the MAST vessel. The locations of the poloidal coils P1-P6 are indicated on both the poloidal cross-section diagram and the 3D illustration; P1 is located in the centre column, while the P2-P6 rings encircle the plasma. A connected double null equilibrium plasma shape (see section 2.1.2) is seen in the poloidal cross-section diagram.

MAST is capable of producing plasmas with currents up to 1.5 MA, although currents of $\sim$ 750 kA are more typical. The maximum beta achieved to date is $\sim 15\%$ and it can also achieve a maximum core T_e of 1.5 keV and a maximum core n_e of 5 x 10^{19} m^3. The shot duration is typically 0.3-0.5 s and the maximum duration possible at present is 0.7 s. This duration time is limited by the Joule heating of the coils, but is predicted to increase to 1-2 s following the planned MAST upgrade. A summary of the main engineering capabilities of MAST is given in table 2.1.

2.1.2 MAST operation and a typical shot

It is possible to generate a range of different scenarios on MAST, principally by adjusting the currents in the poloidal field coils and altering the quantity and onset times of both the gas fuelling and NBI heating. These scenarios can vary in terms of beta, q profile, electron and ion temperatures, as well as plasma current, shape, density and performance; the particular scenario required will depend on the plasma physics issue being investigated. In the case of the NTM investigations (chapter 5), high performance hybrid scenarios have been mainly used, which are characterised by early NBI heat, fast current ramps and strong inboard gas fuelling. In addition, a connected double null (CDND) plasma shape (figure 2.3) is typically used for NTM studies, as it is found to

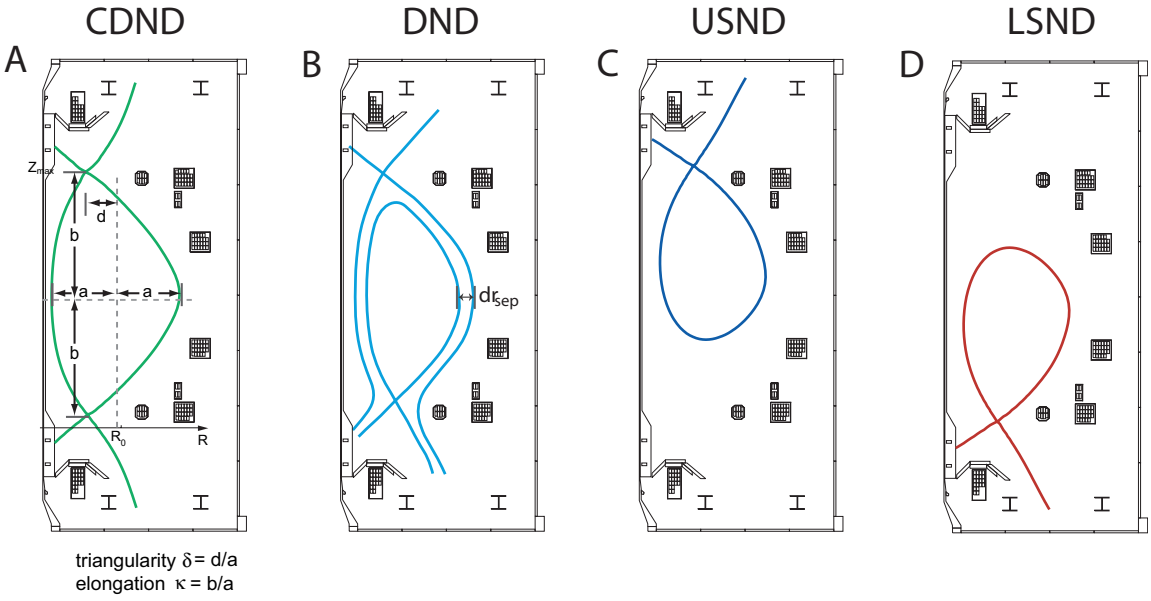

Figure 2.3: Four categories of plasma shape on MAST. These categories are A. connected double null (CDND), B. disconnected double null (DND), C. upper single null (USND) and D. lower single null (LSND). In CDND discharges, the two x-points are located on the same flux surface, whilst in DND discharges the x-points are located on different flux surfaces. The difference between the minor radii of the upper and lower x-point locations of a DND plasma is defined as dr_{sep}. Plasma elongation (κ) and triangularity (δ) are two important parameters which are used describe all plasma shapes and these are defined in A.

produce higher beta values than other shapes. However, the new NTM triggering system on MAST

(section 5.7) changes the plasma from this shape to a disconnected double null (DND) shape, in order to drop plasma beta during beta scan experiments (section 5.7.2).

In a typical MAST shot, the plasma current waveform follows the pattern shown in figure 2.4 and is predominantly controlled by the P1 and P3 coil fluxes. 100 ms prior to the shot, the P1 coil is ramped up to its maximum current ($\sim$ 40 kA) and the P2 coil is used to counteract the stray field from P1 and also to create the magnetic null (x-point). Once P1 has reached $\sim$ 40 kA, deuterium gas is puffed into the vessel at a number of locations and the P1 current is gradually decreased; this downward flux both initiates and sustains the plasma current. At this time, the current in the P3 coils is ramped up to maximum and quickly down again, with the drop starting at the same time as the decrease in P1 current. This reduces the flux required by P1 to initiate the plasma current.

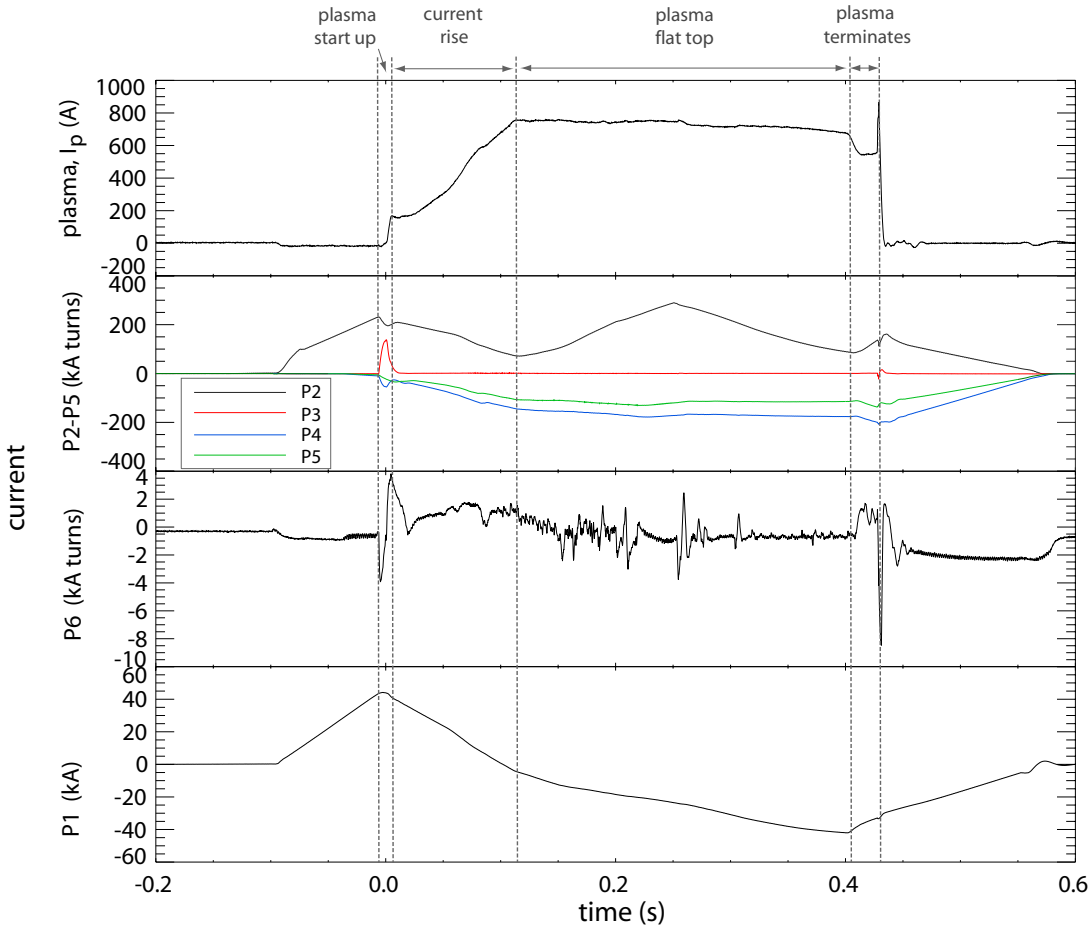

Figure 2.4: The time evolution of a typical MAST shot. All plots show current evolution from -0.2 s to 0.6 s; plasma current is initiated at time 0 s. The top plot shows the plasma current and shows a typical current shape and the key stages during a shot. The lower plots show the poloidal coil currents for P2-P5 (second plot), P6 (third plot) and P1 (bottom plot). These show the waveforms of the P1-P6 currents during a shot and in particular how P1 influences plasma current.

The plasma current increases to 500-900 kA in $\sim$ 0.1 s and then levels out to a specified 'flat

top', with the rate of change of the P1 current reduced to sustain this level (figure 2.4). This flat top continues until the shot is terminated, which either occurs when P1 reaches its current limit ($\sim$ - 40 kA) or the plasma disrupts (e.g. a disruption caused by an NTM). During the entire shot, the P4 and P5 coils are used to control the plasma shape, provide the vertical field and also counteract the hoop force. In addition, the P6 coils, which are connected in anti-series, produce a radial field which is used to control the vertical position of the plasma. ST plasmas are prone to vertical displacement events and real-time control of these, made possible by fast power supplies in the P6 coils, is needed.

2.1.3 Pellet injection

In addition to the components described above, MAST also has a pellet injector. Pellet injection was first suggested by Spitzer in 1954 [32] as a means of refuelling a thermonuclear plasma. It involves injecting frozen pellets of hydrogen into a plasma and generally allows deeper fuelling than using gas puffs from the edge of the plasma. Pellet injection can also be used as a diagnostic technique for perturbative transport studies [33].

MAST has an 8 pellet, gas gun pellet injector. The pellets used are cylindrical and contain $\sim$ 0.5, 1 and 2 $\times$ 10^{20} atoms of deuterium, in the small (1.08 mm length), medium (1.36 mm) and large (1.71 mm) pellets sizes respectively [34]. Pellets are launched either vertically through the x-point or radially from the low field side (LFS) and the pellet velocity (V_p) is typically 300-1200 m/s [34].

The upgraded TS system (described in chapter 4) has been synchronised with the pellet injector to trigger T_e and n_e measurements during injection. This allows detailed investigation of the pellet deposition dynamics, which can be extrapolated to injection on future machines. The results from these injection experiments are discussed in section 4.6.2.

2.2 Diagnostics used in NTM studies

MAST is equipped with a wide range of diagnostics, which can be divided into imaging diagnostics, magnetic coils, electrical probes, spectroscopy and the diagnostics based on the optical effects of free electrons. The diagnostics principally used for NTM investigations are TS, magnetics, SXR, CXRS and MSE. These are summarised below, with the exception of TS as this is discussed in detail in chapter 3.

2.2.1 Magnetic coil measurements

MAST is equipped with a large range of magnetic coils and these allow the plasma current, stored plasma energy, loop voltage and plasma position and shape to be determined, in addition to other plasma parameters as discussed by Wootton et al. [35]. Magnetic coil measurements are also the principal constraint on the EFIT code (see section 2.3.1) used to determine the plasma equilibrium. Mirnov-type magnetic coils are predominantly used for measurements of MHD instabilities, including NTMs. MAST is equipped with a number of these coils at different poloidal and toroidal locations, which measure the vertical component of the magnetic field (B_z). The centre column toroidal Mirnov array consists of 12 Mirnov coils located at the midplane ($Z = 0$ m) and spaced at toroidal angles (ϕ) of $10°$, $50°$, $70°$, $110°$, $130°$, $170°$, $190°$, $230°$, $250°$, $310°$ and $350°$. The outboard Mirnov toroidal array is located at the midplane and spaced at ϕ of $150°$, $270°$ and $330°$. In addition, there also is a centre column and outboard vertical array at $\phi = 270°$. This consists of 59 coils, 40 of which are located on the inboard side and 19 on the outboard side, at vertical positions between -1.5 m and 1.45 m.

Magnetic coils operate on the principle that the flux linking a given magnetic coil can be determined from the induced voltage and that the magnetic field normal to this coil can then be determined from the flux [36]. The Mirnov signals on MAST, which are small cross-section, multiple-turn coils of wire, detect the time derivative of the magnetic field (B) that results from rotating instabilities. These generally rotate at approximately the same rate as the fluid velocity and can be detected even when the resulting magnetic perturbations only represent a very small proportion (a factor of 10^{-3} to 10^{-4}) of the equilibrium poloidal field.

To determine the amplitude, phase, and both toroidal (n) and poloidal (m) mode numbers, of MHD instabilities in a MAST shot, a standard approach is to perform a running fast Fourier transform (FFT) of the Mirnov signals measured. In this approach, the raw Mirnov data is typically sampled at $\geq$ 100 kHz and is divided into segments of $\sim$ 5-10 ms, depending on the sampling frequency. An FFT is then performed on the raw data in each segment and the resulting power spectra are calculated as functions of frequency. These spectra are combined into a spectrogram that shows the power of the Mirnov signal at different frequencies as the shot evolves (figure 2.5). To then identify the poloidal and toroidal numbers of the instabilities, the phase between different Mirnov coils at different poloidal and toroidal locations are compared.

2.2.2 MSE diagnostic

An MSE diagnostic can measure the pitch angle of the plasma internal magnetic field. This angle provides an important constraint for equilibrium codes that determine current density profiles in the tokamak (such as EFIT). Without this constraint, the effects of the current distribution inside

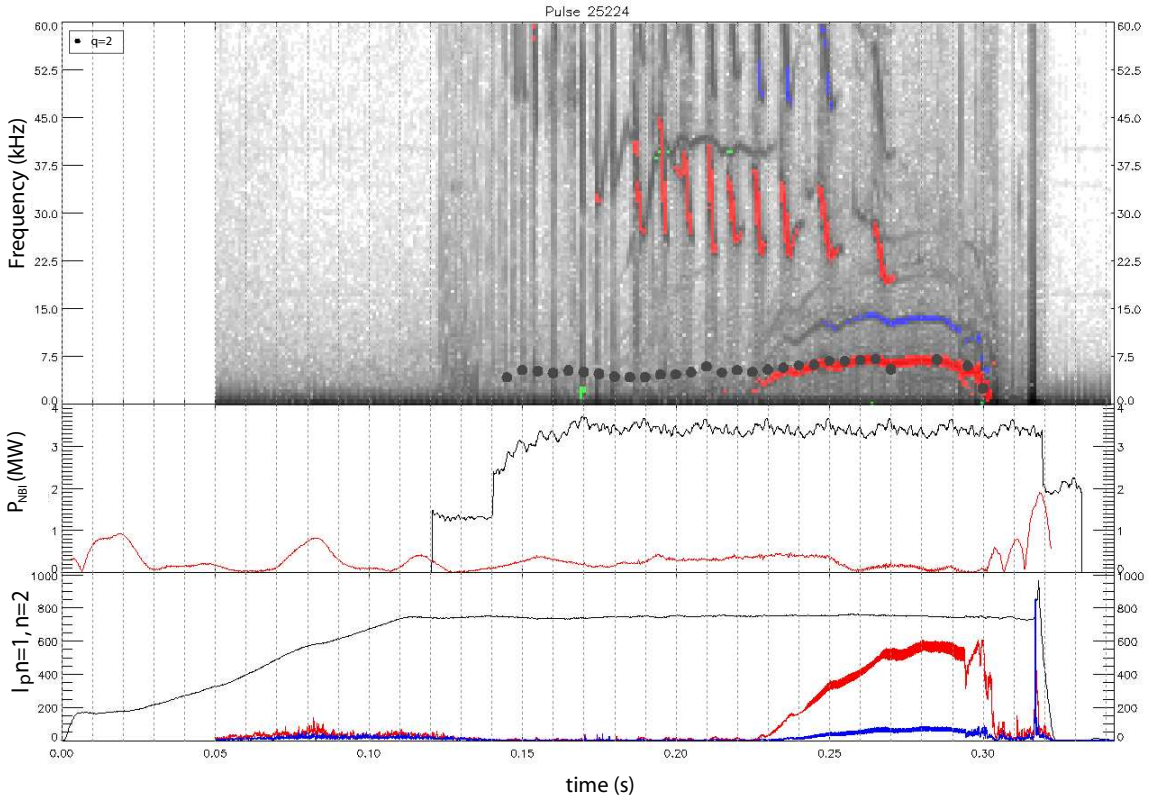

Figure 2.5: Time evolution of a MAST shot, showing magnetic spectrogram and CXRS measurements. Data taken from shot 24225. The top plot shows the magnetic spectrogram, with the n=1 components (red), n=2 components (blue) and n=3 components (green at 37.5kHz and 0.2s). The middle plot shows the waveform of the NBI heating during the shot (black lines) and the saddle coil waveforms (red lines); this coil is used to measure mode locking. The bottom plot shows the plasma current (black line) and thes amplitudes of the n=1 component (red line) and n=2 component (blue line). In this shot, the NBI heating is applied at 0.12 s and a 2,1 NTM appears at 0.23 s, as indicated by the low frequency ($\sim$ 6 kHz) n=1 mode observed on the spectrogram. The frequency of this mode is well matched to that calculated using CXRS (see section 2.2.3) for the q=2 surface, which is overplotted on the spectrogram (black dots). At 0.29 s the 2,1 mode locks to the plasma vessel and this results in its frequency dropping to zero (at 0.30 s), as seen on both the spectrogram and the CXRS frequency trace. The saddle coil signal increases from 0.29 s onward and this locked mode results in a disruption at 0.32 s.

the plasma cannot be fully determined. An MSE diagnostic is installed on MAST and takes measurements from one of the NBI neutral beams. MSE relies on the splitting of the Balmer line as a result of the Stark motional electric field ($E = v \times B$), which is produced in the rest frame of the neutral deuterium atoms. The amplitude of the different split components can then be related to the pitch of the magnetic field. On MAST, the MSE system consists of 35 radial channels (where R = 0.7-1.5 m) and has a spatial resolution of $\sim$ 2.5 cm [37]. This system also has a time resolution of $\sim$ 1 ms at angular uncertainty levels of $\sim 0.5^{\circ}$ [37].

2.2.3 CXRS

The CXRS diagnostic determines the temperature and velocity of impurity carbon ions (C_5^+) using Doppler spectroscopy [36]. These C_5^+ parameters can be assumed to equal those of the deuterium ions, as the energy transfer between these species occurs on a faster time scale than the energy confinement. This diagnostic therefore measures the evolution of the plasma ion velocity and temperature profiles.

When an NBI beam is switched on, C_5^+ ions undergo a charge exchange reaction with the neutral particles of the beam. The Doppler-width of the charge exchange spectrum emitted is proportional to the C_5^+ temperature and the toroidal velocity can be determined using the measured shift of the centre of this spectrum. The chord of the CXRS spectrometer system collects light from a small volume at the intersection of the neutral beam path and its line of sight and, as a result, CXRS can provide local measurements of temperature and velocity. This is useful for analysing fine scale structures associated with MHD instabilities.

On MAST, the CXRS diagnostic [38] comprises a set of 64 lines of sight for each NBI beam. This system has a high spatial resolution, of $\sim$ 1 cm over a radial range of 0.8 - 1.4 m, and also a high temporal resolution, of 5 ms [38]. On MAST, a significant background light is measured by the CXRS diagnostic, due to the high neutral density in this vessel, and must be removed to obtain the net CXRS signal. This background light can thus complicate the diagnostic analysis. However, in the last campaign, a new set of background chords were installed to measure the background signal and these will permit a more accurate background subtraction.

2.3 Codes used in this Thesis

This section briefly outlines the three codes used in the NTM studies described in chapter 5. These are EFIT, NCLASS and the cubic hermite element axisymmetric static equilibrium (CHEASE) code.

2.3.1 EFIT

EFIT is an equilibrium reconstruction code [39, 40] which solves the elliptic second-order, non-linear partial differential Grad-Shafranov equation [3, 6], subject to boundary conditions given by measurements of magnetic flux (ψ) and $\nabla\psi$ taken from magnetic coils at the edge of the plasma. This equation, which describes the force balance in a tokamak, is given by:

$$\Delta^*\psi = -\mu_0 R^2 p^{'} - f f^{'} \tag{2.1}$$
$$\Delta^* = R\frac{\partial}{\partial R}\left(\frac{1}{R}\frac{\partial}{\partial R}\right) + \frac{\partial^2}{\partial Z^2},$$

where Δ^* is the Grad-Shafranov operator and p and f are functions describing the plasma pressure and poloidal current profiles, respectively. To provide a unique solution to equation 2.1, the $p'(\psi)$ and $ff'(\psi)$ functions are described by a low order polynomial or spline. The solution of equation 2.1 is further constrained using TS measurements of plasma pressure and MSE pitch angle measurements.

The calculations of different NTM stability parameters are sensitive to a number of variables determined by the equilibrium reconstruction, in particular the q profile, and high quality equilibria are therefore required for NTM analysis. The variables supplied by EFIT for this analysis are the poloidal flux, the major and minor radii, the magnetic field components and the q profile. A G EQDSK file (the contents of which are fully described by Lutjens et al. [41]), containing information on the plasma equilibrium that was generated from equilibrium data using EFIT [41], is used in the NCLASS and CHEASE codes below.

2.3.2 CHEASE

The CHEASE code was developed by CRPP [41] and also solves the nonlinear partial differential Grad-Shafranov equation (2.1) [3, 6]. It then uses the solution to calculate a number of stability parameters, which are used to calculate the bootstrap and curvature terms (where both terms are based on the approximations of Sauter et al. [26, 42]) of the modified Rutherford equation (MRE). The MRE is used to study NTM stability and is described fully in sections 5.2.4.1 and 5.2.4.2.

The initial inputs for the CHEASE code include the EQDSK file from EFIT, which provides information on the experimental equilibrium. The T_e, n_e, $T_{C_5^+}$ and Z_{eff} profiles are also used as initial inputs and these data are predominantly used to enable calculation of the bootstrap current.

2.3.3 NCLASS

The NCLASS module [43, 44] provides information about the neoclassical transport properties of a plasma and is valid for multispecies plasmas of different aspect ratios, collisionalities and geometries. Important parameters for the study of NTMs have been determined using this code (see chapter 5); specifically, these are the bootstrap current, neoclassical resistivity and the radial electric field (E_r).

The FORCEBAL wrapper [43] is used to call the NCLASS module and input experimental data. These NCLASS inputs include the T_e, n_e, $N_{C_5^+}$, $T_{C_5^+}$ and $V_{C_5^+}$ profiles and the EQDSK file from EFIT.

2.4 Programmable hardware

Two types of programmable hardware have been used during the research for this thesis, complex programmable logic devices (CPLDs) and field programmable gate arrays (FPGAs). These have been used to develop both the ruby TS triggering system (a CPLD device, see section 4.4.7) and an NTM triggering unit (an FPGA device, see appendix B). An advantage of using programmable hardware is that costs are typically lower compared to equivalent off-the-shelf solutions. In addition, these devices allow greater flexibility in both hardware design and configuration.

A potential limitation of these programmable devices is that they require the use of low level programming languages and thus code development could be time consuming. However, in recent years a number of software tools have been developed to reduce FPGA application development time. One example is the Xilinx software development kit [45] and this was employed during the FPGA NTM triggering system development chapter 5, as described in appendix B.

Chapter 3

Thomson Scattering Theory and Experiment

This chapter introduces the theory of Thomson scattering (TS) (section 3.2) and the practical implementation of using TS as a diagnostic tool on tokamaks (section 3.3). The experimental section first outlines the importance of minimising T_e and n_e errors and then describes the three types of TS systems relevant to the work in this thesis: the ruby TVTS and Nd:YAG TS systems on MAST and the LIDAR (Light Detection And Ranging) TS system on ITER. Experimental results to improve the TS systems on the Nd:YAG and LIDAR systems (sections 3.3.3 and 3.3.4 respectively) are then presented, followed by a section outlining improvements to edge pedestal measurements using TS data (section 3.3.5). Experimental TS results continue in Chapter 4 with the upgrade to the ruby TS system. These results outline my contributions to TS system development. This work has been performed in collaboration with Dr. Rory Scannell at the Culham Science Centre.

3.1 Introduction

TS is an important diagnostic tool in plasma physics to measure the T_e and n_e profiles. It describes the elastic scattering of electromagnetic radiation by electrons that occurs when the oscillating field of the incident plane of an electromagnetic wave causes a free electron to oscillate at the wave frequency. Dipole radiation results from the acceleration of the electron and the radiated light is Doppler-shifted, , by a magnitude proportional to the dot product of electron velocity and the difference between the input and scattered wave vectors. In TS plasma diagnostics, the oscillating field of the incident plane wave is provided by a high-power laser and the electrons in the plasma within this laser field are accelerated to produce scattered radiation. This radiation is collected using optics and the scattered spectrum is then split into wavelength channels by a spectrometer. By fitting these detected spectra to theoretical spectra, both the electron temperature (T_e) and electron

density (n_e) can be obtained. TS can be coherent and incoherent (see section 3.2.5), but unless stated otherwise, all reference to TS in this thesis refers to incoherent TS.

TS was brought to recognition as an important diagnostic tool in 1968, when a team at the Culham Laboratory used it to validate the electron temperature claims of the T-3 Tokamak [46]. These measurements also led to the recognition of the high performance of tokamaks and thus contributed to these machines becoming the leading confinement devices in fusion research. Since this time, TS diagnostic capabilities have increased in spatial and temporal resolution, providing measurements of the T_e and n_e profile that have improved our understanding of complex plasma behaviour, including transport and stability in MCF plasmas. TS is widely used on most MCF schemes and in other non fusion applications.

The main alternative diagnostic system for determining local measurements of T_e is electron cyclotron emission (ECE). However, this diagnostic requires information about the internal magnetic field, whereas TS does not rely on the measurement of this nor other external parameters. In addition, TS can be used on a spherical tokamak, whereas an ECE system cannot, due the low ratio of magnetic fields to plasma density of these machines. Furthermore, TS can provide local measurements of n_e, which can also be measured using reflectometry. However, the interpretation of reflectometry data is often complicated by plasma conditions [36]. TS systems do, however, require a combination of high-power lasers, large collection optics and very sensitive detectors to achieve low noise measurements. Measurements can therefore be limited by the repetition rate of these lasers and detectors.

The three TS systems considered in this thesis are either on the MAST tokamak or the prospective ITER machine. On MAST, there are two TS systems, one Nd:YAG laser-based and one ruby laser-based, and on ITER there will be a core LIDAR TS laser system. One important consideration of the ITER machine is that, once built and running, it will be radioactive and it will therefore not be possible change TS system components. These systems vary in laser energies, spatial and temporal resolutions and operational parameters, leading to different potential T_e and n_e profile measurements. Details of each system are given in section 3.3.2 below.

A major consideration when optimising a TS system is the level of resolution. Systems with greater spatial and temporal resolutions are able to probe the smaller scales which affect transport and stability in tokamaks. In particular, NTMs and ELMs represent two of the principal stability limits in tokamaks and both evolve on very fine spatial scales. They can therefore be better understood with higher resolution TS measurements. Both the ruby and Nd:YAG TS systems on MAST have recently been upgraded (section 3.3.3 and Chapter 4 respectively), to improve both spatial and temporal resolution for this purpose. Improvements in resolution were achieved by completely redesigning and building both systems. As a result, these upgraded systems are two of the most

advanced TS systems worldwide and each has a high resolution over a large scattering plasma radius.

Another key factor in optimising TS system performance is the amount of noise; low noise is needed to obtain accurate measurements of T_e and n_e. The accuracy of these measurements are determined by the level of systematic and statistical error that arise in the TS data. Systematic errors tend to occur due to errors in system calibration, whereas statistical errors are related to the number of photons collected and this is determined by the system hardware (see section 3.3.1). Further to the Nd:YAG upgrade, a procedure to remove the systematic errors from this TS system was developed and this is discussed in section 3.3.3.2. In addition, as prevention of systematic errors is an important consideration in the design of the proposed LIDAR system on ITER, since access to components once operational will be very limited, a modelling approach to minimise systematic errors of its optical system is presented in section 3.3.4.

Finally, another important influence on T_e and n_e data is the distortion that occurs in these profiles if the sharp gradients of the edge pedestal are not accounted for. An approximation method to improve interpretation of TS data in the edge pedestal region has been developed and this is outlined in section 3.3.5.

3.2 TS theory

In this section, TS theory is described, starting with simple TS from a single electron and building up to the relativistic TS required to measure T_e and n_e in a tokamak. The relationship between the T_e and n_e of the plasma and the TS light can be determined by first considering the scattered light from a single electron in the formalism of classical electrodynamics. The Doppler shift of the scattered radiation that results from the electron motion within this formalism can then be generalised to the case of multiple electrons and finally to a thermal distribution of electrons in the incoherent scattering limit. These are each discussed in turn, followed by the analytic approximation used to experimentally determine T_e and n_e from TS.

3.2.1 TS from a single electron

In general, the frequency of input light is much greater than the electron cyclotron and the plasma frequencies (10^{12} Hz and $\sim 10^{12}$ Hz respectively) in tokamaks. It can therefore be assumed that the refractive index of the plasma is ~ 1 at the input light frequency and, as a result, that the effects of laser beam refraction and absorption are negligible. These effects have therefore been ignored in the equations below.

To determine the acceleration of an electron in the electromagnetic field of a laser, the electric

and magnetic fields of a laser are first defined. The resulting force on the electron due to these fields (the Lorentz force) is then calculated and used to determine the acceleration (equation 3.4) including relativistic terms. Thus, considering a single electron, located at $\vec{r_p}(t)$, with a velocity $\vec{v}(t)$, and at time t, the electric field of the incident laser beam, as evaluated at the position of the electron ($\vec{r_p}$), is:

$$\vec{E_i}(t) = E_o \cos[\vec{k_i}.\vec{r_p}(t) - \omega_i t] \ , \tag{3.1}$$

where $\vec{k_i}$ and ω_i are the incident wavevector and the incident frequency of the laser respectively. The magnetic field of the input light is then given by:

$$\vec{B_i}(t) = \frac{1}{c}\left(\hat{i} \times \vec{E_i}(t)\right) \ , \tag{3.2}$$

where $\hat{i}$ is the incident unit vector.

The force experienced by the electron in the electromagnetic field of the incident laser beam is given by the Lorentz force:

$$\vec{F} = -e(\vec{E_i} + \vec{v} \times \vec{B_i}), \tag{3.3}$$

and the acceleration of the electron due to this force is given by equation 3.4 [47].

$$\dot{\vec{\beta}} = -\frac{e}{m_0 c\gamma}\left\{\vec{E_i} - \left(\vec{\beta}\cdot\vec{E_i}\right)\vec{\beta} + \left(\vec{\beta}\cdot\vec{E_i}\right)\hat{i} - \left(\vec{\beta}\cdot\hat{i}\right)\vec{E_i}\right\}, \tag{3.4}$$

where $\vec{\beta}$ is the relativistic velocity and is used to calculated γ, the Lorentz factor. The product of γ and the rest mass (m_0) is in turn used to calculate the mass of the electron (m):

$$\beta = \frac{v}{c} \tag{3.5}$$

$$\gamma = \frac{1}{\sqrt{1-\beta^2}} \tag{3.6}$$

$$m = m_0\gamma \ . \tag{3.7}$$

The radiative part of the electromagnetic field is produced by the oscillating electron. The scattered electric field ($\vec{E_s}$) is therefore given by:

$$\vec{E_s}\left(\vec{r},t\right) = \frac{e}{4\pi\varepsilon_0}\left[\frac{1}{(1-\vec{\beta}\cdot\hat{s})^3 sc}\hat{s}\times\left(\hat{s}-\vec{\beta}\right)\times\dot{\vec{\beta}}\right]_{\text{Ret.}} \ , \tag{3.8}$$

where s is the distance between the electron and the observer (figure 3.1) and $\hat{s}$ is the unit vector in the direction of propagation ($\hat{s} = \frac{\vec{s}}{s}$). The subscript Ret indicates that the quantities in brackets are to be evaluated at a retarded time (t'). This is because the scalar and vector potentials depend on the charge motion at an earlier time (t') than measured (t), which is determined by subtracting the time it takes light to travel between the charge and the point of observation:

$$t' = t - \frac{s}{c} \ . \tag{3.9}$$

A more detailed description of the radiative part of the electromagnetic field is described by Feynmann et al. [48].

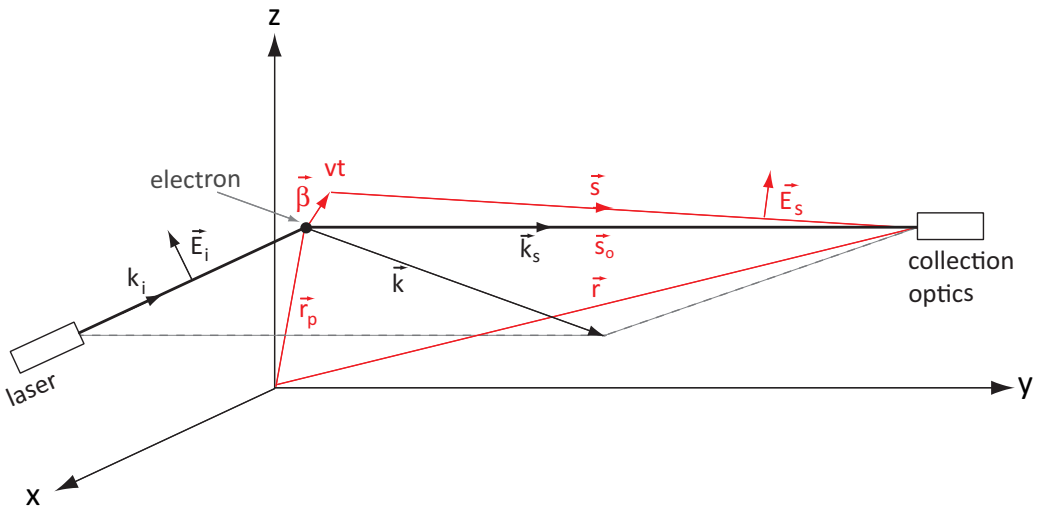

Figure 3.1: Schematic diagram of the scattering geometry of a typical TS system, considering one electron only. The incident electric field (E_i) from a laser accelerates an electron at position $\vec{r_p}$ (red), that is moving at velocity $\vec{\beta}$ (red). The light from the oscillating electron is radiated after the electron travels distance (vt) along the direction $\vec{s}$ and is collected by the collection optics at position $\vec{r}$ (red). $\vec{s}$ is approximately equal to the scattered wavevector $\vec{k_s}$ (black), as vt is much less than the distance to the collection optics. The frequency difference between the input wavevector, k_i (black), and k_s is given by the dot product of the differential wavevector, k (black), times the electron velocity. $\vec{s_o}$ (red) is defined in section 3.2.2. Dotted lines indicate the scattered plane.

3.2.2 The Doppler shift resulting from electron motion

The Doppler shift is the apparent change in frequency due to the motion of the source. Doppler spectroscopy measures the velocity of an object based on the change in the frequency that it emits. In the case of TS, the change in the scattering frequency is proportional to the component of the electron velocity in the direction of k (figure 3.1), where k is the difference between the input and scattered wavevectors. This Doppler shift results from the combination of two effects. The first is that the electron 'sees' the incident wave at a Doppler-shifted frequency, as it is moving relative to the input wave in the lab frame. The second is that electron has a velocity component in the direction of the observer.

The phase of the scattered field ($\Phi(t)$) from an oscillating charge is given by the phase of the incident field (3.1), as evaluated at the retarded time (equation 3.9):

$$\Phi(t) = \vec{k_i}.r(\vec{t'}) - \omega_i t' \ . \tag{3.10}$$

If the velocity ($\vec{v}$) of the electron is constant (figure 3.1), then $\vec{r_p}(t)$ and $\vec{s}(t)$ are:

$$\vec{r_p}(t) = r_{p0} + \vec{v}t \tag{3.11}$$

$$\vec{s}(t) = \vec{s_0} - \vec{v}t \ . \tag{3.12}$$

The retarded time can then be calculated by substituting equation 3.12 into equation 3.9:

$$t' = t - \left(\frac{|\vec{s}_o - \hat{s} \cdot \vec{r_p}|}{c} \right) \ . \tag{3.13}$$

As it is assumed that the electron displacement ($\vec{v}t'$) is very small compared to the distance to the observer then:

$$t' = \left(t - \frac{\vec{s}_o}{c} + \frac{\hat{s} \cdot r_{p,o}}{c} \right) \tag{3.14}$$

$$t' \left(1 - \hat{s} \cdot \beta\right) = t - \frac{\vec{s}_o}{c} + \frac{\hat{s} \cdot r_{p,o}}{c} \ . \tag{3.15}$$

The expression for retarded time (equation 3.15) can now be substituted into the equation 3.10 to give the phase of the scattered wave:

$$\begin{aligned} \Phi(t) &= \vec{k}_i \cdot \vec{r}_{po} - (\omega_i - \vec{k}_i \vec{v})t' \\ &= \vec{k}_i \cdot \vec{r}_{po} - \omega_i(1 - i\vec{\beta})t' \\ &= \vec{k}_i \cdot \vec{r}_{po} - \omega_i \frac{1 - \hat{i} \cdot \vec{\beta}}{1 - \hat{s} \cdot \vec{\beta}} \left(t - \frac{\vec{s}_o}{c} + \frac{\hat{s} - r_p o}{c} \right) \end{aligned} \tag{3.16}$$

The scattered frequency (ω_s) is given by:

$$\omega_s = \omega_i \left(\frac{1 - \hat{i} \cdot \vec{\beta}}{1 - \hat{s} \cdot \vec{\beta}} \right) \tag{3.17}$$

and the phase of the scattered wave can now be redefined as:

$$\Phi(t) = -\vec{k} \cdot \vec{r}_{po} - \omega_s t + k_s \cdot s_o \ . \tag{3.18}$$

The resulting scattered frequency is monochromatic and dependent upon the frequency of the incident laser beam (ω_i) and the velocity of the scattering particle ($\vec{\beta}$). It is assumed that the plasma has a refractive index of ~ 1, so the input and scattered frequencies are each equal to the wavevector multiplied by the speed of light:

$$\omega_i = k_i c \tag{3.19}$$

$$\omega_s = k_s c \ . \tag{3.20}$$

Given the relationship between wavevectors and wave frequencies in equation 3.20, equation 3.16 can be rewritten as:

$$\vec{k_i}.\vec{r}_{po} + \omega_s \frac{s_o}{c} = \vec{k_i}.\vec{r}_{po} + \vec{k_s}.\vec{s_o} = (\vec{k_i} - \vec{k_s}).\vec{r_{po}} + \vec{k_s}.\vec{r} \ . \tag{3.21}$$

The differential wavevector, $\vec{k}$, is the difference between the incident wavevector ($\vec{k_i}$) and the scattered wavevector ($\vec{k_s}$):

$$\vec{k} = \vec{k_i} - \vec{k_s} \ . \tag{3.22}$$

Using this and equation 3.16, the phase of the scattered wave can now be determined:

$$\Phi(t) = \vec{k_s}.\vec{r} - \vec{k}.\vec{r_{po}} - \omega_s t' \ , \tag{3.23}$$

and by also using equation 3.17, an expression can be derived that relates the frequency difference ($\Delta\omega$) between incident and scattered light to the electron velocity:

$$\begin{aligned} \omega_s - \omega_i &= (\vec{k_i} - \vec{k_s}).\vec{v} \\ \Delta\omega &= \vec{k}.\vec{v} \ . \end{aligned} \tag{3.24}$$

Thus, the frequency shift of the scattered light is given by the the dot-product of the differential wavevector and the electron velocity.

3.2.3 Non-relativistic TS

We first consider scattering from particles with velocities much slower than the speed of light. If equations 3.8 and 3.17 are taken within the limit of $\beta << 1$, then all β terms can be neglected, except for the expression describing the phase (equation 3.18). This is because the frequency difference between the incident and scattered light is of the order β. By eliminating these β terms in equations 3.4 and 3.8, the scattered electric field is reduced to:

$$\vec{E_s}(t) = \frac{e^2}{4\pi\varepsilon_0 m_0 c^2 s} \hat{s} \times (\hat{s} \times \vec{E_0}) \cos(\vec{k_i}.\vec{r_p}(t') - \omega_i(t')) \ . \tag{3.25}$$

When determining the scattered power, the phase component can be neglected as this will average out. The vector triple product in equation 3.25 can therefore be reduced to:

$$\vec{A} \times \left(\vec{B} \times \vec{C}\right) = \left(\vec{A} \cdot \vec{C}\right) \vec{B} - \left(\vec{A} \cdot \vec{B}\right) \vec{C} \tag{3.26}$$

$$\hat{s} \times \left(\hat{s} \times \vec{E_0}\right) = \left(\hat{s} \cdot \vec{E_0}\right) \hat{s} = E_0 \sin(\phi) \hat{s} \ , \tag{3.27}$$

where ϕ is the angle between the scattering direction ($\hat{s}$) and the input electric field (E_0). An expression for the scattered electric field ($\vec{E_s}(t)$) can then be determined using equation 3.27:

$$\vec{E_s}(t) = \frac{r_0}{s} \vec{E_0} \sin(\phi) \cos(\vec{k_i}.r - \vec{k}.\vec{r_p} - \omega_i t) \ , \tag{3.28}$$

where $r_0 = \frac{e^2}{4\pi\epsilon_0 m_0 c^2}$ is the classical electron radius constant.

The scattered power (P_s) per unit solid angle (Ω) is:

$$\frac{d\vec{P_s}}{d\Omega} = s^2 \vec{S}.\hat{s} \ , \tag{3.29}$$

where Ω is the solid angle [49] and $\vec{S}$ is the Poynting vector, which is the change in power per unit area radiated by an electromagnetic field. The formula for this is:

$$\vec{S} = \epsilon_0 c^2 \vec{E}_s \times \vec{B}_s \ , \tag{3.30}$$

where B_s is the magnetic field of the scattered light. The equation for the scattered power in terms of the electric field is then obtained by substituting equations 3.2, 3.28 and 3.30 into equation 3.29:

$$\begin{aligned} \frac{d\vec{P}_s}{d\Omega} &= \epsilon_0 c E_s^2 \\ &= r_0^2 \epsilon_0 c \sin^2(\phi)\ E_0^2 \ . \end{aligned} \tag{3.31}$$

It is then convenient to define the differential cross-section as the ratio of $\frac{d\vec{P}_s}{d\Omega}$ to the incident power ($\overline{I_0} = \epsilon_0 c E_0^2$). This can roughly be interpreted as the likelihood that the interaction of the input photon with an electron will result in a scattered photon, which is given by:

$$\frac{d\vec{\sigma}_s}{d\Omega} = r_0^2 \sin^2 \phi \ . \tag{3.32}$$

Thus, the classical differential scattering cross-section is equal to the product of the square of the classical electron radius and the square of the sine of the angle between the input electric field and the scattering direction. TS systems are typically designed so that ϕ is 90°, making $\frac{d\vec{\sigma}_s}{d\Omega}$ equal to r_0^2.

3.2.4 Relativistic TS

Relativistic effects must be considered in TS when the electrons that scatter light have thermal velocities approaching the speed of light, which is frequently the case in tokamaks. A relativistic TS formalism is therefore needed.

The relativistic scattered electric field is determined using equations 3.3, 3.4, and 3.8, with the vector triple product from equation 3.26:

$$\vec{E}_s(\vec{r},t) = \frac{q^2}{4mc\pi\varepsilon_0} \left[\begin{array}{l} \dfrac{1}{(1-\vec{\beta}_s)^3 s} \hat{s} \ \times \ (\hat{s} - \vec{\beta}) \ \times \\ \left\{ \vec{E}_i - (\vec{\beta}\cdot\vec{E}_i)\vec{\beta} + (\vec{\beta}\cdot\vec{E}_i)\hat{i} - (\vec{\beta}\cdot\hat{i})\vec{E}_i \right\} \end{array} \right]_{Ret} . \tag{3.33}$$

The terms in the cross-products of this equation are further simplified by using the following vector identity:

$$\vec{A} \times \left(\vec{B} \times \left(\vec{C} + \vec{D} \right) \right) = \vec{A} \times \left(\vec{B} \times \vec{C} \right) + \vec{A} \times \left(\vec{B} \times \vec{D} \right) \ , \tag{3.34}$$

and after some algebra, the following expression is obtained for the scattered electric field:

$$\vec{E}_s\left(\vec{r},t\right) = \frac{r_0}{\gamma} \left[\begin{array}{l} \dfrac{E_i}{(1-\vec{\beta}_s)^3 s} \left[-(1-\beta_i)(1-\beta_s)\hat{e} - \right. \\ \beta_e(1-\beta_s)\hat{i} + \left\{ (1-\beta_i)\hat{s}.\hat{e} + (\hat{s}.\hat{i} - \beta_s)\beta_e \right\} \hat{s} - \\ \left. \left\{ (1-\beta_i)\hat{s}.\hat{e} - (1-\hat{s}.\hat{i})\beta_e \right\} \vec{\beta} \right] \end{array} \right]_{Ret} , \tag{3.35}$$

where $\hat{e}$ is the unit vector in the incident electric field direction ($\hat{e} = \frac{\vec{E_i}}{E_i}$), β_i is the component of the electron velocity in the direction of the incident light and β_s is the component of the electron velocity in the direction of the scattered light.

The above expression (equation 3.35) can be simplified by considering the case where the polarisation of the incident electric field is perpendicular to the scattering plane. In this situation, all of the dot-products of the incident electric field unit vector and the scattering unit vector would be equal to zero:

$$\hat{e}.\hat{s} = 0 \; . \tag{3.36}$$

Equation 3.35 can be further simplified by selecting only the scattered light that is parallel to $\hat{e}$, which is achieved by placing a polariser in front of the scattered light. Selecting only that scattering light parallel to $\hat{e}$ is equivalent to obtaining the dot-product of $\hat{e}$ and equation 3.35:

$$\hat{e}.\vec{E}_s(\vec{r},t) = \frac{r_0}{\gamma}\left[\frac{E_i}{(1-\vec{\beta}_s)^3 s}\left\{(1-\hat{s}.\hat{i})\beta_e^2 - (1-\beta_i)(1-\beta_s)\right\}\right]_{Ret}, \tag{3.37}$$

and this equation can be reduced to the classical scattered field equation (3.28) by taking the classical limit ($\beta << 1$).

Using equations 3.31 and 3.37, the scattered power per unit solid angle is then calculated as:

$$\frac{dP_s}{d\Omega} = \epsilon_0 c \frac{r_0^2}{\gamma^2}\frac{E_i^2}{(1-\beta_s)^2}\left(\frac{(1-\cos\theta)\,\beta_e^2 - (1-\beta_i)\,(1-\beta_s)}{(1-\beta_s)^2}\right)^2 . \tag{3.38}$$

where θ is the scattering angle and $\cos\theta = \hat{s}.\hat{i}$. This expression can be further simplified to:

$$\frac{dP_s}{d\Omega} = \epsilon_0 c \frac{r_0^2}{\gamma^2}\frac{E_i^2}{(1-\beta_s)^2}\frac{(1-\beta_i)^2}{(1-\beta_s)^2}\left(\frac{(1-\cos\theta)\,\beta_e^2}{(1-\beta_s)(1-\beta_i)} - 1\right)^2 , \tag{3.39}$$

and, using equation 3.17 for the scattered frequency, even further simplified to:

$$\frac{dP_s}{d\Omega} = \epsilon_0 c \frac{r_0^2}{\gamma^2}\frac{E_i^2}{(1-\beta_s)^2}\frac{\omega_s^2}{\omega_i^2}\left(\frac{(1-\cos\theta)\,\beta_e^2}{(1-\beta_s)(1-\beta_i)} - 1\right)^2 . \tag{3.40}$$

This gives the energy per unit time time at the position of the observer. However, it must be multiplied by $(1-\beta_s)$ in order to obtain the energy per unit time at the position of the particle. This is typically referred to as the finite transit time correction [50].

The differential cross-section can now be determined:

$$\frac{d\sigma_s}{d\Omega} = \frac{r_0^2}{\gamma^2}\frac{1}{(1-\beta_s)}\frac{\omega_s^2}{\omega_i^2}\left(\frac{(1-\cos\theta)\,\beta_e^2}{(1-\beta_s)(1-\beta_i)} - 1\right)^2 . \tag{3.41}$$

This equation is not symmetrical for the positive and negative velocities, nor for $\Delta\omega$ around the incident scattering frequency. This causes a greater amount of scattering towards higher frequencies, and hence lower wavelengths, which results from two effects. Firstly, a preferentially greater scattered power is observed from an electron moving towards the observer than one moving away.

When the electron moves towards the observer β_s will be positive and therefore the $\frac{1}{(1-\beta_s)}$ component of equation 3.41 will have a greater value. Secondly, when ω_s is greater than ω_i, the ratio term $\frac{\omega_s^2}{\omega_i^2}$ in equation 3.41 causes a greater amount of scattering power.

The effect of the $\left(\frac{(1-\cos\theta)\beta_e^2}{(1-\beta_s)(1-\beta_i)} - 1\right)^2$ term in equation 3.41 is to depolarise the scattered light. This has a very small influence on the scattered power at a given frequency, but a large effect on the number of scattered photons at high T_e. This term will be discussed with regard to TS spectra from relativistic Maxwellian distributions in section 3.2.7.

3.2.5 Scattering from a number of particles

Only scattering from individual particles has been considered so far. Now we consider TS from multiple particles. In this section, the differences between incoherent and collectively scattered regimes are outlined. In subsequent sections, scattering from a thermal distribution is considered for classical and then relativistic thermal velocities. To determine the total scattered electric field from a number of particles, the sum of the individual scattered electric fields must be calculated:

$$\overrightarrow{E_s} = \sum_j \overrightarrow{E_j} \ . \tag{3.42}$$

This summation is carried out over all of the electrons in the scattering volume and the average scattered power is obtained by summation of all of the scattered electric fields:

$$\begin{aligned}\frac{d\overrightarrow{P}_s}{d\Omega} &= s^2\epsilon_0 c E_s^2 \\ &= s^2\epsilon_0 c \sum_j \overrightarrow{E_j}.\sum_k \overrightarrow{E_k} \\ &= s^2\epsilon_0 c \sum_j \overrightarrow{E_j^2} + s^2\epsilon_0 c \sum_{j\neq k} \overrightarrow{E_j}.\overrightarrow{E_k}.\end{aligned} \tag{3.43}$$

The first term of equation 3.43 is the sum of the power scattered by each electron. The second term is related to the correlation of electron positions. If the electrons are distributed randomly in space, this correlation term will sum to zero. However, a plasma exhibits collective effects, which can lead to correlations between electron positions on different length scales. The regimes where these collective effects play a role in TS scattering can be shown by substituting the classically scattered electric field equation (equation 3.25) into equation 3.43:

$$\sum_{j=0}^{N} \overrightarrow{E_s}(t) = \sum_{j=0}^{N} \frac{r_0}{s}\vec{s}\times(\vec{s}\times\overrightarrow{E_0})\cos(\Phi(t)). \tag{3.44}$$

The equation for the scattered power is thus:

$$\frac{d\overrightarrow{P}_s}{d\Omega} = N\epsilon_0 c r_0^2 \sin^2\phi E_0^2 \sum_j^N \cos(\Phi_j(t)). \tag{3.45}$$

To view a random distribution of electrons, the phase component (Φ_j) of the electric field must sum to zero. The $\sum_{j}^{N} \cos(\Phi_j(t))$ term, which includes the correlation of electron positions, is then equal to 1 and therefore the collective motion of the electrons does not influence the scattered power in equation 3.45. Consider the equation for the phase of the scattered electric field:

$$\Phi(t) = \overrightarrow{k_s}.\overrightarrow{r} - \overrightarrow{k}.\overrightarrow{r_{po}} - \omega_s t. \tag{3.46}$$

The second term of this equation is the projection of the differential vector ($\vec{k}$) onto the position of the electron ($\vec{r}_{po}$). This term is dependent on the relative electron positions. The size of $\vec{k}$ therefore influences whether the electrons are considered to be correlated or uncorrelated.

In a plasma, correlated interactions between the electrons occur on scale lengths greater than the Debye length (λ_D) and below this scale length electrons can be considered to be randomly distributed. The Debye length is given by:

$$\lambda_D = \sqrt{\frac{\varepsilon_0 k_B T_e}{e^2 n_e}}\ . \tag{3.47}$$

The condition which determines whether the scattered light is from a random distribution of electrons is therefore:

$$\lambda_D >> \frac{1}{k}\ , \tag{3.48}$$

where the $\frac{1}{k}$ term can be viewed as the distance over which the particle motion is sampled in relation to the Debye length (figure 3.2). If the Debye length is much greater than 1 over the differential k vector, then phase components are randomly distributed and the collective effects of the plasma are not seen. A term can be defined (α) that shows whether light is incoherently or collectively scattered from a plasma:

$$\alpha = \frac{1}{k\lambda_D}\ . \tag{3.49}$$

The magnitude of this term determines which of the plasma parameters the detected scattered spectrum is related to. If α is much less than 1, the collective scattering effects can be neglected and the scattered light is incoherently scattered. This is because the scattered spectrum results from scattering from individual electrons and is therefore determined by the underlying thermal distribution. When $\alpha > 1$, the scattering contributions from different electrons, and their surrounding shielding clouds, add up coherently. Under such conditions, it is possible to deduce information about the ion velocity distribution and experimental methods to exploit this are being explored, to permit study of fast ion distribution in future fusion devices. Finally, when $\alpha \sim 5-20$ then it is possible to study density fluctuations in the plasma. In the work presented in this thesis, only incoherent scattering has been considered.

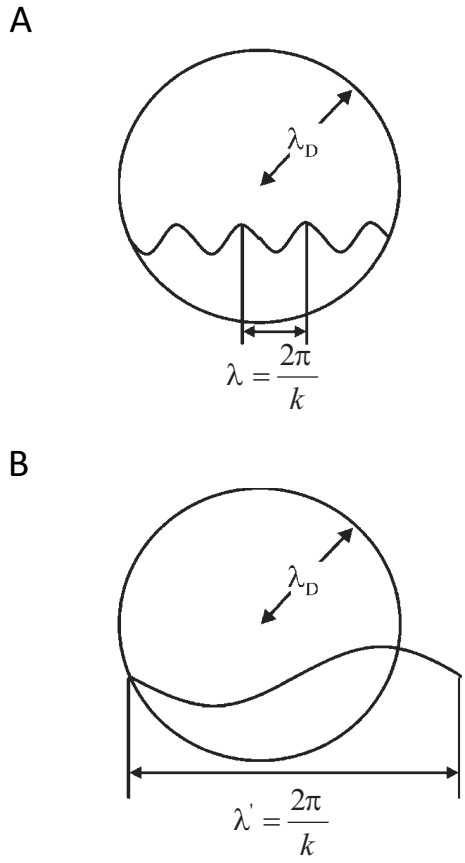

Figure 3.2: Incoherent and collective scattering. The relationship between the differential k vector ($\vec{k}$) and the Debye length determines whether TS is incoherent or collective. The latter is represented by a circle of radius λ_D. The distance over which electron motion is sampled is given by λ. A. The phases of the electron positions are not correlated and the TS light is incoherently scattered. B. The influence of the ions on the electrons is now important and hence the electron positions are correlated and TS light is collectively scattered.

3.2.6 Scattering from a thermal distribution of particles

Electrons velocities in tokamaks are assumed to be in a Maxwell-Bolzmann distribution. The scattered spectrum measured by a TS system will therefore be from a large number of electrons in this type of distribution. The Maxwell-Bolzmann velocity distribution, at temperature T_e, is given by [47]:

$$f(v) = \left(\frac{m_0}{2\pi kT}\right)^{\frac{3}{2}} \exp\left(-\frac{m_0 v^2}{2kT_e}\right) \qquad for\ v << c, \tag{3.50}$$

$$f(\beta) = \frac{\alpha}{2\pi K_2(2\alpha)} \frac{\exp\left[-2\alpha(1-\beta^2)^{-\frac{1}{2}}\right]}{(1-\beta^2)^{\frac{5}{2}}} \qquad for\ v < c, \tag{3.51}$$

where $K_2(2\alpha)$ is the modified Bessel function of the second order and second kind.

The total scattering cross-section, per unit solid angle, for a thermal distribution of particles can now be calculated. This is equal to the volume integral of the product of the electron velocity distribution and the scattering cross-section per unit solid angle. Both terms are evaluated at a particular scattering frequency and scattering angle. This gives the sum of all scattering contributions from all scattering electrons:

$$\frac{d^2\sigma_s}{d\omega_s d\Omega}(\omega_s,\theta) = \iiint f(\beta)\,\frac{d\sigma}{d\Omega}(\omega_s,\theta)\,d^3\vec{\beta} \tag{3.52}$$

This equation can then be used to relate the actual TS spectrum measured to the underlying T_e in the tokamak. It is useful to once again consider the classical low electron velocity limit ($v << c$) before considering the full relativistic case. To calculate the scattering cross-section for this classical limit, the scattering angle is taken to be 90° and equations 3.32 and 3.50 are both substituted into equation 3.52:

$$\frac{d^2\sigma_s}{d\Omega\; d\omega}(\vec{s},\omega_s) = \sigma_0 \frac{1}{\Delta k(\pi v_{th}^2)^{1/2}}\; e^{-(\Delta\omega)^2/(v_{th}k)^2}\;, \tag{3.53}$$

where v_{th} is the thermal velocity and is equal to $2k_BT_e/m_e$; and $\Delta\omega$ is given by equation 3.24. When $\beta << c$ then $(\omega_s - \omega_i) << \omega_i$ and the magnitude of the differential wavevector is therefore:

$$k = 2k_s sin\frac{\theta}{2}\;. \tag{3.54}$$

In this equation it is assumed that the input and scattered wavevectors are of equal length, as shown in figure 3.3.

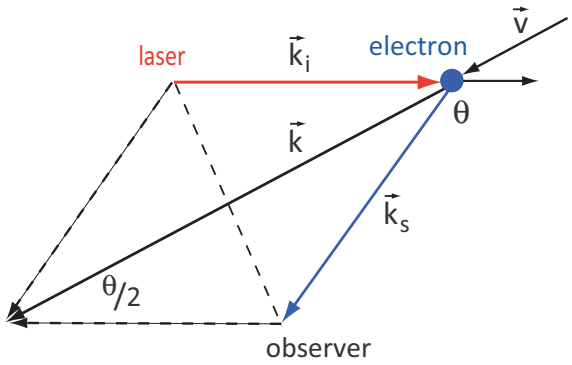

Figure 3.3: Magnitude of the differential k vector, $\vec{k}$ (black). When the input, $\vec{k}_i$ (red), and scattered, $\vec{k}_s$ (blue), wavevectors are assumed to be of equal length, then the scattering geometry can be represented as shown, where θ is the scattering angle and $\vec{v}$ is the electron velocity. After some simple geometry (dotted black lines), the magnitude of $\vec{k}$ can be represented as $k = 2k_s sin\frac{\theta}{2}$.

Since spectrometers measure light by wavelength, it is convenient to convert frequencies (ω) into wavelengths (λ):

$$\frac{\delta\omega}{\omega_i} = -\frac{\delta\lambda}{\lambda_i}\;. \tag{3.55}$$

Then, when inserting equations 3.54 and 3.55 into equation 3.53 to give the wavelength spectrum, we have:

$$\frac{d^2\sigma_s}{d\lambda\, d\omega}(\vec{R},\lambda_s) = \sigma_0 \frac{c}{\sqrt{\pi}2\lambda_i sin(\theta/2)v_{th}} e^{-\{(\Delta\lambda\, c)/(2v_{th}\lambda_i sin(\theta/2)\}^2} \tag{3.56}$$

This equation is a Gaussian distribution which is a function of λ. The T_e can be calculated from the standard deviation of this distribution and the n_e from its amplitude.

3.2.7 Relativistic TS from thermal electrons

Equation 3.56 is only valid for electron temperatures up to a few 100 eV, whereas those in tokamaks are typically in the order of keV. Relativistic effects must therefore be considered for the TS of multiple particles in tokamaks. To permit relativistic experimental scattered spectra to be fitted, an analytical approximation of equation 3.52 was developed by Selden [51, 52]. However, this neglected the effects of scattered light depolarisation (discussed at the end of section 3.2.4). This issue was later addressed by Naito et al. [53], by defining the depolarisation as a product of the Selden spectral function (S_{ZH}) and a polarisation function (q):

$$S(\epsilon,\theta,\alpha) = S_{Zh}(\epsilon,\theta,\alpha)q(\epsilon,\theta,\alpha)\ . \tag{3.57}$$

The form of this Selden-Naito equation requires a change of variables:

$$\epsilon = \frac{\lambda_s}{\lambda_i} - 1 \tag{3.58}$$

$$\alpha = \frac{\frac{1}{2}m_e c^2}{k_B T_e}, \tag{3.59}$$

where ϵ is the normalised wavelength shift and α is a function of temperature.

The Selden spectral function component of equation 3.57 is defined as:

$$\begin{aligned} S_{Zh}(\epsilon,\theta,\alpha) &= \frac{C(\alpha)}{A(\epsilon,\theta)} e^{-2*\alpha*B(\epsilon,\theta)} \\ A(\epsilon,\theta) &= (1+\epsilon)^3\sqrt{2(1-\cos\theta)(1+\epsilon)+\epsilon^2} \\ B(\epsilon,\theta) &= \sqrt{\frac{1+\epsilon^2}{2(1-\cos\theta)(1+\epsilon)}} - 1 \\ C(\alpha) &= \sqrt{\frac{\alpha}{\pi}}\left(1 - \frac{15}{16}\frac{1}{\alpha} + \frac{345}{512}\frac{1}{\alpha^2}\right) \end{aligned} \tag{3.60}$$

and the Naito polarisation function, $q(\epsilon,\theta,\alpha)$, of equation 3.57 is defined in equation 3.61. This equation only provides a first order approximation of the depolarisation, but has been shown to vary less than 1% from true values at 40 keV, and even less at lower temperatures [54]. Hence, as the

temperatures on MAST are typically around 1 keV, this is a valid approximation to use.

$$
\begin{aligned}
q_{(1,1)}(\eta,\theta,\alpha) &= 1 - 4\eta\zeta\frac{2\zeta-(2-3\zeta^2)\eta}{2\zeta-(2-15\zeta^2)\eta} \\
u &= \frac{\sin\theta}{1-\cos\theta} \\
x &= \sqrt{1+\frac{\epsilon^2}{2(1-\cos\theta)(1+\epsilon)}} \\
y &= \frac{1}{\sqrt{x^2+u^2}} \\
\eta &= \frac{y}{2\alpha} \\
\zeta &= xy
\end{aligned}
\tag{3.61}
$$

The scattering spectra calculated from the Selden-Naito formula (equation 3.57), at increasing electron temperatures, are shown in figure 3.4A. When the thermal electron velocity is relativistic, the scattering spectra are shifted to the blue side of the spectrum. At very high T_e , the scattered spectrum is depolarized. The origins of both these effects are as those explained for the single electron case in section 3.2.4.

It is useful to compare the classical and relativistic analytical forms of TS to determine over what T_e ranges each approach is valid. An approximation for the width of a classical TS spectrum ($\Delta\lambda_{width}$) can be determined using equation 3.56 and is given by:

$$
\frac{\Delta\lambda_{width}}{\lambda_0} = \frac{2sin(\theta/2)}{c}\sqrt{\frac{2k_bT_e}{m_e}}, \tag{3.62}
$$

In addition, the blue-shift that occurs due to relativistic effects ($\Delta\lambda_{blue}$) is described by:

$$
\frac{\Delta\lambda_{blue-shift}}{\lambda_0} \approx -2.8x10^{-5}T_e(eV)sin^2(\theta/2), \tag{3.63}
$$

where this equation has been taken from calculations by Sheffield et al. [55]. Figure 3.4B shows comparisons of the TS spectrum width and the blue-shifted peak with their respective low temperature approximations, all as functions of T_e . These simple approximations do not reproduce the observed shifts and widths determined by the Selden-Naito equation [53] as well where $T_e > 2$ keV.

3.3 Experimental TS

This section considers the practical implementation of TS as a diagnostic system in tokamaks and ways to improve and optimise accuracy. Firstly, ways to reduce the T_e and n_e errors in TS data are considered, this being critical for the accurate measurements of NTMs discussed in chapter 5. Three common types of TS system for tokamaks are then introduced, the TVTS, Nd:YAG TS and LIDAR TS systems, each relevant to results in this thesis.

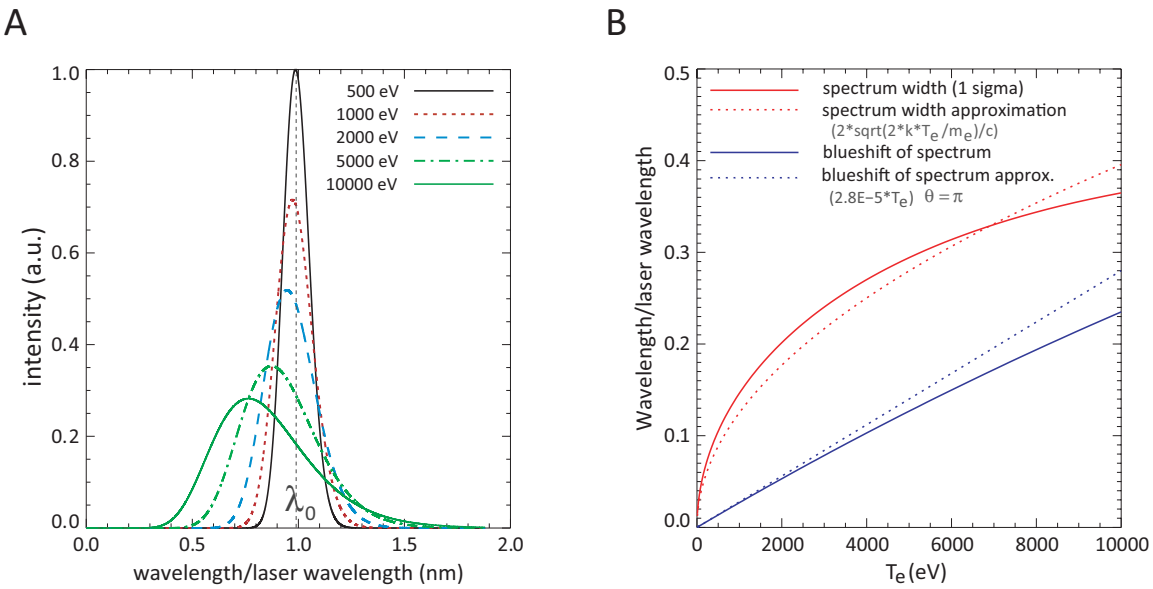

Figure 3.4: A. The relativistic scattered spectrum calculated from the Selden-Naito analytical formula, where λ_0 is the laser wavelength. Higher T_e leads to a broader TS spectrum and a greater blueshift of the intensity peak. B. Variation of the spectrum width (red, solid) and amount of blueshift (blue, solid) with T_e and comparison of these with their low temperature approximations (red, dashed line and blue, dashed line respectively).

Specific TS experimental results are then presented. Briefly, these are the recent upgrade to the Nd:YAG system, simulations of the proposed design of the LIDAR system collection optics and finally, an approximation method to determine the T_e and n_e pedestal parameters using TS. My contribution to each of these is indicated in the relevant sections. TS experimental results continue in Chapter 4 with the MAST ruby TVTS system upgrade.

3.3.1 Minimising T_e and n_e errors

As a result of the low cross-section of TS, only a small number of input photons will be scattered. Furthermore, only a small number of these will be collected by a TS system; typically, only ~ 1 in every 10^{12} input photons results in a scattered photon being detected. It is therefore important to minimise the statistical and systematic errors of the scattered spectrum measured by a TS system to ensure the T_e and n_e profiles are measured as accurately as possible. Statistical errors are determined by the design of a given TS system, whereas the systematic errors result from errors in system calibration; both are discussed below. A critical aspect of the design and improvement of TS systems is therefore identifying the sources of T_e and n_e error and minimising these as far as possible.

3.3.1.1 Minimising statistical error

The statistical error (σ_s) of TS measurements for different spectral channels, and hence the T_e and n_e errors, are principally determined by the number of scattered photons detected ($\sigma_{poisson}$). This is in turn determined by both detector efficiency and the number of photons collected by the system optics. However, noise from the background plasma light ($\sigma^2_{background}$) and the amplifier ($\sigma^2_{amplifier}$) can also affect the error on the T_e and n_e measurements. The noise measured using a TS system can be written as:

$$\sigma_s^2 = \sigma^2_{poisson} + \sigma^2_{background} + \sigma^2_{amplifier} \tag{3.64}$$

The $\sigma^2_{background}$ and $\sigma^2_{amplifier}$ contributions to the overall σ_s^2 are usually determined by measuring the signal on a given system when the laser is not being fired and there is no scattered signal. This assumes that $\sigma^2_{background}$ is similar in the presence and absence of a scattered signal. It is desirable to minimise these spurious noise contributions in a given system and $\sigma^2_{background}$ can be effectively reduced with respect to the $\sigma^2_{poisson}$ by measuring a large scattered signal over a short time window. For this reason, TS lasers are typically high power with pulse widths of 10-50 ns and energies 1-10 J. The effective detector signal is often further amplified before the addition of the amplifier noise. However this can limit the available dynamic range of the measurements. The Poisson noise ($\sigma_{poisson}$) is related to the number of scattered photons collected and is given by:

$$N_s = n_{laser} n_e r_0^2 \Delta\Omega \Delta L \int \frac{S(\lambda, \theta, T_e)}{\lambda_0} d\lambda, \tag{3.65}$$

where ΔL is the scattering length and $\Delta\Omega$ is the solid angle collected. The integral of the Selden-Naito equation is then normalised to 1:

$$\int_0^\infty S(\lambda,\ T_e,\ \theta) \frac{d\lambda}{\lambda_0} = 1. \tag{3.66}$$

Thus, the number of scattered photons detected can be given by:

$$N_s = n_{laser} n_e r_0^2 \Delta\Omega \Delta L \left[\frac{QE}{NF^2}\right] T \int \phi(\lambda) \frac{S(\lambda, \theta, T_e)}{\lambda_0} d\lambda, \tag{3.67}$$

where T is the transmission of the TS optics, r_0 is the classical electron radius, $\left[\frac{QE}{NF^2}\right]$ represents the efficiency of the detector and $\phi(\lambda)$ is the response function of the different spectral channels. QE is the quantum efficiency and represents the number of electrons produced for a given incident photon. NF is the noise factor, which is the ratio of the input and output signal to noise ratios and represents additional losses in the detector.

The number of scattered photons detected can be maximised by optimising each term in equation 3.67, via choices in laser energy and wavelength, collection optics design and detector efficiency. Increasing the laser energy increases the number of input photons (n_{laser}), but it is difficult

to obtain high frequency, high energy lasers in the wavelength regions optimal for detector efficiency. The two most common lasers used in TS systems are the ruby and Nd:YAG lasers; the former having higher energies and the latter with higher repetition rates. The greater the solid angle of the collection optics, the more scattered photons collected. This is achieved by increasing the F/# number of either the collection lens and/or the collection mirror. However, large F/# number lenses are difficult to manufacture and require large access ports to view the scattering volume and in most tokamaks port access is highly restricted. In addition, increasing the amount of light collected also increases the background plasma light collected. In contrast, increasing the laser energy only increases the number of scattered photons (or the $\sigma_{poisson}$).

3.3.1.2 Minimising systematic error

Systematic errors often significantly contribute to T_e and n_e errors and these mainly arise due to errors in system calibration. To determine the T_e and n_e profiles, the scattered signal in each spectral channel must be known. Calibrations are therefore required to calculate the transmission of a TS system. This is typically obtained using calibrated light sources and by filling the tokamak with noble gases and measuring the Raman and Rayleigh scattered signals from these gases using the given TS system. Calibration of TS systems is difficult due to limited access to the tokamak; and will be further limited on ITER due to the radioactive environment it will have. Detailed modeling of TS systems can identify sources of calibration error and thus permit minimisation of systematic errors. This is discussed for the specific cases of the MAST Nd:YAG system and the LIDAR system on ITER in sections 3.3.3.2 and 3.3.4 respectively.

3.3.2 Types of TS system

The three most common types of TS system on tokamaks are the TVTS, polychromator TS and LIDAR TS systems. These systems vary in terms of their repetition rates, laser energies and spatial resolutions. Each TS system type is broadly introduced later in this section, with specific TS systems described in detail elsewhere.

In Television TS (TVTS) systems [56, 57, 58], a diffraction grating spectrometer and an intensified CCD camera are used to take a 2-dimensional (2D) image of the scattered spectrum as a function of plasma radius. The advantage of this type of system is that a large number of spatial points can be detected using a single spectrometer. Ruby lasers are typically used in TVTS systems as they are high energy (10 J) and have a wavelength (693 nm) which produces a TS scattered spectrum that matches the peak wavelength range of the detectors (500 - 900 nm). A disadvantage of ruby lasers is that they typically have a low repetition rate (1 Hz) and this limits the repetition rate of the T_e and n_e measurements. A detailed description of the ruby TVTS system on MAST is

given in section 4.4.1 of chapter 4.

Parameter	**Ruby TVTS (MAST)**	**Nd:YAG (MAST)**	**Nd:YAG (MAST, Edge)**	**LIDAR (JET)**	**LIDAR (ITER)**
Laser energy (J)	10.0	1.6	1.6	1.0	5.0
Laser repetition (Hz)	1	240	240	4	100
typical n_e (m^{-3})	1.0×10^{19}	1.0×10^{19}	1.0×10^{19}	1.0×10^{19}	5.0×10^{19}
typical T_e (eV)	1000	1000	1000	1.0×10^{5}	1.0×10^{5}
Scattering angle (°)	90	90	150	180	180
λ_0 (nm)	694	1064	1064	694	1064
α	1.5×10^{-3}	2.3×10^{-3}	2.3×10^{-3}	1.5×10^{-4}	5.1×10^{-4}
Solid angle (sr)	3.49×10^{-3}	2.18×10^{-2}	2.18×10^{-2}	1.23×10^{-2}	3.07×10^{-3}
No. input photons	3.51×10^{19}	8.60×10^{18}	8.06×10^{18}	3.51×10^{18}	2.69×10^{19}
Scattering length (m)	0.007	0.01	0.008	0.12	0.067
No. scattered photons	6.1×10^{4}	8.9×10^{4}	6.7×10^{4}	2.5×10^{5}	1.3×10^{6}

Table 3.1: Comparison of parameters for the different TS systems on MAST, JET and ITER. The number of scattered photons is calculated using the formula (input photons)*(typical n_e)*(solid angle)*(TS cross-section)*(scattering length)*(fraction of the scattered spectrum taken at a typical temperature)

A polychromator system differs from a TVTS system in that it uses a separate bandpass filter-based spectrometer (a polychromator) for each spatial point. First harmonic Nd:Yag lasers are typically used in this type of system as the it is not possible to produce a TV-type system with high sensitivity at the Nd:Yag wavelength (1064 nm). This produces the principal disadvantage of polychromator systems, in that a separate polychromator is used per spatial channel, which increases the cost of the system. In addition, often only one side of the scattered spectrum is detected to reduce the number of spectral channels required. The laser energies of Nd:YAG lasers (1-5 J) are typically less than ruby lasers (10-20 J), which increases the relative T_e and n_e errors. However, a major advantage of Nd:YAG systems is that Nd:YAG lasers have much greater repetition rates ($\sim$ 50 Hz) than ruby lasers and thus more T_e and n_e measurements can be performed per plasma shot. The Nd:YAG system on MAST is described in detail below (section 3.3.3).

A Light Imaging Detection and Ranging (LIDAR) TS system is currently used on JET and is also planned for ITER. LIDAR systems are characterised by a 180° scattering angle, with the scattered light backscattering from the input laser pulse, instead of the $30^\circ - 150^\circ$ angles typical in conventional TS systems, including Nd:YAG and TVTS. In addition, the spatial position of the scattered spectrum is determined by taking the time of flight of the laser beam, which requires very short laser pulses ($\sim$ 300 ps) and very fast detectors ($\sim$ 300 ps) and digitisers ($\sim$ 400 ps). One

principal advantage of LIDAR systems is that the same port is used for both the laser input and collection of scattered light. This is particularly relevant for future reactors whose port access will be restricted, as their surface areas will be required for blankets to breed the fuel. Another advantage of this system type is that it only requires a single polychromator to measure the scattered spectrum, thus reducing systematic errors related to multiple polychromators. The main disadvantage of the LIDAR system is that the minimum possible spatial resolution is typically less than that of conventional TS systems, as this is determined by detector speeds and laser pulse duration. Both Nd:YAG and ruby lasers can be used for the LIDAR TS systems. The current JET LIDAR system uses ruby lasers whilst the ITER LIDAR system will use Nd:YAG lasers.

Table 3.1 illustrates these differences between these three types of TS system by comparing their major operating parameters. The TS systems on MAST, JET and ITER are used as examples.

3.3.3 Improvements to MAST Nd:YAG TS system

The Nd:YAG system on MAST was recently upgraded in order to provide higher spatial and temporal resolution measurements of the T_e and n_e profile. This was carried out as part of a wider upgrade to the core MAST TS system that also included upgrading the ruby TS system (described in Chapter 4). Figure 3.5 shows the layout of these two upgraded TS systems. Both of these upgraded systems were subsequently used to study the heat transport and evolution of NTMs and enabled this to be done in greater detail (see Chapter 5). The motivation for installing two TS system was to combine the respective advantages of the TVTS system and Nd:YAG polychromator system. The TVTS system can achieve high radial resolution whilst the Nd:YAG system can obtain high temporal sampling. An additional benefit of two independent measurements at similar positions in the plasma is that systematic error can be more easily identified in either measurement.

In addition to upgrading the Nd:YAG hardware, a method was also developed to remove systematic error in the this system. This involved identifying and removing systematic errors in the spectral calibration and is described below. This method has also proven very important for accurate measurements of NTMs (Chapter 5).

Although I was the principal investigator for the upgrade to ruby system, I only contributed partially to improvements to the Nd:YAG system. However, I was involved in the process throughout its entirety.

3.3.3.1 Upgrade of the MAST Nd:YAG system

The upgraded MAST Nd:YAG system utilises 8 Nd:YAG 1.5 J, 30 Hz lasers, each with a wavelength of 1064 nm. The system records T_e and n_e measurements for 130 spatial points, with radial positions ranging between 0.25-1.5 m [59]. The resulting resolution is $\sim$1 cm and the time separa-

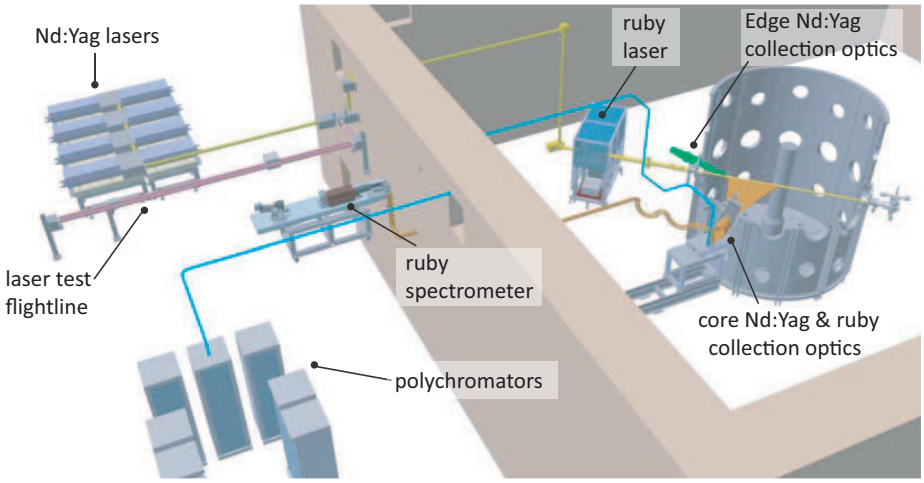

Figure 3.5: Layout of the Nd:YAG and ruby TS systems on MAST. Light from the Nd:YAG lasers travels to the MAST vessel, guided by a flightline, and transverses the vessel 15 mm above the midplane. In contrast, for the ruby system, light from a ruby laser transverses the MAST vessel 15 mm below the midplane. Both systems share the same collection optics, but scattered light for the Nd:YAG system is collected and relayed to polychromators, where the TS signal is digitised, whilst scattered light for the ruby system is relayed to a grating spectrometer and digitised.

tion between the lasers can be adjusted to suit the experimental scenario being studied. In the case of heat transport studies for NTMs this separation is typically set to $\sim$20 μs, to match one poloidal rotation of the island.

The Nd:YAG lasers travel along a 30 m beam path to the MAST vessel and the beam profile is controlled by two cylindrical lenses. The lasers then follow a path 15 mm vertically above the midplane of the MAST vessel and the beams impact upon a stainless steel beam dump. This consists of narrow blades to ensure that any laser beam reflections are at oblique angles and thus do not escape into the MAST vessel. The laser beam path is also fitted with baffles to reduce stray light.

It is crucial that the Nd:YAG lasers are well aligned to the object plane of the collection lens and a number of methods are implemented to ensure this. Firstly, HeNe (helium neon) lasers are aligned to have the same flight path as the Nd:YAG lasers and the HeNe laser positions are then measured on a target by removing the beam dump. In addition, split fibres are used to measure the amount of TS signal in the top and bottom halves of the laser beam at two fixed points to determine the alignment. Finally, a telescopic CCD imaging system measures both beam size and position inside the MAST vessel, utilising the reflected signal from one of the lenses onto the beam path.

The TS light is collected by an upgraded F/6 collection lens, which collects four times more light than the pre-upgrade lens. The light is imaged at F/1.75 onto a fibre backplane consisting

of 132 fibre bundles, which transmit the scattered light across 30 m to 130 polychromators. In each polychromator, bandpass filters are used to split the light into 4 spectral channels below the Nd:YAG laser wavelength. Avalanche photodiodes are used to measure the scattered signal in each spectral channel, which is then fitted with a Gaussian profile. This gives the total scattering signal in each spectral channel (figure 3.6).

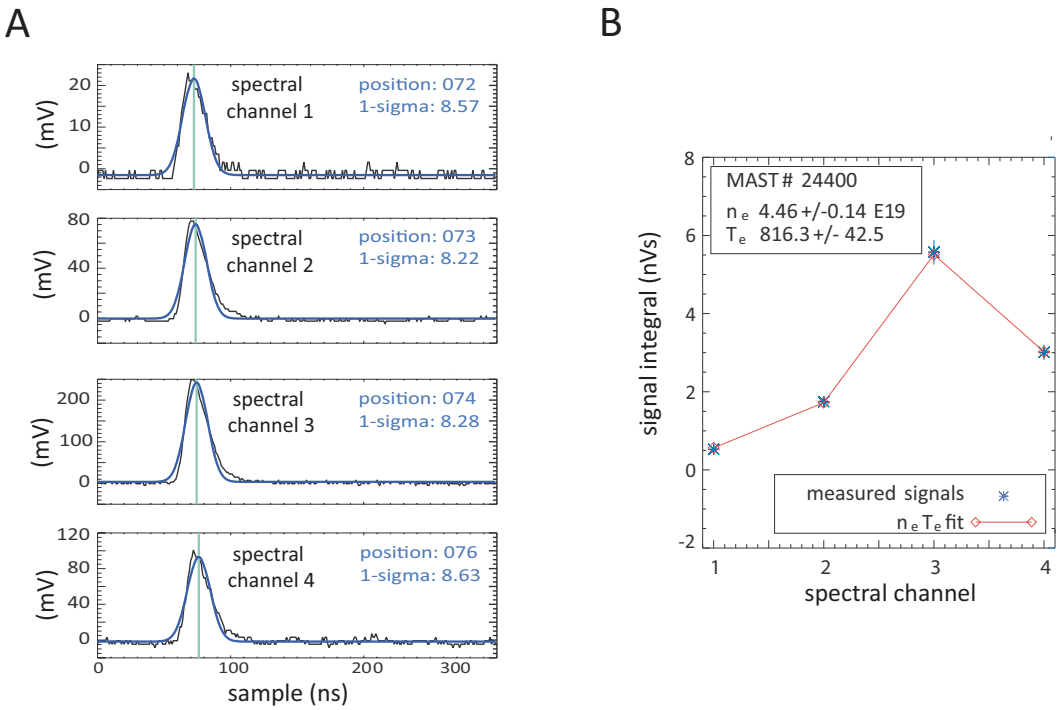

Figure 3.6: Fitting the TS signal in the Nd:YAG system. A. Measured scattered signals (black) overlaid with Gaussian fits performed on the embedded computer system (blue), for the 4 Nd:YAG spectral channels. Position and 1-sigma values are related to the Nd:YAG pulse width and avalanche photo diodes and show good agreement between the channels. The difference in the 1 sigma measurements are a result of the different responses of the digitisers for each channel. B. A fit (red line) of the measured Nd:YAG spectrum (signal integrals from A.) (blue dots) at one spatial point using the Selden-Naito approximation. This gives the T_e and n_e values at this point.

For every 5 spectrometers there is 1 cPCI computer chassis, containing 20 or 24 1 GSample/s ADC and 1 single-board computer (SBC). Each cubicle in figure 3.7 contains 15 polychromators and 3 computer chassis in total. The integration of the scattered signal for each channel is performed by these computer chassis and the data are sent to the MAST data repository. Here it is fitted to the theoretical TS spectra (figure 3.6) using Raman [60] and whitelight calibration data. Real-time T_e and n_e profiles are also calculated using the 26 distributed PC chassis. These are determined using a look-up table, which is tabulated for each spectrometer using its spectral and Raman calibration [61].

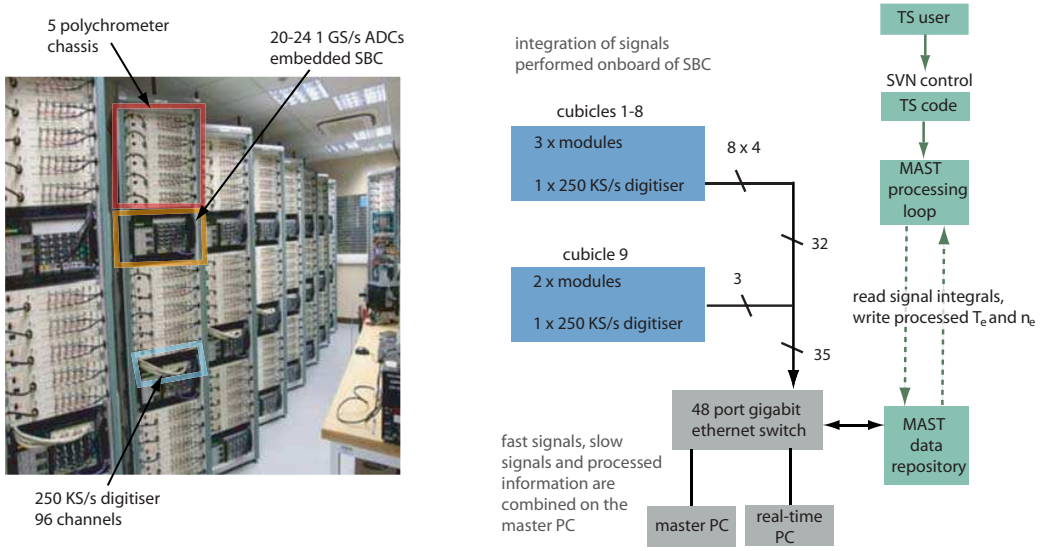

Figure 3.7: Photograph (left) and flow diagram (right) of assembled polychromators and the data acquisition system on the Nd:YAG TS system. The photograph shows the 8 cubicles in the Nd:YAG spectrometer room and for every 5 polychromators (red box) there is an SBC (orange box), and for each cubicle there is a 250 KS/s digitiser (light blue box). The schematic diagram shows how the TS signals in the Nd:YAG system are processed to produce T_e and n_e profiles. Once the TS signal is acquired (acquisition system is shown in blue) it is sent to the PCs (grey) for real-time calculation of the T_e and n_e profiles and to the MAST data repository for analysis post shot (green).

3.3.3.2 Removal of systematic error from the Nd:YAG system

To correctly determine the T_e and n_e from a measured scattered signal ($M(r, \lambda)$), the calibration of each spectral channel in each polychromator must be obtained. Errors in these calibrations result in systematic errors in T_e and n_e across the radial profiles and removal of these systematic errors is therefore necessary for accurate study of magnetic islands and other small structures in T_e and n_e profiles. A method was developed to remove these errors from the MAST Nd:YAG TS system and is described in this section.

The Nd:YAG spectral calibration is obtained by performing an absolute radial calibration ($R(r)$) of one channel in each polychromator, using Raman scattering off of nitrogen. The relative calibration ($I(r, \lambda)$) of the three remaining channels to the absolutely calibrated channel is obtained by illuminating each polychromator with a calibrated whitelight source. The measured scattered signal is given by:

$$M(r, \lambda) = R(r)I(r, \lambda)S_{TS}(r, \lambda) \tag{3.68}$$

where S_{TS} is the scattered TS spectrum. We can rewrite the scattered spectra in terms of the

measured quantities:

$$S_{TS}(r,\lambda) = \frac{M(r,\lambda)}{R(r)I(r,\lambda)} \tag{3.69}$$

To identify systematic errors, an assumption of the 'expected' scattered spectra must be made. A reasonable assumption is that, in the absence of transport barriers, magnetic islands or other MHD events, the T_e and n_e profiles should be smooth and linear over 3 spatial points ($\sim$ 3 cm) (figure 3.8). Using this assumption [62], we can calculate a correction factor to remove the calibration error. The i^{th} spectral point is taken for a given spectral channel and we assume that this point is midway between the adjacent points $(i-1, i+1)$. The correction factor ($C_r(r,\lambda)$) for the i^{th} point is equal to $\frac{y^i}{y^m}$. The effect of this assumption is to smooth out the systematic errors in the spectra between adjacent points. The means that the systematic deviation between neighbouring radial channels can be calculated using experimental data from a large number of times and shots. The spectral calibration is therefore multiplied by $C_r(r,\lambda)$ to remove the mean systematic deviation.

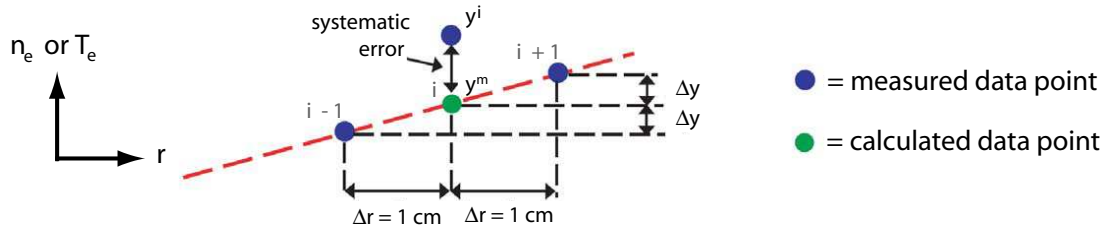

Figure 3.8: Schematic diagram of the assumption made when removing systematic errors, i.e. a linear relationship (red, dashed line) between local points. The central blue dot represents the signal in the i^{th} radial channel for a given spectral channel, whereas the green dot is the calculated data point between points i-1 and i+1, if a linear relationship is assumed.

This corrected calibration has been shown to significantly reduce the systematic T_e and n_e error in the profiles on the Nd:YAG system and an example of this for an individual shot is shown in figure 3.9. Any reduction in systematic error will also result in a reduction of the χ^2 values determined by fitting the experimental data to the theoretical spectrum, as a better agreement between the theoretical spectra and the experimental data is possible. This is shown in figure 3.10, which displays the time-averaged χ^2 ($\langle \chi^2(r) \rangle_t$) before and after the correction has been applied. The correlation of the correction factors over a period of six months was also investigated and the results showed these factors to remain well-correlated over this time (see figure 3.11). As a result of these findings, this correction method is now applied to all Nd:YAG data to remove systematic error.

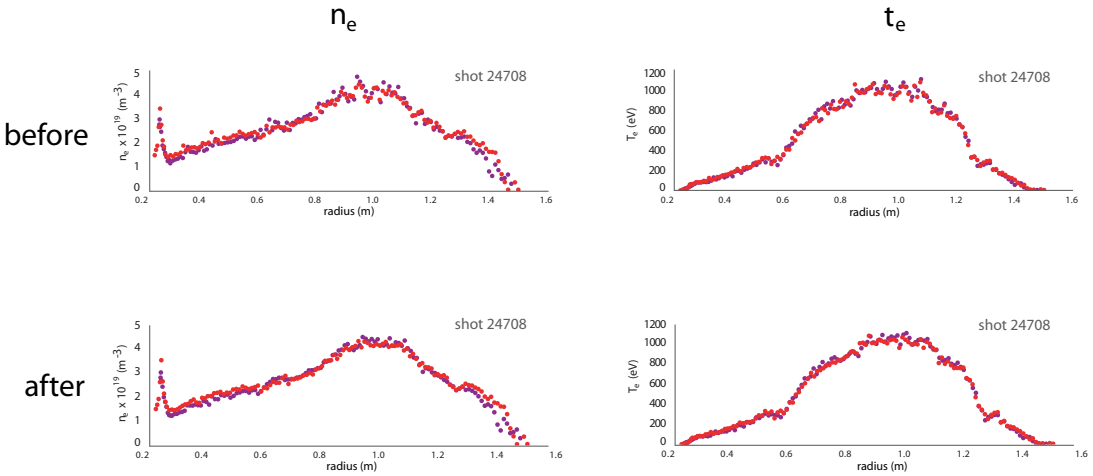

Figure 3.9: The T_e and n_e profiles before and after corrections for systematic errors were applied. Red dots are at time 0.233 ms and purple dots at time 228 ms. The similarity at these separate times confirms the reduction in the systematic error after correction has been applied.

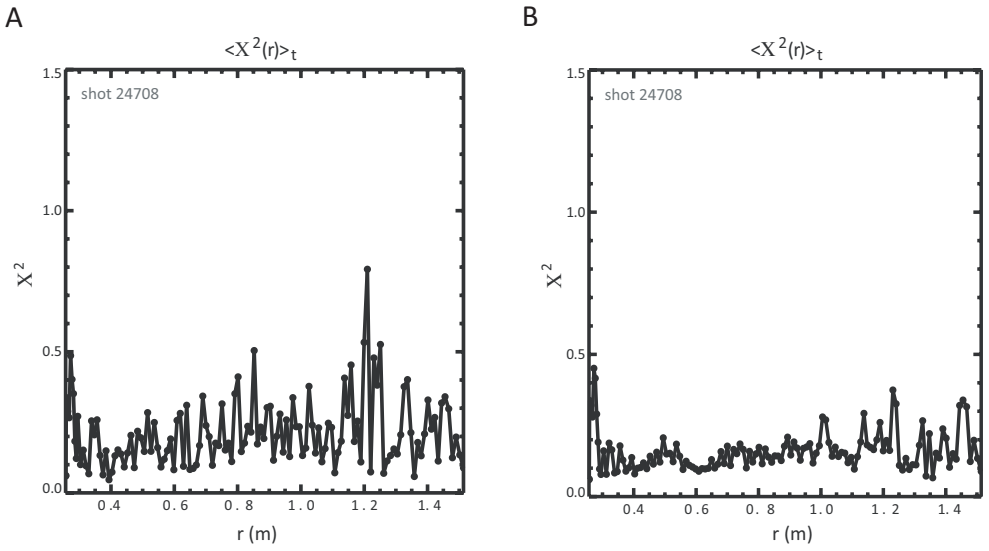

Figure 3.10: $\langle \chi(r)^2 \rangle_t$ at each spatial point which is the time-averaged χ^2 as a function of radius (r) over the plasma pulse. A. The $\langle \chi^2(r) \rangle_t$ before multiplication of the spectral correction factors. B. Reduction of the $\langle \chi^2(r) \rangle_t$ after multiplication.

3.3.4 Simulations for the ITER LIDAR system

It is critical to ensure that the design of components in the vicinity of the ITER vessel perform to specification, as the high neutron dose will restrict any access to these once ITER begins operations. This section describes simulations performed on the proposed design of the collection optics for the ITER LIDAR TS system. Precise collection optics design is necessary to ensure T_e and n_e errors are

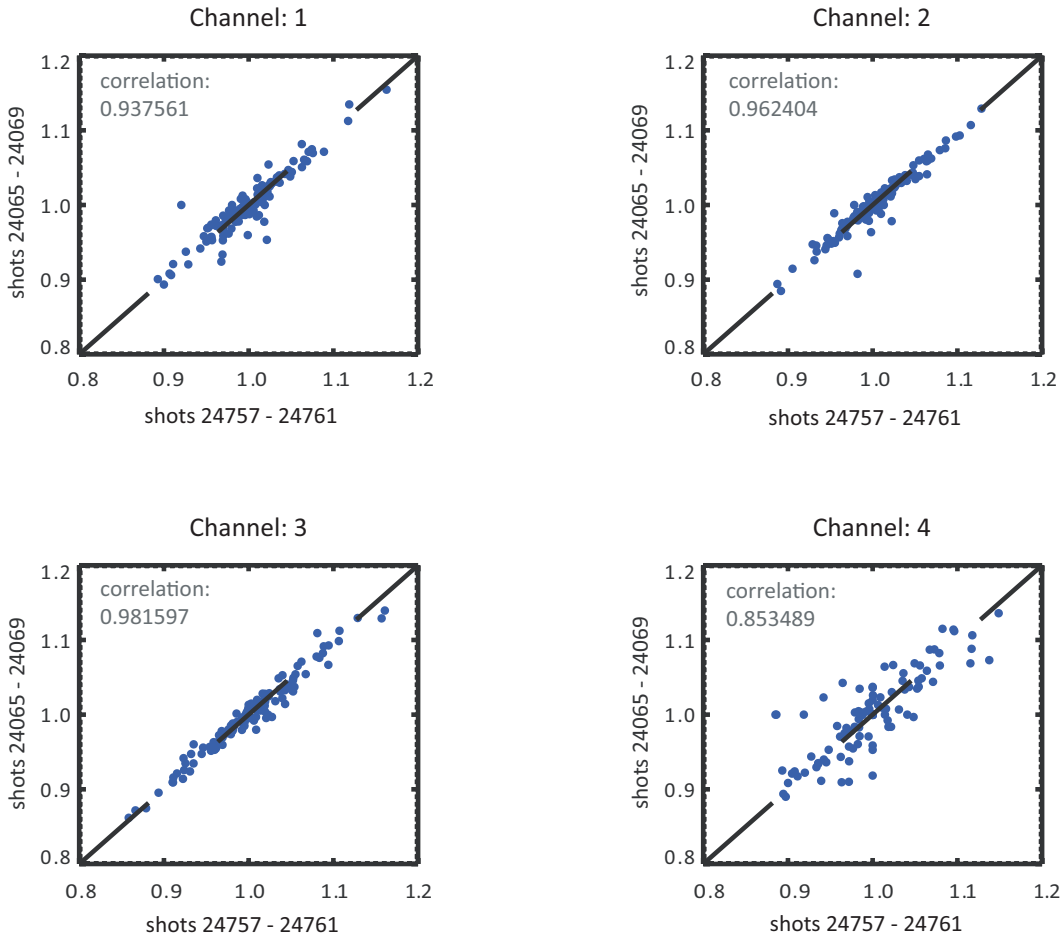

Figure 3.11: Correlation between 130 different correction factors (blue dot) for each spectral channel, determined from two data sets (shots 24065-24069 and shots 24757-24761) separated by 6 months. The correlation for all channels remains high over this time period

minimised in this system and the particular focus of these simulations was to determine the effects of the angular distribution of optical rays on the LIDAR optical bandpass filters. The proposed collection optics for the ITER system are shown in figure 3.12. Scattered light is collected by a mirror at an equatorial port and is then relayed through a labyrinth to a vacuum window at the rear of the port plug. The scattered light is then transmitted to a polychromator via optical fibres. The LIDAR collection optics has a large depth of field in the object plane of the collection lens. As a result, the solid angle collected by this optics system will decrease with distance across the tokamak. At the inner wall, therefore, only the minimum light (F/18) will be collected, with the maximum (F/6) at the outboard of the tokamak. Scattered light from these different radial positions (and F/#s) produces different angular distributions at the bandpass filters of the polychromator system.

If the angle of incidence onto an optical bandpass filter is not normal to its surface the effective wavelength seen by the filter is shifted. This results in a broadened spectral transmission, which

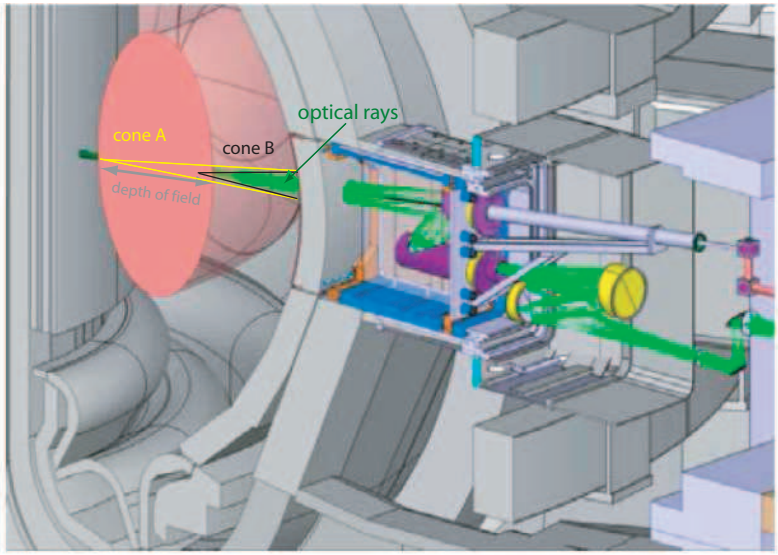

Figure 3.12: A schematic layout of the collection optics planned for the ITER LIDAR system. The F/# of light collected by the system is dependent on the radial position of the scattering volume, as illustrated by two cones of light at two different radial positions (cones A and B).

causes a reduced sharpness in the filter bandstop. This is important to avoid, as a sharp bandstop is necessary for removal of laser light, measuring low electron temperatures and accurate Raman calibration. The relationship between the angle of incidence (θ) and the wavelength shift on an optical filter with an effective refractive index of n_{eff}, in a surrounding medium of index n_0, is given by:

$$\lambda \rightarrow \lambda \sqrt{1 - \left(\frac{n_0}{n_{eff}}\right)^2 sin^2\theta}. \tag{3.70}$$

Simulations were performed which combined equation 3.70 with optical ray tracing of the LIDAR design, in order to calculate the spectral shifts that result from the angular distribution on the bandpass filters. A major consideration in these simulations was the filter diameter, since angular distribution of optical rays on the filters reduces with increasing filter diameter. Current limitations in the construction of these filters prevents diameters greater than 300 mm and, therefore, this value was taken as the upper limit to test in the simulations.

These optical simulations were performed to estimate the spectral shifts of scattered data collected from radial positions (r/a) +1, +0.5, 0, -0.5 and -1, on filters of diameters 170, 215, 260 and 300 mm. The width of the filter bandpass for all combinations of position and diameter was taken to be 0.01 λ_0, where λ_0 is the normalised laser wavelength. For each position in the plasma and for each optical filter, the ray angle distribution was calculated from 100 points. These points were

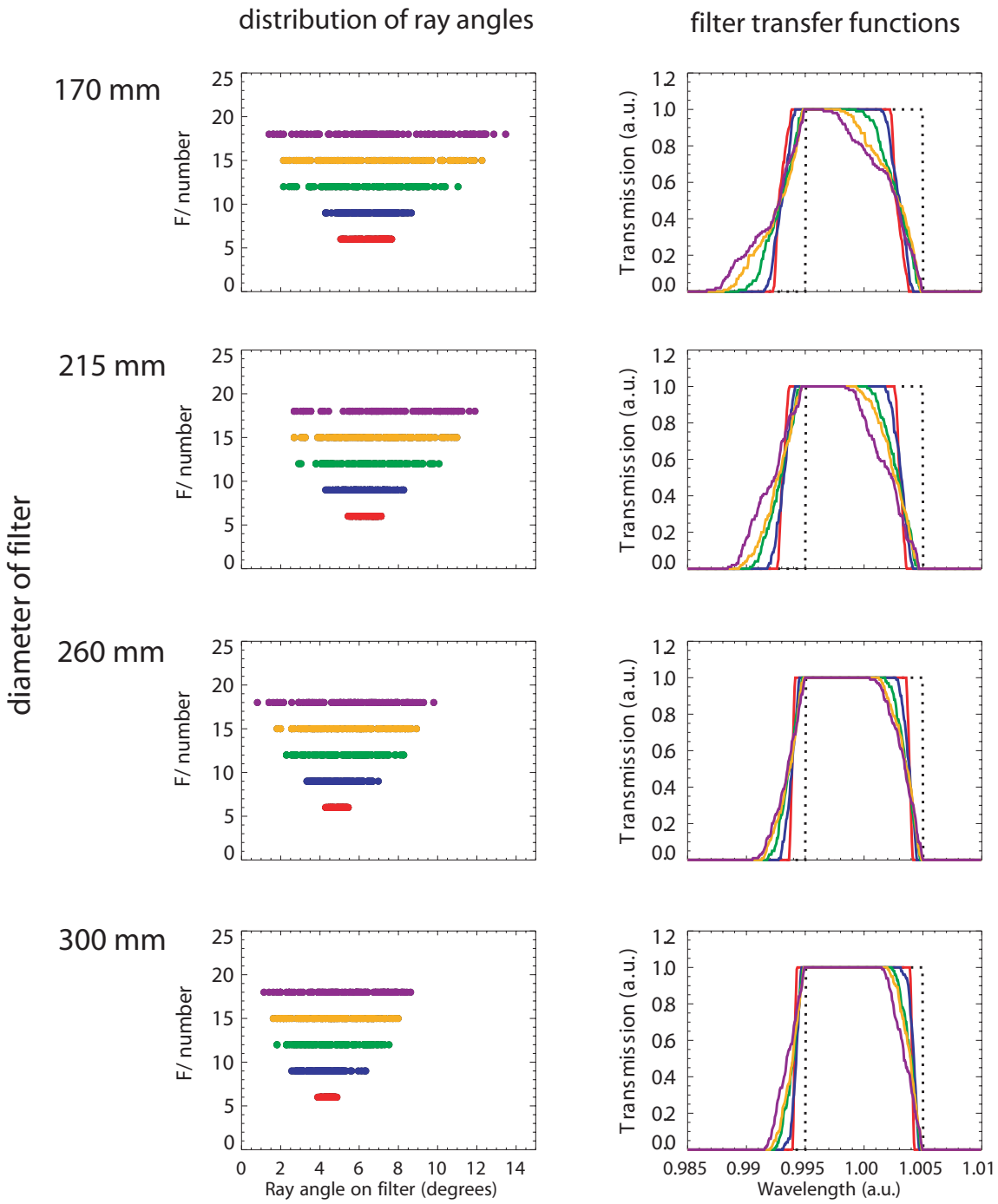

Figure 3.13: The effect of angular distribution on the spectral transmission of filters. For a given F/# number (each represented by coloured line), a larger filter diameter leads to a lower angular distribution (lefthand column), which leads to a reduction in the blueshift of the filter transfer functions (righthand column).

taken from a random position in the field of the scattering centre and the rays from these travelled through to random positions in the pupil of the collection optics.

The simulation results show that larger F/#s, collected at radial locations on the tokamak in-

board side, produce greater broadening of the filter bandstops and that a similar broadening occurs as bandpass filter diameters are reduced (figure 3.13). To be confident that the LIDAR system will work over its full range of F/#s, the minimum bandpass filter diameter required for optimal stray laser light removal and a lower measurable T_e range was assessed at the worst-case F/# scenario (F/18, inboard, r/a = -1).

To remove stray laser light the transmission at the laser wavelength must be of the order of 10^{-5} (optical density of 5). The results (figure 3.13) show that at F/18 smaller diameter bandpass filters close to the laser wavelength will not remove stray laser light as effectively as required due to optical transmission outside the bandstop region. Filter diameters greater than 260 mm will be required to remove stray light sufficiently to prevent interference with TS data. Similarly, at F/18, filter diameters greater than 260 mm are required to place the filter bandstop close to the laser wavelength, which is required to measure low electron temperatures.

In addition, the variation of the F/# with radius also affects the Raman calibration of the system. Raman scattering from nitrogen gas is typically used to provide an absolute density calibration of polychromator-based TS systems [60]. An increase in F/#, which broadens the bandstop, leads to a decrease in the signal due to the Raman scattering as function of the r/a of ITER. To minimise this decrease to permit accurate Raman calibration (to $\sim$ 6 %) a minimum filter diameter of 260 mm is needed. Systematic variation could be further reduced if another filter is included to measure the Stokes lines above the laser wavelength, as the shifts in the spectral transmissions of the filter at each side of this wavelength tend to cancel each other out [63].

These optical ray tracing simulations have shown that the spectral transmission of the filter used in the ITER LIDAR system will vary as a function of the minor radius. Such variation will result in concurrent increased stray laser light, prevent lower electron temperature measurements and likely lead to errors in the Raman calibration if not accounted for in the LIDAR system design. Increasing the bandpass filter diameters to above 260 mm should produce a sufficiently sharp bandstop (within a few nanometers of the laser wavelength) to sufficiently minimise these effects and thus errors in T_e and n_e measurements on ITER (figure 3.13).

3.3.5 The effect of the n_e profile and sampling region on the T_e profile

Previous sections have considered approaches for improving measurements of T_e and n_e data. Here, we look at improving the interpretation of the T_e and n_e data in the edge pedestal. The measurement and scaling of T_e and n_e in this region is one of the most important and well-studied topics in tokamak physics and is principally measured using TS systems. Typically, an $mtanh$ function [64] is used to describe the shape of the T_e and n_e profiles in the pedestal region (figure 3.14) and it can be fitted to these profiles to determine important pedestal parameters. These parameters can

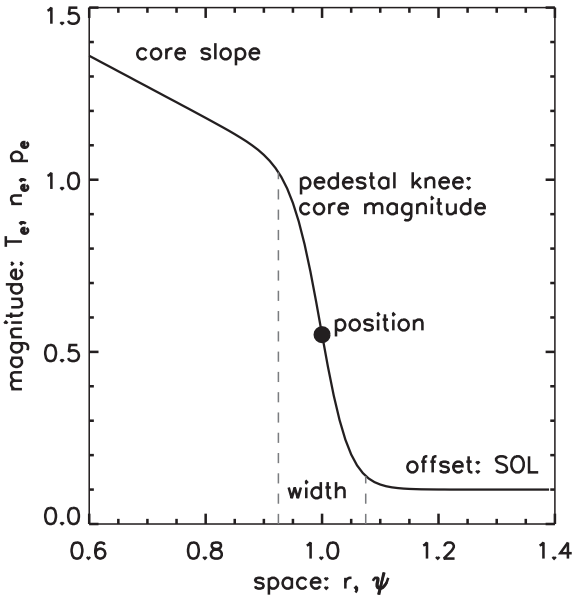

Figure 3.14: The general form of the edge pedestal. The T_e and n_e and p_e edge pedestal can be described by a modified $tanh$ function (black line), which has 5 free parameters - the pedestal width, pedestal offset, pedestal position (black dot), pedestal knee and core slope.

then be used in scaling laws for future devices.However, sharp gradients in T_e and n_e profiles in the edge pedestal are not reproduced accurately by TS systems. A number of effects can lead to a systematic error in the T_e and n_e profiles. The radial sampling of the TS system may be small compared to the n_e gradient that the system measures. In this case, the average $T_e$profile measured is weighted towards the high density part of the sampling volume. Furthermore, the radial resolution of the TS measurement is typical smaller than the sampling and hence light is redistributed between neighbouring sampling volumes. This will also affect the gradient of the T_e and n_e profiles measured and is represented as a radial instrument function ($I(r)$).

In previous work, the effect of the $I(r)$ was included by first convolving the T_e and n_e profiles calculated from the mtanh function by $I(r)$ before fitting this function to the processed TS T_e and n_e profiles in the pedestal region. This method is referred to as forward deconvolution in the literature. However, this method does not account for the effects of the n_e gradient and the fact that the redistribution of light occurs between TS spectra and not the analysed T_e and n_e profile. A full spectral fitting method was later developed to include these effects [54], but requires all of the absolute and spectral calibration information for each spectral channel at each step of the fitting process. However, these data are often not available. A new analytical method to determine the edge pedestal from TS data has since been developed and is presented here. This new method is able to fully account for the n_e gradient and approximate the spectral smoothing effects, but removes the need for the calibration information for each spectral channel and requires only the

processed T_e and n_e data [65].

In TS systems, raw spectral data are detected for a fixed sampling volume. The total spectrum (S_{ob}) detected is given by the sum of the TS spectra from the electrons within that scattering volume. This can be represented by the convolution of the underlying scattered signal $S(\lambda, r)$ and an instrument function:

$$S_{ob} = S(\lambda, r) \otimes I(r). \tag{3.71}$$

When fitting a given TS spectra, it is usually assumed that the mean spectrum detected will give the mean estimate for the T_e and n_e of that sampling volume and thus the convolution in equation 3.71 can be ignored. The T_e are n_e resulting from this fit are referred to as the observed T_e ($T_{e,ob}$) and n_e ($n_{e,ob}$) respectively. In the core of the tokamak, the width of a given sampling size (Δ_r) is sufficiently small, compared to the local gradients in the T_e and n_e profiles, to make this assumption valid. However, at the edge pedestal, a steep gradient in the T_e and n_e profiles develops and the width of this steeply gradated region is often comparable to Δ_r, making the assumption less valid.

The $mtanh$ function, that describes the shape of the T_e and n_e pedestals, contains 5 free parameters: pedestal height ($n_{e,height}$,$T_{e,height}$), width (Δ_{n_e}, Δ_{t_e}), position ($n_{e,pos}$,$T_{e,pos}$), core slope ($n_{e,CS}$,$T_{e,CS}$) and scrape-off layer (SOL) offset ($n_{e,SOL}$,$T_{e,SOL}$). When using the forward deconvolution method, the spectral signal is not convolved with $I(r)$ before fitting S_{ob} to the Selden-Naito approximation. The $T_{e,ob}$ and $n_{e,ob}$ profiles that result from the fit of S_{ob} are instead fitted to an $mtanh$ function, which has first been convolved with the $I(r)$:

$$\begin{aligned} &mtanh\left(\Delta_{n_e}, n_{e,height}, n_{e,sol}, n_{e,CS}, n_{e,pos}\right) \rightarrow n_e(r) \rightarrow n_e(r) \otimes I(r) \Leftrightarrow n_{e,ob} \\ &mtanh\left(\Delta_{T_e}, n_{e,height}, T_{e,sol}, T_{e,CS}, T_{e,pos}\right) \rightarrow T_e(r) \rightarrow T_e(r) \otimes I(r) \Leftrightarrow T_{e,ob} \end{aligned} \tag{3.72}$$

The forward deconvolution method can effectively reproduce the underlying n_e profile, but not the underlying T_e profile (figure 3.15). This is because n_e is not related to the shape of the TS spectrum and is only influenced by its integral, whereas T_e is directly related to the width of the TS spectrum and therefore the forward convolution of $mtanh$ does not reproduce the underlying $T_e(r)$ well. In contrast, the full spectral fitting method includes the convolution that generates S_{ob} (equation 3.71). This convolution is carried out at the spectral level at which it occurs in the measurements and therefore can accurately reproduce the underlying T_e and n_e:

$$\{(T_e(r), n_e(r)) \rightarrow S(\lambda, r) \otimes I(r) \Leftrightarrow S_{ob}(\lambda, r)\} \rightarrow n_e(r), T_e(r). \tag{3.73}$$

The full spectral fitting method requires all of the absolute and spectral calibration information for each spectrometer, at each step of the fitting process. A new method that does not require these data and can be applied to processed T_e and n_e profile has been developed. This method which improves upon the forward deconvolution method by including the effects of n_e gradient and

spectral smoothing on the edge pedestal, is now described. We assume that each TS spectrum in the edge pedestal is approximately Gaussian. The addition of Gaussians with similar intensities and widths ($\Delta\lambda_1$,$\Delta\lambda_2$) produces a Gaussian which has a width ($\Delta\lambda_{ob}$) approximately equal to the mean width of the added Gaussians:

$$\Delta\lambda_{ob} = \frac{\Delta\lambda_1 + \Delta\lambda_2}{2} \tag{3.74}$$

The width of the TS spectra scales as $\sim \sqrt{T_e}$ (see equation 3.62, section 3.2.7). Using equation 3.62, $\sqrt{T_e}$ can be substituted for the spectrum width ($\Delta\lambda$) in equation 3.74. This permits the $T_{e,ob}$ in a scattering volume of constant density to be approximated by:

$$T_{e,ob} \propto \frac{\left(\sqrt{T_{e,1}} + \sqrt{T_{e,1}}\right)^2}{4} \tag{3.75}$$

Due to the n_e variations in a scattering volume, $T_{e,ob}$ is weighted by the high density region and this is given by:

$$T_{e,ob} = \left(\frac{\int \sqrt{T_e(r)} n_e(r) I(r) dr}{\int n_e(r) I(r) dr} \right)^2 . \tag{3.76}$$

This equation only applies to an individual scattering volume. However, it can be generalized to a radial profile using the convolution operator:

$$T_{e,ob}(r) = \left(\frac{(\sqrt{T_e(r)} n_e(r)) \otimes I(r)}{n_e(r) \otimes I(r)} \right)^2 \tag{3.77}$$

This new method has been found to give a good estimate of the underlying T_e profile in the edge pedestal (figure 3.15). Comparison of this approach to the full spectral fitting method shows it reproduces the underlying T_e pedestal parameters to a similar level of accuracy when the edge pedestal width is greater than half of the TS sampling size (Δ_r). At lower widths, this method results in systematically lower estimates for ($\sim 20\%$) than the full spectral model. However, it will be a valid approach for a large number of TS systems, as their spatial sampling is typically greater than, or equal to, the pedestal width. In addition, this new analytical method can be applied to the existing pedestal scaling database, which is currently based on the forward deconvolution model. By doing so, more accurate scaling of edge pedestal parameters for future devices can be determined.

3.4 Conclusions

This chapter has outlined the theory of TS, starting from the case of a single electron and ending with expressions used to fit TS spectra in order to determine the T_e and n_e profiles in tokamaks. In these discussions, an effort has been made to give the reader a summary of the basics of TS, including the origins of the relativistic blue-shift and different scattering regimes.

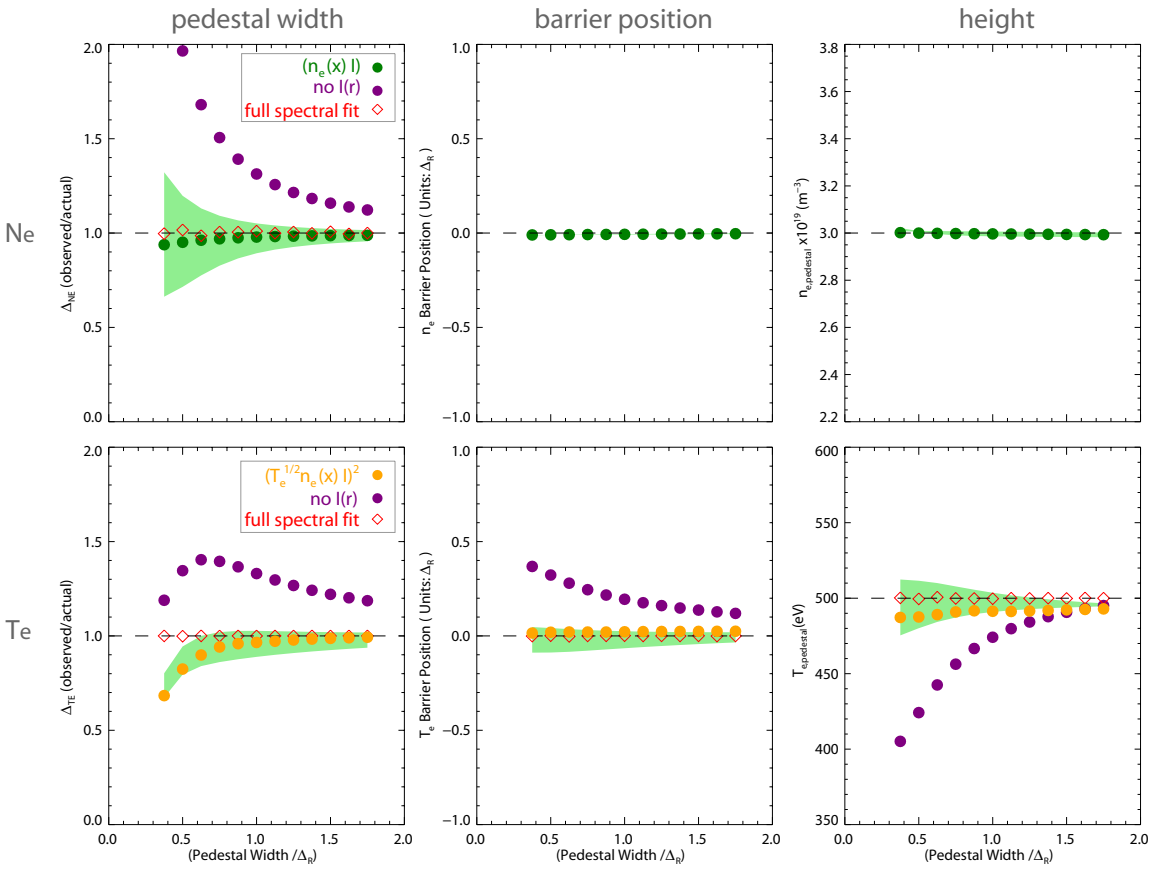

Figure 3.15: A comparison of the T_e and n_e pedestal parameters obtained when using different approaches to account for I(r). The top plots show n_e pedestal width, barrier position and height obtained using the forward deconvolution method (green dots), the full spectral fitting method (red diamonds) and also when I(r) is not accounted for at all (purple dots). The bottom plots show the T_e pedestal width, position and height obtained using the new approximation method (orange dots), the full spectral fitting method (red diamonds) and when I(r) is not accounted for (purple dots)

The experimental TS section introduced the main types of TS system used in MCF. However, the main focus of this section was the minimisation of T_e and n_e errors, this being a major goal of TS system development as reduction will permit more accurate measurements of structures in T_e and n_e , such as NTMs, ELMs, ITBs and the edge pedestal. A number of experimental approaches to reduce T_e and n_e errors have therefore been carried out and the results of these experiments were presented in this chapter. These have either led to notable reductions in T_e and n_e error in existing systems or identified potential sources of error for LIDAR on ITER.

An upgrade to the Nd:YAG TS system to provide higher spatial and temporal resolution measurements of T_e and n_e was carried out. This produced a system with a spatial resolution of 1 cm across the MAST major radius, requiring the construction of 130 polychromators. The temporal resolution of the system is 240 Hz, provided by 8 lasers operating at 30 kHz each. Furthermore,

these lasers can be operated in burst mode and bursted over fast events, for example, NTMs, sawteeth crashes, disruptions and ELMs. The combination of these capabilities permits potentially greater understanding of such instabilities. Studies have already been carried out to investigate sawteeth crashes [66], disruptions [67] and NTMs (see Chapter 5) using this upgraded system.

In addition to the hardware upgrade, a method to remove systematic error in the Nd:YAG system was developed. This focused on removing the systematic errors that result from errors in the spectral calibration. The correction factors used in this method led to a reduction in the χ^2 errors and were shown to be stable, remaining correlated over a 6 month period. This method improved the accuracy of the T_e and n_e measurements on the Nd:YAG system further to the above hardware upgrade and, in particular, enabled greater accuracy of NTM measurements (chapter 5). This method is currently being extended for a more generalised functional relationship between neighboring points using non-parametric regression techniques [68].

Ray tracing simulations of the optical design of the ITER LIDAR TS system highlighted that the angular distribution on the bandpass filters was a potential source of T_e and n_e error on this future system. The F/# will vary with minor radius on this system and the simulation results showed that a greater F/#, with respect to the filter bandpass diameter, leads to larger T_e and n_e errors. It was also found that by choosing filter diameters greater than 260 mm in the system design, these errors could be minimised to a level which permits accurate Raman calibrations and measurements at lower T_e ranges.

Finally, a method to improve TS measurements in the edge pedestal region was developed, as the sharp gradients in this region need to be accounted for to prevent distorted T_e and n_e profiles measurements. However, this has been neglected in most of the current pedestal scaling databases. The full effect of these sharp gradients can be calculated from a spectral fitting method [54], but this requires spectral calibration data which is not often available. The method presented in this chapter is an approximation that allows the current pedestal scalings to be corrected without the strict requirements of spectral fitting. Results using this method have shown it to be in good agreement with the full spectral fitting method at pedestal widths greater than half the sampling width, which is typically the case for TS system. This method has been recently been applied for pedestal scaling of DIII-D, Asdex and JET [69].

Chapter 4

Design and Implementation of a Full Profile Sub-cm Ruby Laser TS System on MAST

This chapter describes the design and implementation of the upgrade to the MAST ruby TS system to permit enhanced studies of plasma evolution and transport. Section 4.2 first gives a broad overview of the ruby TS system and its upgrade. This is followed by a discussion about what factors were important to consider in the upgrade, in order to maximise spatial resolution and reduce statistical errors (section 4.3). Full details of the upgraded system are then outlined (section 4.4), with the specifications for each component and a discussion of how each contributes to the overall system resolution and error levels. The calibration and fitting of the new system are then discussed (section 4.5) and the results compared to the design parameters. The final section outlines initial measurements made using the upgraded ruby TS system (section 4.6), which confirm its function and its potential use for future studies. Examples of the use of data from this upgraded system, to study NTMs, is presented in chapter 5.

4.1 Introduction

One of the challenges of plasma physics diagnostics is to achieve greater spatial and temporal resolution measurements of the H-mode pedestal, ELMs, magnetic islands, internal transport barriers and other phenomena related to plasma evolution and transport. Higher resolution measurements of the plasma electron temperature (T_e) and electron density (n_e) profiles can constrain more accurate models of these phenomena, allowing greater understanding and predictions of plasma behaviour. To achieve greater resolution and reduce noise, a major upgrade to the ruby TS system on the MAST tokamak was therefore carried out and its design and implementation are outlined and dis-

cussed in this chapter. Importantly, this upgrade permits probing of sub-centimetre spatial scales and although existing systems have been designed to measure sub-centimetre radial resolutions, one of the novelties of this upgraded system is that high radial resolution is maintained over a large 1.4 m laser chord. In particular, the improved spatial resolution of the new system permits enhanced study of the width of the H-mode pedestal (which is 1-2 cm on MAST) and the seed island physics of NTMs (the flattening of the T_e profile for the onset of an NTM on MAST is predicted to be of the order of $\sim$ 1 cm).

4.2 Overview of ruby system and its upgrade

The ruby system is in the TVTS category (see section 3.3.2 in Chapter 3) [56, 57, 58]. It is one of two TS systems on MAST, the other being the Nd:YAG laser system (see section 3.3.2). Each system provides independent measurements of the T_e and n_e profiles, but shares common collection optics. Thus, the timing of the ruby system upgrade was set to coincide with an upgrade to the Nd:YAG system [70], to ensure both systems were compatible with a new F/6 collections lens that was installed.

The schematic layout of the upgraded ruby TS system is shown in figure 4.1. In this system, light from a Q-switched ruby laser is first injected into the plasma along the mid-plane of the MAST tokamak. The scattered light (between scattering angles 83-120°) from a 1.4 m laser chord is then collected by an F/6 collection lens and imaged onto 85 fibre bundles. Each fibre bundle is 4.95 mm x 1.82 mm and collects scattered light at F/1.75. The light is transported 12 m along these fibres to a grating spectrometer, where the bundles are arranged to form an 8.5 mm x 130 mm input slit. A coupling lens system within the spectrometer collects F/4 of the F/1.75 light cone delivered, dropping the effective F number (F/#) of the collection lens to F/15. From the coupling lens system, the light is guided onto two holographic notch filters using a telecentric lens system. It then passes through a Littrow lens, grating and spherical field mirror onto an F/0.7 image intensifier lens. A GaAsP generation 3 (GEN3) filmless image intensifier is contact-mounted to this lens system and light from the phosphor of the image intensifier is lens-coupled to a cooled, fast frame-transfer CCD camera. An new intensified CCD camera design allows the ruby TS system to take two images, separated by a minimum of 230 μs. The system is fully automated for each MAST discharge.

The overall layout of the previous ruby system on MAST was the same as that shown in figure 4.1. However, the majority of individual components have been replaced in the upgrade, in order to achieve improved spatial resolution and reduced error in T_e and n_e measurements. The previous ruby TS system on MAST [71, 72] was only a single pulse system and had a spatial resolution of 300 points, with only 100 points at high optical contrast (which is defined as greater than 50% modulation transfer function (MTF)). In comparision, the upgraded ruby system [73] is a 512 point

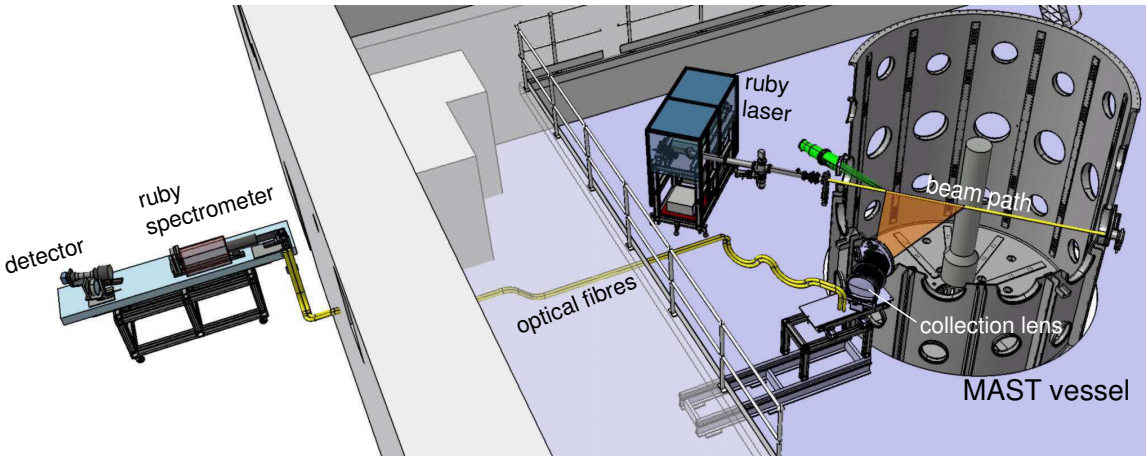

Figure 4.1: Layout of the ruby TS system on MAST. The ruby laser generates a 15 ns pulse which passes through the MAST vessel. Scattered light from this laser beam is collected by the collection lens and imaged onto the optical fibres which transmit light to the spectrometer. The TS spectrum is measured by an intensified CCD camera (detector).

dual snapshot TS system, with $\sim$ 200 points ($\sim$ 7 mm) at high optical contrast (see section 4.4.6), and can be used to either measure two T_e and n_e profiles (double pulse) or one T_e and n_e profile and one measurement of the plasma background light (single pulse) (see section 4.6.1). This spatial resolution and the effective number of points the new system can resolve is greater than similar TVTS systems. Finally, the system upgrade has also increased the number of scattered photons that can be detected by a factor of $\sim$ 3, compared to the previous system. This was achieved by replacing the previous GaAs image intensifier with a filmless GaAsP image intensifier that has a greater effective quantum efficiency (EQE) (see section 4.4.4.1). Table 4.2 in section 4.4.5 gives an estimated photon budget for the upgraded and previous core TS systems on MAST.

4.3 Design considerations

The two major design objectives for the ruby system upgrade are to maximise the spatial resolution and to minimise the statistical error of measurements (maximising the number of scattered photons collected), whilst effectively eliminating stray laser and plasma light. The ruby TS system can be broken down into five major components: the ruby laser, the collection lens, the optical fibres, the spectrometer and the detector system. Here, we discuss the factors that must be considered for each of these components to ensure the upgrade design objectives are met; and in the following discussions, the spatial resolution of each component is represented by a point spread function (PSF). A PSF is the response of an imaging system to a point source or point object. The response of an individual fibre bundle has also been modeled as a PSF. This provides a convenient method

to characterize their contribution to the system resolution. Figure 4.2 assists these discussions by illustrating how each component contributes towards the resolution and statistical error, and also the T_e range, of the ruby system. The latter is an important consideration because all TS systems, being spectrometers, are designed to function over a particular T_e and thus a particular spectral range.

Firstly, we consider the ruby laser design. The greater the laser energy, the more scattered photons there will be and the lower the statistical error of the T_e and n_e (see section 3.3.1 in chapter 3). Another factor to consider is the width of the laser beam from which scattered light is collected. This is important because the most expensive component of the ruby TS system is its fibre bundle array and a reduction in the area of scattered light collected from the laser beam would therefore reduce the overall upgrade cost significantly. However, this approach is not appropriate, as simulations show that such reductions in area would lead to large inaccuracies, due to the need for a highly precise laser alignment that is not currently realistic in a tokamak environment. The laser path and the width of the laser beam must also be considered as these influence the spatial resolution. These are discussed in section 4.4.1.

The next component to consider is the collection lens. The greater the quantity of light collected by the lens (determined by the solid angle ($\Delta\Omega_{CL}$)), the lower the statistical errors in T_e and n_e. However, it is difficult to achieve both a large solid angle and high resolution (PSF_{CL}) simultaneously in an optical system. The lens design must therefore be highly optimised to achieve both a high etendue and spatial resolution (see section 4.4.2). Furthermore, due to its proximity to the tokamak, it is necessary to use radiation-hardened glass in the collection cell, and this results in a slightly reduced spectral transmission ($T_{CL}(\lambda)$) in the red part of the spectrum and influences the T_e range of the ruby system. The magnification (M_{CL}) of the collection lens determines the area, and the input solid angle, of the optical fibre bundle array (ΔA_{FB}) at the backplane of the collection lens. The limiting factors for the optical resolution (PSF_{FB}) of these fibres are the fibre diameter (F_d) and the overlap resulting from fibre packing. At the input end of the fibre bundles (fibre backplane, see figure 4.5) five of the fibres at either end of each fibre bundle collect light from the two neighbouring spatial points. To include this smearing in the overall spatial resolution of the system the response of an individual fibre bundle has also been modelled as a PSF. This PSF (PSF_{FB}) has been modelled as three top hats representing the fibre bundle and its two neighbouring fibre bundles. The central top hat contains 82% of the signal while each neighbouring top hat contains 9% of the signal. Using the correct magnification factors, this PSF can be combined with other PSFs which arise in the system on the final image plane of the CCD camera (figure 4.9). It is also important to conserve etendue in the design of optical systems and the etendue of a system is limited by the mimimum etendue of each of its components. In this case, the major limiting factor

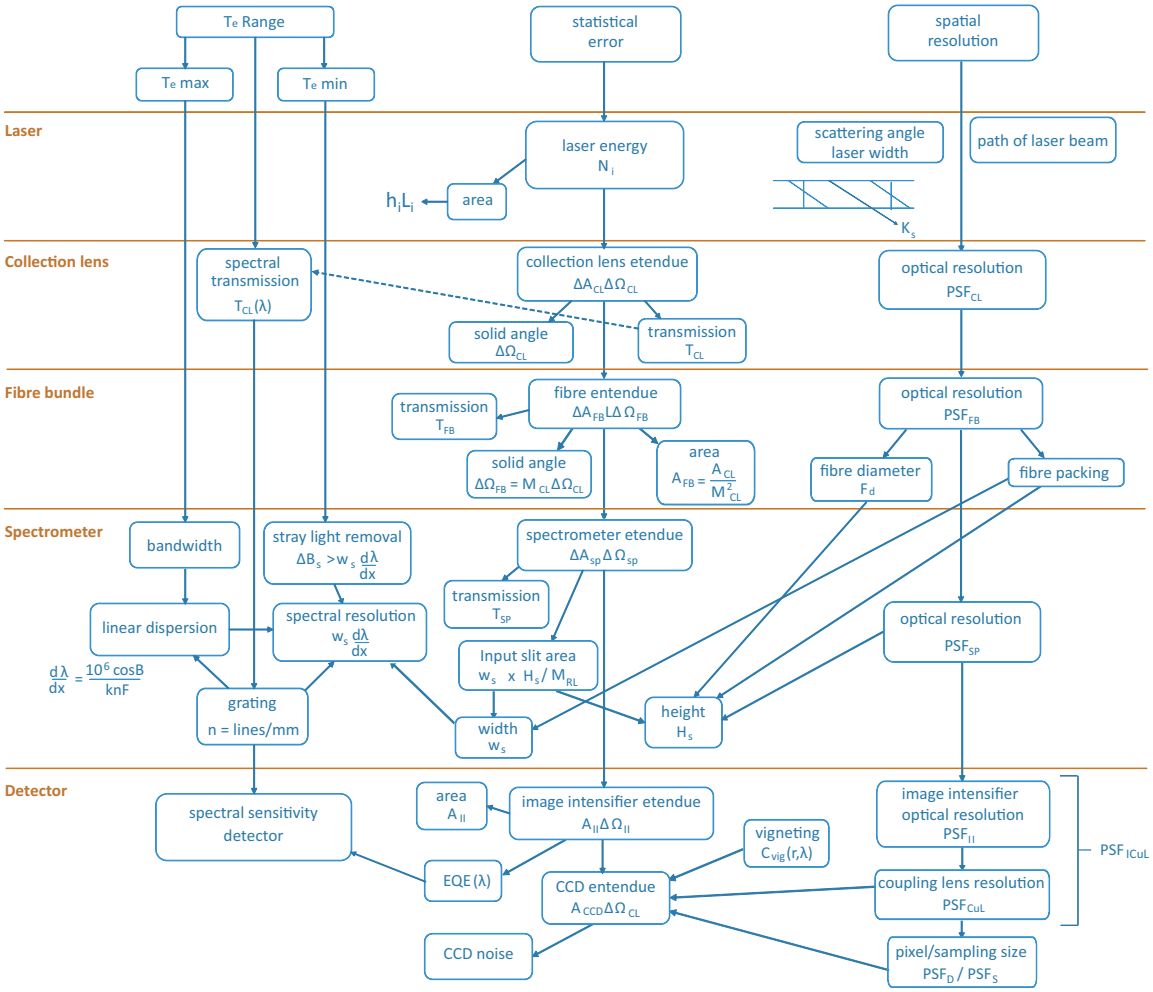

Figure 4.2: Schematic diagram of the design considerations for the ruby TS system upgrade. The influence of each components of the TS system (the laser, collection lens, fibre bundles, spectrometer and detector) on the design objectives of optimised T_e range, spatial resolution and statistical error reduction are shown. The blue arrows indicate how the different design factors for each component are interconnected and also how optimising these for one component influences the design of other components and system design overall.

is the spectrometer, which has an etendue of a factor of four less than that of the new collection lens. This is because it is not currently possible to build a GEN3 image intensifier with a diameter greater than 25 mm. However, matching the etendue of the fibre bundles to the collection lens would permit a further upgrade to the spectrometer in the future without the need to reinstall the fibres, although only a quarter of this total etendue would be collected using the current spectrometer. The choice of a fibre solution is also highly constrained by the present availability, transmission efficiency and cost of optical fibres.

Next we consider the spectrometer design. When building a TVTS system, the area of the fibre backplane must be remapped to the input slit of the spectrometer system. This remapping will affect the spatial resolution and etendue of the spectrometer. A number of radial fibres on the backplane of the collection lens are typically mapped to one radial point at the input slit (figure 4.5 in section 4.4.2). This method of mapping increases the etendue of the spectrometer and decreases the radial resolution of the system. Increasing the width (w_s) of the spectrometer input slit also reduces the spectral resolution. This in turn affects the size of the bandstop (ΔB_s) at which the laser and D_α emission line can be removed and thus the statistical error for a given T_e range. The choice of grating (lines/mm) can also influence the T_e range by altering the linear dispersion ($\frac{d\lambda}{dx}$). Finally, it is highly important to optimise the optical resolution of the spectrometer (PSF_{SP}), which is determined by the convolving the optical resolutions of each of its lenses.

The final component we consider is the detection system, which consists of an image intensifier lens coupled to a CCD camera. The statistical error and T_e range will predominantly be determined by the spectral sensitivity ($EQE(\lambda)$) of the image intensifier. This is because the gain introduced into the signal by the image intensifier will virtually negate the effects of the reduced transmission of the coupling lenses ($C_{vig}(r, \lambda)$) and the sensitivity of the CCD camera on the statistical noise. As noted above, a GEN3 image intensifier with high spectral sensitivity is limited to a 25 mm diameter and this will ultimately limit the etendue of the spectrometer. The spatial resolution of the detection system is determined by a combination of the PSFs of the image intensifier (PSF_{II}), coupling lenses (PSF_{CuL}) and CCD camera (PSF_D, PSF_S).

4.4 New system hardware

In this section each component in the upgraded ruby TS system is described, with the specifications and final design of each component discussed in detail. In addition, the contribution each components makes to overall system performance is outlined.

4.4.1 Ruby laser

The laser used in the upgraded ruby TS system is a Q-switched ruby 10 J, 1 Hz laser. It consists of an oscillator and three amplifier sections (figure 4.3B). The energy of the laser beam is 10 J, the pulse full width half maximum (FWHM) is 15 ns and the full angle beam divergence is 0.5 mrad. It is possible to double pulse this laser to also produce two 5 J pulses separated by 230 μs at 1 Hz. To produce two laser pulses, the Pockels cell is opened twice during a 1 ms pulse of the flash lamp. This 230 μs time separation between the Pockels cell openings is found to give two approximately equal energy pulses.

A flight line guides the laser beam to the plasma and the laser beam is focused at the centre of the plasma, passing the centre column at a distance of $\sim 45mm$, and finally terminating on a graphite beam dump. Throughout this ex vessel flightline, baffles are used to minimise stray light. In the upgraded system, the chord passes along the midplane (Z = -0.015 m) of the MAST vessel and is approximately parallel to the radial direction, except near the MAST centre column. In this region, it passes perpendicular to the radial coordinate to produce a much greater radial resolution on the HFS of the MAST plasma.

The laser must be accurately aligned so that its image can be fully collected by the fibre bundles. To ensure this, the position of a HeNe alignment laser beam on two spatial markers at either side of the MAST vessel is used to monitor the laser alignment daily. The image of the ruby laser is coherently mapped to the spectrometer slit and small segments of the fibre input slit can be masked to determine the laser alignment during experimental campaigns (figure 4.3A). However, this does perturb the intensity of the TS signal detected and the n_e profile must therefore be recalibrated to account for the effects of these masks.

4.4.2 Collection lens and fibre bundles

The design of the collection lens determines the quantity of scattered photons that are collected. The etendue of the collection lens is defined as the product of the solid angle of light collected and the area of object being imaged. The solid angle collected by a lens is inversely proportional to its F/#, which is the ratio of the focal length to the aperture. Therefore, the closer an object is to the lens, the greater the solid angle of light that is collected for a given lens aperture. It is desirable to measure the full T_e and n_e profile across the centre of the MAST vessel and the resulting ~ 2 metre distance between the laser beam and the collection lens requires a large aperture, in order to collect a given solid angle of light.

The collection cell (figure 4.4) has a diameter of 520 mm and a length of 650 mm. The combined weight of the collection cell and its lenses is ~ 90 kg. TS light is collected at F/6 from the 1.4 m Nd:YAG and ruby laser chords. The observation volumes are imaged with a magnification

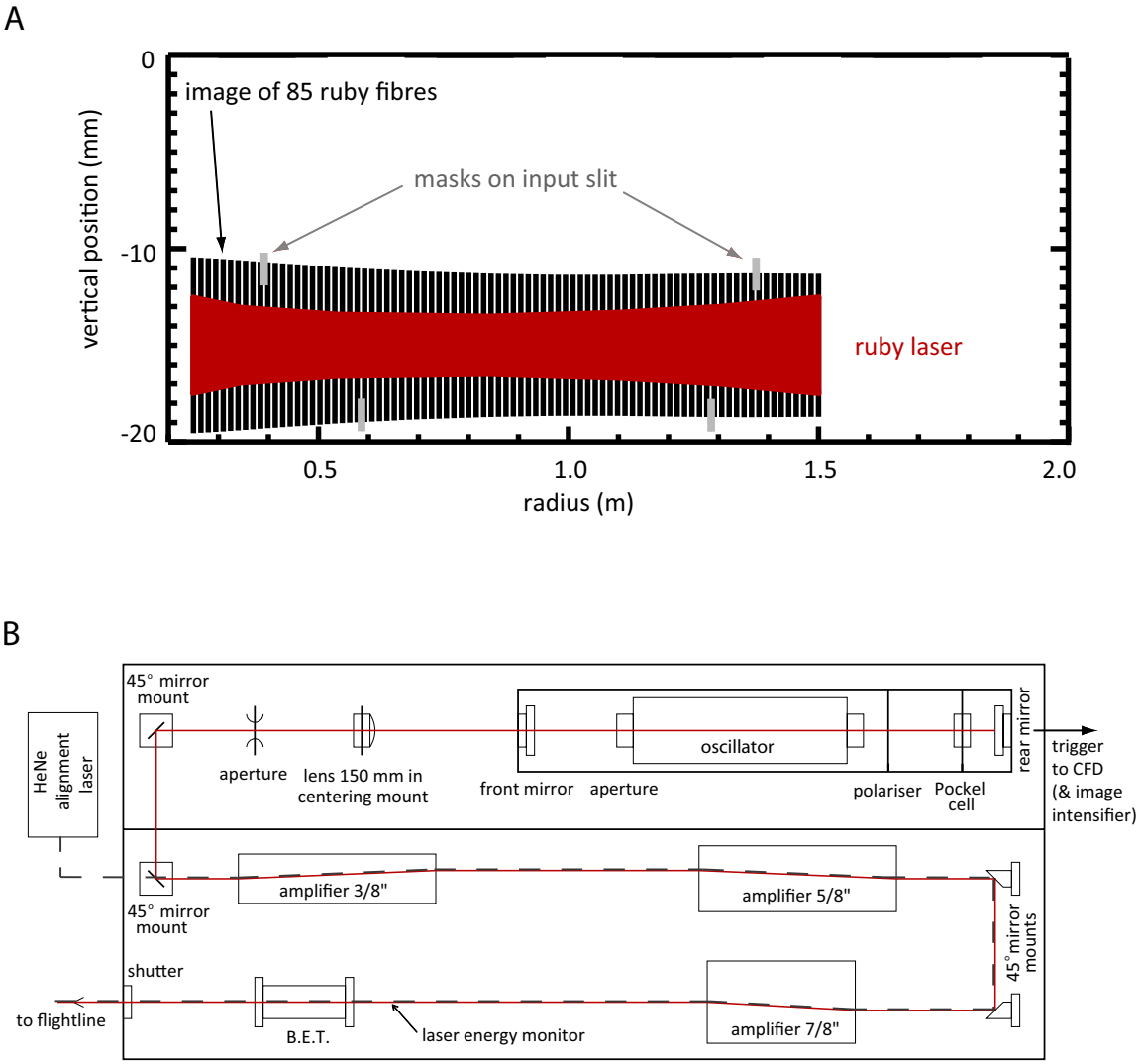

Figure 4.3: Ruby laser. A. The ruby laser is imaged onto 85 fibre bundles. These fibres are remapped to the spectrometer slit. At the spectrometer slit, masks (grey lines) can be placed in front of the fibre bundles to check the laser alignment. B. The ruby laser system consists of one oscillator and three amplifier sections. When the ruby laser is fired a small amount of the signal is taken from the oscillator to trigger the CFD and finally the image intensifier. The laser energy is determined by a calibrated avalanche photo diode (APD) located after the final amplifier stage. A HeNe laser (grey, dashed line) is used to accurately align the ruby laser (red line).

of 0.29 at F/1.75 onto sets of fibre bundles (1 set for the Nd:YAG TS system, the other for the ruby laser TS system). The collection cell has six radiation-tolerant lenses that can withstand the effects of neutral beam generated neutrons. Four of these lenses are made from silica and the remaining two are manufactured from radiation-hardened flint glass (figure 4.4).

Eighty-five coherent fibre bundles are used to map the image of the ruby laser chord to the input slit of the ruby spectrometer (figure 4.5). Each of these fibre bundles is 12 m long and contains 243

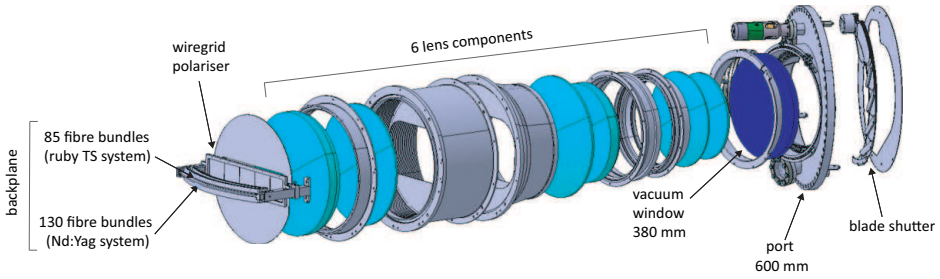

Figure 4.4: Components of the combined collection lens and window. Scattered light collected from the laser beams passes through six lenses (cyan disks) which image it onto two fibre backplanes, one ruby and one Nd:YAG. A wire grid polariser is used to ensure only the perpendicularly polarised light reaches the backplanes and is collected by the fibres. A blade shutter is used to protect the window during glow discharge cleaning between MAST dicharges.

fibres. The inner diameter of each fibre is 210 μm and the outer diameter, including cladding, is 230 μm. The numerical aperture of each fibre is 0.37. These fibres are made from plastic clad silica (PCS) and are not radiation resistant. However, calculations based on the worst-case neutron damage estimates predict only a 10 to 15% reduction in transmission in the red part of the spectrum over the next ten years of MAST operation. These estimates are based on published measurements [74] of the induced absorption of PCS fibres.

The maximum spatial resolution is determined by mapping the fibre bundles and is 2.4 mm of the laser chord for this system. The fibres are hexagonally packed to collect as much scattered light as possible ($\sim 50\%$) from the fibre backplane. However, this close packing results in a redistribution of scattered light into the neighbouring radial channels and at the collection lens there is a 9% redistribution of light into neighboring channels, with a further 5% at the spectrometer input slit (figure 4.5).

The fibre bundle array is imaged onto the input slit by means of a relay lens system, which is based on a Petzval lens configuration (M = 1.5). Scattered light is collected from the output of the fibre bundles at F/4 and is telecentrically imaged onto two holographic notch filters. The notch filters are placed on the outer edges of the spectrometer slit and remove the laser light at high optical density (6 OD) around a narrow 10 nm bandstop. The narrow bandstop of these filters increases the detected fraction of the TS spectra in the 10 to 100 eV range by up to 20% (figure 4.14) at lower T_e.

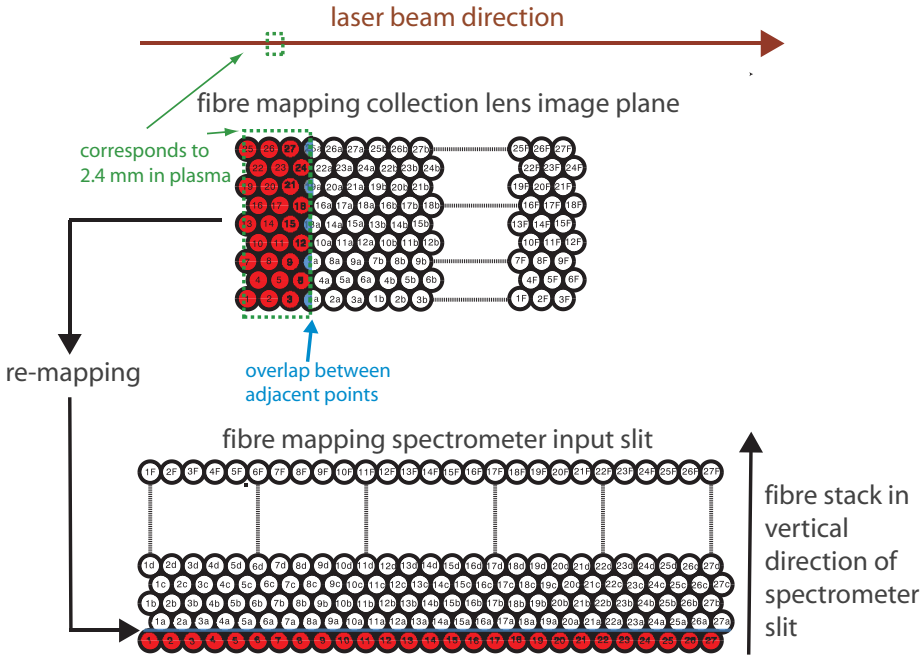

Figure 4.5: Mapping the fibre bundles from the collection lens to the spectrometer input slit. An area that is 9 fibres high by 3 fibres wide at the backplane of the collection lens is mapped to a single row in the spectrometer input slit, as illustrated by fibres 1-27 (red filled circles). This area corresponds to 2.4 mm horizontally (green dashed box) along the laser, but due to the hexagonal fibre packing fibres overlap between these 2.4 mm segments which results in redistribution of light into the neighboring channels (half blue circles).

4.4.3 Spectrometer

The spectrometer is a diffraction grating spectrometer set on a Littrow mount. The fibres, which are in the object plane, are imaged onto the CCD camera (in the image plane) in both radial and wavelength space. The spectrometer has two intermediate image planes: one at the field mirror and one at the image intensifier (figure 4.6). The intermediate image plane formed at the concave field mirror corrects for the curvature introduced by the lens system.

A 600 lines/mm grating is used with a singlet Littrow lens to disperse the light onto a field mirror. The grating in the ruby spectrometer is blazed at an 11.21° angle, where blazing means tilting the grooves of the grating with respect to the grating surface. This allows the concentration of spectral energy to be focused into a particular diffraction order [75], thus improving grating efficiency. A blaze angle of 11.21° focuses the spectral energy into the first diffraction order for input light of 656.3 nm wavelength giving a grating efficiency of $\sim 70\%$. The equation describing the diffraction from a grating is:

$$sin\alpha + sin\beta = kn\lambda, \tag{4.1}$$

where α is the angle of incident light, β is the angle of diffracted light, both with respect to the

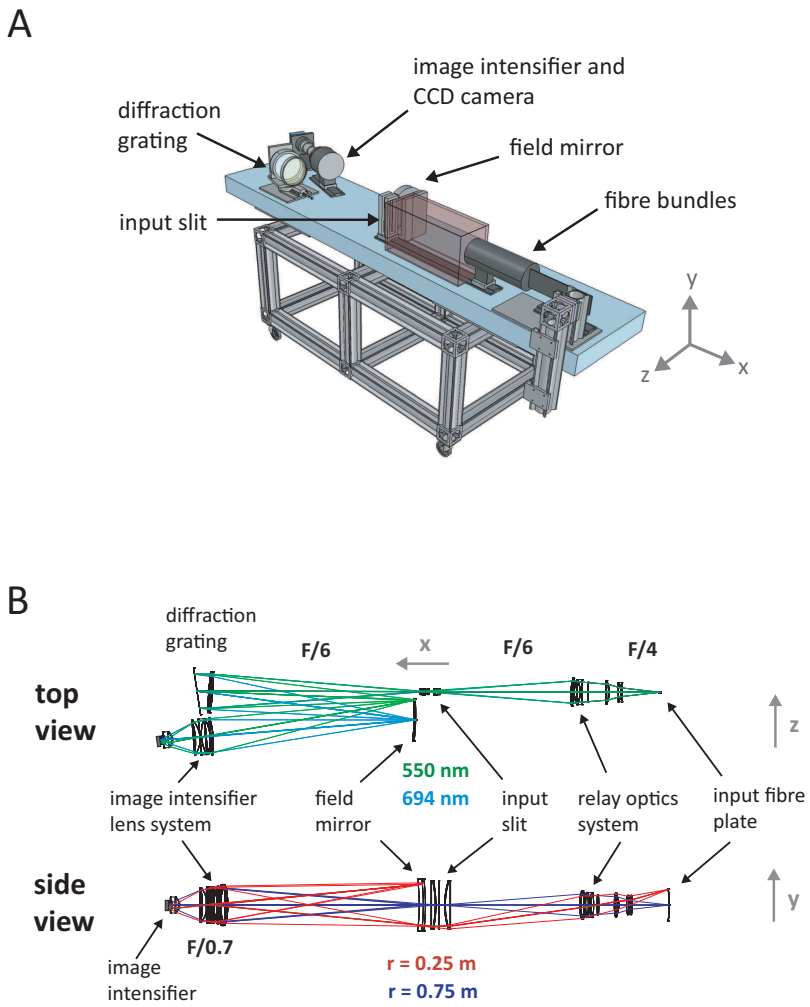

Figure 4.6: The grating spectrometer with image intensifier and CCD camera. A. The layout of the new spectrometer showing its different subcomponents. Scattered light from the fibre bundles enters the spectrometer and the different wavelengths are imaged in the z direction, while the different radial positions are imaged in the y direction. B. Optical ray tracing showing how wavelength and radial points respectively are imaged by the spectrometer. In the top view, two different wavelengths are traced, 550 nm (green) and 694 nm (cyan). In the side view, two different radial positions are traced, corresponding to 0.25 m (red) and 0.75 m (blue). The rays form intermediate image planes at the input slit and field mirror before finally being imaged at the front of the image intensifier. Details of the CCD camera coupling lenses are not shown here as these are commercial lenses and the lens designs are not available. The F/# of each part of the spectrometer is given.

normal from the grating, k is the diffraction order, λ is the wavelength and n is the number of lines per unit length.

As the ruby spectrometer is in a Littrow configuration, and the light is therefore reflected back at a similar angle to which it was incident on the grating($\alpha = \beta$), the diffraction grating equation

can be simplified to:

$$2sin\beta = kn\lambda. \tag{4.2}$$

The angular dispersion of the grating can be determined from the derivative of the grating equation 4.1, holding the incident angle (α) constant [49], as given by:

$$\frac{d\beta}{d\lambda} = \frac{kn}{cos\beta}. \tag{4.3}$$

The linear dispersion is a measure of the number of nanometers per unit length of the spectrum. This can be determined for the grating from the reciprocal of the product of the angular dispersion and the effective focal length (F) of the grating, given by:

$$\frac{d\lambda}{dx} = \frac{d\lambda}{d\beta} \times \frac{1}{F} \tag{4.4}$$

$$\frac{d\lambda}{dx} nm/mm = \frac{10^6 cos\beta}{knF}. \tag{4.5}$$

The spectral instrument function $I(\lambda)$ is important as it determines the lower T_e measurable by the system. This is because the width of a given spectrum is $\sim 2 * \sqrt{T_e}$ for 90° scattering. Hence the system cannot measure below $\sim$ 50 eV in the regions covered by the field mirror mask. $I(\lambda)$ is defined as the product of the linear dispersion of the grating and the width of the input slit of the spectrometer. The linear dispersion of the ruby spectrometer is 1.6 nm/mm, whilst the width of the input slit of its spectrometer is 8.5 mm, which gives an $I(\lambda)$ of $\sim$ 14 nm. The $I(\lambda)$ calculated from Rayleigh scattering calibration (discussed in section 4.5.1) is shown in figure 4.11. In addition, the upper T_e range of the system is determined by the linear dispersion combined with the wavelength sensitivity of the image intensifier. The system design has been optimised to have the lowest T_e and n_e error over the typical $T_e$range experience on MAST (5 eV to 2 keV). The lowest T_e that this system can measure is ~ 50 eV. The T_e and n_e errors predicted for the final system design are shown in figure 4.8.

The field mirror has a spatial mask consisting of two black strips which remove light at the D_α emission line (656 nm) and the ruby laser wavelength (693 nm). The width of each black strip is $\sim$ 15 mm, which corresponds to 10 nm in wavelength. The width of the ruby slit at the location of the notch filters has been reduced to $\sim$ 5 mm to allow more scattered light at wavelengths closer to the laser wavelength, which permits measurements at lower temperatures.

Light leaving the field mirror is imaged onto a 25 mm diameter image intensifier using an F/0.7 lens. An extremely low F/# is exploited to couple as much light as possible to the image intensifier. In addition, a cylindrical lens is contact-mounted to the front of the image intensifier to correct for any optical aberrations across the field. Finally, the light is coupled to the CCD camera by using two camera lenses, that provide a total magnification of 0.37.

4.4.4 Detector System

The scattered light is detected using a GaAsP GEN3 filmless image intensifier lens coupled to a cooled, back-illuminated, fast frame transfer CCD camera. In the following sections the components of this detector system are discussed in detail. In addition, the parameters which determine the efficiency of this system are presented in table 4.1.

4.4.4.1 Image intensifier

The image intensifier amplifies the optical signal and can be gated around a short time interval. It consists of a photocathode, a micro channel plate (MCP) and a phosphor screen (figure 4.7). The photocathode converts incoming photons to photoelectrons and the MCP then intensifies them. Finally, at the far end of the image intensifier, there is a phosphor screen that converts the photoelectrons back into photons. This is a P46 phosphor with a decay time of 0.2 μs and permits two images to be taken in quick succession.

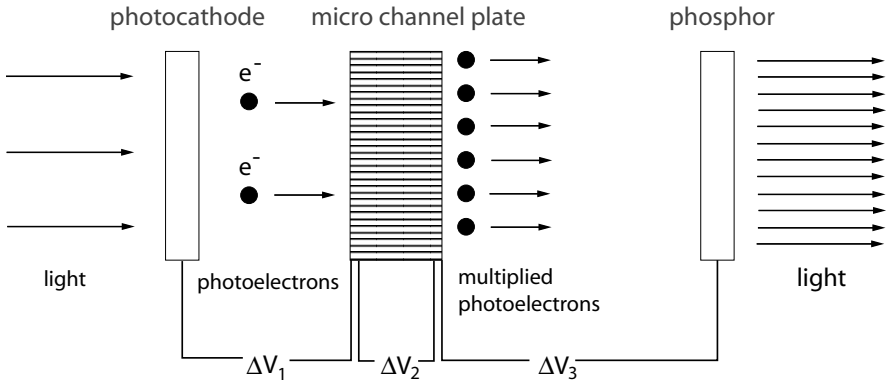

Figure 4.7: Overview of the image intensifier. Incoming photons are converted to photoelectrons at the photocathode, which are then multiplied by the MCP and then converted to light upon hitting the phosphor. By changing the voltage between the photocathode and the MCP (ΔV_1) from 200 V to -100 V the system is gated on and off respectively. A second voltage (ΔV_2) of 500-1000 V is then used to control the photon gain (G_p) and finally, a voltage (ΔV_3) of 5000 V is used to accelerate the photoelectrons onto the phosphor.

A Hamamatsu filmless GaAsP 25 mm diameter GEN3 image intensifier was shown to be the most suitable for the ruby system upgrade requirements because of its high quantum efficiency (QE) at the relevant wavelengths. The photocathode has a peak QE of 35%. The peak EQE ($EQE = \frac{QE}{(N_f)^2}$) is $\sim 18\%$ over the spectral range (550-800 nm) of the spectrometer. N_f is the noise factor, which is the ratio of the input signal to noise ratio (SNR) to output SNR and represents additional

noise arising due to the image intensifier.

The photon gain (G_p) of the image intensifier is given by:

$$G_p = QE \times G_c \times P_e, \tag{4.6}$$

where G_c is the electron gain of the MCP (500-1000) and P_e is the conversion factor of input electrons to photons at the phosphor ($\sim$ 21 photons/electrons). The maximum achievable gain is $\sim$ 8000 at the peak MCP voltage.

4.4.4.2 CCD camera

The CCD camera is a cooled, ProEM camera from Princeton Instruments ([76]). This camera uses a back-illuminated CCD and has $\sim$ 90% QE for wavelengths between 550-700 nm, which is well matched to the output spectrum of the phosphor. The camera has two readout amplifiers. The first is a slow (100 kHz) low noise amplifier and is this is currently being used. The second is a 10 MHz electron multiplication amplifier which could be used for potential future high repetition measurements of the T_e and n_e profiles.

The CCD chip consists of 16 μm square pixels in a 512 $\times$ 1040 grid. In the ruby TS system the camera is used in frame transfer mode, where 512 $\times$ 512 pixels (8.2 mm $\times$ 8.2 mm) are active and the remaining pixels are used for storage. The read noise at 100 kHz is 3.5 electrons (e^-) rms and the vertical transfer time is 450 ns per row. Thus, the minimum time required to transfer a 512 $\times$ 512 image into the storage region is 230 μs. Two images can therefore be captured at a separation of 230 μs and the second image recorded can either be the plasma background light or a second snapshot of the T_e and n_e profiles. This time lapse between captured images is well matched to the optimum separation required to double pulse the ruby laser.

The PSF of the CCD camera is a combination of both the detector and sampling PSFs. The detector PSF (PSF_D) is determined by the width of the detector, which in this case is one 16 μm pixel. Optical distortion makes it impossible to align a CCD pixel perfectly with discrete object points and this leads to a reduction in the final image resolution, which is represented by the sampling PSF (PSF_S). This is calculated using an approach developed by Park et al [77], where the sampling PSF is represented by a tophat with a width equal to the centre-to-centre spacing in the pixel array. For the CCD chip in the upgraded system, this width is equal to the detector size.

4.4.4.3 Coupling lenses

CCD cameras can be coupled to image intensifiers using either fibre stubs or lenses. Although coupling efficiency (ϵ) is typically greater for fibre stubs, these provide less flexibility in terms of magnification (M), CCD camera choice and the area of image intensifier utilised. Lens coupling

Parameter	**upgraded ruby system**	**original ruby system**
CCD Quantum Efficiency at 550 nm (%)	90	70
Image intensifier EQE (%)	18	6
Spectral range of spectrometer (nm)	550-800	600-900
Efficiency of phosphor (photons/electrons)	21	70
CCD read noise ($e^- rms$)	3.5	4
CCD gain (counts/e^-)	1.5	0.5
Coupling efficiency of coupling lenses (%)	4	4
Counts/photoelectron [1]	180	100

Table 4.1: Efficiency of the detector system on the original and upgraded ruby TS systems. [1] The number of counts/photoelectron is given by the product of the image intensifier photon gain (G_p), the efficiency of the coupling lenses (ϵ) and the CCD camera gain and Q.E.

was therefore chosen for the upgraded ruby system. Here, the coupling efficiency between the image intensifier and the CCD camera is determined by a transmission coefficient of the optics (T) multiplied by the ratio of the solid angle collected to the solid angle emitted by the phosphor. The coupling efficiency of a perfect lens, illuminated by a Lambertian source [78], is given by:

$$\epsilon = \frac{T}{4F^2(M+1)^2}, \tag{4.7}$$

where F is the F/# number of the lens system, calculated from the ratio of the limiting aperture diameter to the focal length of the lens system. In the ruby TS system a Canon 80-150 mm F/2.8 zoom lens is coupled to a Canon 50 mm F/1 lens. The first lens acts as a collimator and converges the divergent light from the phosphor into a parallel beam. The second lens focuses the light onto the CCD camera. The magnification for these lenses is adjusted to 0.37 to match the area of the CCD chip. The coupling efficiency of this system is $\sim$ 4%, which is greater than would be expected from equation 4.7, because the phosphor screen produces more forward directed light than a Lambertian source. Optical vignetting is the reduction of an image's brightness at its periphery compared to its centre. At the edge of the field, optical vignetting reduces the coupling efficiency to $\sim$ 1%. This reduction at the field edge is a result of the relative separation of each lens stop. However, the low CCD read noise and the high photon gain of the system produce an acceptable signal to noise ratio at the edges of the image.

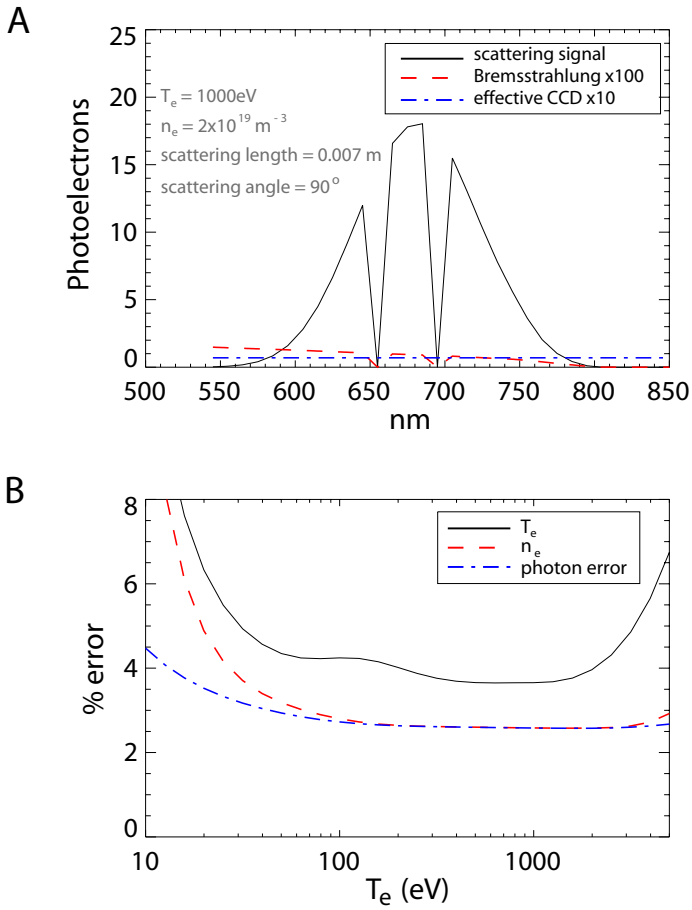

Figure 4.8: Monte Carlo models of the TS spectra and errors in T_e and n_e as predicted from parameters in tables 4.1 and 4.2. A. Predicted TS spectra. The number of photons (scattering signal, black line) is the number of detected photons evaluated at the image intensifier photocathode. The noise is dominated by the Poisson noise of the scattered signal, making the effects of the brehmsstrahlung (red, dashed line) and the effective CCD amplitude (blue, dashed line) negligible. The effective CCD amplitude was determined by dividing the square of the CCD read noise by the product of the image intensifier gain, CCD gain and coupling lens efficiency (see table 4.1). B. The predicted variation of the percentage T_e (black line) and n_e errors (red dashed line) as a function of T_e. The photon error (blue dashed) is the Poisson error of the number of scattered photons detected. This figure shows the optimum T_e range for low error measurements.

4.4.5 System noise performance

Extensive Monte Carlo modelling using repeated random samples was performed during the design of the upgraded system to predict how it would perform in terms of T_e and n_e statistical errors. The fractional errors in both T_e and n_e as a function of T_e are shown in figure 4.8, with the measurement error for a 7 mm radial point shown to be < 4 % of T_e and < 3 % of n_e , in the 40 eV to 2 keV range. The fractional error in T_e in the lower T_e range (< 40 eV) increases as the TS spectral width approaches the bandstop of the notch filters. The removal of the D_α emission

line wavelength results in a slight increase in the fractional error of T_e in the 80-200 eV range. The fractional error in n_e is determined by the photon statistics of the photons detected. One of the major factors that determines the statistical error for both the T_e and n_e measurements is the choice of photocathode in the image intensifier. GaAsP photocathodes have a higher QE than GaAs ones, but their sensitivity tends towards zero beyond 800 nm. However, simulations have shown that for the T_e range expected on MAST (0 to 5000 eV) the higher quantum efficiency of GaAsP photocathodes has a greater influence in reducing statistical error than the wider spectral range of the GaAs photocathodes.

The main contributors to background noise are Bremsstrahlung, line emission and CCD noise. The amount of Bremsstrahlung is determined by the gate duration of the image intensifier (50 ns) and is therefore very low in the upgraded system. The ratio of Bremsstrahlung to scattered signal in this system is also very low, due to the high energy of the ruby laser pulse (figure 4.8), making the contribution of Bremsstrahlung negligible. The level of line emission is determined by plasma impurity conditions and, typically, no line emission is observed in the ruby TS spectra. In the case of plasma start-up and low density measurements, the ruby system can be operated to measure the background light 230 μs after measurement of the TS spectra, which can be used to prevent fitting errors. Finally, the level of the CCD noise is determined by the product of G_p and ϵ. If this is sufficiently high then the effect of the CCD noise is negligible (figure 4.8). In addition, the CCD noise can be further reduced by binning pixels and reducing the number of spectral bins.

Table 4.2 shows the photon budget of the upgraded system compared to the previous ruby and Nd:YAG systems. The upgrade permits higher resolution measurements with more scattered photons detected, principally as a result of the higher EQE of the detector system.

The very low background noise on this system (figure 4.8) means that it can be used to measure the very low electron densities that occur in plasma start-up experiments on MAST. The signal can even be binned to reduce the radial resolution, which increases the number of scattered photons and thus reduces the error in T_e and n_e.

4.4.6 Improved resolution

The contribution of each component to the spatial resolution of the upgraded system has been modelled and the components that limit the resolution are shown to be the fibre bundles, the coupling lens system and the CCD detector. The performance of the upgraded system agrees well with predictions from these modelling results.

The spatial resolution achievable with the ruby TS system is determined by the convolution of the PSF for each of the system components that the scattered light passes through. The contribution of the collection optics (PSF_{CL}) and spectrometer optics (PSF_{SP}) to the overall PSF can be esti-

Parameter	**upgraded ruby**	**previous ruby**	**Nd:YAG**
Resolution (mm)	7	15	10
F/#	15	15	6
Input slit width (mm)	8.5	7.5	N.A
Laser energy (J)	10	10	1.6
EQE (%)	18	6.7	8-15
Transmission (%)	20	20	40
$f_{detected}$ (%) [1]	90	90	60
p.e. (/cm/10^{19}) [2]	3300	1100	2900

Table 4.2: Photon budget for upgraded MAST TS systems and the previous ruby TS system. [1] detected fraction of photoelectrons at 1 keV. [2] effective number of detected scattered photons per centimetre of scattering length per 10^{19} m^{-3} of plasma density.

mated using optical ray tracing techniques. This was carried out using the optical design program Zemax ([79]) and the estimated PSF values are shown in figure 4.9A. These PSF values are then convolved with PSF_{FB}, which represents the redistribution of light due to the fibre bundle mapping. The combined optics PSF (PSF_{CO}), which represents the contributions of PSF_{CL}, PSF_{SP} and PSF_{FB}, has been evaluated at different positions in the field of the lens system and is well represented by a Gaussian with an FWHM of 0.024 mm. Finally, this Gaussian is convolved with the PSFs from the coupling lenses (PSF_{CuL}), image intensifier (PSF_{II}) and the CCD camera pixel size (PSF_D) and sampling (PSF_S) to give the system PSF (figure 4.9B). The system PSF has an FWHM of 0.035 mm and $\sim$ 200 points (2.2 pixels), resolved at 50% MTF.

The major limiting factor for the resolution is the combined optics PSF and, following this, the component with the next largest influence on the resolution is the coupling lens that couples light from the phosphor of the image intensifier to the CCD chip. In this coupling lens, two commercial camera lenses are combined and each focused at infinity. The first lens is an F/2.8 zoom lens, which is reversed and attached to the front of a second, F/1 lens. The overall resolution of these combined lenses is $\sim$ 40 cycles/mm, at 50% contrast. In the future, further improvement could be made to this lens component by employing a purpose-built lens solution.

4.4.7 Triggering

Plasma events are typically much faster than the repetition rate of a ruby laser. To gain the maximum possible information from a MAST shot a 'SMART' real-time triggering unit has been developed [80] to trigger the ruby laser on specific plasma events, such as pellet injection and rotating magnetic

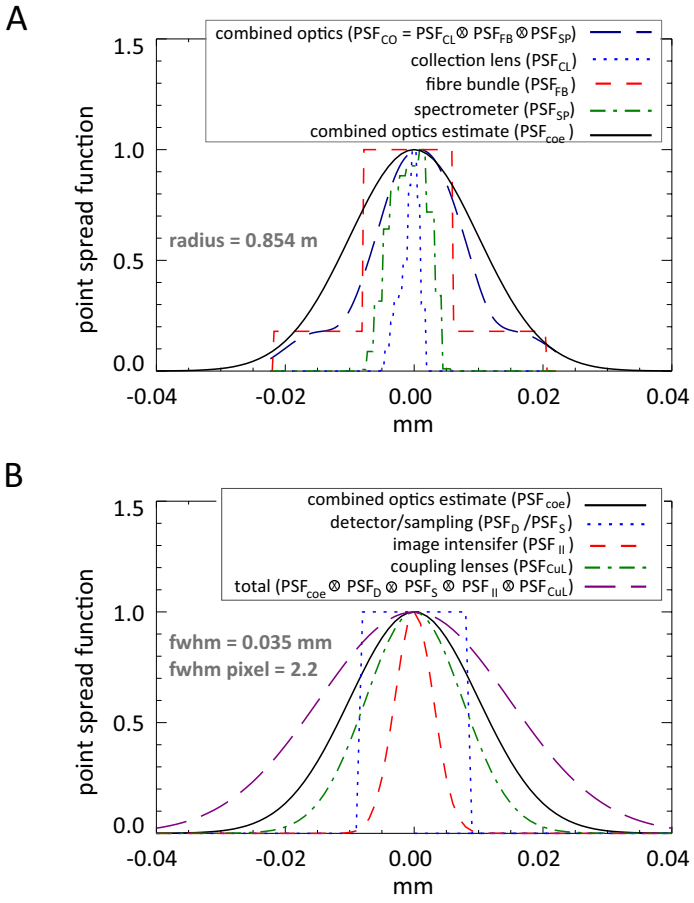

Figure 4.9: Contribution of the different components to the spatial resolution of the ruby TS system, evaluated on the CCD camera. A. Contribution of the components prior to the image intensifier. The PSF_{CL} (blue, dashed line) and PSF_{SP} (green, dashed) were determined by tracing optical rays though each component for a radial location of 0.854 mm. PSF_{CL}, PSF_{SP} and PSF_{FB} (red, dashed) can then be convolved to estimate their combined effect (PSF_{CO}, black, dashed line), and this is well represented by a Gaussian (PSF_{coe}, black solid line) with an FWHM of 0.024 m. B. Contribution of the Gaussian and components after the image intensifier. The PSF of the entire system (purple, dashed) has a FWHM of 0.035 mm. This is determined by convolving the Gaussian estimate PSF_{coe} (black, solid), PSF_{II} (red, dashed), PSF_{CuL} (green, dashed), PSF_D and PSF_S (both as blue, dashed line).

islands (see Chapter 5 and Appendix B for further discussion of these). This unit triggers both the ruby laser and a custom designed unit which controls the triggering of the image intensifier and CCD camera (figure 4.10).

The detector system must be gated around the laser pulse to ensure that the plasma noise is not greater than the scattered light signal. This is achieved using the image intensifier, which acts as a fast optical gate and has a gate width of 50 ns. A small fraction of the laser oscillator beam is used to trigger a constant fraction discriminator (CFD), which in turn triggers a complex programmable

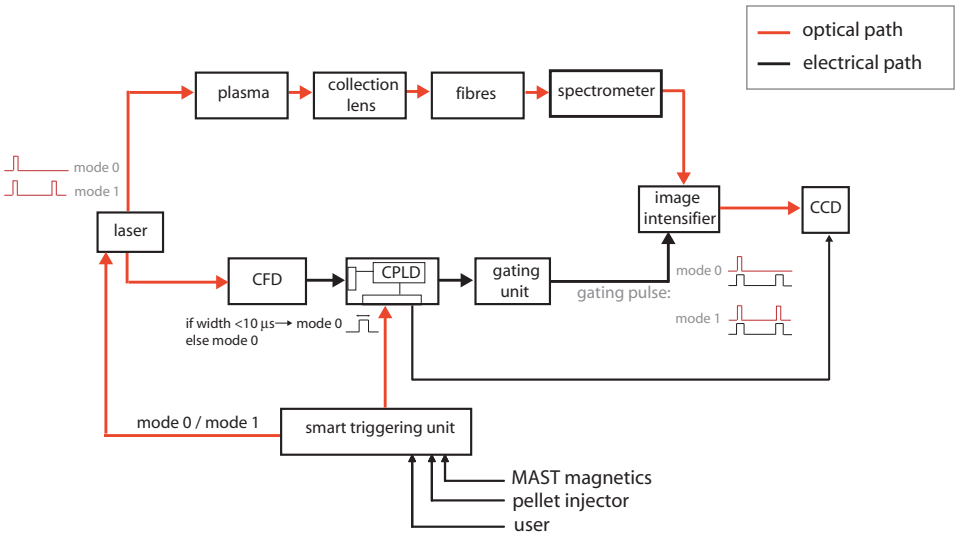

Figure 4.10: Upgraded ruby TS system triggering. The optical path (red lines) of the scattered light, which travels through the laser flight line, plasma, collection lens, fibres and spectrometer to reach the image intensifier. The image intensifier triggering is timed to ensure that the gate is opened when the scattered light from the optical path arrives at it. An optical signal from the laser oscillator is sent to the CFD, which starts the electrical path (black arrows), whereby the CFD triggers the CPLD, the gating unit and, finally, the image intensifier. The SMART trigger unit sends optical pulses to both the laser and the CPLD unit; and this system can operate in either single pulse (mode 0) or double pulse (mode 1) mode. During single pulse operation, the second image intensifier gate measures the plasma background radiation, whereas for double pulse operation, the image intensifier opens in synchronisation with the ruby laser pulses.

logic device (CPLD) unit, then a gating unit and, finally, the image intensifier (figure 4.10). The CFD generates an electrical pulse from the optical input signal and is used because its trigger point is largely independent of the signal amplitude. This eliminates any jitter of the image intensifier gate which can arise due to variations in laser energy. The CFD then triggers the CPLD unit, which has been programmed asynchronously in VHDL hardware description language ([81]) to generate the pulses required by the gating unit.

The CPLD can operate in two modes and these are controlled by an optical trigger sent by the SMART triggering unit. In the first mode of operation, the laser is triggered once, with one image of the TS light and one image of the background light taken. In the second mode of operation, the laser is triggered twice and two images of the TS are taken. It is critical that the CPLD unit operates as fast as possible to ensure that the image intensifier gate opening is synchronised with the arrival of the scattered light. Because the CPLD is programmed asynchronously, the time delay between the rising edge input and the output pulses can be reduced to 14 ns. By comparison, the

fastest off-the-shelf pulse generator available at the time of the ruby upgrade would have introduced a time delay of 50-80 ns and increased the hardware costs by a factor of ten.

4.5 New system calibration and fitting

In this section the calibration of the new system is first discussed (section 4.5.1) and then the fitting routines, used to determine the electron T_e and n_e profiles, are described (section 4.5.2). In addition, as the PSF of the coupling lenses of the image intensifier in TVTS systems suppresses high frequency noise, which can lead to false filamentary structures in the T_e and n_e profiles, the effects of this optical smoothing must be correctly estimated to determine the statistical error on the T_e and n_e profiles. This has been carried out for the upgraded ruby TS system and we show that the noise estimates agree well with the design parameters (section 4.5.3).

4.5.1 Calibration

Routine Rayleigh and white light calibrations are performed once or twice during a MAST campaign to assess system performance and ensure accurate T_e and n_e profiles are determined. A large number of the parameters that are used in these calibrations were measured at the completion of the system upgrade. The Rayleigh calibration is used to determine the relative transmission of the ruby system in radial space, while the white light calibration is used to determine the relative transmission in wavelength space.

4.5.1.1 Rayleigh calibration

A Rayleigh calibration is performed by filling the MAST vessel with nitrogen (N_2) gas and calculating the intensity of the Rayleigh scattered light. Rayleigh scattering is the scattering of radiation by neutral atoms or molecules, in which there is no change in the photon frequency. The Rayleigh cross-section is proportional to $\frac{1}{\lambda^4}$ of the input photons. In the case of the ruby laser the scattering cross section is $2.1 \times 10^{-24} m^{-2}$ [60]. The number of Rayleigh scattered photons (N_R) is given by:

$$N_R = n_{laser} n_{gas} \left[\frac{d\sigma}{d\Omega}\right]_{rs} \Delta\Omega\Delta L \left[\frac{QE}{NF^2}\right] T \int_0^\infty \Omega(\lambda) R(\lambda) d\lambda \tag{4.8}$$

where n_{laser} is the number of incident laser photons, n_{gas} is the density of the nitrogen gas, $\left[\frac{d\sigma}{d\Omega}\right]_{rs}$ is the differential Rayleigh cross section and T is the optical transmission. If it is assumed that the Rayleigh scattering spectral distribution ($R(\lambda)$) is a delta function, then the integral in equation 4.8 reduces to the spectral response of the wavelength channels ($\Omega_i(\lambda_L)$):

$$\int_0^\infty \Omega(\lambda) R(\lambda) d\lambda = \Omega_i(\lambda_L). \tag{4.9}$$

The number of scattered photons can be expressed in terms of the laser energy, and the gas density in terms of its pressure (P_{gas}) and temperature (T_{gas}), using the ideal gas law:

$$N_R = C_s(\lambda_L)\Omega_i(\lambda_L)\frac{P_{gas}}{k_b T_{gas}}, \tag{4.10}$$

where:

$$C_s(\lambda_L) = n_{laser}\left[\frac{d\sigma}{d\Omega}\right]_{rs}\Delta\Omega\Delta L\left[\frac{QE}{NF^2}\right]T. \tag{4.11}$$

The linear relationship between the number of scattered photons and the pressure inside the vessel is used to determine the Rayleigh coefficients (C_r):

$$C_r = C_s\Omega_i(\lambda_L) \tag{4.12}$$

$$N_R = C_r P_{gas} \tag{4.13}$$

After substituting in the known constants and measured quantities into C_r, it is then possible to determine a relative intensity calibration for the ruby system. Figure 4.11A shows the Rayleigh signal as a function of radius at 150 mbar. Figure 4.11B shows the Rayleigh coefficients C_r as a function of radius and these coefficients agree with the relative whitelight calibration and optical vignetting after the image intensifier. This agreement shows that the laser is well aligned, since the drop in transmission is a result of the optical vignetting in the CCD coupling lenses. The stray light pressure is also shown in figure 4.11B and this parameter, calculated from the zero offset of the Rayleigh calibration linear fit, is indicative of the level of stray light. Stray light intensity is greatest near the inboard side of the tokamak, as the laser light is reflected off the centre column in this region.

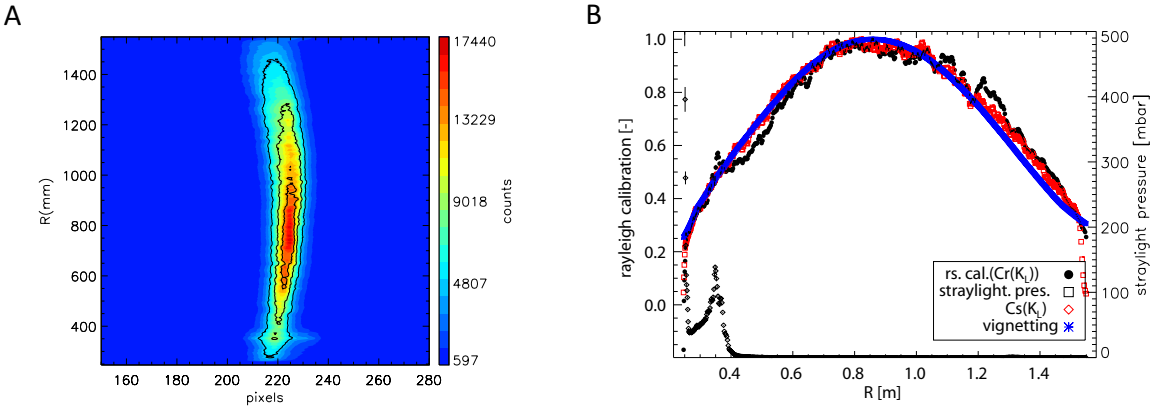

Figure 4.11: Rayleigh calibration measurements. A. The raw signal detected from Rayleigh scattering at 150 mbar. The $I(\lambda)$ at each radial point is determined by a cross-section in the wavelength direction. B. The Rayleigh coefficients (C_r) as a function of radius. The radial calibration (black) agrees with the relative whitelight calibration (red) and the optical vignetting profile (blue) of the coupling lenses.

4.5.1.2 Whitelight calibration

A whitelight calibration is performed using a broadband spectral source (tungsten lamp) and calculates the spectral transmission of the ruby system. A white piece of paper is placed at the focal length of the collection lens and is illuminated by the tungsten lamp. The light reflected off this paper provides a useful calibration light source as it has a uniform spread (Lambertian reflection) and the spectral emission of the tungsten filament (N_{WL}) is known to high accuracy (within $\sim 1\%$). The spectral transmission ($|C_s(\lambda)|$) of the system is given by the normalised signal measured ($|N_{c,WL}|$) divided by the calibrated spectral transmission (N_{WL}) of the lamp.

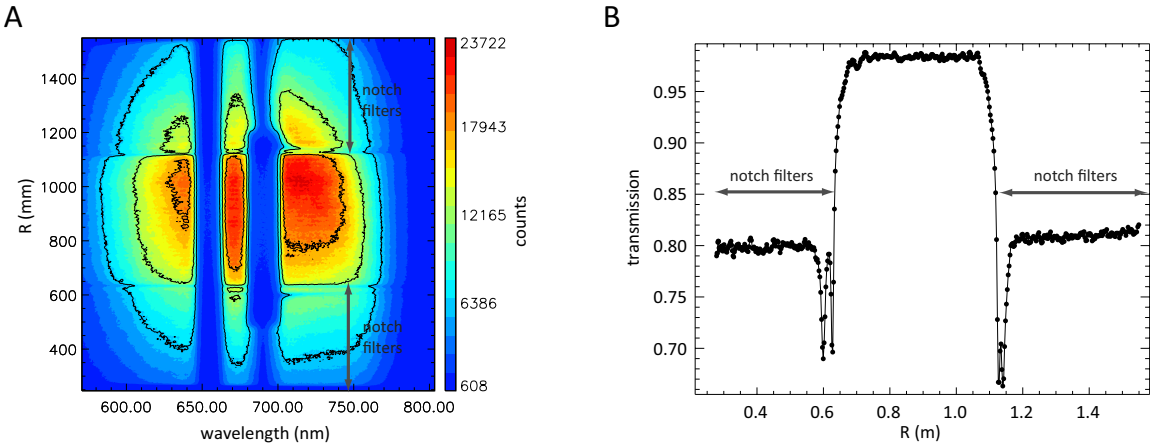

Figure 4.12: Whitelight calibration. A. The number of CCD counts detected as a function of radius and wavelength. A reduction in signal intensity is seen between the centre of the image and the edges due to optical vignetting in the CCD coupling lenses. The radial positions of the notch filters are indicated (black arrows) on both figures. Notch filters are placed at the top and bottom of the spectrometer input slit, corresponding to the region of lower temperature at the edge of the MAST plasma. B. The transmission of the notch filters as a function of radius. Where the notch filters are present (grey arrows) the transmission is reduced by 20%, with a further 10% reduction occurring at the physical edge of the filter plates.

An example of a whitelight image is shown in figure 4.12A. The effect of the optical vignetting present in the CCD camera coupling lens can be seen as the gradual reduction of signal intensity from the centre of the image to the edges. The transmission is also reduced, as a result of the notch filters, at radial positions between 200-600 cm and 1100-1500 cm. The notch filters are designed to remove light that is at the laser wavelength. The variation of transmission in the radial direction therefore cannot be determined from the Rayleigh calibration and must instead be determined from the whitelight calibration. To do this, a series of images are taken both with and without the notch filters present and this gives their transmission. This radial transmission (figure 4.12B) is then interpolated at the laser wavelength and multiplied by the Rayleigh calibration to give the radial transmission of the ruby system with the notch filters installed. Although the presence of the notch

filters reduces the transmission of the system by 20%, this is is offset by the narrow bandpass of these filters, which increases the number of detected photons at the lower T_e ranges typical at the edge regions. However, a further 10% drop in transmission occurs at the edge of these filters, which corresponds to radial points at 0.6 and 1.1 m (figure 4.12B).

4.5.1.3 Radial positions and scattering angles

To determine the radial coordinates of the T_e and n_e points, the position of the scattering volumes that are imaged by the fibre bundles must be measured. This was done by back-illuminating the input slit of the spectrometer and measuring the radial position of each fibre bundle (inside the MAST vessel) along the HeNe alignment laser beam that is aligned to the ruby laser beam.

In addition, the width of the TS spectra is proportional to $\sin(\frac{\theta}{2})$, where θ represents the scattering angles. The scattering angles must therefore be known to allow accurate measurements of T_e, which is also proportional to the width of the TS spectra. The angles were determined using optical ray tracing in the Zemax model of the collection lens. Optical rays from each fibre bundle were traced to the laser chord and the angle between each ray and the laser chord was estimated.

4.5.2 Fitting

T_e and n_e profiles are calculated by fitting a model (F_{TH}) to the TS spectra at each radial point using a non linear χ^2 fitting routine. Figure 4.13 shows a schematic outline of the parameters used to calculate the χ^2 parameter. The experimental spectra (D_{TH}) is determined by subtracting the background CCD image from the scattered image or, if the system is operating in double pulse mode, an average background image (taken during previous shots) is subtracted.

The data points of the model (F_{TH}) are calculated using the Selden-Naito formula ($S(\lambda, \theta, T_e)$) (see equation 3.60 in Chapter 3), with an initial estimate of T_e and n_e made. The spectra calculated using this formula are then convolved with the $I(\lambda)$ that is determined during the Rayleigh calibration. The effect of the ruby TS system on the transmission and noise must then be determined. This effect is represented by the C_s parameter, which can be broken down into radial and wavelength dependent components. The radial transmission at the laser wavelength is determined by the Rayleigh calibration, as explained above, while the wavelength dependence on the transmission is determined from the whitelight calibration.

Figure 4.14A shows 512 point profiles of T_e and n_e. A fit to the spectra at one radial point is shown in Figure 4.14B and Figure 4.14C shows the number of scattered photons detected by the system, as a function of radius and wavelength. Here, the χ^2 values determined from the experimental data are lower than expected, as the fitting assumes each data point to be independent, which is not the case on the ruby TS system. Instead, a correlation exists between neighbouring

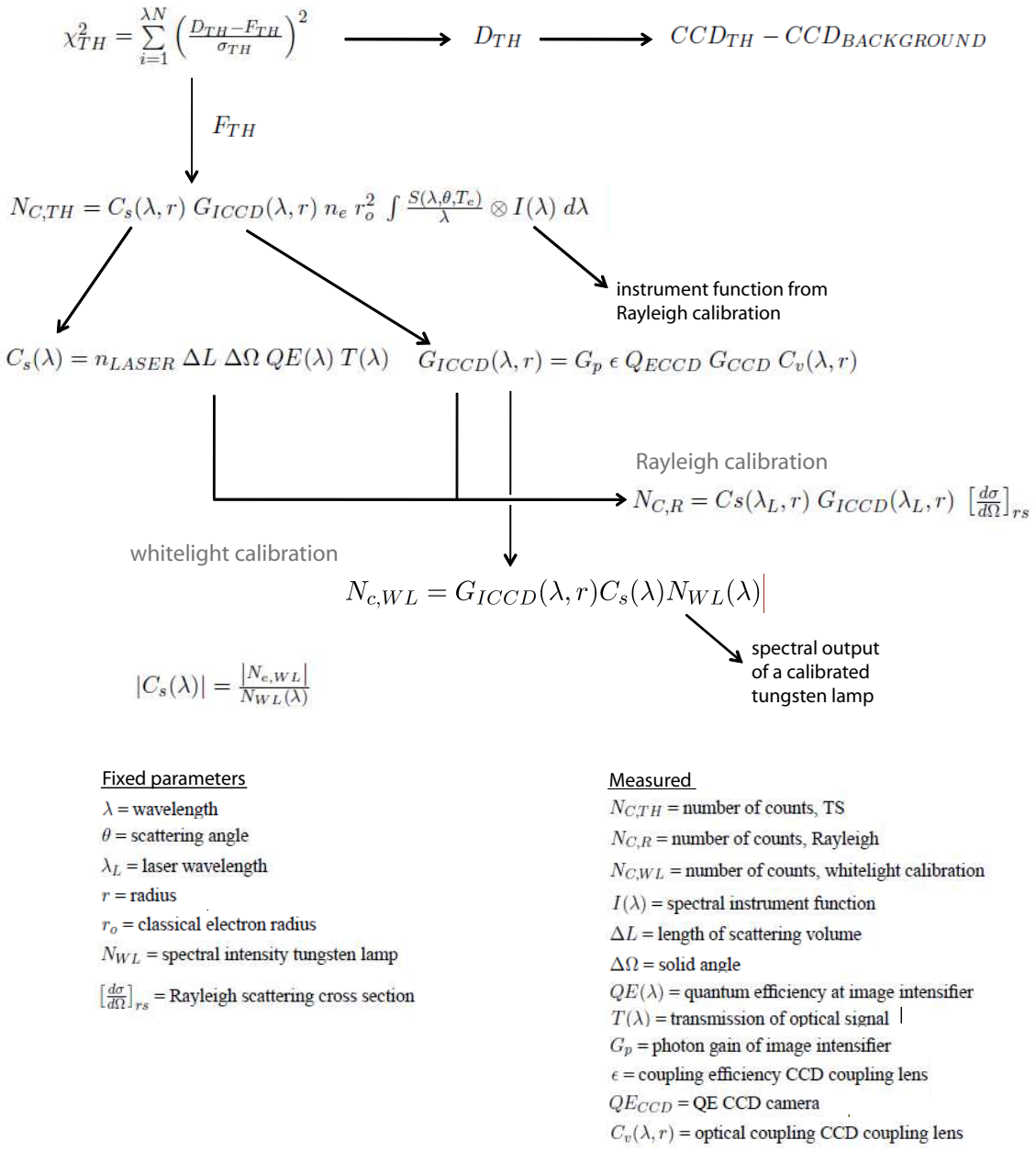

Figure 4.13: Calculation of the TS spectral model (F_{TH}) using calibration measurements and fixed parameters. The dependencies between these measurements and parameters are shown. The radial dependence ($N_{C,R}$) of the intensity of the spectra is given by the Rayleigh calibration. The spectral transmission measurement ($C_S(\lambda)$) is determined using a calibrated tungsten lamp. This model is then fitted to the raw experimental data (D_{TH}).

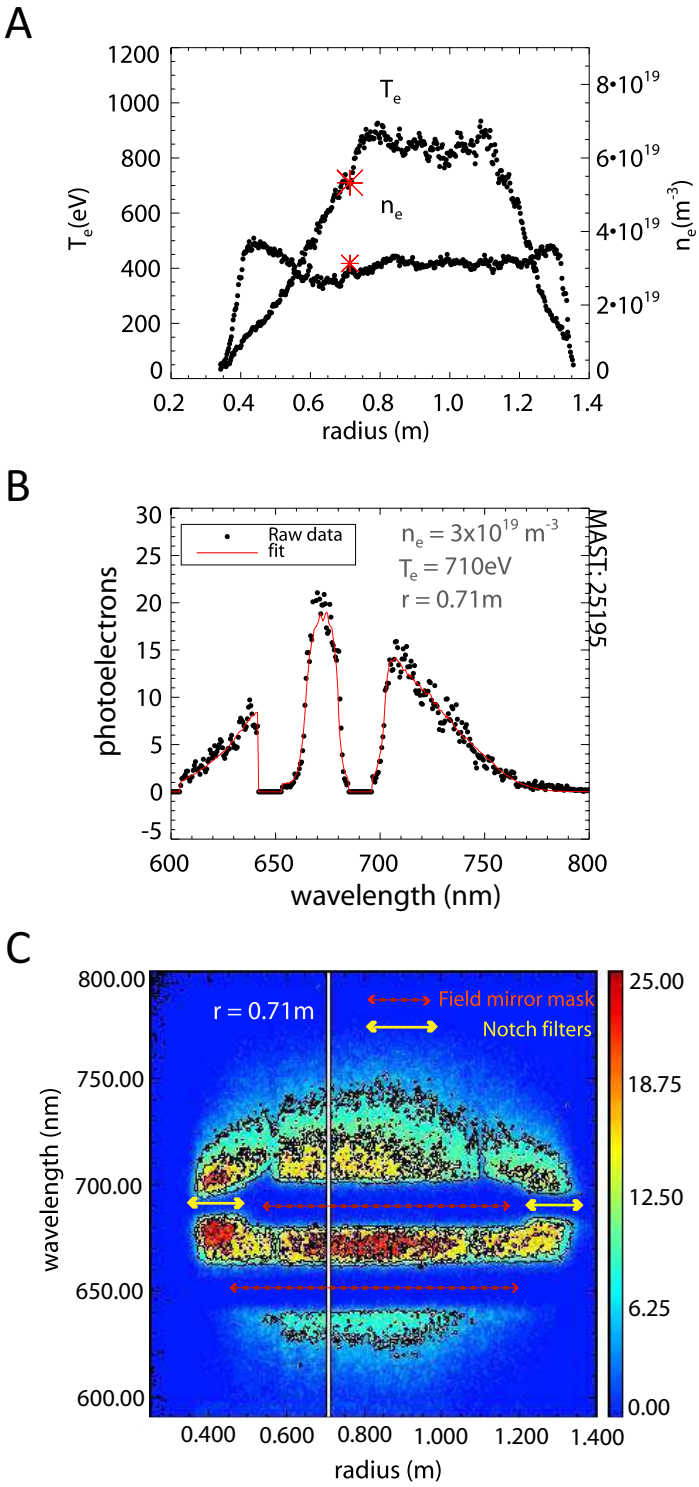

Figure 4.14: Ruby TS T_e and n_e profiles from a typical shot on MAST (shot number 25195). A. The complete T_e and n_e profiles for this shot, generated by fitting a model for the TS spectra to the raw data. This process is shown for an example radial point (0.71 m, red stars). B. The raw data (black dots) and fitted TS spectrum (red line) corresponding to radial point 0.71. C. The raw data (scattered photons recorded by the CCD camera) for shot 25195. The white line corresponds to the cross section of wavelength data at radial point 0.71 m, which was used to generate the raw data points in plot B. Notch filters at the edge of the image (yellow arrows) remove less of the scattered signal around the laser wavelength than the field mirror mask (red dashed arrows) used for the hot central regions.

data points due to the smoothing of the signal by the CCD coupling lens prior to the CCD sensor.

4.5.3 Noise smoothing

The optical smoothing that results from the CCD coupling lens suppresses the high spatial frequency part of the noise spectrum. This can lead to the appearance of filamentary structures in the fitted T_e and n_e data. Such structures have been misinterpreted on a TVTS system in the past [82], where the fluctuation in data was attributed to filamentation of the plasma. Thus noise smoothing is an important consideration in a TVTS system and extra care must be taken when interpreting fluctuations.

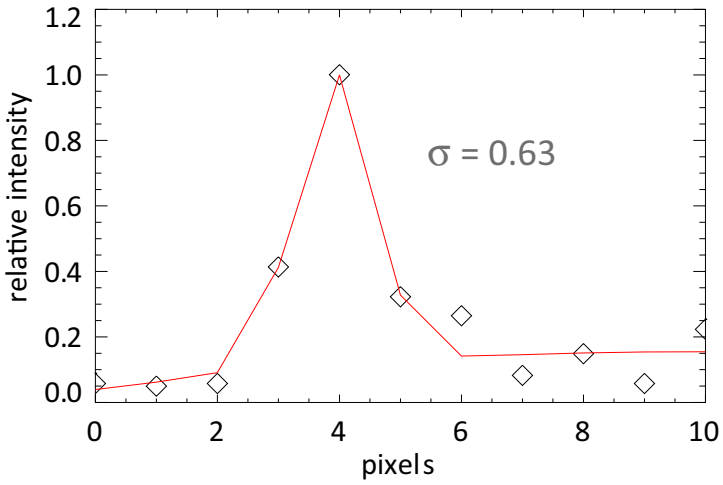

Figure 4.15: PSF of the image intensifier and coupling lenses PSF_{ICuL}. The points (black) show the measured signal from a single photon incident on the image intensifier. These can be represented by a Gaussian (red) with a standard deviation (σ) of 0.63 pixels. This Gaussian is used to represent the noise smoothing which occurs in the upgraded ruby TS system.

For intensified CCD-based systems, the noise statistics detected (N_c) are determined by two factors, the number of photons (N_p) and the convolution of the PSF image intensifier and coupling lenses, $PSF_{ICuL}(h, l)$, where h and l refer to the indices on a two dimensional grid. The PSF_{ICuL} is measured by operating the detection system in photon counting mode and measuring the PSF resulting from a single photon incident on the photo cathode (figure 4.15).

A Gaussian was fitted to the experimental PSF_{ICuL} and from this the standard deviation was calculated to be 0.63 (figure 4.15). A simulation of the predicted noise spectrum was then convolved

using this Gaussian and compared to the noise spectrum of a whitelight calibration image, as shown in figure 4.16. A good agreement is observed in the suppression of the high spatial frequency part of the spectrum between the simulation and experimental data spectra. The difference between these power spectra may be attributed to the fact that the PSF_{ICuL} is not a perfect Gaussian.

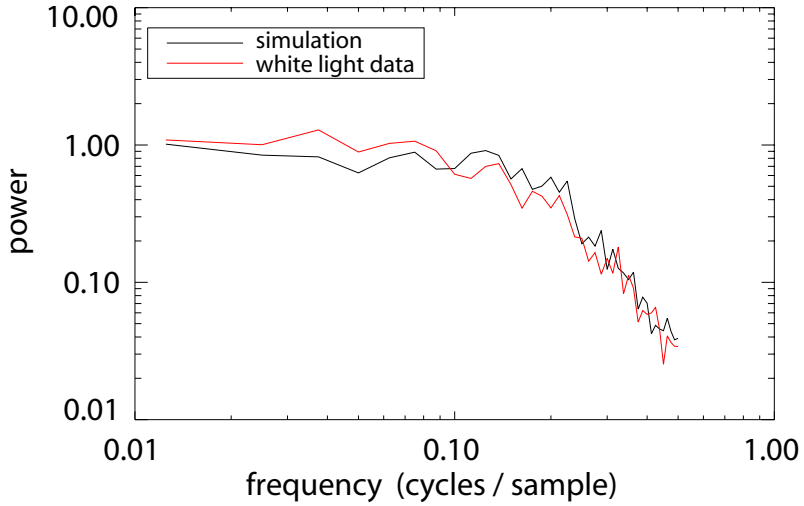

Figure 4.16: Power spectra of measured and simulated noise in the ruby TS system. This graph shows a comparison of the simulated power spectrum (black line) and the power spectrum calculated from a whitelight calibration data (red line). These spectra show good agreement, particularly in the high spatial frequency regions.

To determine the correct noise statistics on the TS data the effects of this smoothing must be further quantified. This is done by calculating a factor that quantifies the effects of smoothing on the noise, which is then used to rescale the noise to the correct value. To determine this correction factor, the probability distribution (over pixels (i,j)) for a particular photon to hit the pixel (h, k) is calculated:

$$PSF_{ICuL,bin}(i-h, j-l) = \int\int_{\lambda,r\in(i,j)} PSF_{ICuL,(h,l)}(\lambda, r)d\lambda dr. \tag{4.14}$$

As the total of this probability distribution is equal to 1, this gives:

$$\sum_{i,j} PSF_{ICuL,bin}(i-k, j-l) = 1. \tag{4.15}$$

The number of counts recorded by the CCD camera (N_c) in pixels (i,j) is given by:

$$N_c(i,j) = \sum_{h,l} G_p PSF_{ICuL,bin}(i-h, j-l)N_p(h,l), \tag{4.16}$$

where G_p is the photon gain and N_p is the number of photons. The variance of the number of counts ($VAR(N_c)$) detected by the CCD camera is given by:

$$VAR(N_c) \approx \sum_{h,l} G_p^2 PSF_{ICuL,bin}^2(i-h, j-l)N_p(h,l). \tag{4.17}$$

$VAR(N_c)$ is not equal to N_c so this parameter is not Poisson distributed. It is therefore useful to define the effective number of scattered photons detected, N_p^{eff}, which is a Poisson variable. The variance of N_p^{eff} is:

$$VAR(N_p^{eff}) = \sum_{h,l} \alpha^2 G_p^2 PSF_{ICuL,bin}^2(i-h, j-l) N_p(h,l) \equiv N_p^{eff}, \tag{4.18}$$

where α is:

$$\alpha = \frac{1}{G_p \sum_{h,l} PSF_{ICuL,bin}(i-h, j-l)}. \tag{4.19}$$

It is assumed that PSF_{ICuL} is both symmetrical and a Gaussian function in the radial (r) and λ directions. This is represented by:

$$PSF_{ICuL}(\lambda, r) = \frac{1}{\sqrt{2\pi}\sigma_\lambda} exp\left(\frac{\lambda^2}{2\sigma_\lambda^2}\right) \cdot \frac{1}{\sqrt{2\pi}\sigma_r} exp\left(\frac{r^2}{2\sigma_r^2}\right) = PSF_{ICuL,\lambda}(\lambda) \cdot PSF_{ICuL,r}(r). \tag{4.20}$$

The r and λ directions can now be treated independently and the α parameter can be split into parameters for each respective direction, as shown by:

$$\alpha = \frac{1}{G_p} \cdot \frac{\sum_{h,l} PSF_{ICuL,bin}(i-h, j-l)}{\sum_{h,l} PSF_{ICuL,bin(i-h,j-l)}^2} \equiv \alpha_r \cdot \alpha_\lambda. \tag{4.21}$$

A single photon effectively contributes to h pixels in the λ direction and l pixels in the r direction. The T_e and n_e fitting process is equivalent to first binning the entire spectrum in the λ direction before fitting it to a given radial spectrum. As this bin is much wider than the width of the PSL_{ICuL} parameter in the λ direction, only its impact in the radial direction (α_r) needs to be considered when determining the effect of the 2D PSL_{ICuL} smoothing. Finally, the effective number of scattered photons in the spectrum ($N_{p,spectrum}^{eff}$) is given by the product of α_r and N_c:

$$N_{p,spectrum}^{eff}(j) = \sum_i N_p^{eff}(i,j) = \sum \alpha_r N_c(i,j). \tag{4.22}$$

A calibrated white light (tungsten lamp) source was used to determine the noise statistics of the upgraded ruby TS system using the above formulae (equations 4.14 to 4.22). The light source was used to illuminate a Lambertian diffuser which was placed in front of the collection lens and the noise was calculated by determining the variance of the signal over a large number of pixels. This noise is dominated by the photon statistics of the detected scattered photons.

A good agreement is found between the noise measured (figure 4.17) and the theoretical performance calculated using the above formulae with the parameters given in tables 4.2 and 4.1. This confirms that the upgraded system is operating as designed and the number of detected scattered photons is similar to initial predictions. The analysis provided here shows how to account for the effects of the optical smoothing on the noise characteristics, which is important to distinguish between real structure in the T_e and n_e profile and and those introduced by this smoothing.

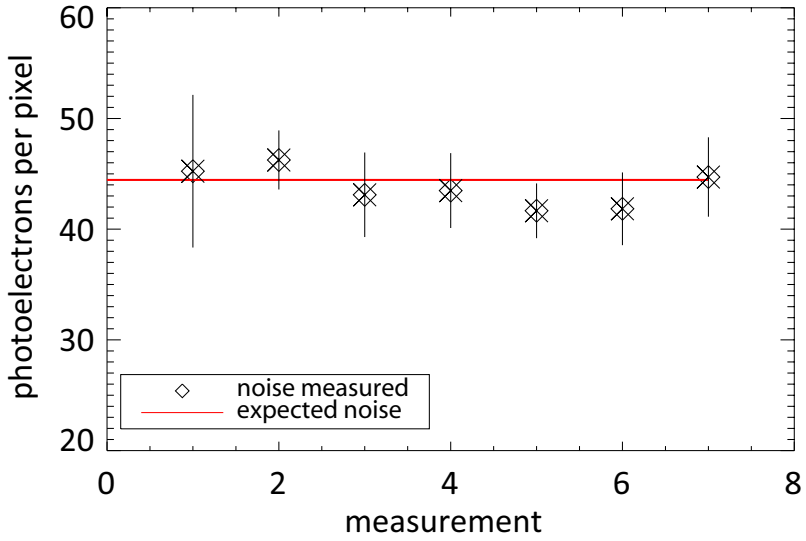

Figure 4.17: Theoretical and measured number of photons detected by the upgraded ruby TS system. The number of photons detected (diamond points) was determined using the variance of the noise from a white-light source. This compares well to the noise levels predicted (red line) using the parameters from tables 4.1 and 4.2.

4.6 Initial measurements from the upgraded system

The ruby TS system was upgraded in summer 2009 and the first results were obtained in the September of that year. In this thesis, the majority of experimental results using data from this upgraded system are the NTM investigations in chapter 5. However, initial results have also been used to test the double pulse mode (section 4.6.1) and also to study pellet fuelling (section 4.6.2).

4.6.1 Double pulse mode

The new double pulse mode on the ruby TS system provides two measurements separated by 230 μs and thus provides more information about the evolution of a T_e and n_e profile. In the previous MAST experimental campaign, the system was only operated in this double pulse mode for a small proportion of the experimental shots performed. However, those shots carried out confirmed that it operates as planned in this mode. An example double pulse shot is shown in figure 4.18 and shows a good initial agreement between the two ruby T_e and n_e profiles generated and an equivalent

Nd:YAG system profile. This confirms the feasibility of using the ruby system in the double pulse mode and it is therefore expected to be used for a greater number of shots in this mode during the next MAST experimental campaign.

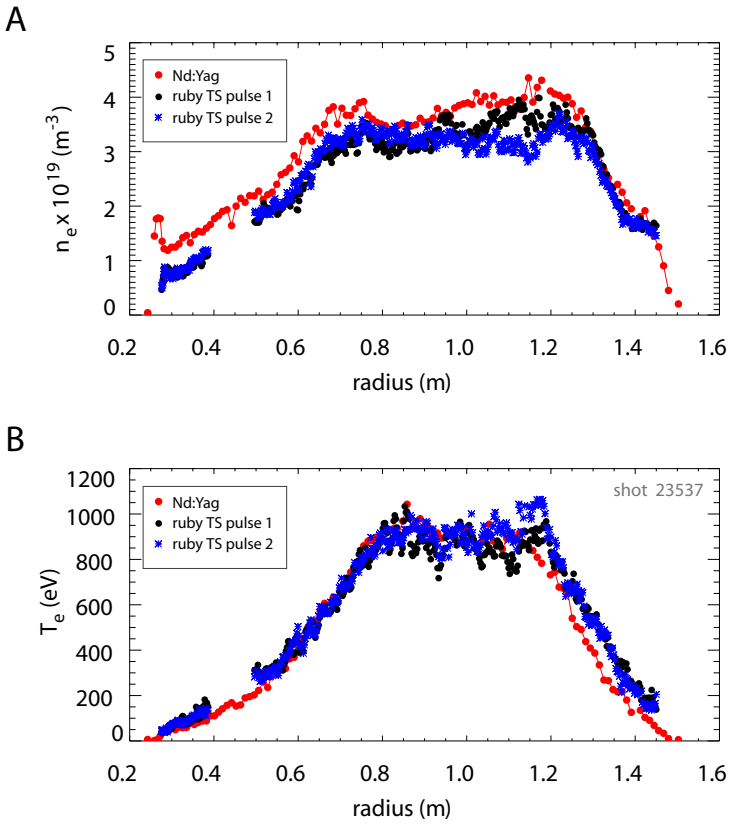

Figure 4.18: T_e (plot A) and n_e (plot B) profiles obtained using the double pulse mode on MAST. Both plots show good agreement between the T_e and n_e profiles measured using the ruby TS and Nd:YAG systems. Pulse 1 (black) on the ruby system was measured at 0.29985 s, pulse 2 (blue) at 0.30015 s, and the Nd:YAG pulse (red) at 0.30000 s. In this specific example the scattered spectrum between 0.4 and 0.5 m have been removed. This is because helium had been injected into the plasma to permit the radial electric field to be determined using the Eceleste diagnostic and unfortunately led to a high intensity Helium impurity line affecting the background light emitted. The scattered spectrum in this region was therefore unusable in this case.

4.6.2 Pellet Injection

Particle transport in MAST is studied using pneumatically accelerated pellets (see section 2.1.3 in chapter 2). Pellets with speeds between 250 ms^{-1} < vpellet > 400 ms^{-1} are injected at the top of the machine, from the HFS, and are deposited between $0.6 \geq \rho_{pel} \leq 0.9$, where ρ_{pel} is the pellet deposition radius in normalised flux. The ruby system can be triggered from the pellet injector and

the timing of this triggering adjusted to study different stages of the evolution of pellet ablation. The initial pellet injection and pellet ablation experimental results from the upgraded ruby system are presented here.

Experimental data from the previous ruby system [83] were used to investigate two key parameters controlling the pellet fuelling efficiency, the pellet deposition radius and the pellet retention time. Initial results from the upgraded ruby system agree with these findings and confirm the suitability of this new system for further pellet injection studies. Results from the upgraded system show that as an injected pellet evaporates, n_e gradually increases (figure 4.19C), whilst T_e decreases simultaneously (figure 4.19B), making the pellet deposition process close to (but not exactly) adiabatic. The pellet creates a positive density gradient and a region of increased temperature gradient, and simulations show these regions could increase the penetration of the pellet into the core of the plasma. The pellet retention time is related to the edge transport barrier and decreases as the pellet deposition radius moves toward the plasma edge.

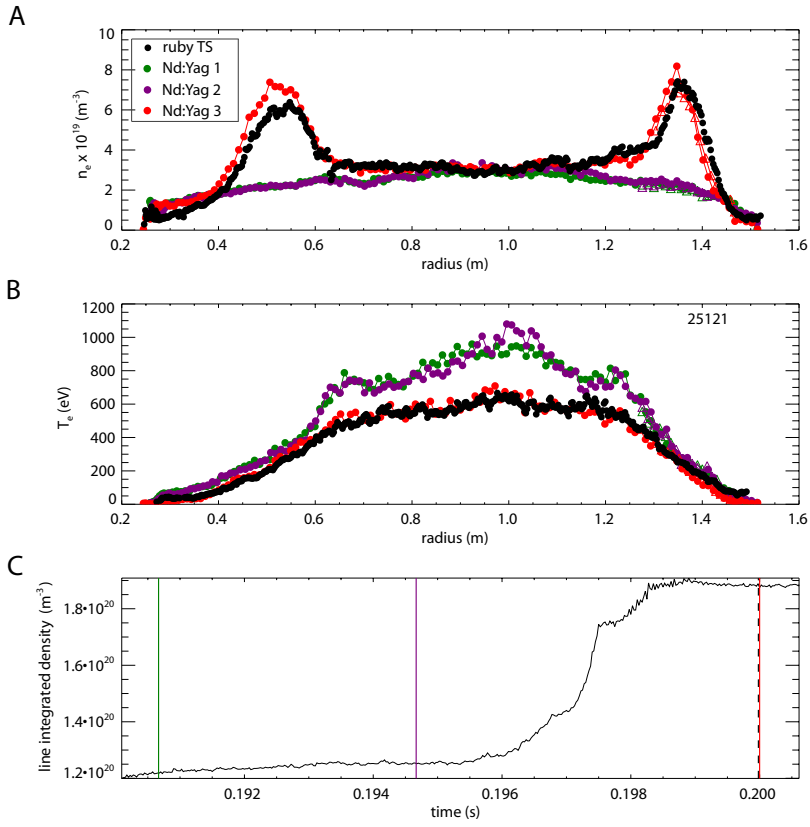

Figure 4.19: The T_e and n_e profiles before and after pellet injection. The T_e and n_e are measured twice before injection of a pellet (green, purple) and then twice afterwards (red, black). The pre-pellet measurements and the first post-pellet measurements are taken from the Nd:YAG system. A. The n_e profile before and after the pellet injection. B. The T_e profile before and after the pellet injection. C. The timing of lasers with respect to the line integrated density measurement from the interferometer.

Prior to the ruby upgrade, the effect of magnetic field gradient (∇B) drift on pellet fuelling [84] was studied. ∇B causes pellet material deposited in a tokamak plasma to drift towards the low field side of the torus and plasma fuelling in ITER will rely on the beneficial effect of this drift to increase the pellet deposition depth and fuelling efficiency. Interpretive analysis of the ruby data shows that the drift results in a displacement of 0.1, in terms of ψ_N, between the ablation and the deposition profile; and this is in agreement with previous predictive modelling based on the MAST injection geometry. The data from the upgraded ruby system obtained in the last experimental campaign are currently being analysed and the results are expected to further contribute to our understanding of pellet fuelling.

4.7 Conclusions

An upgraded TVTS system has been built that can resolve 200 points at high contrast along a 1.4 m chord, which is greater number of points than other TVTS systems. This has been achieved by optimising the resolution of the individual components in the design of the system. In addition, the scattered photons detected have been increased by a factor of ~ 3, which has reduced the T_e and n_e error compared to the previous system. This means the measurement error for a 7 mm radial point is now $< 4\%$ of T_e and $< 3\%$ for n_e in the range of 40 eV to 2 keV ,for a density of $n_e = 2 \times 10^{19}$ m^{-3}. The main factor which has enabled this improvement in detection, is the improved EQE of the image intensifer used (GEN 3 GaAsP). The combination of increased resolution and decreased noise in the upgraded ruby system produces better T_e and n_e profile data and this can be exploited to gain a greater understanding of the physical processes which influence transport and stability on MAST plasmas. The collection lens, fibre bundles and detection elements of the upgraded system have been designed to be compatable with potential future upgrades to the spectrometer and the laser, that could further increase optical throughput and temporal resolution.

An additional improvement to the ruby system is the ability to measure two images at a separation of 230 μs, which can be used to measure either two T_e and n_e profiles (double pulse mode) or one T_e and n_e profile and the background light. This was achieved using a fast frame transfer CCD camera lens coupled to an image intensifier with a fast P46 phosphor and a CPLD unit, programmed in VHDL, to control the triggering of both devices. Initial results from the new system indicate that it works well in double pulse mode and that it can be used to investigate the temporal variation of T_e and n_e profiles. The additional ability to measure one T_e and n_e profile with the background plasma light will also be useful in situations where impurities are present in the MAST vessel, such as plasma startup studies and impurity injections to study the electric field.

Measurements from the upgraded ruby TS system have been compared to those from the Nd:YAG system and show good agreement in their T_e and n_e profiles. Comparing these two inde-

pendent TS systems on MAST is a very useful approach to identify and remove systematic errors in both systems; and the good agreement seen indicates that both systems are correctly calibrated and have low systematic errors. The new ruby TS system is currently being used in studies of NTMs, pellet injections, H-mode pedestals, transport and also plasma start-up experiments. The ability to trigger the upgraded system on NTMs and pellet injections, using the SMART triggering unit, means that more information about these events can be gathered compared to the previous system. Results using the upgraded system to investigate NTMs on MAST are presented in chapter 5.

Chapter 5

Neoclassical Tearing Modes on MAST

This chapter describes an investigation of the onset thresholds and seed island physics of 2,1 NTMs on MAST. Section 5.2 outlines NTM theory and includes a description of the stabilising and destabilising terms of the modified Rutherford equation (MRE), which determines NTM growth and onset. Experimental results are then presented. Each results section focuses on a particular stability term of the MRE, investigated using MAST data, including magnetic measurements of the island width (section 5.3), TS measurements of the finite island width (section 5.4) and predictions of the ion polarisation current (section 5.5). Finally, a new triggering system on MAST is described (section 5.7.1).

5.1 Introduction

A neoclassical tearing mode [17] (NTM) is a beta-limiting instability which forms on a rational surface inside a tokamak plasma (see details in section 5.2). Specifically, it is a magnetic island which has exceeded a threshold value, as typically occurs when other instabilities (e.g. sawteeth or ELMs) provide a seed island of a sufficient size. Once it has exceeded this threshold, the magnetic seed island is driven to be unstable by a perturbed bootstrap current. NTMs are likely to be a dominant performance-limiting instability on large tokamaks such as ITER, as they result in a large drop in confinement and can potentially cause a disruption. Although many NTM measurements have been performed on different machines, there remains a large degree of uncertainty about the potential NTM thresholds on ITER. A greater understanding of NTM onset and stability is therefore needed for their effective control and avoidance on this machine.

The thresholds and evolution of NTMs are typically described using the MRE, which contains both stabilising and destabilising terms (see section 5.2.4). The MRE predicts the evolution of the island width (w), which indicates the overall stability of an NTM in a given plasma. Typically, this equation is used to model the contribution of each stability term in different conditions, in order

that the results can be extrapolated to future devices. Magnetic measurements taken at the edge of the plasma can be used to infer the island width and can be used to measure island width evolution. This permits a comparison with the NTM evolution predicted by the MRE and thus permits stability term contributions to be estimated (during beta scans, see below). Section 5.3 outlines the magnetic measurement results for MAST, where TORFLD [85] code has been used to simulate the magnetic signals on this machine to provide an estimate of the island width. TORFLD calculates the field due to a number of current filaments at a specific location. In this case, the current filaments are placed on a rational surface to represent the island.

The principal destabilising term of the MRE results from the bootstrap current drive, which occurs when the T_e profile is flattened within an island. The finite island width (w_d) determines the size of the magnetic island at which this occurs. T_e measurements taken over one NTM period allow the island structure to be fitted to a heat transport model [86] and from this, w_d can be determined. Further to the upgrade of the ruby and Nd:YAG TS systems, this measurement of w_d is now possible using TS data from MAST (see section 5.4). A comparison of the TS measurements of w_d can also be made to the simple approximations typically used to determine w_d, in order to test the validity of these approximations, and this is also described in section 5.4.

The size of the ion polarisation current term in the MRE is also important for determining the onset threshold of NTMs. A large amount of uncertainty exists in terms of whether this term is stabilising or destabilising. The magnitude and direction of the island rotation frequency in the rest frame determines whether the ion polarisation current is stabilising or destabilising and also indicates the size of its contribution. This rotation frequency can be determined using a combination of charge exchange measurements (CXRS) of the ion velocity and temperature and magnetic measurements of the island rotation frequency in the lab frame. In this chapter, the size of the ion polarisation term on MAST has been estimated using this approach. This has not previously been carried out and previous magnetic measurements were unable to distinguish the contributions from the ion polarisation and w_d terms.

Assessing the relative contribution of each stability term to the MRE is important to understand the influences on NTM stability and make predictions for NTM thresholds for future devices. Beta scans, where beta poloidal (β_p) is reduced, can be a useful means to estimate these relative contributions by exploiting the relationship between each stability term and β_p. This approach which avoids the uncertainties in the size of the NTM triggers, has previously been used on a number of tokamaks to study the evolution of NTMs, including the study of 3,2 NTM evolution on MAST [87]. Beta scan results for 2,1 NTMs on MAST, using the above stability term and magnetic measurements, are discussed in section 5.6.

Finally, an FPGA-triggering system that has been developed to trigger the MAST TS systems in

real-time, on different amplitudes and phases of NTMs. This system was built in order to increase the number of w_d measurements and beta scans possible and is described at the end of this chapter.

5.2 NTM Theory

The basic principles which underlie the formation of magnetic islands and tearing modes are outlined in this section, followed by an introduction to classical and neoclassical tearing modes. The MRE is then described in detail and its important stability terms are discussed.

5.2.1 Resistive magnetohydrodynamics and magnetic reconnection

A plasma may be modelled as a single, neutral, conducting fluid whose motion is influenced by an external magnetic field and magnetohydrodynamic (MHD) theory describes this. The MHD model consists of Maxwell's equations of electromagnetism,

$$\nabla \times \vec{E} = -\frac{\partial \vec{B}}{\partial t}, \tag{5.1}$$

$$\nabla \times \vec{B} = \mu_0 \vec{J}, \tag{5.2}$$

$$\nabla \cdot \vec{B} = 0, \tag{5.3}$$

$$\tag{5.4}$$

the mass equation,

$$\frac{d\rho}{dt} + \rho \nabla \cdot \vec{v} = 0, \tag{5.5}$$

the equation of momentum,

$$\rho \frac{d\vec{v}}{dt} = \vec{J} \times \vec{B} - \nabla p, \tag{5.6}$$

Ohm's law,

$$\vec{E} + \vec{v} \times \vec{B} = 0 \quad \text{for ideal MHD,} \tag{5.7}$$

$$\vec{E} + \vec{v} \times \vec{B} = \eta \vec{J} \ \text{ for resistive MHD,} \tag{5.8}$$

and finally, an energy equation,

$$\frac{d}{dt}\left(\frac{p}{\rho^{\nu}}\right) = 0. \tag{5.9}$$

Complete derivations and mathematical descriptions of this theory can be found in a large number of physics textbooks (for example [6]).

The link between the electric field and the other variables in MHD can be examined using the generalised Ohm's equation (equation 5.8). In ideal MHD, electrons in the plasma are assumed to

be so mobile that it can be treated as a perfectly conducting fluid ($\eta = 0$). This is a reasonable assumption for most of applications of MHD on tokamaks, as the resistivity of core tokamak plasmas is very low. However, resistivity can become important over small regions and can result in a number of instabilities, including tearing modes.

Taking the curl of equation 5.8 gives an equation which describes the evolution of the magnetic field:

$$\frac{\partial B}{\partial t} = \nabla \times (v \times B) - \nabla \times (\eta \nabla \times B) \tag{5.10}$$

The first term on the right hand side of this equation describes the variation of the magnetic field moving with the plasma, due to its convection. The second term represents the variation of the magnetic field due to diffusion, as driven by gradients. The size of the diffusion coefficient in this term is given by $\frac{\eta}{\mu_0}$ (in equation 5.11). For a perfectly conducting, ideal plasma (η = 0), the magnetic flux on any surface moving with the plasma would remain constant. This would mean that the magnetic flux would effectively be 'frozen' into the fluid and move along with it. This frozen-in condition of ideal MHD theory is the basis of the topology-conserving evolution of the real system. However, as noted above, resistivity can become important in the global dynamics and break the frozen-in condition. In the case of uniform finite η the evolution of the magnetic field can be rewritten as:

$$\frac{\partial \vec{B}}{\partial t} = \nabla \times (\vec{v} \times \vec{B}) + \frac{\eta}{\mu_0} \nabla^2 \vec{B} \tag{5.11}$$

Equation 5.11 is fundamental for defining the magnetic behaviour in resistive MHD and it can be used to determine the magnetic field (B) if the fluid velocity (v) is known. The magnetic Reynolds number (R_m) is given by the ratio between the first and second terms of the right-hand side of equation 5.11, specifically:

$$\frac{\nabla \times (v \times B)}{\eta \nabla^2 B} \approx R_m = \frac{L_0 V_0}{\eta} \tag{5.12}$$

where V_0 and L_0 are the typical velocity and length scales in a plasma. If the Reynolds number is much greater than 1, the second term of equation 5.11 becomes negligible. This true in most regions of hot tokamak plasmas and therefore ideal MHD can be applied to describe the magnetic field evolution. However, an exception to this rule occurs when the length scale (L_0) is very small. This causes both $R_m \leq 1$ and the second term of 5.11 to become important and thus resistive effects significantly influence magnetic field evolution and topology. Hence, in narrow layers, where the plasma is subject to particular resonant conditions, the magnetic field evolution must be described by the full induction equation to account for the role of the resistivity, which breaks and reconnects the magnetic field lines.

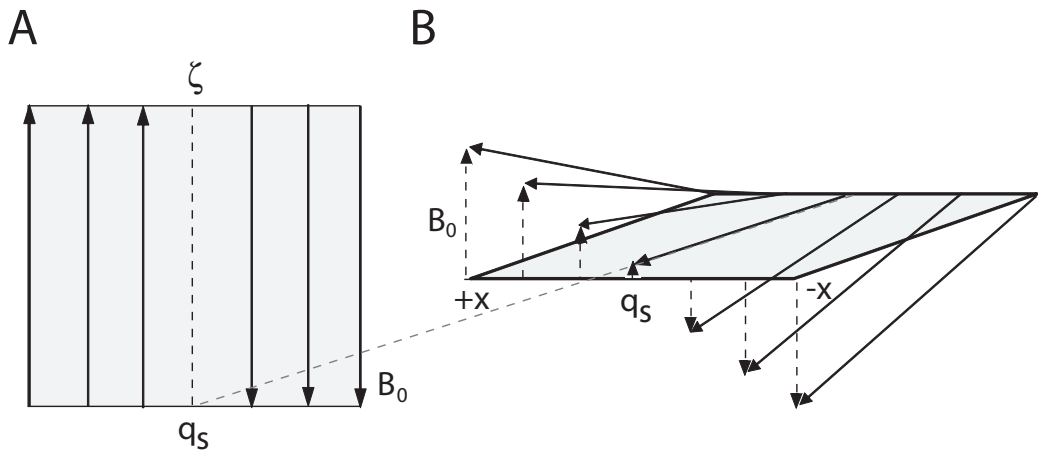

Figure 5.1: Magnetic field lines in the vicinity of the rational surface. A. Lines shown in a slab geometry. The direction of the perturbed field changes with respect to the rational surface in the r_χ plane. B. Lines shown in a realistic tokamak case. The magnetic field lines have a different pitch with respect to the rational q surface (q_s).

5.2.2 Tearing modes

The breaking and reconnection of magnetic field lines due to the effects of resistivity leads to the formation of magnetic islands. This occurs on rational magnetic surfaces where a perturbation is resonant. It is convenient to describe the magnetic field geometry in terms of 3 coordinates [18], the radial variable (r), the poloidal angle (θ) and the new helical angle (ζ). ζ is directed along a line perpendicular to that connecting the island x points and can be written in terms of the toroidal (θ) and poloidal (ϕ) angles:

$$\zeta = \theta - \phi\frac{n}{m}. \tag{5.13}$$

where m is the poloidal mode number and n is the toroidal mode number. The equilibrium field (B_0) (see figure 5.1) and flux (ψ_0) close to the resonant magnetic surface can then be written as:

$$x = r - r_s \tag{5.14}$$

$$B_0 = B_\theta(1 - \frac{q}{q_s}) \tag{5.15}$$

$$B_0 = \left(B_\theta\frac{q'}{q}x\right) \text{ (Taylor expansion of equation 5.15)} \tag{5.16}$$

$$\psi_0 = \psi_0(r_s) + \frac{1}{2}B_\theta\frac{q'}{q}x^2 \tag{5.17}$$

where r_s is the position of the resonant surface (s), q is the safety factor and x denotes the distance from the surface.

The magnetic island is generated by a perturbed current along the field line, which is taken to have a sinusoidal form. The perturbations of the tearing mode magnetic field ($\tilde{B_r}$) and magnetic

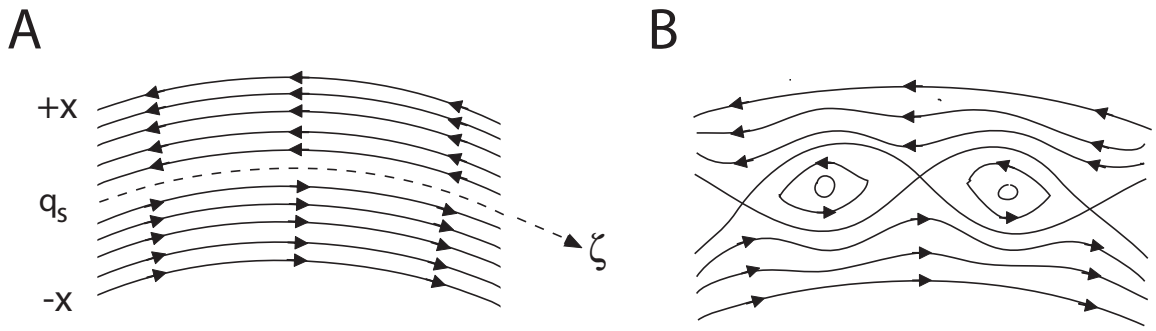

Figure 5.2: The formation of magnetic islands as a result of magnetic reconnection occurring in the thin layer centred on the rational surface. A. The equilibrium field before reconnection occurs. B. The equilibrium and perturbed flux surfaces resulting in a magnetic island.

flux ($\tilde{\psi}$), on the rational surface, are given by:

$$\tilde{B}_r = \tilde{B}_r Sin(m\zeta) \tag{5.18}$$

$$\tilde{\psi} = \tilde{\psi}_1 Cos(m\zeta) \tag{5.19}$$

The superposition of the equilibrium and the perturbed magnetic field or flux results in a magnetic island and this is centred on a given resonant surface (figure 5.2). The direction of the magnetic field lines on this surface is given by:

$$\frac{1}{r_s}\frac{dx}{d\zeta} = \frac{\tilde{B}_r}{B_0} \tag{5.20}$$

To find the field line traces which describe the magnetic island geometry, equation 5.20 must be integrated from $\chi = 0$ to $m\pi$:

$$d(\frac{1}{2}x^2) = \frac{r_s \tilde{B}_r}{mB_0} d(1 - \cos(m\zeta)), \tag{5.21}$$

and the resulting equations are:

$$x^2 = \frac{1}{8}w^2(1 - cos(m\zeta)) \tag{5.22}$$

$$w = 4\sqrt{\frac{rq\tilde{B}_r}{mq'B_\theta}} \tag{5.23}$$

$$w = 4\sqrt{\frac{q\tilde{\psi}}{q'B_\theta}} \tag{5.24}$$

where w is the width of the magnetic island. The size of w is dependent on the magnitude of the local magnetic shear and is also proportional to the square root of the magnetic perturbation.

5.2.3 The Rutherford equation and classical tearing modes

The evolution of a magnetic island is governed by the perturbed helical currents in the rational surface where it forms. Generally, to describe the dynamics of a tearing mode in the plasma, it is

sufficient to apply Ohm's and Ampere's laws to the perturbed flux function (ψ_1) along the magnetic field lines [18]:

$$\Delta^{'}\tilde{\psi} = 2\mu_0 \int_{-\infty}^{\infty} dx \oint d\zeta J_{\parallel} \cos\zeta. \tag{5.25}$$

This island evolution equation tells us how much current is flowing in the island, but does not directly describe how the island evolves in time. This evolution can only be described if the mechanisms responsible for the perturbed parallel current ($J_{\parallel}$) are specified.

In the case of classical tearing modes, only the contribution of the Ohmic current determines the evolution of the island. This means $J_{\parallel} = j_{Ohm}$ and in this case, equation 5.25 reduces to the classical Rutherford equation for island evolution:

$$\frac{\tau_R}{r_s}\frac{dw}{dt} = r_s\Delta^{'}(W) \tag{5.26}$$

$$\tau_s = \frac{\mu_0 r_s}{1.22\eta_{NC},} \tag{5.27}$$

where τ_R is the resistive time and η_{NC} is the neoclassical resistivity. In equation 5.27, a positive $\Delta^{'}$ indicates that the island is growing. However, $\Delta^{'}$ is usually considered independent of w and this means that the Rutherford equation predicts unstable islands to grow exponentially.

The classical stability of magnetic islands is determined by the equilibrium toroidal current profile. The value of $\Delta^{'}$ is dependent on the plasma equilibrium and has to be evaluated by matching the ideal MHD solution for ψ_1, for the region $0 < r < r_s + \frac{W}{2}$, to the solution for $r_s - \frac{W}{2} < r < \infty$. This evaluation method causes a discontinuity in $\frac{d\psi_1}{dr}$ at the rational surface. In cylindrical geometry, the perturbed flux (ψ_1) is calculated using the tearing mode equation [88]:

$$\frac{d^2\psi_1}{dr^2} + \frac{1}{r}\frac{d\psi_1}{dr} - \left(\frac{m^2}{r^2} + \frac{dj/dr}{B_\theta(r)(1-nq(r)/m}\right)\psi_1 = 0 \tag{5.28}$$

This equation can be solved numerically for a given radial profile of current density, safety factor and poloidal magnetic field as shown in figure 5.3.

5.2.4 Neoclassical tearing modes and the modified Rutherford equation

In addition to the the Ohmic current, there are a number of currents which contribute to the perturbed parallel current ($J_{\parallel}$) on tokamaks, influencing island stability and growth. These include the bootstrap current (j_{bs}), the current generated by the tokamak curvature (j_{ps}) and the polarization current (j_{pol}). Tearing modes which are driven by all of these currents are referred to as NTMs.

If the effects of these currents are included in the classical Rutherford equation, we obtain the modified Rutherford equation (MRE) which more accurately describes the evolution of an island:

$$\frac{\tau_R}{r_s}\frac{dw}{dt} = r_s\Delta'(w) + r_s\Delta'_{BS} + r_s\Delta'_{GGJ} + r_s\Delta'_{pol} \tag{5.29}$$

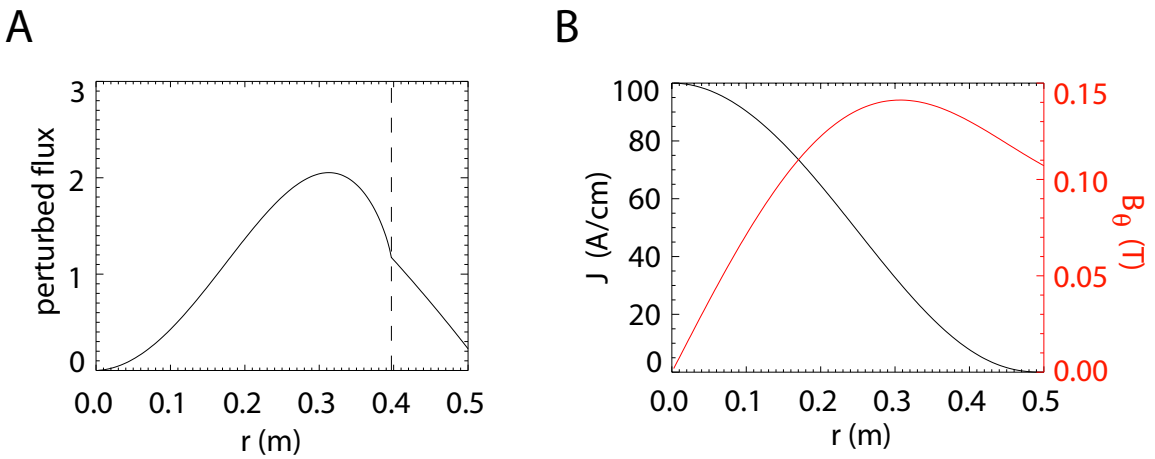

Figure 5.3: A. The classical tearing stability evaluated in cylindrical geometry. B. The input current density (J) and poloidal field profiles (B_θ) used to calculated the classical tearing stability in a cylindrical geometry.

Each of the Δ' terms in this equation are used to describe how each additional current affects the evolution of an island. The origin of each of these current terms and their calculations will now be discussed in more detail. Although not considered here, additional currents can also be externally injected by the electron cyclotron current drive (ECCD) to stabilise island growth and can be included in the MRE.

5.2.4.1 Bootstrap drive

The effects of the bootstrap current were predicted and modelled theoretically in a number of papers in the early 1970s [15]. This current is proportional to the pressure gradient and when a magnetic island forms, rapid parallel transport causes pressure flattening across the magnetic island. This leads to a reduction in the pressure-driven bootstrap current and, in turn, an increase in island size. An initial modified form of the Rutherford equation was developed to include the effects of both the bootstrap and Ohmic currents:

$$\frac{\tau_R}{r_s^2}\frac{dw}{dt} = \Delta^{'} + \epsilon^{1/2}\frac{L_q}{L_p}\frac{\beta_p}{w} \tag{5.30}$$

NTMs were first observed experimentally in 1995 on TFTR supershots [89] and were found to be triggered from seed islands that are generated from other MHD instabilities (e.g. ELMs or sawteeth). Only seed islands greater than a threshold island width are found to trigger NTMs and this threshold level can be explained by the degree of flattening of the pressure profiles, which influence the bootstrap drive, for a given NTM.

Fitzpatrick ([86]) predicted a critical island width below which an island would shrink and disappear. This effect is a result of the large connection length adjacent to a rational surface and the

stagnation of the magnetic field lines in the vicinity of the island separatrix. T_e and n_e, and hence p_e, can be assumed to be flux functions when the transport from one location to another is dominated by parallel transport. However, both the large connection length close to a rational surface and the field line stagnation near the island separatrix mean that the parallel distance connecting a radial point can become orders of magnitude greater than the perpendicular distance. The parallel and perpendicular transport channels can compete in these conditions, making a gradient parallel to the flux surfaces possible.

The equilibration of T_e along a field line can be understood by solving a heat transport equation in the vicinity of the rational surface, as described in section 5.4 and Appendix A. In solving this equation, a critical island width can be found, below which the parallel transport cannot guarantee that T_e is a flux surface quantity. The result of this heat transport calculation is a finite island width (w_d), which forms part of the bootstrap contribution to the MRE equation. w_d limits the bootstrap contribution to MRE for small island widths and as a result larger triggers (greater than the w_d threshold) are needed for NTMs to occur.

The majority of the bootstrap current (70-90%) results from the electron pressure gradient and the remainder results from the ion pressure gradient. The ion bootstrap drive is also affected by particles which drift inside the banana orbits and these increase the bootstrap current inside an island [90]. This effect is significant when the island width is greater than the banana width, $w_{b,i} = \sqrt{(\epsilon)}\rho_p$, where $\rho_p = \frac{(2m_i k_B T_i)^{\frac{1}{2}}}{eB_p}$ is the poloidal Larmor radius.

A more accurate calculation of the bootstrap term, than given by equation 5.30, is based on the Sauter approximation for the bootstrap current [91] and is used for the remainder of this chapter. This is given by:

$$\Delta'_{BS} = r_s \beta_p a_{bs} \left(\frac{f_{bse} w}{w^2 + w_d^2} + \frac{(1 - f_{bse}) w}{w^2 + w_{d,i}^2} \right), \tag{5.31}$$

where f_{bse} is the trapped particle fraction, $w_{d,i} = \sqrt{28} w_{b,i}$ and the a_{bs} coefficient is given by:

$$a_{bs} = a_2(-L_{bs}) \frac{L_q}{-L_p}, \tag{5.32}$$

where $L_q = q/q'$ and $L_p = p/p'$ are the pressure and safety factor gradient scale lengths respectively, L_{bs} is the bootstrap current scale length (defined in detail by Sauter et al. [91]) and a_2 is a coefficient used to scale these quantities in equation 5.32, (a_2=3.2; as derived from large aspect ratio results).

w_d is the principal stabilising term in the calculation of the bootstrap contribution to island stability. In the case of MAST, the ion contribution to the bootstrap current is found to be negligible because of the high bootstrap fraction (f_{bse}).

5.2.4.2 Tokamak curvature

A tearing mode island in a toroidal plasma, with finite plasma pressure, bends the field lines in such a way as to increase the magnetic energy. The curvature has the effect of increasing the plasma stability against the tearing mode [92]. This is described by the Glasser Green Johnson curvature term:

$$\Delta'_{GGJ} = r_s \beta_p \frac{a_{GGJ}}{\sqrt{w^2 + 0.2 w_d^2}} \tag{5.33}$$

The stabilising effect of this curvature term is reduced at small island widths, as suggested by Lutjens et al. [93]. The size of this modification is given in terms of the finite island width. The a_{GGJ} term is related to the resistive interchange parameter (D_r) and is given by:

$$a_{GGJ} = 6\frac{D_R}{\beta_p} \approx 6\frac{\epsilon^2}{s}\frac{L_q}{-L_p}\left(1 - \frac{1}{q^2}\right). \tag{5.34}$$

The stabilising effect of Δ_{GGJ} comes from the negative sign of D_R. D_R scales as $\beta \sim= \epsilon^{1/2}\beta_p$ and thus introduces an $\epsilon^{3/2}$ (ϵ being the inverse aspect ratio) dependence, relative to the bootstrap drive. The bootstrap drive itself scales as $\epsilon^{1/2}\beta_p$ and hence, in low aspect ratio plasmas, the Δ_{GGJ} and Δ'_{BS} terms become comparable and in this description make STs less susceptible to NTMs.

5.2.4.3 Polarisation current

A magnetic island inside a tokamak will rotate at a characteristic frequency (ω) in the rest frame of the plasma flow. Electrons respond to this moving island faster than ions, which results in a perpendicular current (J_{pol}). J_{pol} is not divergence-free and thus a parallel current, the ion polarisation current ($J_{\|}$), is induced to conserve $\nabla . J = 0$. The ion polarisation current influences the island's stability in addition to the bootstrap current and tokamak curvature.

The interaction between a propagating island and the plasma is a highly non-linear process and particle responses are dependent on the relative sizes of ω and the diamagnetic frequency (ω_{ii}). The ion diamagnetic frequency for a tokamak is given by:

$$\frac{\omega_{ii}}{2\pi} = \frac{mB_\phi}{2\pi r}\frac{(T_i/L_{pi})}{B^2} - \frac{nB_\theta}{2\pi R}\frac{(T_i/L_{pi})}{B^2} \tag{5.35}$$

The ion polarisation current can be either stabilising or destabilising, depending on the relative sizes of ω and ω_{ii}. In the MRE, the contribution of this current to island stability is described by:

$$\Delta'_{pol} = r_s \beta_p a_{pol} \frac{w}{w^4 + w_{b,i}^4} \tag{5.36}$$

Δ'_{pol} is expected to contribute to NTM stability when the island width is of the order of the ion banana width ($w_{b,i}$) and hence, the additional $\frac{w}{w^4+w_{b,i}^4}$ term has been added to equation 5.36 to

restrict its influence below the ion banana width. The a_{pol} coefficient is given by:

$$a_{pol} = a_3 \left(\frac{L_q}{-L_p} \right)^2 w_{bi}^2 f(\omega) g(\epsilon, \nu_{ii}^*) \tag{5.37}$$

where $v_{ii} = \frac{ln\Delta}{12\epsilon_0^2 \pi^{3/2}} \frac{Z^4 e^4 n_i}{m_i^{1/2} (k_B T_i)^{3/2}}$ is the ion collision frequency and $f(\omega)$ describes the dependence on ω, where ω is the island propagation frequency in the frame of the plasma flow. The collisional dependence ($g(\epsilon, \nu_{ii}^*)$) of a_{pol} is given by:

$$g(\epsilon, v_{ii}) = \begin{cases} 1.64\epsilon^{1/2} & v_{ii}/\epsilon\omega \to 0 \\ \epsilon^{-1} & v_{ii}/\epsilon\omega \to \infty \end{cases} \tag{5.38}$$

The collision frequency regime of the plasma is defined by the $v_{ii}/\epsilon\omega$ term The $g(\epsilon, \nu_{ii})$ term has a value of $1.64\epsilon^{1/2}$ in the collisional regime [94] and ϵ^{-1} in the collisionless regime [95].

5.3 Magnetic measurements of NTM widths

Magnetic island evolution is typically described in terms of the radial island width (w) and this can be calculated from magnetic coil measurements. In this section such calculations are presented, using magnetic measurements taken on MAST during the last experimental campaign. These estimates of w have also been used as a comparison to the island evolution predicted by the MRE (as described in section 5.6). MAST is equipped with a large number of Mirnov coils, which are lo-

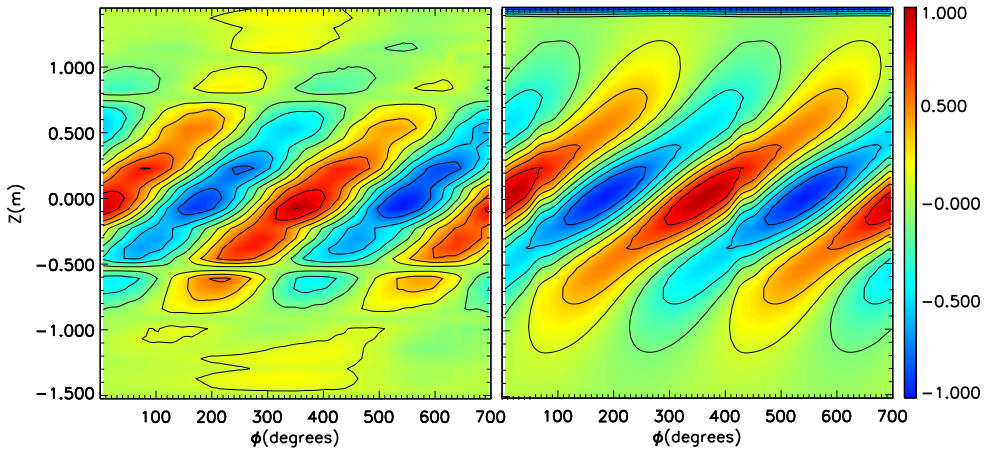

Figure 5.4: Comparison of the real (A) and simulated (B) $\tilde{B_z}$ measurements of the perturbed magnetic field amplitude on the vertical Mirnov array. Data is from a single shot on MAST. This shows a good agreement between the TORFLD simulations and $\tilde{B_z}$ measurements.

cated at the inboard and outboard of the vessel and these sensors measure the oscillating perturbed magnetic field in the vertical plane ($\tilde{B_z}$) that results from a rotating magnetic island. We have seen (equation 5.24) that w is related to the perturbed radial magnetic field ($\tilde{B_r}$) at the rational surface,

but this cannot be measured directly. Therefore, in order to calculate w from magnetic measurements, the $\tilde{B}_r$ at the rational surface must be determined from the $\tilde{B}_z$ at the edge of the MAST plasma. The cylindrical approximation is frequently used to calculate the relationship between these terms and is given by:

$$\tilde{B}_r = \left(\frac{b}{r}\right)^{m+1} \frac{\tilde{B}_z}{2}, \tag{5.39}$$

where b is the distance between the rational surface and the magnetic sensor and m is the poloidal mode number.

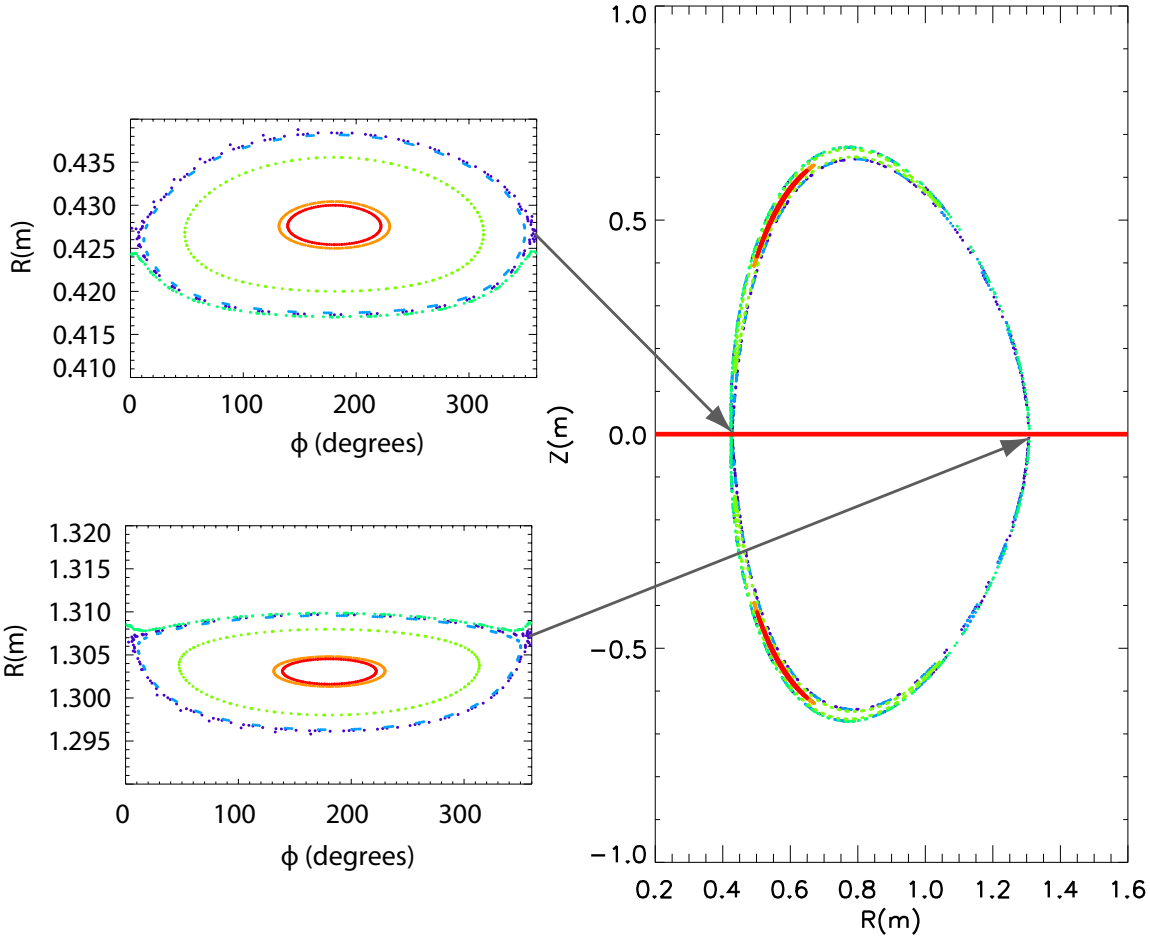

Figure 5.5: Puncture plots of magnetic island structures resulting from current filament models, determined using field line tracing. The figure on the right is the poloidal cross-section of the MAST vessel taken at a toroidal angle of $\phi = 90°$. Puncture plots of islands at the outboard (A) and inboard (B) sides of the tokamak are plotted as a function of the toroidal angle. The size of each islands is determined by the amplitude of the Mirnov signal at the mid-plane ($Z = 0$). The island on the outboard side is narrower, as predicted, due to flux expansion.

TORFLD code was used to determine $\tilde{B}_r$ at the rational surface from $\tilde{B}_z$ on the coils. This was carried out by first using equilibrium code EFIT [40] to calculate the equilibrium magnetic field

and using TORFLD to place a sheet current perturbation, which represents the island, on a given rational surface. This perturbation has a toroidally sinusoidal current variation and is represented by a number of helical current filaments (typically 40) which are distributed evenly around a given rational surface. The currents in these filaments flow along the magnetic field lines and do not produce any charge accumulation (divergence-free).

In TORFLD, the size of the current perturbation in the filaments was adjusted so that the amplitude of the simulated $\tilde{B_z}$ was equal to the measured $\tilde{B_z}$ on the centre column Mirnov array (Figure 5.4). Once a good match between these quantities was found, the $\tilde{B_r}$ at the rational surface could be measured in TORFLD.

Another approach to determine the size of a given island is to perform field line tracing of the EFIT equilibrium combined with the sheet current perturbation that represents the island. Both approaches to determine w were carried out for a number of shots and the field line tracing results (figure 5.5) were found to agree well with the results determined when using equation 5.24 where $\tilde{B_r}$ had been calculated using TORFLD.

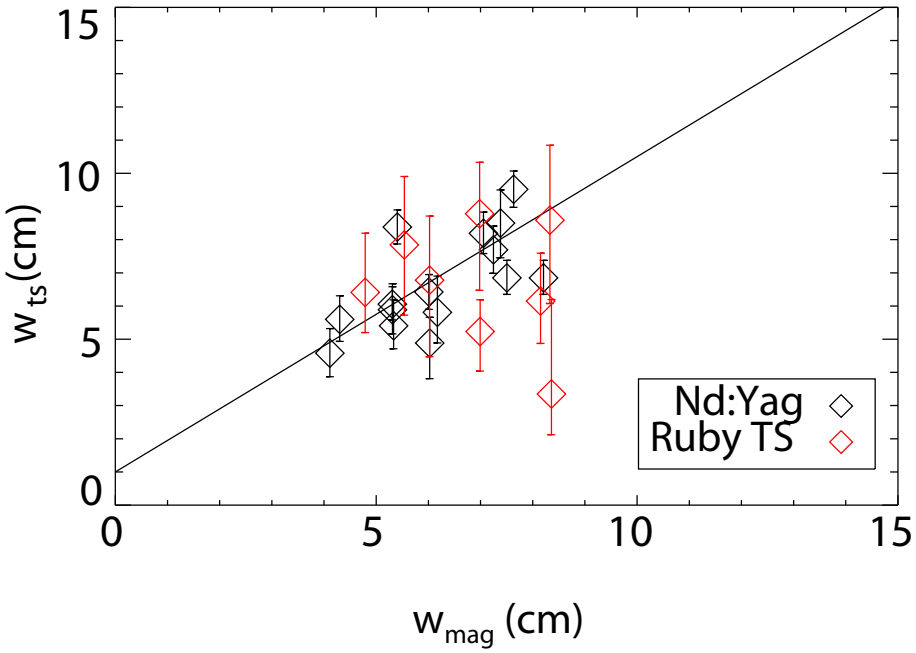

Figure 5.6: Comparison of the 2,1 island widths determined using TORFLD code (w_{mag}) and using fits of the MAST TS data (w_{TS}). Each data point represents one island and both ruby (red) and Nd:YAG (black) TS data have been used in this comparison.The error bars on the Nd:YAG measurements are smaller than those of the ruby TS system measurements, as the width can be constrained by 8 measurements when the Nd:YAG system is operated in burst mode.

Following the upgrades to the TS systems on MAST, a comparison between the magnetic estimates of w and the width inferred from the TS system is now possible. However, unlike magnetic

measurements, TS measurements can only be taken a small number of times during the islands evolution. The TS approach uses a model to fit the island width from the T_e measurements (this model is discussed in detail in section 5.4). A good agreement was found between the magnetic island widths and the TS island widths, within the error bars of the measurements (Figure 5.6). TThese measurements were taken from similar MAST discharges.

5.4 Heat transport across a magnetic island and estimation of the critical island width

Here, the finite island width term (w_d) of the MRE is determined using MAST TS data. This is done by fitting the flattening of the T_e profile, measured using TS, to a heat transport model developed in collaboration with University of York [96, 97]. The results are then used to investigate the influence of the w_d term on NTM thresholds and evolution. In addition, the measured w_d has been compared to approximations typically used for w_d in order to examine their validity using MAST data.

5.4.1 TS measurements of w_d

Heat transport across a magnetic island occurs via a boundary layer centered on the island separatrix. In this boundary layer, parallel gradients in T_e are possible. The width of the boundary layer is the largest at the x-point and is approximately equal to the critical island width term (w_c). This term is important for the solution of the heat transport equation and is defined as:

$$w_c = \sqrt{8}\left(\frac{\chi_\perp}{\chi_\parallel}\right)^4 \sqrt{\frac{R_0 r_{rs}}{L_s n}} \tag{5.40}$$

where R_0 is the major radius, L_s is the local magnetic shear and r_s is the value of the minor radius coordinate. This parameter is related to the w_d parameter, where $w_d = 5.1 w_c$ [86]. The width of the boundary layer at the o-point is $\sim w_c^2/w$. The effect of an island greater than w_c is to flatten the T_e profile inside the boundary region. The boundary layer is associated with curved regions in the T_e profile and these regions are dependent on the size of w_c. The boundary region matches the flat region inside the island and the gradient T_e outside the island. This relationship was first demonstrated by Fitzpatrick [86] and contributes to the triggering threshold observed in NTMs. The effect of different values of w_c on the contour of T_e is shown in figure 5.8. It can be observed that as the size of w_c increases, the width of the boundary layer also increases.

Fitzpatrick investigated the temperature profiles around a magnetic island using a diffusive model for the heat transport [86]. In the absence of heat sources or sinks, the heat transport that occurs parallel and perpendicular to the magnetic field lines is given by:

$$\chi_\parallel \nabla_\parallel^2 T + \chi_\perp \nabla_\perp^2 T = 0 \tag{5.41}$$

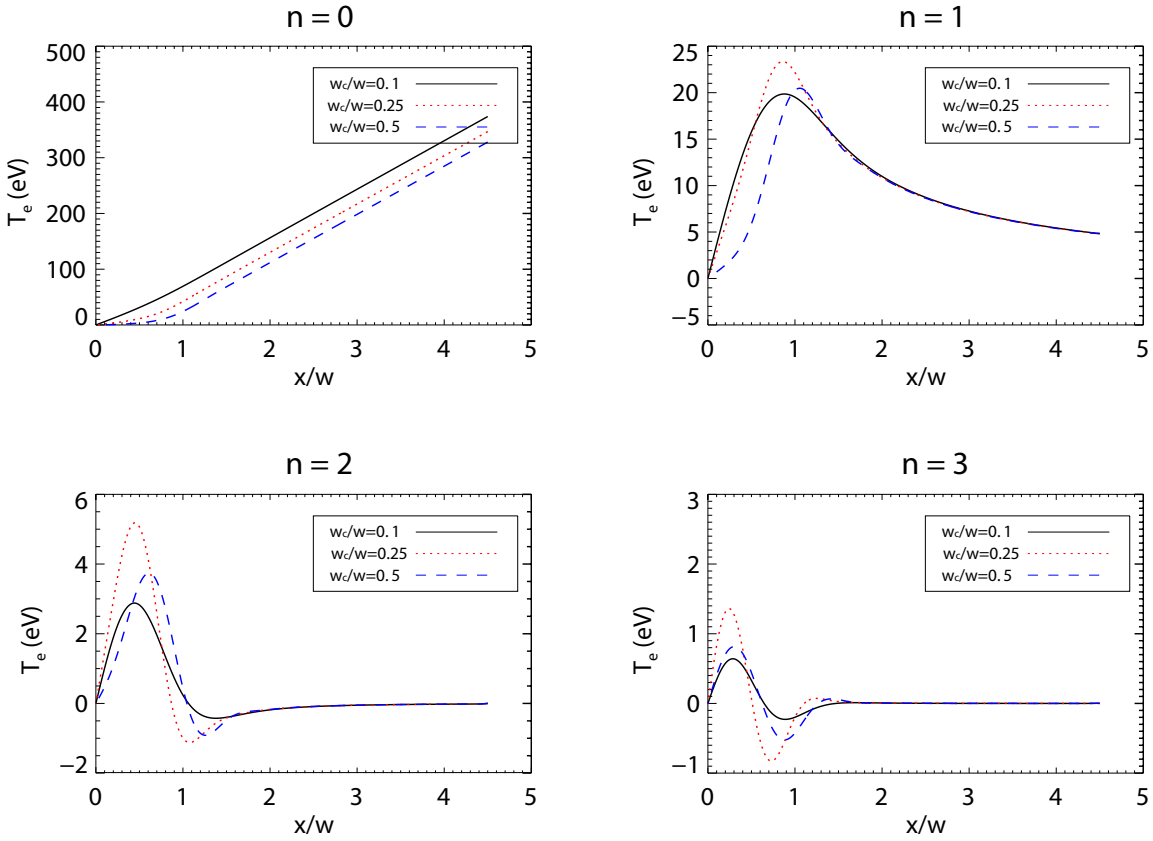

Figure 5.7: The solution for the $n = 0 - 3$ Fourier harmonics as a function of normalised island width (x/w). Three different values of w_c/w are considered, 0.01 (black lines) 0.25 (red) and 0.5 (blue). The magnetic island is symmetric around the it's central radial position and the x/w scale in this picture goes from the center to 4 island widths. Here T_e (eV) is the NTM contribution to the temperature, relative to that at the island centre. The boundary conditions of the model have been carefully determined to ensure that the electron temperature gradient far from the island can be matched to the real experimental gradient.

where $\chi_{\|}$ and $\chi_{\perp}$ are thermal diffusivities parallel and perpendicular, respectively, to the field lines. The perpendicular heat transport across field lines is a result of small scale turbulence. The parallel heat transport is the product of the electron mean free path and the electron collisionality and is typically orders of magnitude greater than the perpendicular [98].

We can obtain (see Appendix A) a partial differential equation of T_e, which describes the diffusive transport in the heat transport model:

$$\left(X \left.\frac{\partial}{\partial \zeta}\right|_X + \frac{1}{4}\sin\zeta \left.\frac{\partial}{\partial X}\right|_\zeta \right)^2 T + \frac{w_c^4}{w^4}\frac{\partial^2 T}{\partial X^2} = 0 \tag{5.42}$$

this equation can be reduced to a 1D problem by expressing T as a Fourier series:

$$T(X,\zeta) = \sum_{n=0}^{N} T_n(X)\cos n\zeta \tag{5.43}$$

and this solution can be substituted into equation 5.42, then multiplied by $cosk\zeta$ (integer k) and integrated over $\frac{1}{2\pi}\int_{-\pi}^{\pi} ... \, d\zeta$ to produce an equation of the form:

$$\sum_{n=0}^{N}\left[A_{Kn}\frac{d^2T_n}{dX^2} + B_{kn}\frac{dT_n}{dX} + C_{kn}T\right] = 0 \tag{5.44}$$

Equation 5.44 is an $N+1$ coupled differential equation for the different Fourier mode amplitudes, where A_{kn}, B_{kn} and C_{kn} are matrices which are functions of k, n, w_c and x. A finite difference scheme is used to determine a numerical solution to this equation and a full derivation of this scheme is included in Appendix A. The solution of this equation (figure 5.7) is the Fourier solution to the the heat transport equation (equation 5.41). The full 2D solution can then be reconstructed from this Fourier series and is shown in figure 5.8.

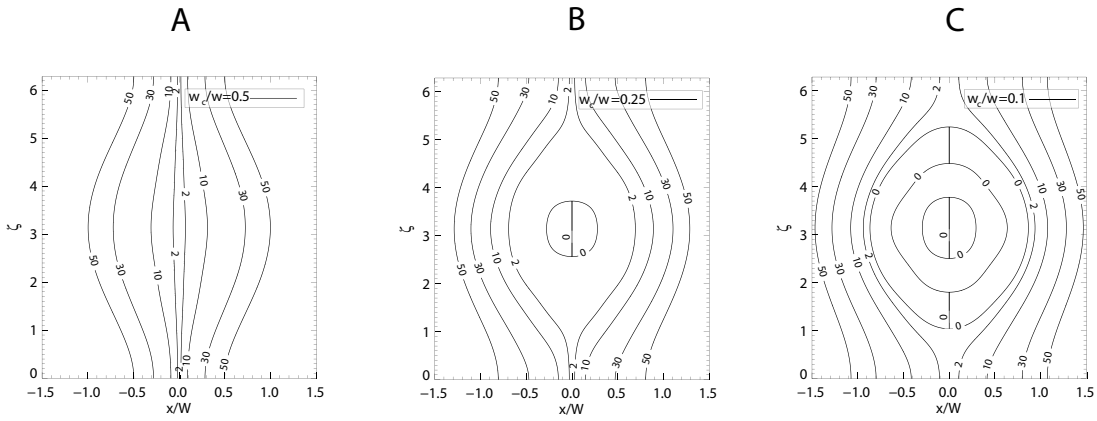

Figure 5.8: Boundary layers resulting from the 2D solution of the heat transport equation. The effect of different w_c/w ratios (0.125, 0.25,0.5) on perturbed T_e (T_e - T_e (island centre)) contours are shown. As the w_c parameter is increased, the boundary layer centred on the island separatrix also increases. The x-points are located at ζ = 0 and 2π and the o-point is located at $\zeta = \pi$.

A solution to the heat transport equation (equation 5.41) can be fitted to the MAST TS data, in order to determine both the island width (w) and the critical island width (w_c). Data has been taken from the HFS because the flux expansion and geometry of TS systems allows greater resolution in this region than at the LFS. On the outboard side displacements of the rational surfaces occuring during the NTM rotation period complicates the analysis of islands in this region. For the ruby TS system, the Fitzpatrick model was first convolved with the instrument function representing the spatial smoothing as described in section 4.4.6, Chapter 4). In contrast to the mtanh pedestal model discussed in section 3.3.5 the T_e and n_e gradient in the vicinity of the NTM are relativity small so the additional effects of spectral smoothing need not have been considered. Examples of such fits to the HFS TS data from both ruby and Nd:YAG are shown in figure 5.9. A good agreement is found between the experimental ruby and Nd:YAG $T_e$profiles and the heat transport model (figure 5.9).

However, the error bars resulting from fitting the experimental data are typically large for both the island width and critical width. In the case of a single ruby TS measurement, the minimum of the χ^2 space can be broad with a number of possible local minima. This can be understood as multiple solutions of the Fitzpatrick equation that match the experimental data. The increased number of measurements possible using the Nd:YAG system results in a better defined χ^2 minimum in most cases, although large error bars still occur on the measured parameters. There also exists a large correlation between the width and the critical width parameters, which can be seen as the contours figures 5.9C and D. This correlation could be exploited to constrain the critical island width more accurately using magnetic measurements of the island width.

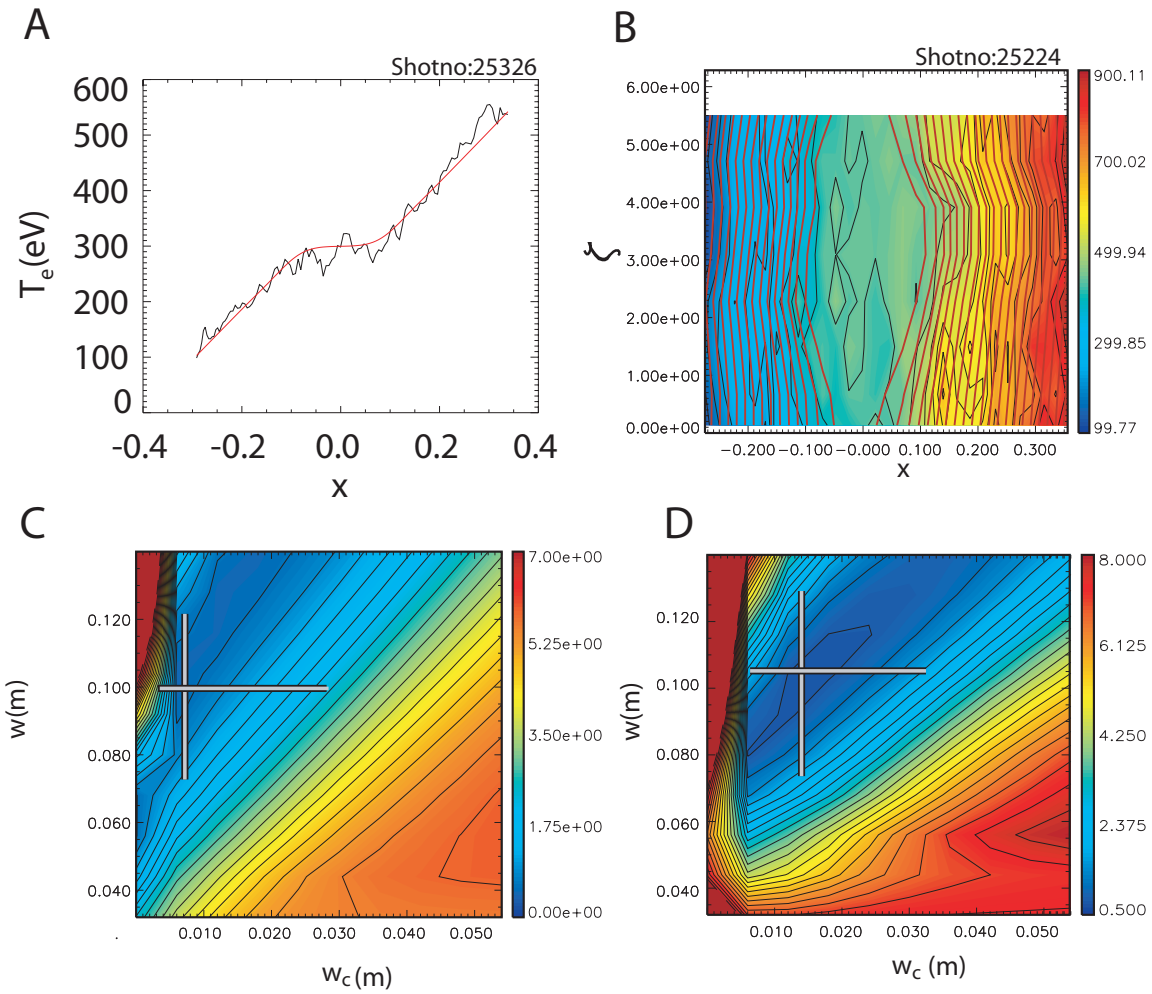

Figure 5.9: Example of typical fits of ruby (shot 25326) and Nd:YAG TS (shot 25224) T_e data to the heat transport model, in the presence of a large NTM. A. Ruby TS data (black line) and the heat transport model fit (red line). Data is taken at the island o-point. B. Nd:YAG data (colors on contour), from 8 lasers operated in burst mode, fitted to the heat transport model (lines on contour). Island structure measured from x-point to x-point. C. χ^2 contours for the ruby fit, as a function of w and w_c. D. χ^2 contours for the Nd:YAG fit, also as a function of w and w_c. For C and D, values and error bars for both w and w_c are shown as white lines.

During the last experimental campaign, TS measurements were taken from either the ruby or Nd:YAG TS systems and the above approach was used to determine 20 measurements of both the w and w_d terms. The results are shown in figure 5.10. The value of w_d is shown to vary significantly between the individual shots. Each shot in figure 5.10 has similar values for the L_s, R_0 and r_s terms of equation 5.40 and this indicates that the variations observed for w_d are related to $(\chi_\perp/\chi_\parallel)^{1/4}$. The size of this variation is more than the expected typical variation of the $\chi_\perp$ parameter alone as the w_c parameter is dependent on quarter power on this parameter requiring large changes in $\chi_\perp$ to explain the observed w_c variation.

5.4.2 Comparison of w_d from TS measurements and approximations

In order to compare the value of w_d from TS measurements to the w_d approximations typically employed in NTM studies (where measurements are not possible), a number of different estimates for both $\chi_\perp$ and $\chi_\parallel$ can be substituted into equation 5.40. This gives an estimate for w_d. The first estimate of $\chi_\perp$ assumes a Gyro-Bohm scaling for the heat transport [95]. When this assumption is made, then $\chi_\perp$ should scale as:

$$\chi_\perp = \frac{\rho_i^2 v_{thi}}{r}, \tag{5.45}$$

which gives $\chi_\perp$ values in the order of 100 m^2/s. The second estimate takes $\chi_\perp$ values that have been measured using TRANSP [99] for H-mode plasmas on MAST. These values are in the order of 10 m^2/s, where the electron heat transport can approach neoclassical values (2-4 m^2/s). Figure 5.10 shows example values of w_d calculated using these methods to estimate $\chi_\perp$.

The Spitzer conductivity [98] is typically used as an estimate of $\chi_\parallel$, which is thus given by:

$$\begin{aligned}\chi_\parallel &= v_{TH}\lambda_e \\ &= 2.25\times 10^{10}\left(\frac{T_{keV}^{5/2}}{n_{19}}\right),\end{aligned} \tag{5.46}$$

where v_{TH} is the thermal velocity and λ_e is the electron mean free path ($\lambda_e = v_{TH}/\nu_e$, where ν_e is the electron collisionality). This definition assumes that the measurements are in the collisional regime, where the electron mean free path is short compared to the parallel temperature gradient ($L_\parallel$). If this is not the case, a conductivity of $\chi_{\parallel,con}$ has been proposed by Meskat et al. [27], where a correction is applied to the Spitzer conductivity, as given by:

$$\chi_{\parallel,con} = \frac{1}{\sqrt{1+(3.16\frac{\lambda_e}{L_c})^2}}\chi_\parallel \tag{5.47}$$

In the above correction, the $L_\parallel$ is approximated by the field line connection length L_c which can be determined from ($\sim \frac{R_o L_q}{nw}$). In the case of the 2,1 modes on MAST an L_c of (20-40 m) is found, with a λ_e of a similar range. It is therefore important to include this correction when

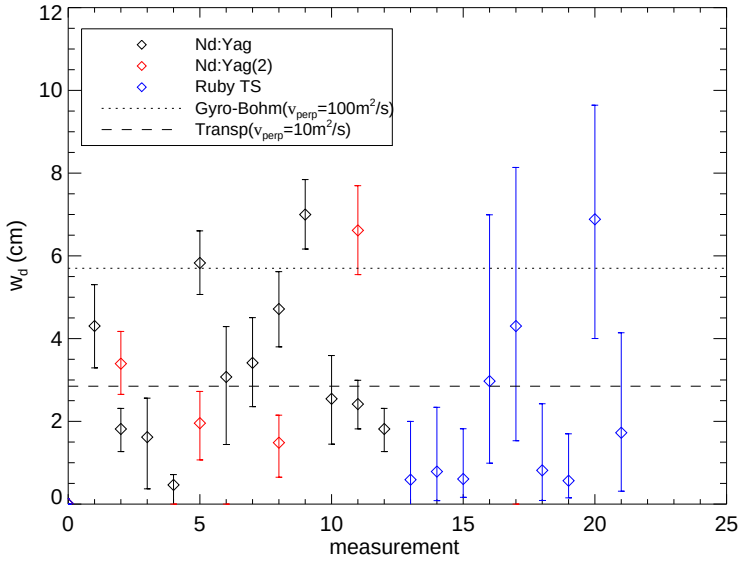

Figure 5.10: Ruby and Nd:YAG measurements of the w_d parameter. The error bars on the ruby TS measurements are typically greater than the Nd:YAG measurements, as only a single ruby TS measurement is possible, compared to the eight possible using the Nd:YAG system. The value of w_d is estimated using Gyro-Bohm scaling and typical TRANSP values for the $\chi_\perp$in H-mode MAST plasma. The other parameters in equation 5.40 are calculated using EFIT and are found not to vary significantly between shots. The conditions of the NTM evolution are therefore similar for this subset of MAST discharges.

determining $\chi_\parallel$ for these modes on MAST. For these modes, $\chi_{\parallel,con}$ is found to be a factor of ~ 3 greater than $\chi_\parallel$ calculated using equation 5.46. Using $\chi_{\parallel,con}$ thus increases the size of the estimated w_d by $\sim 3^{1/4} \sim 1.3$.

The upgraded TS system has allowed measurements of w_d for the first time on MAST. These w_d measurements are, on average, slightly lower than w_d predicted from TRANSP measurements $\chi_\perp$. A potential cause of this discrepancy is that the heat transport model is limited. If the model were extended to include a heat source term or to allow for asymmetric islands in the solutions this may resolve the discrepancy. However, further measurements are needed to investigate the exact cause of this discrepancy and the new triggering system described in section 5.7 will facilitate these.

5.5 Island rotation frequency and estimation of the ion polarisation current

In this section, NTM rotation frequencies are calculated for 2,1 NTMs on MAST for a number of shots and the size of the ion polarisation contribution to the MRE estimated. As detailed in section 5.2.4.3, the contribution of the ion polarisation current (Δ'_{pol}) to the MRE is dependent on the size

of the island rotation frequency in the rest frame of a plasma fluid. This frequency term determines whether the $g(\epsilon, \nu_{ii}, \omega)$ term in Δ'_{pol}, and thus Δ'_{pol} itself, is stabilising or destabilising in the MRE. It also influences the size of the Δ'_{pol} contribution to the island stability. $g(\epsilon, \nu_{ii}, \omega)$ is a function of the island rotation frequency, normalised by the ion diamagnetic frequency (ω_{ii}) and the ion collisionality. The island rotation frequency (ω) is given by $(f_{mirnov} - f_{E_r=0})/2\pi$, where f_{mirnov} is the measured frequency in the lab frame (determined from the Mirnov coils) and $f_{E_r=0}$ is the frequency of the frame in which $E_r = 0$. Thus the frequency of the mode is n times the frequency which would transform E_r to zero:

$$f_{E_r=0} = \frac{nE_r}{2\pi RB_\theta} \tag{5.48}$$

$$= \frac{-nv_{\phi j}}{2\pi R} + \frac{nv_{\theta j}(B_\phi/B_\theta)}{2\pi R} + \frac{n\nabla p_j}{2\pi Z_j n_j RB_\theta}, \tag{5.49}$$

where the radial electric field (E_r) is calculated using the C_5^+ species [100]. This is the frequency of the mode for rigid rotation with the plasma fluid (i.e. $\omega = 0$).

NCLASS code [43] is used to determine E_r for shots on MAST. This code is constrained by measurements of the C_5^+ temperature, density and rotation velocity which were determined from CXRS measurements. It was found that the toroidal rotation ($v_{\phi j}$) is the principal contributing term to the E_r on MAST (figure 5.11). In contrast, the poloidal rotation ($v_{\theta j}$) is shown to be negligible on this machine [30] and can thus be neglected. The contribution of the diamagnetic term is also small in most cases (figure 5.11).Similar results for the contribution of the toroidal,poloidal and diamagnetic term to the E_r has been found on NSTX [101].

When islands are large ($w > w_d$), f_{mirnov} is observed to approach $f_{E_r=0}$ in MAST data (figure 5.12) and this indicates that the ion polarisation term tends towards zero in these conditions. When the island size is smaller ($w \sim\leq w_d$), for the discharges considered here,it is found to rotate in the electron diamagnetic direction. Island rotation in this direction is predicted to result in a stabilising contribution from the ion polarisation term [102]. The rotation direction results for MAST agrees with those from Asdex [103], Textor[104] and NSTX [101]. However, results from DIII-D [100] and TCV [105] have shown NTM rotation in the ion diamagnetic direction on these machines.

Having determined ω from the above measurements and having calculated ϵ, the size of $g(\epsilon, \nu_{ii}, \omega)$ was calculated using a drift kinetic model [102] and given by $G(\nu_{ii}, \omega)$ where $G(\nu_{ii}, \omega) = a_3 g(\epsilon, \nu_{ii}, \omega)$. NTMs studied on MAST are typically in a collisional regime ($log(\nu_{ii}/\omega) < -4$) and also have a normalised ion rotation frequency ($\widetilde{\omega}$), given by a ($\frac{\omega}{\omega_{ii}}$) value between -0.4 and -0.2 when the island size is in the vicinity of a banana island width. Using these values, the drift kinetic model [102] estimates the size of $G(\nu_{ii}, \omega)$ to be $\sim$ 0.05-0.1 for 2,1 studies on MAST (figure 5.13). Using the estimate for $G(\nu_{ii}, \omega)$, the size of the Δ'_{pol} parameter was then calculated using equation 5.36. The contribution of the ion polarisation term to the MRE for 2,1 NTMs on MAST is discussed in section

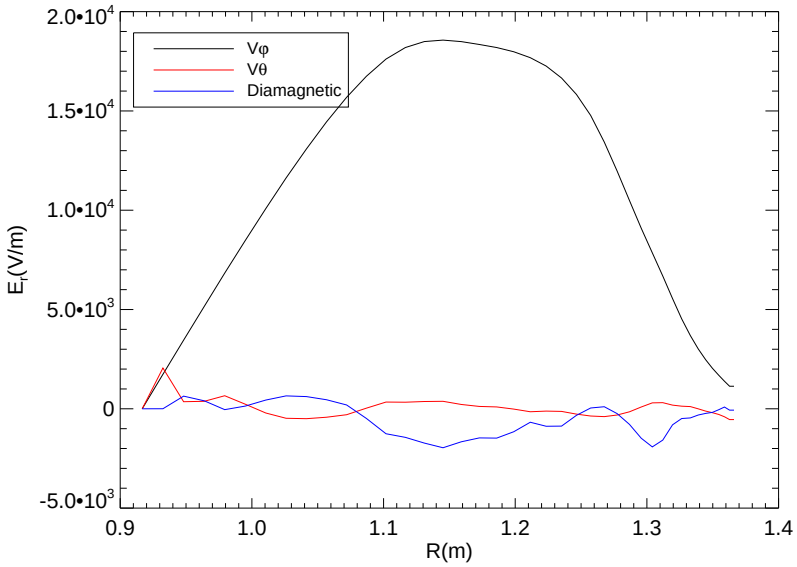

Figure 5.11: The radial electric field (E_r) calculated from the CXRS measurements. This shows the contribution of $v_{\phi j}$ (black), $v_{\theta j}$ (red) and the diamagnetic term (blue) to E_r for an example shot on MAST.

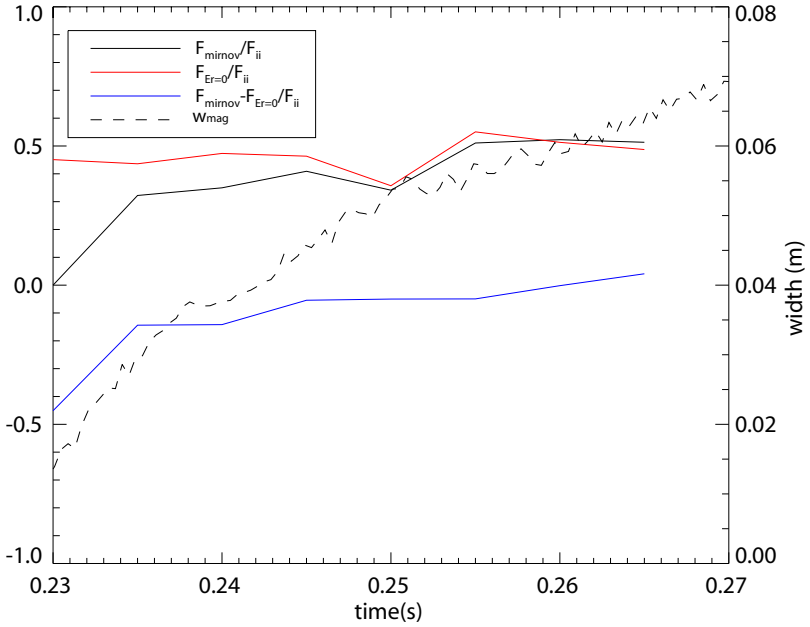

Figure 5.12: The evolution of the island rotation frequency at the onset of a 2,1 NTM for shot 25224 on MAST. The NTM rotates in the electron diamagnetic direction at onset. As the pressure gradient flattens, F_{mirnov} (black line) approaches $F_{Er=0}$ (red line) and the island rotation frequency (ω, blue line) initially rotates in the negative (electron diamagnetic) direction, but $\rightarrow 0$ with increasing island size. All frequency terms shown are normalised by the ion diamagnetic frequency ($F_{ii} \equiv \omega_{ii}/2\pi$). The width at which the $F_{Er=0}$ terms goes to zero is postulated to be the finite island width.

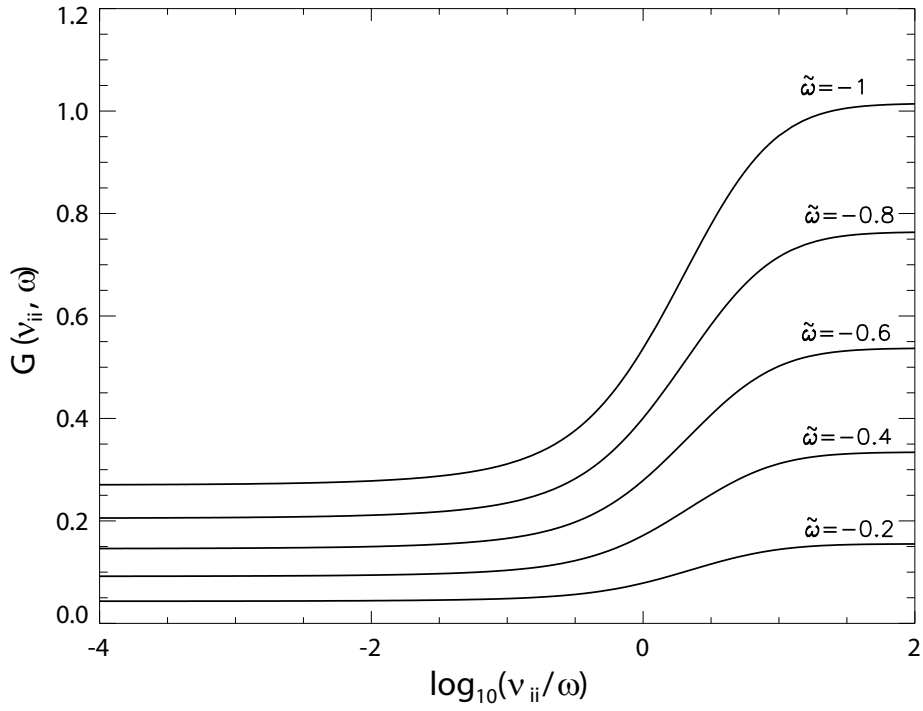

Figure 5.13: The size of the $G(\nu_{ii}, \omega)$ as a function of ion collisionality (ν_{ii}),ω, at a fixed ϵ based on drift kinetic modelling. For a fixed ϵ, $g(\epsilon, \nu_{ii}, \omega)$ is given by $G(\nu_{ii}, \omega)$. The value of $G(\nu_{ii}, \omega)$ is shown to be lower for smaller values of $\widetilde{\omega}$ and increase with ν_{ii}/ω.

5.6.

There is still a high level of uncertainty about which physics mechanisms determine the rotation frequency of MHD instabilities [106]. In the case of 2,1 NTMs on MAST, the evolution of the island frequency may be dependent on the electron diamagnetic frequency (ω_e). At the onset of an NTM ω typically starts from a frequency in the ω_e direction, but as the island grows it tends towards zero. ω_e is related to the evolution of the electron pressure gradient, which is described by the Fitzpatrick transport model (see section 5.4). To investigate this relationship further, the mean flattening of a normalised pressure gradient was calculated using the Fitzpatrick model. The results show that the pressure gradient tends towards zero as w_d is approached (figure 5.14) and this suggests that if ω is dependent on ω_e, then $\omega \rightarrow 0$ when $w \rightarrow w_d$.

The time at which $\omega \rightarrow 0$ has been calculated from CXRS measurements. In addition, the evolution of the magnetic island width from magnetic measurements was interpolated at this time, in order to calculate the width at which $\omega \rightarrow 0$, which is given by $w_{d,mag}$. This width was compared to the w_d determined by TS ($w_{d,ts}$) and, as shown in figure 5.15, a good agreement is found between $w_{d,mag}$ and $w_{d,ts}$ for a number of shots. This agreement indicates that ω is dependent on ω_e. If ω is dependent on ω_e the size of the w_d can influence the ω which will in turn effect the size of the ion polarisation contribution to the island stability, coupling the effect of these stability terms.

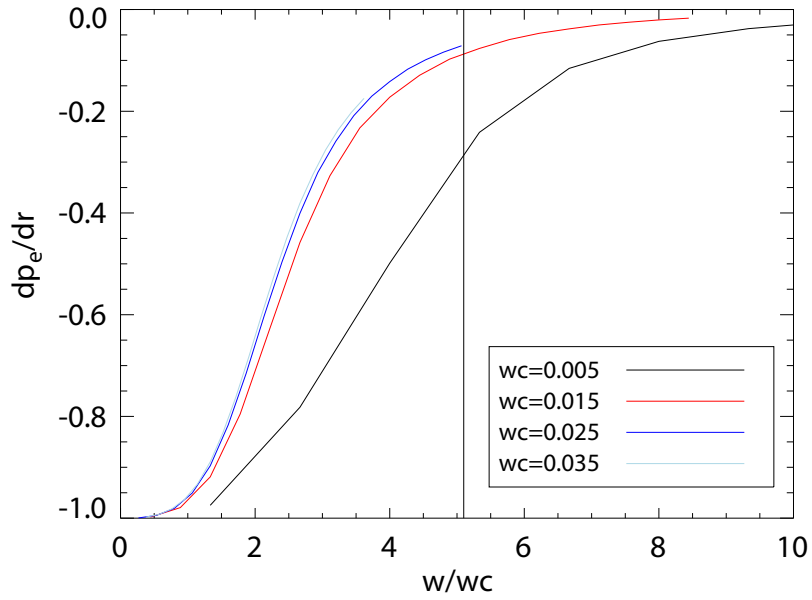

Figure 5.14: The change in the average normalised electron pressure gradient (dp_e/dr), determined using the Fitzpatrick model for heat transport, as a function of w/w_c. Each curve shows a different value for w_c and the position of w_d is indicated by a vertical black line. For most values of w_c, dp_e/dr tends towards zero when w/w_c is approximately equal to 5.1 or $w = w_d$, with an exception where w_c is very small.

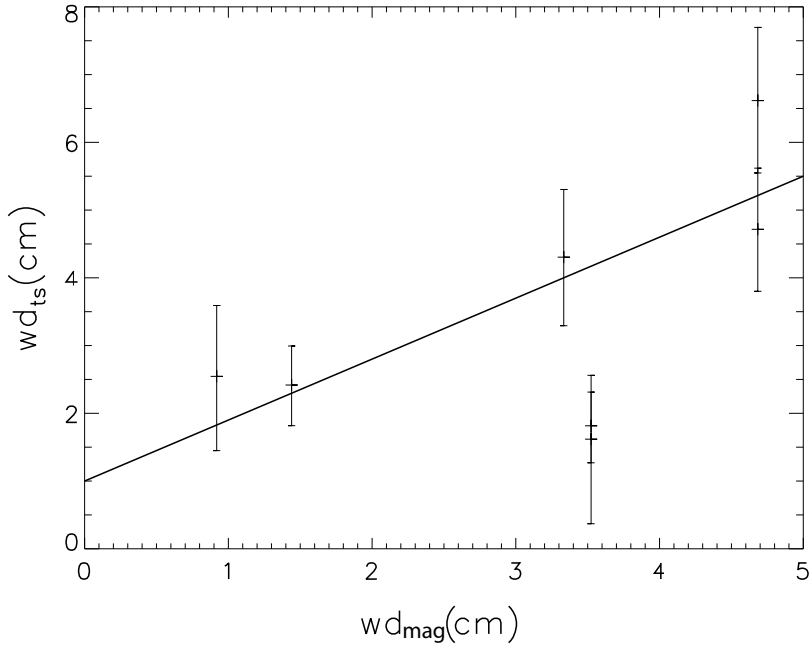

Figure 5.15: Comparison of the width at which the island frequency equals the CXRS rotation frequency of the q=2 surface to the w_d measured by TS. If the width that the island rotation frequency equals that of the w_d then the rotation in the ω_e direction may have resulted from the electron pressure gradient and disappears when the pressure gradient is flattened at w_d.

5.6 Beta scan experiments to determine the marginal island width

In this section beta scan experiments on MAST, which investigate the MRE and the relative importance of the different MRE stability terms, are described.

5.6.1 Beta scans

Changing beta poloidal (β_p) provides a method of influencing the evolution of an NTM, as the growth rate (rate of change of the island width) of an island is given by:

$$\frac{dw}{dt} = \frac{r_s}{\tau_R}\left[r_s\Delta^{'} + r_s\beta_p\left(a_{bs}\left(\frac{f_{bsc}w}{w^2+w_d^2} + \frac{(1-f_{bsc})w}{w^2+w_b^2}\right) + \frac{a_{GGJ}}{\sqrt{w^2+0.2w_d^2}} + a_{pol}\frac{w}{w^4+w_{d,pol}^4}\right)\right], \tag{5.50}$$

where as,discussed previously a_{bs} is the bootstrap term, a_{GGJ} is the tokamak curvature term, a_{pol} is the ion polarisation term, w_d is the finite island width and $\Delta^{'}$ is the classical tearing stability term. This is an expansion of the MRE given by equation 5.29 in section 5.2.4, where each of these stability terms have been discussed fully.

In beta scan experiments, the beta poloidal (β_p) is reduced after an NTM is triggered and reaches its saturated island width. Once this occurs, there is a back transition of the plasma to L mode and the island width (w) immediately decreases until a point of marginal stability is reached, where the NTM shrinks away rapidly. On MAST β_p is dropped by turning off the NBI beams and, as it is not currently possible to trigger the NBI system on a specific plasma event, this time must be estimated from previous shots.

β_p measurements made during the beta scan are used in conjunction with estimates of the MRE stability terms, in order to reconstruct the evolution of the island width (w_{MRE}). This is carried out by taking an initial value of the island width from an initial magnetic measurement and then integrating equation 5.50 over the time of the beta scan. The estimates of the a_{bs}, a_{GGJ} and a_{pol} terms used for this reconstruction are taken before the onset of the NTM. a_{bs} and a_{GGJ} are calculated using CHEASE code, which uses an EFIT equilibrium that is constrained with TS and CXRS measurements (see section 5.2.4), while a_{pol} is calculated using CXRS measurements (see section 5.5). w_d is calculated from TS measurements (see section 5.4) taken at a time close to the saturated island width (w_{sat}) and finally, $\Delta^{'}$ is estimated from $(a_{bs} - a_{GGJ})/w_{sat}$. As discussed in section 5.4 TS measurements at large island widths ($\sim w_{sat}$) can be used to infer w_d.

A comparison of w_{MRE} to the evolution of the island width measured by magnetics (w_{mag}) can provide information about both the validity of the stability terms used in the MRE and their influence on island stability. Magnetic measurements of w are performed continuously during the

island evolution in order to determine w_{mag}. A least squared fit is performed between w_{mag} and w_{MRE}, allowing the MRE terms to vary as free parameters, with the predicted stability terms taken as the initial guess. The w_{MRE} are assumed to remain constant over the island evolution.

Stability term	**24082 (predicted)**	**24082**	**24082 ($a_{pol} = 0$)**	**24622 (predicted)**	**24622**	**24622 ($a_{pol} = 0$)**
a_{bs}	4.32	4.70	4.18	4.30	4.27	4.09
a_{GGJ}	-3.11	-2.38	-2.00	-2.95	-3.00	-3.00
Δ	-3.00	-3.42	-3.00	-3.00	-2.70	-2.45
$\tau_R(ms)$	340	340	340	340	340	340
w_d	1.9 (TS fit)	2.5	2.8	4.8 (TS fit)	2.6	3.5
a_{pol}	-0.0002	-0.0002	0.000	-0.0002	-0.0015	0.000

Table 5.1: Comparison of the predicted and fitted MRE stability terms, with and without the a_{pol} term included, for shots 24082 and 24622. The a_{bs} and a_{GGJ} predicted terms are determined using the CHEASE code and the w_d predicted term is determined by fitting the heat transport model to the $T_e$data. The $\tau_R(ms)$, Δ and a_{pol} predicted terms are determined as discussed in section 5.6. It is only possible to calculate the error in the w_d term as the other predicted terms are dependent on the equilibrium parameters for which no error bars are currently estimated. The number of significant parameters in the fitted terms can be estimated from the sensitivity of the fitting procedure.

Beta scans were carried out for two MAST shots, shots 24082 and 24622, using this approach and the results are discussed below. Both shots are of 2,1 NTMs and are hybrid scenarios, both with a weakly reversed q profile and a central $q > 1$. The global β_p at the NTM onset is also quite high (about 0.7) for each shot. The NBI heating differs between these shots. In both shots the south west NBI (1 MW) turns on at 70 ms. However, in shot 24082 the south NBI (1.5 MW) switches on at 90 ms, whilst in shot 24622 it turns on at 135 ms. Despite this difference, the T_e , n_e and T_i profiles between these shots match well until 200 ms, when a steep gradient in the electron temperature typical of an electron internal transport barrier (ITB) becomes visible on the T_e profiles of shot 24622. This ITB may explain the difference in the initial growth rates of the NTMs in shots 24082 and 24082.

5.6.1.1 Beta scan and MRE fit for shot 24082

In shot 24082, a 2,1 NTM begins to grow at approximately 0.21 seconds and it evolves from a small island to a saturated island over $\sim$ 20 ms. The TS measurements of the w and w_d parameters for this shot were taken at 255 ms. The NBI beams were switched off at 0.225 s.

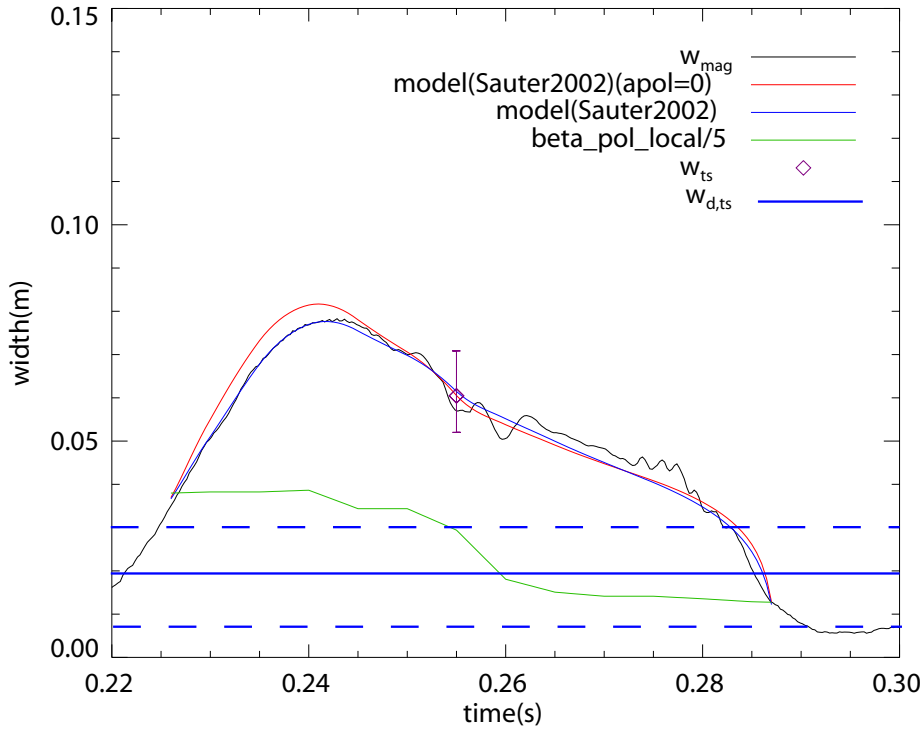

Figure 5.16: A comparison of the predicted and measured evolution of a 2,1 NTM in shot 24082. The w_{mag} determined from the magnetics is shown in black. w_{MRE} with (red), and without (blue), the a_{pol} term included are compared to w_{mag}. The TS measurements of w (w_{ts}) are in good agreement with w_{mag} for the same time point. The prediction of the w_d term from TS is placed at 0.28 s, so that it can be compared to the marginal island width where the NTM begins to decay rapidly.

The measurements and calculations of the different stability terms for this shot were used to form the MRE. The island width determined using the MRE (w_{MRE}) was then fitted to the island width measured using magnetics (w_{mag}), as described in section 5.6, and a good agreement is found (figure 5.16). In addition, a good agreement is found between the TS measurement of the island width and the w_{mag} measured at that time, which indicates that the magnetic measurements are reliable.

The different stability terms for the MRE of this shot are each now considered, both in terms of their contribution to the stability of this NTM and how well the predicted and fitted terms agree. Table 5.1 provides a reference of the predicted and fitted values.

The a_{pol} term for this shot is not found to influence the NTM stability. When this term is included in the fitting, the best solution obtained for w_{MRE} shows a greater deviation from w_{mag} than if this term is neglected (figure 5.16). Furthermore, the inclusion of a_{pol} in the MRE fit significantly reduces the agreement between the other stability terms and their predicted values (table 5.1).

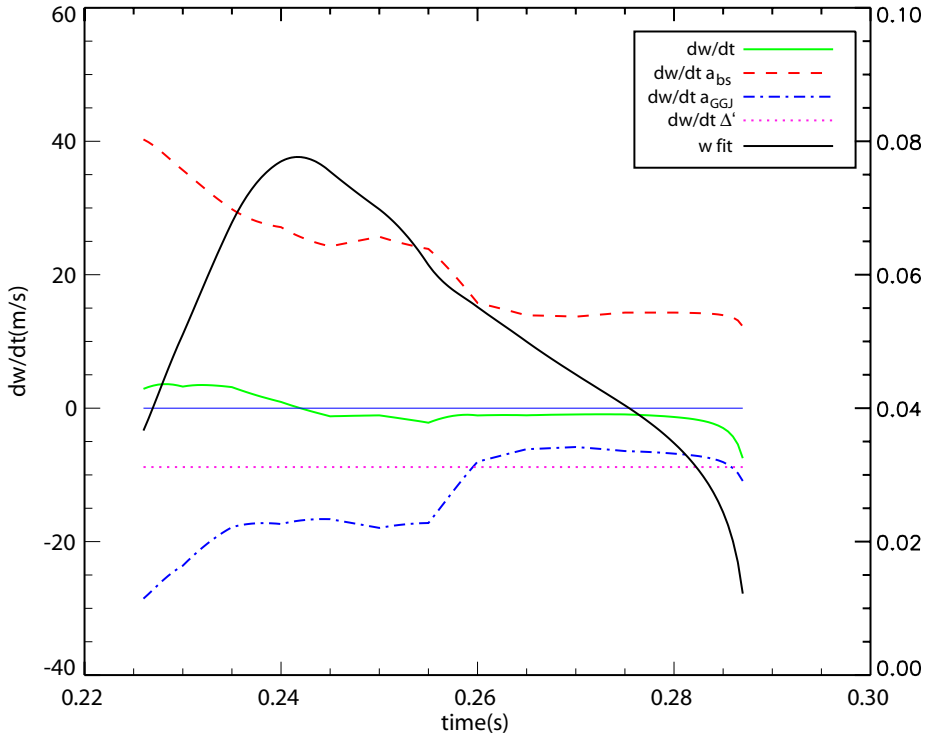

Figure 5.17: Contribution of the fitted stability terms to the total island growth rate predicted by MRE (dw/dt) for shot 24082. The growth rates for each fitted stability term, neglecting the a_{pol} term, are shown. The fit of island evolution w_{MRE} is shown with the y axis for w on the left hand side.

The a_{bs} term is found to be the only destabilising term and its strength is found to be significant in this shot. The contribution of the fitted Δ'_{bs} to the total growth rate, as a function of w, is shown in figure 5.17. A good agreement is found between the predicted (4.32) and fitted (4.18) values of a_{bs}. The size of the w_d term determines the size of both the bootstrap and curvature terms at small island widths. The predicted value (1.9) is found to be less than the fitted value (2.8) of w_d. A greater value of w_d reduces the size of the bootstrap current and increases the size of the curvature term at small island size increasing the onset threshold for an NTM.

The a_{GGJ} term is particularly important for MAST plasmas, as they have a small aspect ratio. This term is found to be the principle stabilising term at the onset of the NTM (figure 5.17). The stability of the NTMs is found to be dependent on the delicate balance between principally the bootstrap and curvature terms. The fitted value (-2.00) of a_{GGJ} is found to be significantly less than the predicted value (-3.11) in this shot. The $\Delta^{'}$ parameter is found to be stabilising and a good agreement is seen between its predicted and fitted values (table 5.1). After the H-L mode transition, $\Delta^{'}$ becomes the principal stabilising parameter (figure 5.17).

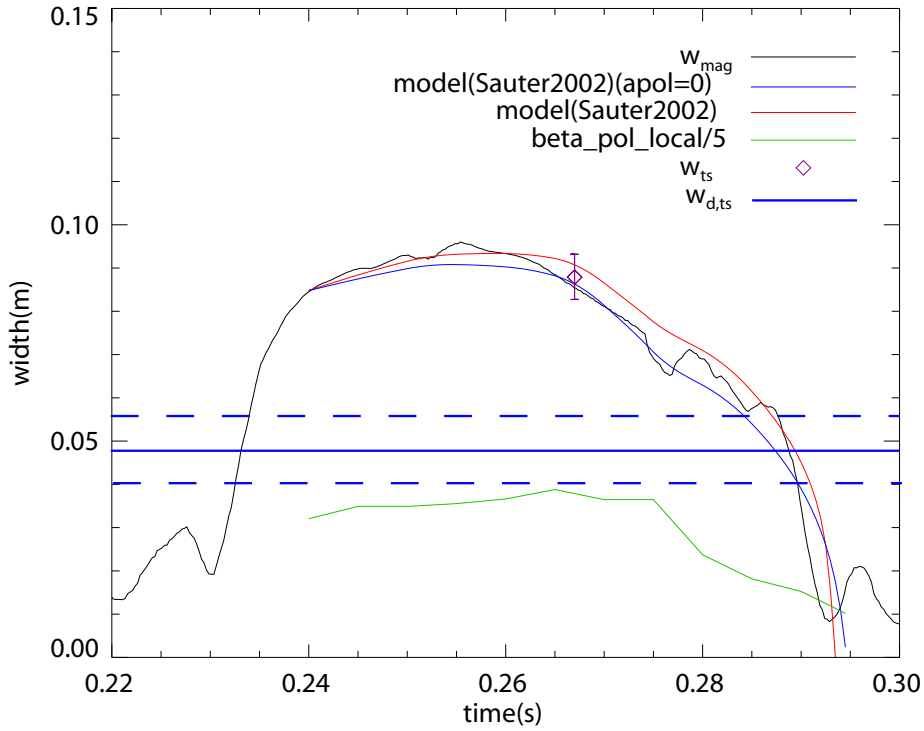

Figure 5.18: A comparison of the predicted and measured evolution of a 2,1 NTM in shot 24622. The w_{mag} determined from the magnetics is shown in black. w_{MRE} with (red), and without (blue), the a_{pol} term included are compared to w_{mag}. The TS measurements of w (w_{ts}) are in good agreement with w_{mag} for the same time point. The prediction of the w_d term from TS is placed at 0.28 s, so that it can be compared to the marginal island width where the NTM begins to decay rapidly.

5.6.1.2 Beta scan and MRE fit for shot 24622

For shot 24622, the TS measurement of the w_d parameter was taken at 265 ms and the NBI beams were switched off at 0.27 s. During the onset of this shot, a low frequency mode is observed in the magnetic spectrogram at 0.21 s and its size and frequency do not increase greatly until 0.23 s, at which time rapid growth is observed; which is in contrast to the more constant growth rate seen in shot 24082. The early growth rate of this NTM cannot be reproduced using the MRE equation without some further modelling of the $\Delta^{'}$ parameter and, for this reason, the MRE is only fitted after 0.24 s, where the mode is close to its saturated size and Δ' should return to $\sim -2m$. There is again a good agreement between w_{mag} and w_{MRE} for this shot. It is not possible to ascertain whether the a_{pol} influences the NTM stability in this shot, as the best solution for w_{MRE} is obtained whether or not the a_{pol} term is included in the fit to w_{mag} (figure 5.18). However, the inclusion of this term reduces the agreement between the predicted and fitted values of the other stability terms (table 5.1).

As in shot 24082, the strength of the bootstrap term is found to be significant and is again the

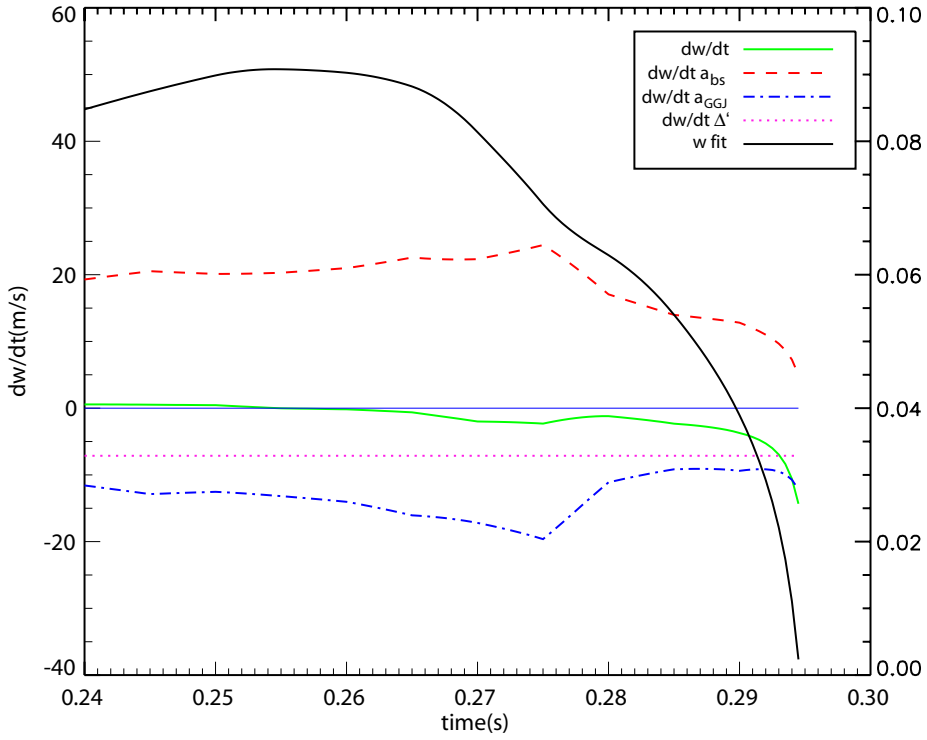

Figure 5.19: Contribution of the fitted stability terms to the total island growth rate predicted by MRE (dw/dt) for shot 24622. The growth rates for each fitted stability term, neglecting the a_{pol} term, are shown. The fit of island evolution w_{MRE} is shown with the y axis for w on the left hand side.

principal destabilising term. The size of a_{bs} is also of a similar size to that in the previous shot. The contribution of the fitted Δ'_{bs} to the total growth rate is shown in figure 5.19. A good agreement is found between the predicted (4.30) and fitted (4.27) a_{bs} terms, which is slightly better than that in shot 24082 (table 5.1). The predicted w_d (4.8) is found to be larger than the fitted term (3.5) in shot 24622, with both values larger than those in shot 24082.

In this shot a much better agreement is found between the predicted (-2.95) and fitted (-3.00) a_{GGJ} terms than in shot 24082, although the value of the predicted term is similar in this previous shot. The contribution of the fitted Δ'_{GGJ} to the total growth rate is shown in figure 5.19 and once again, a delicate balance is seen between the stabilising contribution of Δ'_{GGJ} and the destabilising contribution of Δ'_{bs}.

5.6.2 Contribution of the MRE terms

In both shots a relatively good agreement is found between w_{MRE} and w_{mag} and this indicates that the terms used in the MRE describe the island stability accurately. These shots also show similar values for the predicted a_{bs} and a_{GGJ} terms and show good agreement between the predicted and fitted a_{bs} terms. The a_{bs} and a_{GGJ} terms are found to dominate during the early island evolution

(see figures 5.19 and 5.17).

The a_{GGJ} term is found to be the principal stabilising term during island onset. Although is has a significant effect on the island stability, this is lower that the predicted values. In shot 24082, the MRE fitting produces an a_{GGJ} term that is 40% reduced from its predicted term, in order to allow the NTM to be destabilised, whereas a better agreement between these terms is seen for shot 24622. However, this is likely because the early evolution of the NTM is neglected in this latter shot and the influence of a_{GGJ} is typically less during the beta scan phase. a_{GGJ} is found to be comparable in size to a_{bs}, as has been predicted theoretically [87], an increase in a_{GGJ} can be used to stabilise the bootstrap drive and prevent 2,1 NTMs from occurring. Further scenario development on MAST could therefore investigate this use of a_{GGJ} to prevent NTMs in STs.

A relativity good agreement is found between the measured and predicted values of the w_d parameter in each shot. As discussed in section 5.4, w_d is dependent upon a number of equilibrium parameters and the ratio of the perpendicular and parallel thermal diffusivities. Estimates from EFIT predict a $\sim 10\%$ decrease in w_d size between NTM onset and stabilisation. The thermal diffusivities are difficult to measure. However, an estimate of the w_d dependence on these terms has been calculated using equations 5.46 and 5.45 (see section 5.4) with TS measurements from the island onset and from after the mode has stabilised. This estimate shows an increase of $\sim 10\%$ in w_d between these times. It appears that the influence of the equilibrium change and the diffusivities on w_d may cancel each other out, making w_d stable over the island evolution. This means that it is valid to compare the TS measurement of w_d to the value predicted by MRE fitting. Finally, the predicted island widths for estimates of $\chi_\perp$ and $\chi_\parallel$ tend to overestimate both the TS measurements and the allowable values determined from MRE fitting. A large degree of uncertainity also exists for these quantities and therefore more measurements and modelling are required to improve the accuracy of w_d estimates.

The a_{pol} term is not found to have a significant effect of the stability of these shots. This is likely a result of the high collisionality of these shots and because the island frequency (f_{is}) tends towards 0 when a_{pol} is predicted to be most stabilising. In shot 24082, the inclusion of the a_{pol} term is found to reduce the agreement between w_{mag} and w_{MRE}. Although this is not the case in shot 24622, the inclusion of this term reduces the agreement between the other predicted and fitted MRE terms for both shots. However, the results indicated that inclusion of a_{pol} at the marginal island width may permit the fast decay of w to be better modelled. More information is required on the island rotation frequency (ω) and banana width (w_b) terms of a_{pol}, to test for hysteresis in this term during beta scan experiments. It would be interesting to determine if any hysteresis occurs between the a_{pol} value at NTM onset and its value during marginal island width, as a number of beta scan results on other machines suggest that the NTM threshold is a result of the a_{pol} term.

However, no measurements of ω at the marginal island width have been made to confirm that its effect is similar to that at NTM onset.

The Δ' parameter is taken to be a constant value in these shots. This parameter is very sensitive to the current density profile and the early onset of both shots is likely to be related to a pole in Δ', as both shots approach ideal stability.As the plasma approaches the ideal stability limit, the value of the Δ' parameter increases rapidly to positive values, making classical tearing modes unstable at the q=2 surface. This pole has been predicted theoretically in these conditions [107] and has also been modelled numerically in DIII-D shots [108, 109]. However, more work is required to understand the early influence of Δ' on the onset of NTMs. Preliminary investigations of this onset mechanism are being carried out using T7 and PEST3 codes [107] to calculate the pole in the Δ' parameter.

Although fitting the MRE equation to w_{mag}, provides useful information about the relative influence of each stability term, this method has a number of limitations which must be considered. Firstly, the MRE assumes NTM stabilisation conditions are similar to those at NTM onset, which may not always be the case. Hysteresis may exist between the onset of the NTM and the stabilisation that occurs during a beta scan and therefore the inability to obtain all predicted parameters at both times may lead to errors in the MRE fit. Secondly, the island evolution is a result of the sum of the different terms in the MRE and therefore a large correlation exists between these terms and influences how the MRE is fitted to w_{mag}. For instance, an increased growth rate of the overall NTM evolution can be explained by either an increase in a stabilising contribution or a decrease in a destabilising term. Despite these limitations, fitting the MRE to w_{mag} provides one of the most effective methods to investigate NTM evolution.

The current methodology also has a number of limitations, which can be mitigated. Firstly, the predicted stability terms each have dependencies on a number of equilibrium parameters and their gradients, but no error calculations on these parameters are possible using EFIT. As a result, no error bars can be associated with the predicted quantities. To permit these error calculations, a Bayesian approach could be employed to include the relative dependencies of these parameters in the MRE model in a self-consistent way.

Secondly, switching off the NBI beams results in a loss of momentum and thus both the plasma and NTM rotation slow down. As the NTM slows, it generates an eddy current in the MAST vessel that causes it to slow down even further and, as the NTM toroidal velocity tends to zero, a locked mode results. Only two successful beta scans of 2,1 NTMs were performed during the last MAST campaign as a consequence of these locked modes occurring, despite a large number of beta scan experiments performed. Switching off both beams also prevents ion velocities and temperatures from the CXRS system, and pitch angle constraints from the MSE system, to be measured during

a beta scan and this represents a loss of potentially useful data. However, a new NTM triggering system has been developed which triggers beta scans without switching off the beams. This new triggering system permits both the TS lasers to be triggered and β_p to be dropped on a particular NTM amplitude (as described in section 5.7). As a result, more reliable beta scan experiments can be performed and the effect of the a_{pol} contribution can be measured. In addition, this triggering system permits more measurements of w_d to be made over the total NTM evolution.

3,2 and 4,3 NTMs are also observed on MAST. Although these are relativity infrequent and have smaller w values compared to 2,1 NTMs, measurements of these modes could provide more information about the w_d and a_{pol} terms for NTMs. In general as the lower collisionality of the plasma at the location of these NTMs is predicted to increase the influence of these terms. Both carrying out more beta scan experiments on MAST, and extending the types of NTMs studied, will therefore further our understanding of the different stability parameters in NTM evolution.

5.7 Triggering of TS lasers on the NTM phase

This section describes an FPGA triggering system [80] that has been developed to permit real-time triggering of the MAST TS lasers on particular NTM amplitudes and phases. The previous approach relied upon pre-programmed TS times based on the evolution of NTMs in previous shot results and this limited the number of successful measurements. As this new system triggers the TS lasers in real-time, it will permit more measurements of w_d to be made and provide more data for investigations of heat transport around NTMs. In addition, this system has has recently been upgraded to trigger shifts in the Z position of the MAST plasma. Z shifts have been found to drop the β_p at the $q = 2$ surface and can be exploited to improve beta scan experiments on MAST. They may also allow the triggering system to be used as a means of avoiding locked modes on MAST plasmas.

5.7.1 Design and testing of new triggering unit on MAST

The helical motion of an NTM around the torus results in an oscillatory magnetic signal which can be measured by Mirnov coils at the edge of the plasma. The FPGA triggering system in the MAST area receives signals from these coils, where the raw data is first passed through a bandpass finite impulse response (FIR) filter. These filters remove frequency components below 5 kHz and also above 15 kHz, as the NTM frequency is typically between these two values. The signal from each coil is multiplied by a complex number ($e^{ni\theta}$) that is dependent on the phase (θ) difference between the Mirnov coils for a given toroidal mode number (n). In the case of an $n = 1$ NTM, where 4 coils are at toroidal angles of $0°$, $90°$, $180°$ and $270°$, the multiplication factors ($e^{ni\theta}$) are 1, -1, i, -i

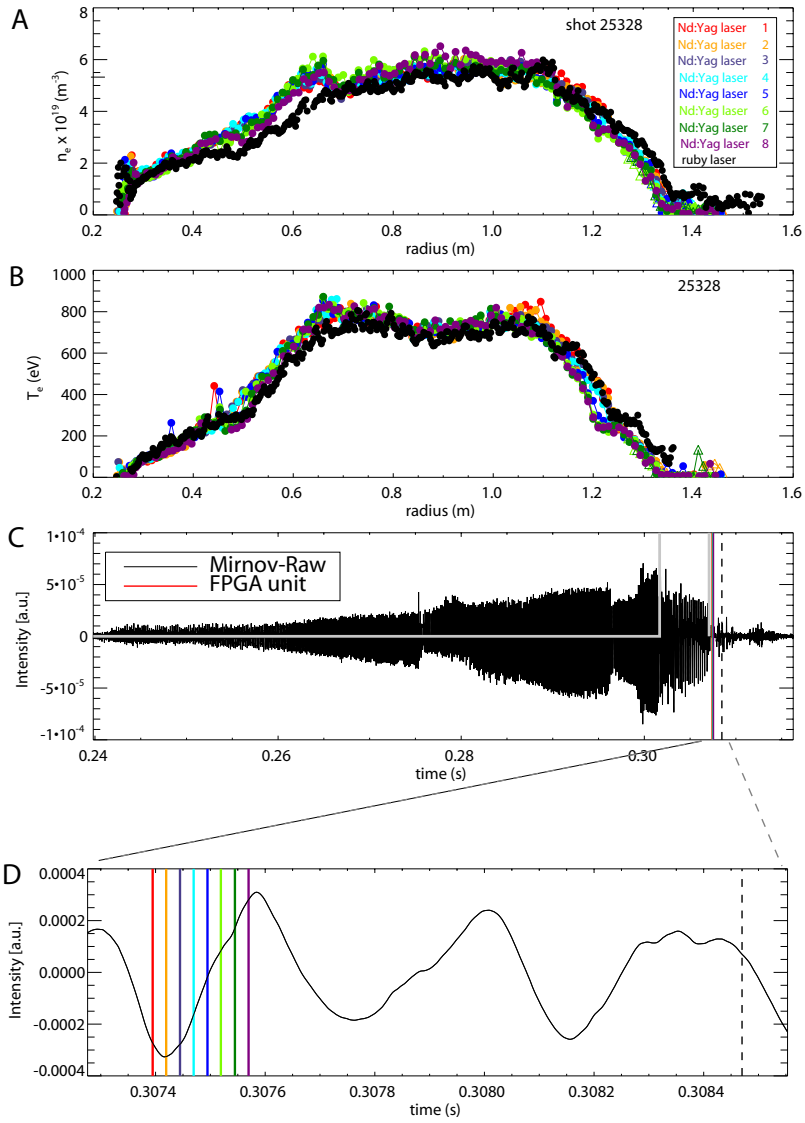

Figure 5.20: Example shot illustrating TS triggering. A. The n_e profiles from the different ruby and Nd:YAG lasers. B. The T_e profiles from both TS system lasers. The flattening of these T_e profiles at 0.5 and 1.25 metres is a result of a 2,1 NTM. C. The $n = 1$ signal from the Mirnov coils as a function of time. The ruby (black dotted line) and Nd:YAG lasers (vertical lines, zoomed-in version given in D.) are fired at ~ 0.31 seconds. A diagnostic trace (light grey line) is output from the FPGA triggering unit to indicate when the system is armed (rising edge) and fired (falling edge). D. The colours of the vertical lines represent the times a which the different lasers are fired in order to obtain the n_e and T_e profiles in A. and B. respectively.

. A Hilbert FIR filter is used to determine the imaginary component, which is 90° out of phase with the filtered data. Multiplication by a complex number is performed in the hardware by swapping the real and imaginary components.The real and imaginary components of each coil signal can be mapped from Cartesian to polar coordinates in order to determine the amplitude and phase of the oscillating signal. A CORDIC algorithm performs this transform and provides an efficient method

for calculating the phase and amplitude evolution in real-time.

When the amplitude and phase of an NTM match a user-defined input criteria, the FPGA unit sends triggering events to a SMART trigger unit, which in turn can trigger the ruby or Nd:YAG TS lasers, as fully described in Appendix B. Currently this system enables trigger events on the decay phase of an NTM, so as to catch a magnetic island before it reaches marginal stability. The system is armed on an upper trigger point and fired when a second, lower, trigger point is reached. To ensure the Nd:YAG lasers are available to fire when triggers are received from the FPGA triggering unit, the laser sequence is interrupted at a fixed time in anticipation of an NTM.

There is a delay between changes detected on the Mirnov coils due to an NTM and the firing of the TS lasers. This is predominantly due to a delay between the SMART triggering unit receiving a trigger pulse and the TS lasers firing ($\sim 300\ \mu$s). The FIR filters introduce a smaller delay ($\sim 90\mu$s), which changes linearly with the NTM frequency and can be calculated using a look-up table. This frequency must be determined to permit the system to extrapolate what the phase of the NTM will be when the lasers are fired and ensure it matches the user-defined trigger phase.

The firmware necessary for FPGA triggering unit was developed using the Mathworks Simulink system generator toolbox [110]. The unit was extensively tested with experimental data prior to being initially commissioned on MAST in the M7 campaign. Example ruby and Nd:YAG triggering TS data from this campaign is shown in figure 5.20. This shows T_e and n_e profiles triggered on an NTM and shows the triggering system can operate as designed. However, the system was found to suffer from a number of reliability issues and was therefore further developed and tested after the campaign finished (see Appendix B). No further NTM experiments have performed in the current MAST campaign, but the tests carried out indicate that the triggering unit performance reliability has been significantly improved (Appendix B).

5.7.2 Z shifts

As discussed in section 5.6, one of the major challenges for successful beta scans is to reduce β_p whilst avoiding the NTM locking to the vessel wall. The current approach which turns off the NBI beams in order to drop β_p carries a high risk of mode locking. A Z shift method has been developed and is an attractive way to adjust β_p on MAST shots, as it is relatively easy to implement and, importantly, avoids the mode locking that can occur when NBI beams are switched off to drop β_p.

The pedestal performance on MAST is related to the dr_{sep} parameter [111], which represents the degree of separatrix separation. dr_{sep} can be altered by making fine adjustments (~ 1 cm) to the plasma Z position using the MAST P6 coils. The effect of these small adjustments of vertical position is to reduce the height of the edge transport barrier, which reduces the local β_p for a large

region inside the pedestal. These shifts have been used as a means of investigating the L-H mode transition. During a number of shots 2,1 NTMs have been stabilised after a back transition to L mode caused by a small vertical shift. These results confirm that β_p at the q=2 surface can be reduced by this method (figure 5.21). Based on this evidence, the FPGA triggering unit (described in section 5.7.1) was upgraded to trigger Z shifts to occur on specific NTM amplitudes, which will cause β_p to drop once a user-defined island width has been reached.

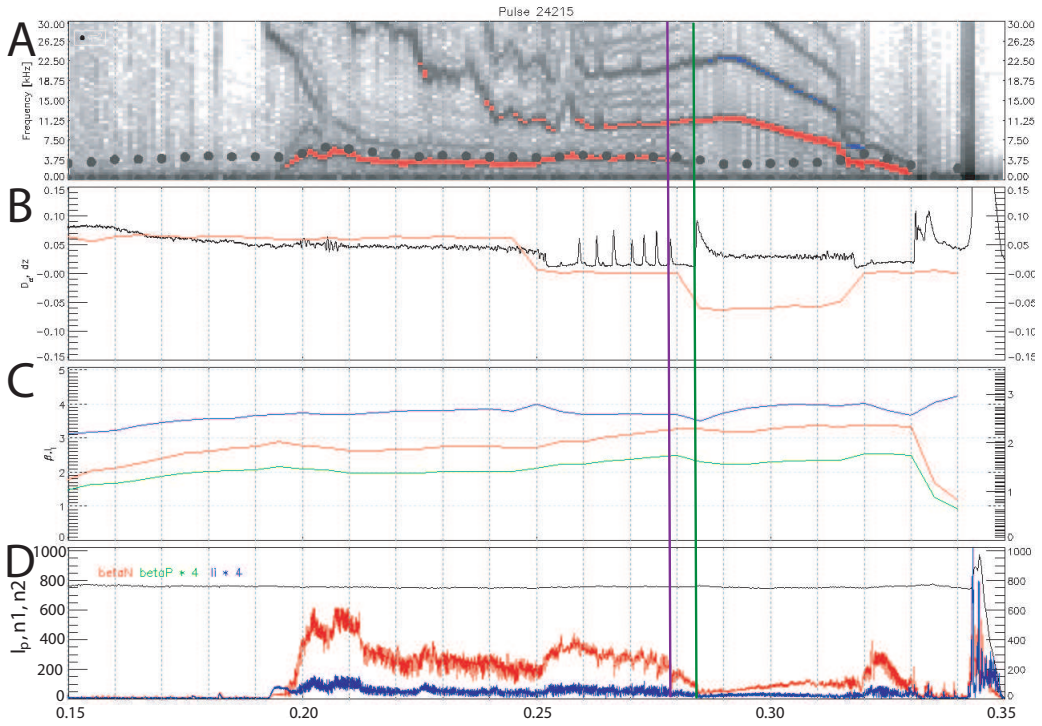

Figure 5.21: Stabilisation of a 2,1 NTM after a Z shift is shown. A. magnetic spectrogram with the $n = 1$ signal (red line), frequency where $q = 2$ is overplotted (black dots). B. The D_α signal (black) and Z position of MAST plasma. The first shift of the plasma axis from 5 to 0 cm occurs at 0.245 s and this results in a transition into H mode, as visible from the D_α signal. At 0.28 s, a Z shift from 0 to - 5 cm occurs. This results in back transition to L mode and a drop in global β_p, causing the 2,1 NTM to disappear (green trace in C). C. The green signal is the global β_p, the red signal is β_n and the blue signal is the internal inductance, li. D. The amplitude of the $n = 1$ signal (red), which shows the 2,1 NTM disappearing after the Z shift. Purple vertical line shows the start of the Z shift and the green line the end.

This system has been shown to function, but in the 2011 MAST campaign there have been no high β_p NTM shots, which has precluded further testing. However, a number of beta scan experiments exploiting this system are planned once high β operation begins.

An alternative use for the FPGA triggering system is to use Z shifts to avoid locked mode disruptions by removing NTMs as soon as they appear. This is potentially a useful method, as it avoids the need for the massive gas injections typically used to mitigate locked mode disrup-

tions by preventing this type of disruption from developing. A series of dedicated experiments are planned to investigate the use of this approach for disruption prevention on MAST and this may have implications for future machines.

5.8 Conclusions

In this chapter, we have obtained novel estimates of the principal stability terms of the MRE for MAST 2,1 NTMs. This data was then used to calculate the MRE and compare it to magnetic measurements of the island evolution (w_{mag}) for two MAST shots during a beta scan. TS measurements of w were compared to equivalent magnetic measurements of w and these were found to agree well.

A number of approaches were used to obtain the stability term predictions from the MAST data. For the a_{GGJ} and a_{bs} terms, CHEASE calculations, based on EFIT equilibrium data, were used. These data were constrained by the n_e, T_e and T_i profiles, measured using TS and CXRS.

TS T_e measurements were used to determine the w_d term. This is the first time w_d has been directly measured on MAST and is now possible because the upgraded TS systems on this machine have improved radial resolution. Specifically, w_d was calculated by fitting a heat transport model to the T_e data. This measurement of w_d also provided a benchmark against which to compare predicted values of this term using simple approximations for $\chi_\perp$ and $\chi_\parallel$. This comparison revealed that the measured w_d is slightly lower than the approximated value, which requires further investigation through more w_d measurements.

The a_{pol} term is dependent on the island rotation frequency in the plasma rest frame (ω). ω is determined using NCLASS and found to rotate in the electron diamagnetic direction when $w \sim< w_d$. If $w > w_d$ then the island rotation frequency is found to tend to zero, resulting in the ion polarisation term moving to zero. The ion polarisation term has been calculated using ω and results from a gyrokinetic code. The size of this term has been shown to be small in the $w \sim< w_d$ limit.

The results from the MRE fit during the beta scan experiments have shown a_{GGJ} to be the principal stabilising term for the 2,1 NTMs in the shots analysed and the magnitude of this term was found to be comparable to that of the principal destabilising term (a_{bs}). This suggests that the a_{GGJ} term may have a potential role in stabilising NTMs on STs and therefore further scenario developments to investigate this are indicated.

The size of w_d term influences both the size of a_{GGJ} and a_{bs} and is found to be the crucial parameter for the onset threshold of 2,1 NTMs on MAST. The comparison of the measured and MRE-fit w_d terms shows good agreement. Finally, the a_{pol} term was found not to have a influence on the island evolution, in agreement with the predictions above.

To permit further investigation of NTMs on MAST, by permitting a greater number of w_d measurements and more reliable beta scans, a triggering system has been designed and tested. This

has been fully described in this chapter and Appendix B and the system will be used during future MAST campaigns.

Chapter 6

Summary and Conclusions

The TS diagnostic systems on MAST have been upgraded and the new capabilities of these systems have been exploited to study 2,1 NTMs on MAST plasmas in greater detail than previously possible. Additional diagnostic measurements and codes have been used in this work and an improved TS triggering system developed. This is an important area to investigate as instabilities such as NTMs are one of a number of issues that need to be resolved in the development of commercial fusion reactors.

6.1 Summary of TS diagnostics improvements

The main types of TS system are TVTS, Nd:YAG TS and LIDAR and these TS systems measure the T_e and n_e profiles of a plasma. The main objectives for the ruby and Nd:YAG MAST TS system upgrades were improved spatial and temporal resolution and reduced T_e and n_e errors, in order that more accurate measurements of structures in the T_e and n_e can be made, including NTMs, ELMs, ITBs and the edge pedestal.

The upgraded Nd:YAG TS system now has a 1 cm spatial resolution and a 240 Hz temporal resolution. This was achieved by increasing the number of lasers to 8 and building 130 polychrometers to cover the minor radius of the MAST plasma. In addition, the lasers are now capable of firing in burst mode and this permits bursting over fast events, such as NTMs, to provide more detailed information about their evolution. Further to this upgrade, work was carried out to reduce systematic errors resulting from spectral calibration on the Nd:YAG system. This improved the accuracy of the T_e and n_e measurements further to the hardware upgrade improvements, providing a reduction in systematic errors. This upgraded TS system has been used to investigate NTM evolution, as described in chapter 5.

Concurrently, an upgrade to the ruby TS system on MAST was carried out and led to improvements in the resolution of T_e and n_e measurements. As all components of a TS system contribute

cumulatively to the overall resolution, the design of each components was optimised to permit the maximum resolution possible, within the constraints of available budget and current technological limitations. In this upgrade, improvements made to the optical design of the spectrometer and the fibre bundles had the greatest influence on increasing the overall spatial resolution, whereas the higher EQE of the image intensifier (GEN 3 GaAsP) contributed to the major proportion of the noise reduction achieved. The upgraded ruby TS system can now therefore resolve 200 points at high contrast along a 1.4 m chord, which is a greater number of points than any other TVTS system at present. In addition, the statistical noise has been reduced to $< 4\%$ of T_e , and $< 3\%$ for n_e , for a 7 mm radial point in the range of 40 eV - 2 keV and at a $n_e = 2 \times 10^{19}$ m^{-3} density, by increasing the scattered photon detection by a factor of ~ 3.

The sampling interval of the upgraded ruby TS detector system has also been improved. It is now possible to measure two images at a separation of 230 μs and this can be used in either double pulse mode (where two T_e and n_e profiles are measured) or single pulse mode (where one T_e and n_e profile and the background light are measured). Improved capabilities of the camera and image intensifier, in addition to a custom-designed triggering unit, have enabled these improvements in temporal resolution. The main advantage of this double pulse mode is that high resolution measurements of the T_e and n_e profiles can be made in quick succession, which is useful for the study of fast instabilities such as NTMs. An advantage of the single pulse mode is that a large proportion of spurious background noise can be subtracted from the TS measurements. This background noise can arise if impurities are present in the MAST vessel, which most frequently occurs during plasma startup studies and impurity injections to study the electric field.These impurities have emission lines within the spectral range of the ruby spectrometer and can make the background signal comparable to the TS signal. Initial tests of the double pulse mode function show it works as designed and the single pulse mode was used extensively during the last MAST campaign.

System calibrations, using a number of methods, and initial measurements carried out on the upgraded ruby TS system both show that the system is operating as designed. In addition, measurements from the upgraded ruby TS system have been compared to those from the Nd:YAG system and show good agreement in their T_e and n_e profiles. These results also indicate that both systems are correctly calibrated and both have low systematic errors. This upgraded ruby system is therefore now being used for studies of pellet injections, H-mode pedestals, transport and plasma start-up experiments, in addition to the NTM studies described in chapter 5.

In addition to the MAST TS system upgrades, ray tracing analysis of the optical design of the ITER LIDAR TS system has been carried out. Light cones of different angular spreads are incident on the bandpass filter in this system, depending on the radial location of the TS measurement. It was found that the angular distribution on the bandpass filters is a potential source of T_e and

n_e errors on this future system and that, during system design, choosing filter diameters greater than 260 mm would minimize these errors to an acceptable level. Finally, a method to improve TS measurements of the edge pedestal region on all TS systems was briefly discussed. The edge pedestal can be described by a modified hyperbolic tan function, which provides useful parameters for pedestal scaling. TS measurements are modified by smoothing between spatial channels in this pedestal region. An approximation is presented which corrects the T_e and n_e measurements, post-processing, for the effects of this smoothing. This model agrees well with simulations where the radial smoothing is included in the TS spectral fitting, when pedestal widths are greater than the TS sampling size.

6.2 Summary of NTM results

An investigation of the contribution of different MRE stability terms to 2,1 NTMs on MAST plasmas was also carried out using data from MAST shots. This was made possible by the improved resolutions of the upgraded TS systems, which enabled an important stability term (the finite island width, w_d) to be measured for the first time on MAST.

w_d was calculated by fitting a heat transport model to the T_e data from both upgraded Nd:YAG and ruby TS system measurements and a derivation of this model has been described in Appendix A. In addition to measurements of this term, novel estimates of the other principal stability terms of the MRE for 2,1 NTMs on MAST were made. CXRS was used in conjunction with the NCLASS code to determine the island rotation frequency in the plasma rest frame and from this a gyrokinetic code was used to estimate of the ion polarisation (a_{pol}) stability term. The curvature (a_{GGJ}) and bootstrap (a_{bs}) stability terms were calculated by using TS, CXRS and EFIT equilibrium measurements in the CHEASE code. This is the first time all these MRE stability terms have been calculated using experimental measurements for a particular MAST shot.

As overall NTM stability is dependent on the β_p parameter, beta scan experiments can be used to investigate NTM evolution. Beta scan experiments were carried out for a number of MAST shots, where the MRE stability terms were measured (as described above) and used to calculate the MRE. The island evolution described by this calculated MRE was then compared to magnetic measurements of island evolution and a good agreement was found. This indicates that the NTM evolution is well described by the MRE in the case of these shots. In order to confirm the accuracy of the magnetic measurements of island width were accurate, these were compared to TS measurements of island width and these were found to agree well.

In these beta scan experiments, the relative contributions of the different stability terms were investigated, by fitting the MRE-calculated island evolution to the magnetic measurements. From these results, a_{GGJ} term was found to be the principal stabilising term for the 2,1 NTMs in the

shots analysed and the magnitude of this term was found to be comparable to that of the principal destabilising term (a_{bs}). The size of fitted w_d term agrees well with the TS-measured w_d and is found to be a crucial parameter for determining the onset threshold of 2,1 NTMs on MAST. Finally, the a_{pol} term was found not to have an influence on the island evolution, which is in agreement with the predictions that this term is small in the $w \sim< w_d$ limit from CXRS measurements. These beta scan results therefore indicate that the a_{GGJ} term may have a potential role in stabilising NTMs on STs and therefore further scenario developments to investigate this are needed.

Finally, to permit further investigation of NTMs on MAST, by permitting a greater number of w_d measurements and more reliable beta scans, a triggering system has been designed and tested. This has been fully described in this chapter and Appendix B and the system will be used during future MAST campaigns.

6.3 Future plans

The NTM stability results represent the first step in this research on MAST and further measurements are needed to better understand the stability of 2,1 NTMs on this machine. Therefore, a number of beta scan experiments on MAST are planned for the current (2011) experimental campaign to further investigate 2,1 NTMs. In addition, a number of improvements are planned to improve both the accuracy of the stability parameter measurements and the approach used to perform beta scans.

To obtain more accurate measurements of w_d, a number of improvements can be made to the current heat transport model, including the addition of external heat sources and asymmetric island solutions. These improvements are currently being developed at the University of York. In addition, a new drift-kinetic model is being developed to describe the density transport around an NTM, which can be compared to the TS n_e measurements and provide more accurate and self-consistent estimates of w_d, and also a_{pol}.

One limitation of the beta scan experiments described in this thesis was that β_p could not reliably be dropped without resulting in a locked mode. This is due to a loss of momentum when the NBI beams are turned off to drop β_p. A Z-shift method using an FPGA triggering system has been developed (see chapter 5) and shown to be an effective solution to this problem. It is therefore planned to employ this Z-shift method in future MAST beta scan experiments for NTM studies. An additional use for this Z-shift method is to remove 2,1 NTMs as they appear in order to prevent locked mode disruptions and this is potentially a very useful method, as it may avoid the need for the massive gas injections currently used to mitigate locked mode disruptions. A series of dedicated experiments are planned to test this approach of disruption prevention on MAST and this may have implications for future machines.

Finally, in addition to 2,1 NTMs, 3,2 and 4,3 NTMs are also observed on MAST, although less frequently with smaller island width. Measurements of these modes could potentially provide more information about the w_d and a_{pol} MRE terms for NTMs in general as the lower collisionality of these NTMs is predicted to increase the influence of these stability terms. Both by carrying out more beta scan experiments on MAST, and extending the types of NTMs studied, we improve our understanding of how the different stability parameters influence NTM evolution.

Appendix A

NTM Fitzpatrick Derivation

This appendix outlines the solution to the Fitzpatrick heat transport equation [86]. This solution was fitted TS data to determine the finite island width (w_d), as described in section 5.4 in chapter 5. This derivation is based on both the original derivation by Professor Howard Wilson and on private communications with Professor Wilson and Jack Snape.

A.1 Fitzpatrick heat transport equation

In the absence of heat sources or sinks, heat transport parallel and perpendicular to the magnetic field lines is given by:

$$\chi_{\parallel}\nabla_{\parallel}^2 T + \chi_{\perp}\nabla_{\perp}^2 T = 0, \tag{A.1}$$

where $\chi_{\parallel}$ and $\chi_{\perp}$ are the thermal diffusivities, which are, respectively, parallel and perpendicular to the field lines. It is convenient to use a coordinate system [86, 18] where x is the radial flux coordinate (where $x = r - r_s$), ζ is the helical angle constant along the unperturbed field line and Ω is the normalised flux coordinate , which is given by:

$$\Omega = \frac{2x^2}{w^2} + \cos\zeta \tag{A.2}$$

The parallel gradient is given by equation A.3 as described by Wilson [18]:

$$\nabla_{\parallel} = \frac{-K_\theta x}{L_s}\frac{\partial}{\partial\zeta}\bigg|_{\Omega}, \tag{A.3}$$

where L_s is the magnetic shear and:

$$K_\theta = \frac{2\pi}{L}, \tag{A.4}$$

where L is the island length.

At the separatrix, $\Omega = 1$ and x can therefore be written as:

$$\frac{2x^2}{w^2} = 1 - \cos\zeta = 2\sin^2(\frac{\zeta}{2})$$
$$x = \pm w\sin(\frac{\zeta}{2}). \tag{A.5}$$

It is convenient to normalise the radial coordinate to the island width (w), which defines a new variable X, where $X = \frac{x}{w}$. The chain rule can then be used to calculate the derivative of X:

$$\frac{\partial^2 T}{\partial x^2} = \frac{1}{w^2}\frac{\partial^2 T}{\partial X^2}, \tag{A.6}$$

$$x\left.\frac{\partial}{\partial \zeta}\right|_{\Omega} = wX\left.\frac{\partial}{\partial \zeta}\right|_{\Omega} = wX\left.\frac{\partial}{\partial \zeta}\right|_{X} + wX\left.\frac{\partial X}{\partial \zeta}\right|_{\Omega}\left.\frac{\partial}{\partial X}\right|_{\zeta}. \tag{A.7}$$

The $X\frac{\partial X}{\partial \zeta}$ term can simplified by differentiating equation A.2 with respect to ζ, keeping Ω constant:

$$\begin{aligned}
\Omega^2 = \frac{2x^2}{w^2} + \cos\zeta &= 2X^2 + \cos\zeta \\
0 = 4X\left.\frac{\partial X}{\partial \zeta}\right|_{\Omega} &- \sin\zeta \\
X\left.\frac{\partial X}{\partial \zeta}\right|_{\Omega} &= \frac{1}{4}\sin\zeta.
\end{aligned} \tag{A.8}$$

Substituting equation A.8 into equation A.7 and combining the resulting equation with equation A.6, we can rewrite the equation A.1 as:

$$\frac{\chi_{\parallel}}{\chi_{\perp}}\frac{k_\theta^2}{L_s}\left(\omega\, X\left.\frac{\partial}{\partial \zeta}\right|_{x} + \frac{w}{4}\sin\zeta\left.\frac{\partial}{\partial X}\right|_{\zeta}\right)^2 T - \frac{1}{w^2}\frac{\partial^2 T}{\partial X^2} = 0, \tag{A.9}$$

and finally, by introducing the critical island width w_c (where $w_c^4 = \frac{\chi_\perp L_s^2}{\chi_\parallel k_\theta^2}$), we obtain the partial differential equation originally derived by Fitzpatrick [86]:

$$\left(X\left.\frac{\partial}{\partial \zeta}\right|_{X} + \frac{1}{4}\sin\zeta\left.\frac{\partial}{\partial X}\right|_{\zeta}\right)^2 T + \frac{w_c^4}{w^4}\frac{\partial^2 T}{\partial X^2} = 0. \tag{A.10}$$

A.2 Fourier series solution

The form of equation A.10 can be further simplified by expressing the solution for T_n as a Fourier series:

$$T(X,\zeta) = \sum_{n=0}^{N} T_n(X)\cos n\zeta. \tag{A.11}$$

The squared terms in equation A.10 can then be expanded out:

$$X^2\frac{\partial^2 T}{\partial \zeta^2} + \frac{1}{4}X\frac{\partial}{\partial \zeta}\left(\sin\zeta\frac{\partial T}{\partial X}\right) + \frac{1}{4}\sin\zeta\frac{\partial}{\partial X}\left(X\frac{\partial T}{\partial \zeta}\right) + \frac{1}{16}\sin^2\zeta\frac{\partial^2 T}{\partial X^2} + W_r\frac{\partial^2 T}{\partial X^2} = 0 \tag{A.12}$$

Equation A.11 can then be substituted into equation A.12 to give:

$$\begin{aligned}
\sum_n \Big\{ &-n^2X^2T_n\cos n\zeta + \frac{X}{4}T_n'\frac{\partial}{\partial \zeta}(\sin\zeta\cos n\zeta) - \\
&\frac{n}{4}\sin\zeta\sin n\zeta T_n - \frac{n}{4}XT_n'\sin\zeta\sin n\zeta + \frac{T_n''}{16}\sin^2\zeta\cos n\zeta + W_rT_n''\cos n\zeta\ \Big\} = 0
\end{aligned} \tag{A.13}$$

where $W_r = w_c^4/w^4$). Equation A.13 can then be simplified by substituting in the following trigonometric identities:

$$\begin{aligned}\frac{\partial}{\partial\zeta}(\sin\zeta\cos n\zeta) &= \cos\zeta\cos n\zeta - n\sin\zeta\sin n\zeta\\ \cos(X+Y) &= \cos X\cos Y - \sin X\sin Y\\ \cos(X-Y) &= \cos X\cos Y + \sin X\sin Y,\end{aligned} \tag{A.14}$$

$$\begin{aligned}\cos X\cos Y &= \frac{1}{2}[\cos(X+Y)+\cos(X-Y)]\\ \sin X\sin Y &= \frac{1}{2}[\cos(X-Y)-\cos(X+Y)],\end{aligned} \tag{A.15}$$

$$\begin{aligned}\sin^2\zeta\cos\zeta &= \frac{1}{2}(1-\cos 2\zeta)\cos n\zeta\\ &= \frac{1}{2}\cos n\zeta - \left[\frac{1}{2}\cos(n+2)+\frac{1}{2}\cos(n-2)\zeta\right].\end{aligned} \tag{A.16}$$

Substituting the trigonometric identity equations (A.14, A.15 and A.16) into equation A.13 gives:

$$\begin{aligned}\sum_n\Bigg\{-n^2X^2T_n\cos n\zeta + \frac{X}{8}T_n^{'}[\cos(n+1)\zeta+\cos(n-1)\zeta] -\\ \frac{nX}{4}T_n^{'}[\cos(n-1)\zeta-\cos(n+1)\zeta] - \frac{n}{8}T_n[\cos(n-1)\zeta-\cos(n+1)\zeta]\\ +\frac{T_n^{''}}{32}\cos n\zeta - \frac{T_n^{''}}{64}[\cos(n+2)\zeta+\cos(n-2)\zeta] + W_rT_n^{''}\cos n\zeta\Bigg\} = 0\end{aligned} \tag{A.17}$$

Equation A.17 is then multiplied by an arbitrary $\cos K\zeta$ and integrated over ζ:

$$\frac{1}{2\pi}\int_{-\pi}^{\pi}...d\zeta. \tag{A.18}$$

and the Dirac delta function can now be used to simplify equation A.17:

$$\frac{1}{2\pi}\int_{-\pi}^{\pi}\cos m\theta\cos n\theta\cdot d\theta = \frac{\delta_{m,n}}{2} \quad \text{for } m,\, n>0, \tag{A.19}$$

$$\frac{1}{2\pi}\int_{-\pi}^{\pi}\cos m\theta\cos n\theta\cdot d\theta = 1 \qquad \text{for } m=0,\, n=0. \tag{A.20}$$

Substituting equations A.19 and A.20 into equation A.17 and separating the terms into the order

of the derivatives gives:

$$\sum_{n=0}^{N}\Bigg\{\frac{-n^2X^2}{2}T_n(\delta_{K,n}+\delta_{K,-n})+\frac{X}{16}T_n^{'}\left(\delta_{K,n+1}+\cancel{\delta_{K,-n-1}}+\delta_{K,n-1}+\delta_{K,1-n}\right)$$
$$-\frac{nX}{8}T_n^{'}\left(\delta_{K,n-1}+\delta_{K,1-n}-\delta_{K,n+1}-\cancel{\delta_{K,-n-1}}\right)-$$
$$\frac{n}{16}T_n\left(\delta_{K,n-1}+\delta_{K,1-n}-\delta_{K,n+1}-\cancel{\delta_{K,-n-1}}\right)+$$
$$T_n^{''}\left[\frac{1}{64}(\delta_{K,n}+\delta_{K,-n})-\frac{1}{128}(\delta_{K,n+2}+\cancel{\delta_{K,-n-2}}+\delta_{K,n-2}+\delta_{K,2-n})\right.$$
$$\left.+\ \frac{W_r}{2}(\delta_{K,n}+\delta_{K,-n})\right]\Bigg\}=1, \qquad \text{(A.21)}$$

where the terms which have a negative n subscript can be neglected. Matrices can now be constructed for the different derivatives of T:

$\frac{d^2T}{dX^2}$ term:

$$A_Kn=\frac{1}{128}\left[2(\delta_{K,n}+\delta_{K,-n})-(\delta_{K,n+2}+\delta_{K,n-2}+\delta_{K,2-n})+64W_r(\delta_{K,n}+\delta_{K,-n})\right]$$
$$A_{Kn}=\frac{1}{128}\left[(2+64W_r)(\delta_{K,n}+\delta_{K,-n})-\delta_{K,n+2}-\delta_{K,n-2}-\delta_{K,2-n}\right] \qquad \text{(A.22)}$$

$\frac{dT}{dX}$ term:

$$B_{Kn}=\frac{X}{16}[\delta_{K,n+1}+\delta_{K,n-1}+\delta_{K,1-n}-2n(\delta_{K,n-1}+\delta_{K,1-n}-\delta_{K,n+1})]$$
$$B_{Kn}=\frac{X}{16}[(1+2n)\delta_{K,n+1}+(1-2n)(\delta_{K,n-1}+\delta_{K,1-n})] \qquad \text{(A.23)}$$

T term:

$$C_{Kn}=\frac{-n^2X^2}{2}(\delta_{K,n}+\delta_{K,-n})-\frac{n}{16}(\delta_{K,n-1}+\delta_{K,1-n}-\delta_{K,n+1}) \qquad \text{(A.24)}$$

There are $N+1$ coupled equations for the $N+1$ Fourier mode amplitudes. For each K, (where $0\leq K\leq N$) we have:

$$\sum_{n=0}^{N}\left[A_{Kn}\frac{d^2T_n}{dX^2}+B_{kn}\frac{dT_n}{dX}+C_{kn}T\right]=0 \qquad \text{(A.25)}$$

A.3 Finite difference solution

To find a numerical solution to equation A.25 we can use the finite difference method. T is discretised onto a grid in X, with i as the grid point index and Δ as the grid point spacing:

$$\frac{d^2T_n}{dX^2}=\frac{T_n^{i+1}-2T_n^i+T_n^{i-1}}{\Delta^2}$$
$$\frac{dT_n}{dX}=\frac{T_n^{i+1}-T_n^{i-1}}{\Delta}$$
$$T_n=T_n^i. \qquad \text{(A.26)}$$

Rewriting equation A.25 as a finite difference then gives:

$$\sum_n \left[A_{Kn} \frac{T_n^{i+1} - 2T_n^i + T_n^{i-1}}{\Delta^2} + B_{K-1} \frac{T_n^{i+1} - T_n^{i-1}}{\Delta} + C_{Kn} T_n^i \right] = 0$$

$$\sum_n \left[\left(\frac{A_{Kn}}{\Delta^2} - \frac{B_{Kn}}{\Delta} \right) T_n^{i-1} + \left(\frac{-2A_{Kn}}{\Delta^2} + C_{Kn} \right) T_n^i + \left(\frac{A_{Kn}}{\Delta^2} + \frac{B_{Kn}}{\Delta} \right) T_n^{i+1} \right] = 0. \quad \text{(A.27)}$$

The new matrices P_{Kn}, Q_{Kn} and S_{Kn} can be substituted into the above equation:

$$P_{Kn} = \frac{A_{Kn}}{\Delta^2} - \frac{B_{Kn}}{\Delta},$$

$$Q_{Kn} = C_{Kn} - \frac{2A_{Kn}}{\Delta^2},$$

$$S_{Kn} = \frac{A_{Kn}}{\Delta^2} + \frac{B_{Kn}}{\Delta}.$$

We can now solve the problem, provided we know the boundary conditions at $X = 0$ and $X = X_{max}$, where $X = 0$ is the centre of the island (and at this point $T = 0$). The Fourier coefficient for T can be written as the sum of a basis set:

$$T_n^i = \sum_{m=0}^{N} a_m t_{nm}^i = t_{nm}^i a_m. \quad \text{(A.28)}$$

and a boundary condition can then be imposed:

$$t_{nm}^{'} = 0. \quad \text{(A.29)}$$

This boundary condition arises because $T(x = 0) = 0$.

We can set t_{nm}^I (where X_I is the edge of the computational domain) to an arbitrary value, to be determined later (see equation A.73). To derive this basis set we must choose a reference point ($X = X_o$), between $X = 0$ and $X = X_I$:

For $X < X_o$ we write

$$t_{nm}^i = \alpha_{nj}^i t_{jm}^{i-1} + \beta_{nm}^i \quad \text{(A.30)}$$

For $X > X_o$ we write

$$t_{nm}^i = \alpha_{nj}^i t_{jm}^{i+1} + \beta_{nm}^i \quad \text{(A.31)}$$

For $X = X_o$ we write

$$\alpha_{nj}^i = 0 \quad \text{(A.32)}$$

$$\beta_{nm}^i = \delta_{nm} \quad \text{(A.33)}$$

For the $X < X_o$ region, we can derive the α_{nj}^i and β_{nm}^i terms in equation A.30 by substituting this equation into equation A.27, giving:

$$P_{Kn}^i t_{nm}^{i-1} + Q_{Kn}^i t_{nm}^i + S_{Kn}^i (\alpha_{nj}^{i+1} t_{jm}^i + \beta_{nm}^{i+1}) = 0. \quad \text{(A.34)}$$

where the matrices $\underline{\underline{\alpha}}^i$ and $\underline{\underline{\beta}}^i_m$ can be expressed in terms of $\underline{\underline{P}}$,$\underline{\underline{Q}}$ and $\underline{\underline{S}}$ matrices:

$$\underline{\underline{\alpha}}^i = -(\underline{\underline{Q}}^i + \underline{\underline{S}}^i \cdot \underline{\underline{\alpha}}^{i+1})^{-1}\underline{\underline{P}}^i \tag{A.35}$$

$$\underline{\underline{\beta}}^i_m = -(\underline{\underline{Q}}^i + \underline{\underline{S}}^i \cdot \underline{\underline{\alpha}}^{i+1})^{-1}\underline{\underline{S}}^i \cdot \underline{\underline{\beta}}^{i+1}_m \tag{A.36}$$

For this $X < X_o$ region, we can therefore derive all α^i and β^i_m terms if we start from α^o and β^o_m (o here meaning the point where $X = X_o$). We can then set the $t^i_m(x = 0)$ term to 0 and generate $N + 1$ solutions for t^i_m in this region.

For the $X > X_o$ region, we can derive the α^i_{nj} and β^i_{nm} terms in equation A.31 by substituting this equation into equation A.27, giving:

$$\underline{\underline{P}}^i \cdot (\underline{\underline{\alpha}}^{i-1} \cdot \underline{t}^i_m + \beta^{i-1}_m) + \underline{\underline{Q}}^i \cdot \underline{t}^i_m + \underline{\underline{S}}^i \cdot \underline{t}^{i+1}_m = 0 \tag{A.37}$$

where the matrices $\underline{\underline{\alpha}}^i$ and $\underline{\underline{\beta}}^i_m$ can be expressed in terms of $\underline{\underline{P}}$,$\underline{\underline{Q}}$ and $\underline{\underline{S}}$ matrices:

$$\underline{\underline{\alpha}}^i = -(\underline{\underline{P}}^i \cdot \underline{\underline{\alpha}}^{i-1} + \underline{\underline{Q}}^i)^{-1}\underline{\underline{S}}^i \tag{A.38}$$

$$\underline{\underline{\beta}}^i_m = -(\underline{\underline{P}}^i \cdot \underline{\underline{\alpha}}^{i-1} + \underline{\underline{Q}}^i)^{-1}\underline{\underline{P}}^i \underline{\underline{\beta}}^{i-1}_m \qquad X > X_o \tag{A.39}$$

For this $X > X_o$ region, we can again derive all α^i and β^i_m terms if we start from α^o and β^o_m. We can then set the t^I_m at $X = X_{max}$ and generate $N - 1$ solutions for t^i_m in this region.

For the $X = X_o$ region, equation A.27 can be rewritten as:

$$P^o_{Kn} t^{-1}_{nm} a_m + Q^o_{Kn} t^o_{nm} a_m + S^o_{Kn} t^1_{nm} a_m = 0 \tag{A.40}$$

This equation can then be written as a eigenvalue equation of the form $\underline{\underline{M}} \cdot \underline{a} = 0$ and the zero eigenvalue is found by iterating over the boundary condition $T_n(X_{max}) = T^I_n$.

A.4 Boundary conditions at $X = X_{max}$

We now require the solution of equation A.10 in the limit of $X \longrightarrow \infty$. First we define a parameter (ϵ) that compares $\frac{\partial T}{\partial X}$ to $X\frac{\partial}{\partial \zeta}$ (where $\frac{\partial T}{\partial X} \sim \epsilon X \frac{\partial T}{\partial \zeta}$). This makes equation A.10 become:

$$\left(X\frac{\partial}{\partial \zeta} + \frac{\epsilon}{4}\sin\zeta\frac{\partial}{\partial X}\right)^2 T + \epsilon^2 W_r \frac{\partial^2 T}{\partial X^2} = 0 \tag{A.41}$$

$$X^2\frac{\partial^2 T}{\partial \zeta^2} + \epsilon\frac{1}{4}X\frac{\partial}{\partial \zeta}\left(\sin\zeta\frac{\partial T}{\partial X}\right) + \epsilon\frac{1}{4}\sin\zeta\frac{\partial}{\partial X}\left(X\frac{\partial T}{\partial \zeta}\right) + \epsilon^2\frac{1}{16}\sin^2\zeta\frac{\partial^2 T}{\partial X^2} + \epsilon^2 W_r\frac{\partial^2 T}{\partial X^2} = 0 \tag{A.42}$$

Note: ϵ just labels size, we set it back to 1 at the end.

We can now expand T in ϵ:

$$T = T_o + \epsilon T_1 + \epsilon^2 T_2 + ... \tag{A.43}$$

and this equation can next be substituted back into equation A.41, which is then expanded in terms of the different orders of ϵ, these being ϵ^0, ϵ^1, ϵ^2 and ϵ^3.

A.4.1 $O(\epsilon^0)$

$$X^2 \frac{\partial^2 T_o}{\partial \zeta^2} = 0 \tag{A.44}$$

Integrating equation A.44 with respect to ζ then gives:

$$X^2 \frac{\partial T_o}{\partial \zeta} = C_o \tag{A.45}$$

If we define $< ... >= \frac{1}{2\pi} \int ...d\zeta$, we observe that T_o is periodic and therefore:

$$< \frac{\partial T_o}{\partial \zeta} = 0 > \tag{A.46}$$

and $C_o = 0$, $\frac{\partial T_o}{\partial \zeta} = 0$ and T_o is a function of X only ($T_o = \overline{T}_o(X)$).

A.4.2 $O(\epsilon^1)$

$$X^2 \frac{\partial^2 T_1}{\partial \zeta^2} + \frac{X}{4} \frac{\partial}{\partial \zeta} \left(\sin\zeta \frac{\partial T_o}{\partial X} \right) + \frac{1}{4} \sin\zeta \frac{\partial}{\partial X} \left(X \cancelto{0}{\frac{\partial T_o}{\partial \zeta}} \right) = 0 \tag{A.47}$$

Integrating equation A.47 with respect to ζ gives:

$$X^2 \frac{\partial T_1}{\partial \zeta} = -\frac{X}{4} \sin\zeta \frac{\partial T_o}{\partial X} + \cancel{C_1} \tag{A.48}$$

If we define $< ... >= \frac{1}{2\pi} \int ...d\zeta$, we observe that T_1 is periodic and therefore $C_1 = 0$. Integrating with respect to ζ again gives:

$$\begin{aligned} X^2 T_1 &= \frac{X}{4} \cos\zeta \frac{\partial T_o}{\partial X} + X^2 \overline{T}_1(X) \\ T_1 &= \frac{1}{4X} \cos\zeta \frac{\partial T_o}{\partial X} + \overline{T}_1(X) \end{aligned} \tag{A.49}$$

A.4.3 $O(\epsilon^2)$

$$\begin{aligned} X^2 \frac{\partial^2 T_2}{\partial \zeta^2} + \frac{X}{4} \frac{\partial}{\partial \zeta} \left(\sin\zeta \frac{\partial T_1}{\partial X} \right) + \frac{1}{4} \sin\zeta \frac{\partial}{\partial X} \left(X \frac{\partial T_1}{\partial \zeta} \right) \\ + \frac{1}{16} \sin^2\zeta \frac{\partial^2 T_o}{\partial X^2} + W_r \frac{\partial^2 T_o}{\partial X^2} = 0 \end{aligned} \tag{A.50}$$

A $\langle ... \rangle$ operator can be used on this equation and gives:

$$\frac{1}{4}\frac{\partial}{\partial X}\left\langle \sin\zeta \frac{\partial T_1}{\partial \zeta}\right\rangle + \frac{1}{32}\frac{\partial^2 T_o}{\partial X^2} + W_r\frac{\partial^2 T_o}{\partial X^2} = 0 \tag{A.51}$$

Equation A.48 can then be substituted into this equation (A.51), giving:

$$-\cancel{\frac{1}{16}\frac{\partial}{\partial X}\left\langle \sin^2\zeta \frac{\partial T_o}{\partial X}\right\rangle} + \cancel{\frac{1}{32}\frac{\partial^2 T_o}{\partial X^2}} + W_r\frac{\partial^2 T_o}{\partial X^2} = 0$$

$$\Rightarrow \frac{\partial^2 T_o}{\partial X^2} = 0 \quad \text{providing } w_c = 0 \tag{A.52}$$

this results in the boundary condition at T_o:

$$T_o = AX + B. \tag{A.53}$$

Substituting equation A.48 into the $O(\epsilon^2)$ differential equation (A.50) gives an expression that will be useful for calculating $O(\epsilon^3)$ (equation A.55). First equation A.48 is substituted into the third term of equation A.50:

$$X^2\frac{\partial^2 T_2}{\partial \zeta^2} + \frac{X}{4}\frac{\partial}{\partial \zeta}\left(\sin\zeta\frac{\partial T_1}{\partial X}\right) + \frac{1}{4}\sin\zeta\frac{\partial}{\partial X}\cancel{\left(-\frac{1}{4}\sin\zeta\frac{\partial T_0}{\partial X}\right)}$$

$$+\frac{1}{16}\sin^2\zeta\frac{\partial^2 T_o}{\partial X^2} + W_r\frac{\partial^2 T_o}{\partial X^2} = 0 \tag{A.54}$$

and then equation A.48 is substituted into the 2nd term of this equation (A.54), giving:

$$X^2\frac{\partial^2 T_2}{\partial \zeta^2} + \frac{X}{4}\frac{\partial}{\partial \zeta}(\sin\zeta\cos\zeta)\frac{\partial}{\partial X}\left(\frac{1}{X}\frac{\partial T_o}{\partial X}\right) + \frac{X}{4}\cos\zeta\frac{\partial \overline{T}_1}{\partial X} + W_r\frac{\partial^2 T_o}{\partial X^2} = 0 \tag{A.55}$$

A.4.4 O(ϵ^3)

$$X^2\frac{\partial^2 T_3}{\partial \zeta^2} + \frac{1}{4}X\frac{\partial}{\partial \zeta}\left(\sin\zeta\frac{\partial T_2}{\partial X}\right) + \frac{1}{4}\sin\zeta\frac{\partial}{\partial X}\left(X\frac{\partial T_2}{\partial \zeta}\right) + \frac{1}{16}\sin^2\zeta\frac{\partial^2 T_1}{\partial X^2} + W_r\frac{\partial^2 T_1}{\partial X^2} = 0 \tag{A.56}$$

Performing the $< ... >$ operator, and ignoring the T_3 terms as these are small, gives:

$$\frac{1}{4}\frac{\partial}{\partial X}\left\langle \sin\zeta X\frac{\partial T_2}{\partial \zeta}\right\rangle + \frac{1}{16}\left\langle\sin^2\zeta\right\rangle\frac{\partial^2 \overline{T_1}}{\partial X^2} + \left\langle W_r\frac{\partial^2 T_1}{\partial X^2}\right\rangle = 0 \tag{A.57}$$

The first term in this equation can then be simplified using integration by parts, to give:

$$\left\langle \sin\zeta\frac{\partial T_2}{\partial \zeta}\right\rangle = \cancel{\left[\sin\zeta\frac{\partial^2 T_2}{\partial \zeta^2}\right]_0^{2\pi}}^{0} + \left\langle \cos\zeta\frac{\partial^2 T_2}{\partial \zeta^2}\right\rangle. \tag{A.58}$$

Equation A.49 is then substituted into the remaining terms:

$$\frac{1}{4}\frac{\partial}{\partial X}\left[X\left\langle cos\zeta\frac{\partial^2 T_2}{\partial \zeta^2}\right\rangle\right] + \frac{1}{16}\frac{\partial^2}{\partial X^2}\left[\frac{1}{4X}\cancel{\left\langle \sin^2\zeta_o\cos\zeta\right\rangle}^{0}\frac{\partial T_o}{\partial X}\right]$$

$$+\frac{1}{16}\left\langle\sin^2\zeta\right\rangle\frac{\partial^2 \overline{T_1}}{\partial X^2} + W_r\frac{\partial^2 \overline{T_1}}{\partial X^2} = 0. \tag{A.59}$$

By performing a $< ... >$ operation on the equation obtained at the end of the $O(\epsilon^2)$ section (equation A.55) we get:

$$X^2 \left\langle \frac{\partial^2 T}{\partial \zeta^2} \right\rangle = - \left\langle \frac{\partial}{\partial \zeta}(\sin\zeta\cos\zeta) \right\rangle \frac{\partial}{\partial X}\left(\frac{1}{X}\frac{\partial T_o}{\partial X}\right) - \frac{X}{4}\langle\cos\zeta\rangle \frac{\partial \overline{T}_1}{\partial X}. \tag{A.60}$$

This equation can then be substituted into equation A.59 to give:

$$-\frac{1}{4}\frac{\partial}{\partial X}\left[\frac{1}{X}\cancel{\left\langle \cos\zeta \frac{\partial}{\partial\zeta}(\sin\zeta\cos\zeta)\right\rangle}^{0} \frac{\partial}{\partial X}\left(\frac{1}{X}\frac{\partial T_o}{\partial X}\right)\right] - \cancel{\frac{1}{16}\frac{\partial}{\partial X}\left[\langle\cos^2\zeta\rangle \frac{\partial \overline{T}_1}{\partial X}\right]}$$
$$+\cancel{\frac{1}{16}\langle\sin^2\zeta\rangle \frac{\partial^2 \overline{T}_1}{\partial X^2}} + W_r \frac{\partial^2 \overline{T}_1}{\partial X^2} = 0 \tag{A.61}$$

All of the terms in the above equation cancel, with the exception of the final term, which is:

$$W_r \frac{\partial^2 \overline{T}_1}{\partial X^2} = 0 \tag{A.62}$$

If $W_r \neq 0$, then $\overline{T}_1$ is linear in X and can be absorbed into T_o. The final boundary conditions can then be given by:

$$T_o = AX + B \tag{A.63}$$

$$T_1 = \frac{1}{4X}\cos\zeta \frac{\partial T_o}{\partial X} \tag{A.64}$$

A.5 Boundary conditions Fourier harmonics

Having determined the boundary conditions (equations A.63 and A.64) for the heat transport equation, we must now determine the boundary conditions for the numerical solution. At large X, all but the first two harmonics of t_m^I are negligible. The boundary conditions are given by:

$$\begin{aligned} t_{1m}(X) &= \frac{1}{4X}\frac{\partial t_{0m}}{dX} \\ t_{1m}^I &= \frac{1}{4X}\frac{t_{0m}^I - t_{0m}^{I-1}}{X^I - X^{I-1}} \\ t_{1m}^I &= \frac{1}{4\Delta X}(t_{0m}^I - \alpha_{00}^{I-1} t_{0m}^I - \alpha_{01}^{I-1} t_{1m}^I - \beta_{0m}^{I-1}) \end{aligned} \tag{A.65}$$

where $\Delta = X^I - X^{I-1}$. The boundary conditions can therefore be written as:

$$(\alpha_{01}^{I-1} + 4\Delta X) t_{1m}^I = (1 - \alpha_{00}^{I-1}) t_{0m}^I - \beta_{0m}^{I-1} \tag{A.66}$$

$$t_{1m}^I = \frac{(1 - \alpha_{00}^{I-1}) t_{0m}^I - \beta_{0m}^{I-1}}{(\alpha_{01}^{I-1} + 4\Delta X)} \tag{A.67}$$

Taking the boundary condition at X^I we get:

$$t^I_{om} = t_0 \text{(for all m)} \tag{A.68}$$

$$t^I_{1m} = \frac{(1-\alpha^{I-1}_{00})t_0 - \beta^{I-1}_{0m}}{(4\Delta X + \alpha^{I-1}_{01})} \tag{A.69}$$

$$t^I_m = \begin{pmatrix} t_0 \\ t^I_{1m} \\ 0 \\ 0 \\ 0 \end{pmatrix} \tag{A.70}$$

The electron temperature can now be reconstructed using these boundary conditions:

$$\underline{T_i} = \sum_m \underline{t^i_m} a_m \tag{A.71}$$

where t^I_{om} is a function of the P, Q and S matrices and the eigenvalue equation,

$$\underline{\underline{M}}.\underline{a} = 0, \tag{A.72}$$

provides the a_m term. The boundary condition at X^I can be varied to get the solution to the equation A.72, which means T can then be scaled by an arbitrary constant to give:

$$\lim_{x\to\infty} \frac{\partial T_o}{\partial X} = w \frac{\partial T_o}{\partial X}, \tag{A.73}$$

where the constant chosen is such that the temperature gradient of the solution matches the equilibrium temperature gradient.

Appendix B

The NTM Event Generator

In this appendix the design of the NTM event generator is described. This field programmable gate array (FPGA) system triggers the TS (ruby and/or Nd:YAG) lasers on a particular amplitude and phase of an NTM, which enables the T_e and n_e profiles of NTMs at specified stages to be measured. In addition, improvements to this FPGA system are described. This includes extending its function to permit triggering of vertical shifts of the MAST plasma. These shifts induce a drop in the beta poloidal (β_p) and represent a potential alternative to switching off the NBI beams in beta scan experiments and may also prevent locked modes on MAST.

B.1 NTM event generator design

Figure B.1 shows a photograph of the event generator with its different subcomponents labelled. This system takes the signals from the magnetic coils and uses them to calculate the amplitude and phase of a given NTM. When these calculations match the user-defined input criteria, which are sent from the SMART triggering unit, the event generator provides triggering events back to the SMART triggering unit which, in turn, triggers the lasers. The FPGA event generator was programmed using version 12.4 of the Xilinx Software Development Kit [45] and Mathworks Simulink System Generator Toolbox [110]. A block model of the FPGA code produced using the Simulink toolbox is given in figure B.2 and shows the major subsystems of the FPGA design. Each of these subsystems will now be considered in turn.

The first subsystem of the FPGA unit is the analogue to digital converter (ADC) block. This contains the firmware to convert the analogue magnetic coil signal to a 12 bit, 1 MHz signal. This signal is then sent to the FIR (finite impulse response) block, which performs most of the processing in the event generator unit. Here, the signals from each ADC channel are multiplied by the coefficients of the Hilbert and bandpass FIR filters, which are optimised for the frequency range of a 2,1 NTM. The Hilbert filter gives the imaginary component of an NTM oscillation which is

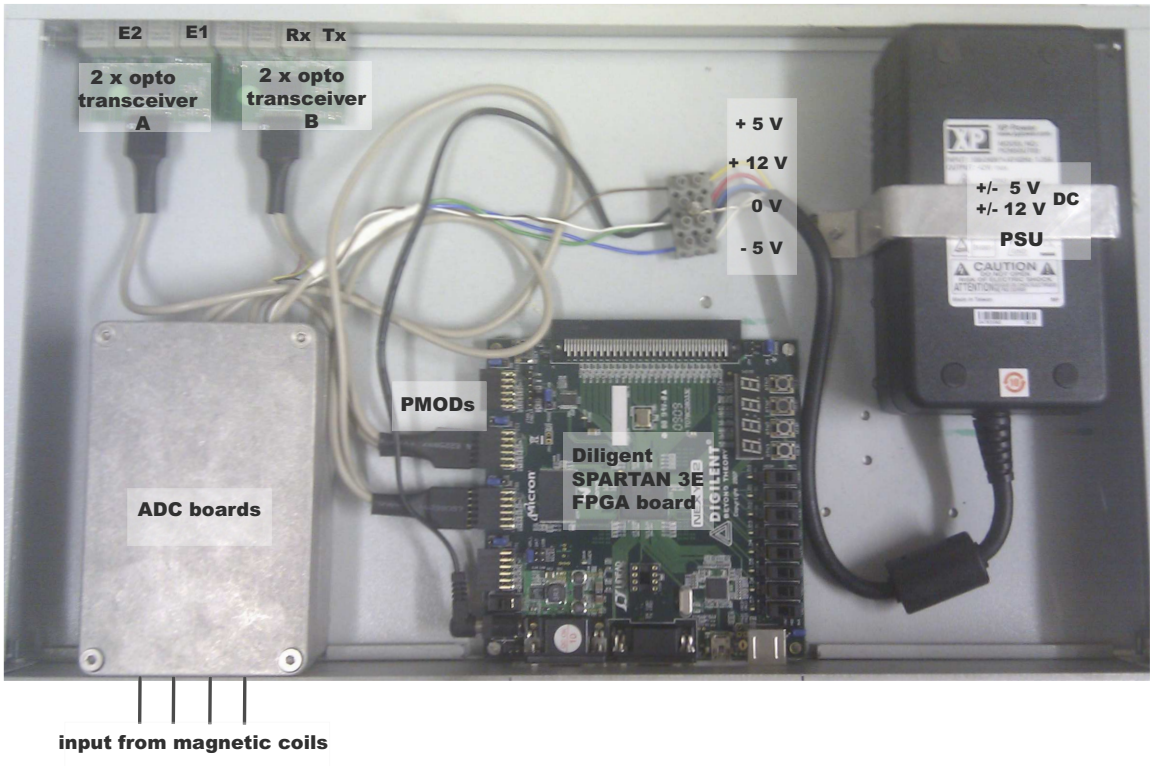

Figure B.1: The NTM event generator. The input signal from the magnetic coils is digitised by two Digilent 12 bit PmodAD1 boards (ADC boards), which both operate at 1 MHz. This digital signal is then processed by a Digilent Nexys2 FPGA board, which is built around a Xilinx Spartan-3E FPGA. Operation is controlled using an embedded picoblaze microprocessor, which communicates with the SMART triggering module over a pair of fibres that both receive commands (Rx) and transmit triggers (Tx) via universal asynchronous receiver/transmitter (UART) modules. These modules are implemented in the FPGA at either end.

90° out of phase with the bandpass filter signal and the complex select parameter determines how to add the output of these filters to select a particular toroidal mode number. The amplitude of the oscillating component of the NTM can then be determined by taking the Cartesian-to-polar transform of the real and imaginary components from each filter. This transform is performed using a CORDIC algorithm and returns the amplitude and phase of the NTM. The NTM frequency is then calculated from the finite difference of the phase and finally, the NTM period is determined using a zero crossing algorithm.

The NTM amplitude and phase are sent from the FIR block to the triggering logic subsystem. The other inputs for this subsystem are the upper and lower triggering thresholds that are sent from the user interface. The logic subsystem is currently designed to trigger the TS laser on the falling edge of an NTM amplitude. Therefore, once the NTM amplitude has fallen below both the upper and lower thresholds, the enable lamp threshold goes high. When this parameter is high the system can be triggered when a particular phase matches the phase requested by the user.

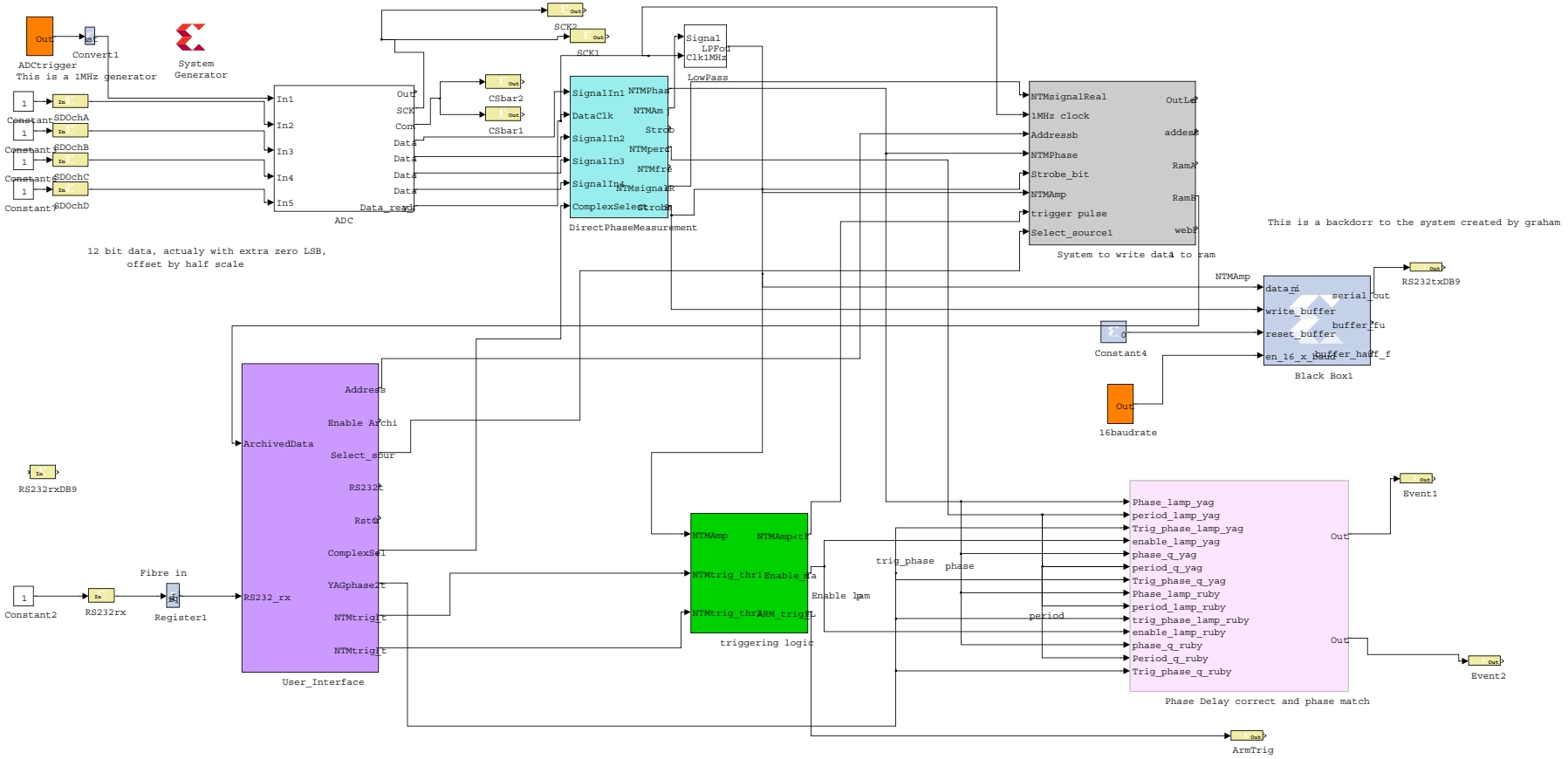

Figure B.2: The FPGA model, with the subsystem firmware of the NTM event generator shown. The input signal from the magnetic coils enters the ADC block (white box) and is then sent to the FIR block (cyan box), which calculates the NTM phase and amplitude. This data is then sent to the triggering logic block (green). The desired NTM amplitude and phase are set by the user and interpreted by the user interface block (purple box), which then sends this signal to the triggering logic block. When the NTM phase and amplitude match the user requirements in the triggering logic box, the laser Q-switch and lamp triggers are generated by the Q-switch lamp box (pink) and these are sent to the SMART triggering unit.

The next subsystem contains the firmware that provides the triggering events for both the ruby and Nd:YAG laser lamps and Q-switches, at a given NTM phase (the user-defined trigger phase). The phase at which the lasers are actually triggered is adjusted, in order to compensate for the delays incurred by both event generator processing and laser lamp triggering. The delays in the event generator consist of the group delay of the pre-amp ($11.6\mu s$), the group delay of the FIR filter ($64\mu s$), the 12 FPGA clock cycles ($0.25\mu s$) and also the transit time delays in both the fibres and the laser flight line ($\sim 0.2\mu$s). The laser lamp triggering delay for the Nd:YAG lasers is $\sim 300\mu$s and is 1250μs for the ruby laser. The range of the phase is scaled from -128 to 128 units in the FPGA unit. Thus, if an NTM period is k μs and a trigger at phase p is required, then the lamp triggers must be sent at $k-(300+76)\times\frac{256}{p}$ μs (Nd:YAG lasers) and $k-(1250+76)\times\frac{256}{p}$ μs (ruby laser). The Q-switch triggers are issued at $k-76\times\frac{256}{p}$ μs for both systems.

The Event 1 (Nd:YAG) and Event 2 (ruby) outputs are sent to the SMART trigger unit (see figure B.2). The rising and falling edges of an Event output provide the triggers for the laser lamp(s) and the Q-switch respectively. The lasers are only triggered on these outputs if they are available to be triggered. In dedicated NTM experiments, a hold-off period is therefore introduced at a fixed time to ensure all lasers are available for triggering when NTM events occur.

Two further subsystems are used to debug the operation of the event generator unit. Either the NTM signal or the NTM amplitude can be sampled at 6 kHz and stored to the block RAM on the FPGA board. Alternatively, it can be output over a serial interface to a PC. The serial commands to control this unit are shown in table B.1.

B.2 Improvements in the design of the NTM event generator

The previous NTM event generator was used on a number of shots during the last experimental campaign on MAST (M7), but did not trigger reliably for the majority of NTM events. Tests were therefore carried out to determine the system faults and based on the results found, improvements were made to improve its reliability to trigger on specific NTM events. The system was also further improved to permit triggering of vertical shifts (section B.2.4). During improvements, the overall design of this event generator was not altered from the above description (section B.1), but modifications were made to specific subsystems as described in the relevant sections.

B.2.1 System testing

The frequency range at which NTMs occur is within the audio range and accessible from PC sound cards. In addition, the magnetic signals used to trigger the NTM event generator are recorded for each MAST shot. These previous shots can be replayed to the NTM unit using a PC sound card,

thus providing a simple means of generating an input magnetic signal for testing the event generator unit (figure B.3).

After the magnetic signal of an NTM from a previous MAST shot is loaded from the MAST database and played on the PC soundcard, the signal is sent through an amplifier and then to an oscilloscope. The oscilloscope has an impedance of 20 kOhms, which is chosen to match the impedance of the ADC which measures the magnetic signal. This ensures that the amplitude of the signal sent from the signal generator is the same as that in the MAST shot. This signal then be used to test the NTM event generator.

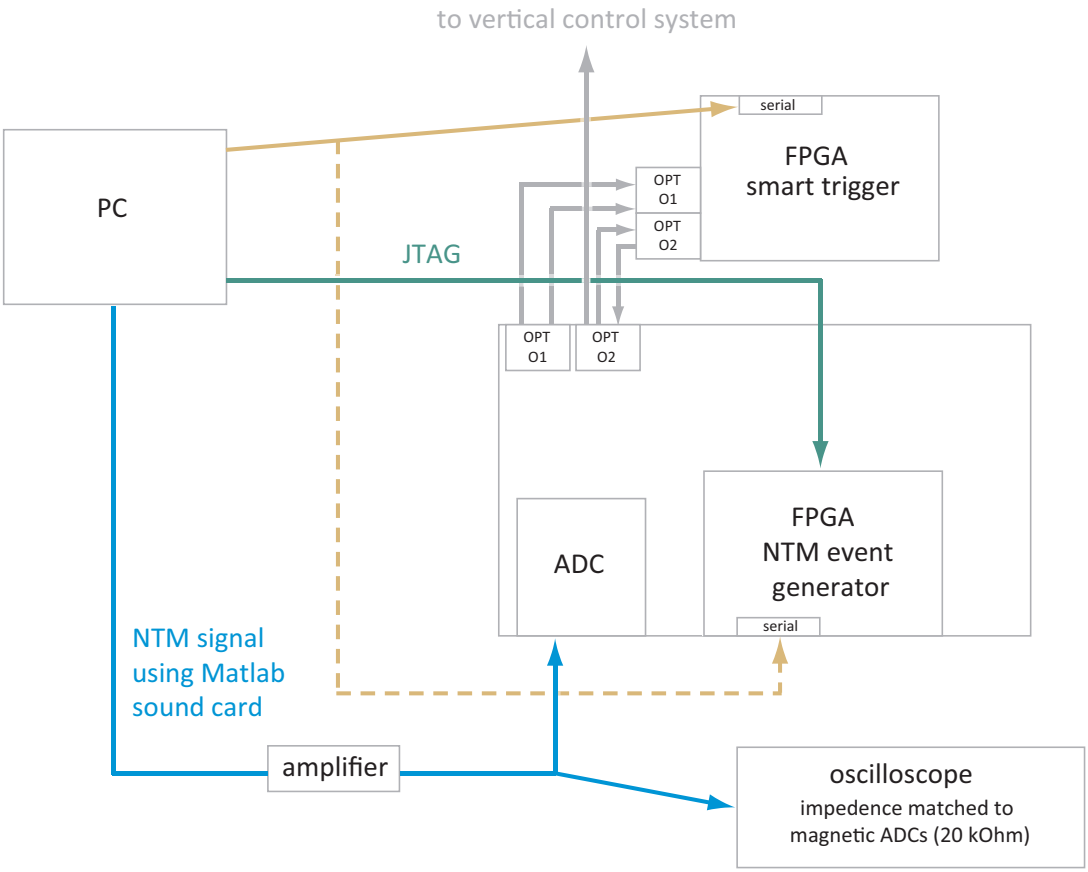

Figure B.3: A schematic diagram showing the hardware used to test and develop the FPGA triggering system.

Two principal methods were used to test the NTM event generator. The first method used Chipscope Pro software [45]. This software allows a logical analyser to be inserted into an FPGA design and an internal FPGA signal to then be monitored and recorded at the speed of its FPGA operation. Although a limit of this approach is the small number of samples that can be recorded, it can still be used to effectively test the system if measurements are triggered to occur at key points

(as set in the internal triggering conditions). Figure B.6 shows an example of the NTM amplitude taken from the FPGA signal during testing using this method.

The second approach to test the event generator involved simulating the FPGA design in Simulink using the System Generator Toolbox from Xilinix, to assess individual design elements. Only the FPGA design, and not the hardware, was tested using this approach. The principal disadvantages of this approach is that it can take several hours to simulate a single MAST shot (each lasts 0.5 s). However, this time can be reduced by a factor of 10 by using hardware co-simulation, where the calculations are performed on the FPGA board instead of on the PC.

A number of small issues were identified and resolved using a combination of these two approaches. In addition, larger modifications were made to the FIR filters (section B.2.2) and the triggering logic (section B.2.3) to enable large improvements in NTM triggering reliability.

B.2.2 Design of the FIR filters

FIR filters are used to determine the amplitude and phase of the NTM magnetic signal in the NTM event generator (see details in section 5.7.1). A bandpass FIR filter determines the real component (Q) of an NTM signal and a Hilbert FIR filter determines the imaginary component (I), which is 90° out of phase with Q. A CORDIC algorithm is then used to calculate the polar transform of Q and I, to give the amplitude and phase of the magnetic signal.

Ideally, both FIR filters would produce an identical frequency response over the frequency range of an NTM (2-10 kHz) and this would ensure NTM amplitude and phase calculations were accurate. In the original event generator design, a slight difference in response was found in the lower frequency range ($\sim 2-7$ kHz). Additionally, in this original design, 128 FIR filter coefficients were used to represent the I and Q filters and it was not possible to obtain a good response (figure B.4) at frequencies lower than 4 kHz with this number of filters. This is a particular problem for beta scan experiments on MAST, as the marginal island width rotates at or below this frequency range. The number of FIR coefficients and the design of both FIR filters were re-optimised to address both of these issues.

Two FIR filter optimisation algorithms were used, the Parks-McClellan algorithm [112] and the least squared method [113]; these algorithms attempt to match a FIR frequency response to a desired response input. The results from these algorithms were compared to the original filter designs coefficients (figure B.4). During these tests it was found that the minimum number of coefficients needed to produce good low frequency response was 180. This does result in an increased delay due to the greater number of coefficients compared to the previous system, but this is still well within an acceptable range.

Differences in the frequency responses between the two FIR filters results in non-linear vari-

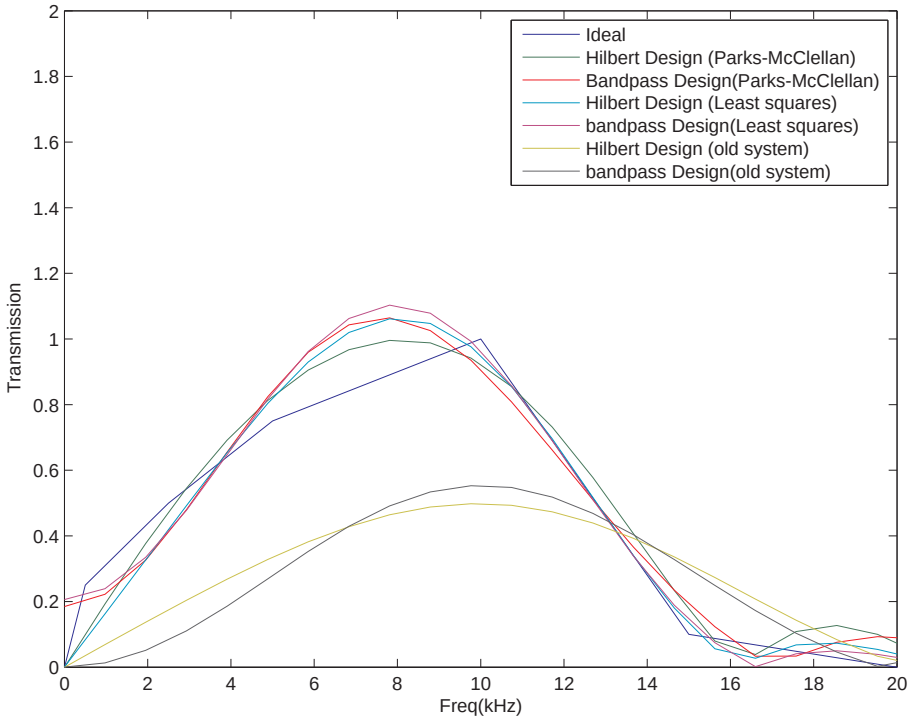

Figure B.4: The ideal frequency response of the bandpass and Hilbert filters are shown in blue. FIR filters results from Parks-McClellan and least squared with 180 coefficients are compared with the original FIR design.

ation in the phase, which can lead to incorrect phase triggering. The least squared optimisation algorithm results show less difference between the I and Q filter responses compared to the Parks-McClellan results (figure B.5). As a result, the least squared algorithm coefficients were used to improve the FIR filters. Figure B.7 shows the level of phase error reduction in the improved NTM event generator, which results from these changes.

B.2.3 False triggering resulting from edge localised modes

The system tests in section B.2.1 revealed that the high beta shots on which NTMs occur are frequently interrupted by ELMs. These ELMs have the effect of dropping the toroidal velocity of the MAST plasma and reducing the beta poloidal. This causes the magnetic signal (used to trigger the NTM event generator) to rapidly drop in both amplitude and frequency and typically lasts for $\sim$ 1 ms (for type 1 ELMs). In beta scan experiments, false triggers can therefore occur due to these ELM-induced amplitude drops.

Having identified these false triggers, it was found that they could be prevented using a control parameter to limit the allowable rate of change of the mode amplitude and frequency. Once a derivative of the NTM amplitude and frequency is greater than the control parameter, the triggering

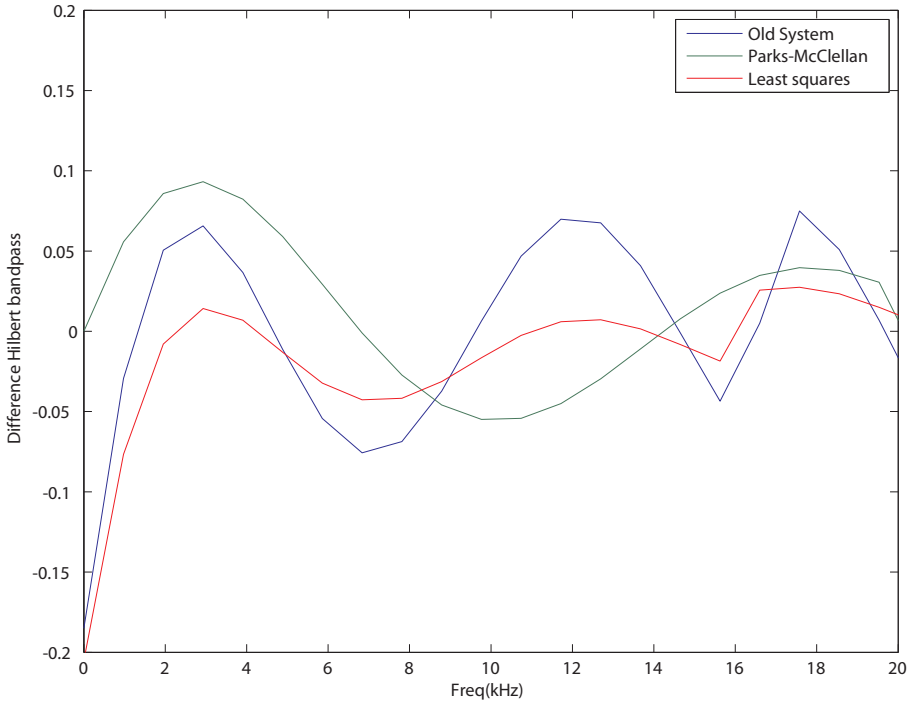

Figure B.5: The difference between the I and Q filters when different filter optimisation methods are used. The least squared method (red line) is found to give the lowest difference between the result I and Q filters.

of the NTM event generator is prevented. The size of the control parameter is determined from previous MAST data. Figure B.6 shows measurements of the calculated derivatives (using Chipscope Pro) carried out during an ELM event on MAST during tests of the NTM event generator.

B.2.4 Triggering of vertical shifts

During beta scan experiments in the last MAST experimental campaign, the NBI beams were switched off to reduce beta poloidal. The main aim of beta scan experiments is to reduce beta poloidal enough for an NTM to stabilise. However, when the NBI beams are switched off, the input momentum of the plasma is eliminated and this increases the probability that an NTM will lock to the wall.

The height of the density pedestal obtained on MAST is dependent on the dr_{sep} parameter [111]. This parameter represents the degree of seperatrix separation. This parameter can be varied by fine (¡ 1 cm) adjustments of the Z position of the MAST plasma using the P6 coils. The beta poloidal at the $q = 2$ surface is dependent on the height of the density pedestal achieved and thus changing the Z position provides a potential method to control beta poloidal without having to turn off the NBI beams. Furthermore, the adjustment of the Z position can be triggered on the NTM amplitude by coupling the NTM event generator to the MAST plasma control system (PCS),

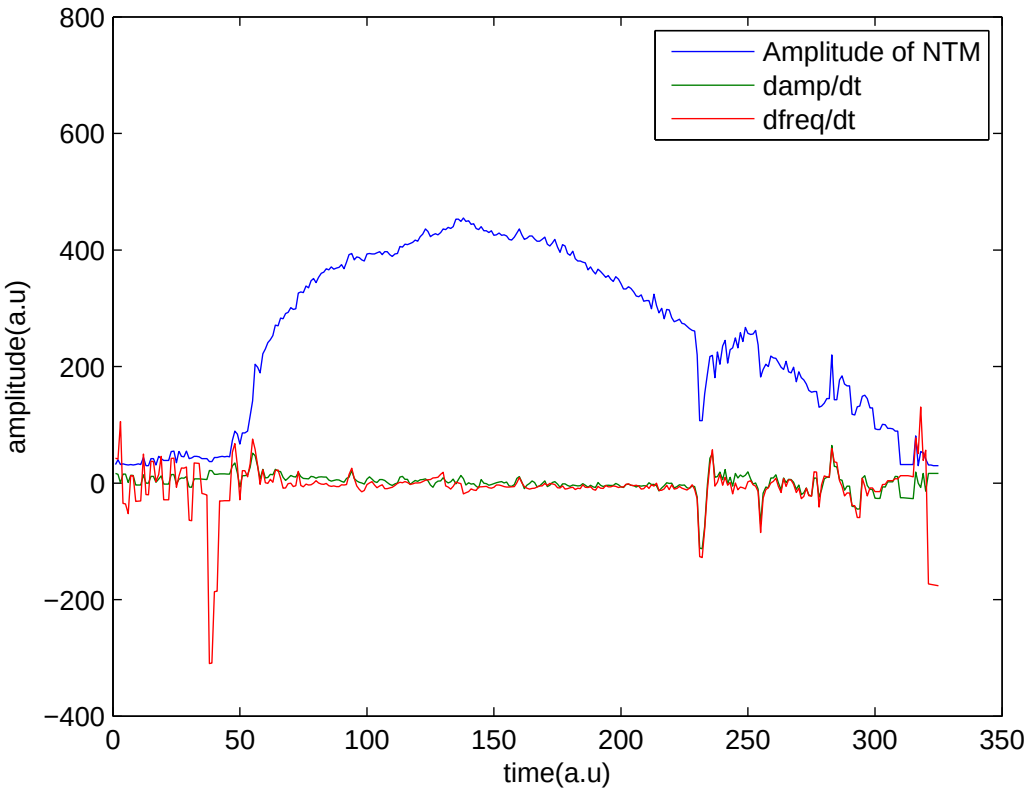

Figure B.6: The frequency (dfreq/dt, green line) and amplitude (damp/dt, red line) derivatives calculated in real-time for shot 24622 on MAST. The sizes of these different quantities have been measured using Chipscope Pro software. The amplitude of the NTM is overplotted in blue for reference.

allowing real-time control of β_p

The MAST PCS system controls the position and shape of the MAST plasma using real-time feedback from both currents in the P1-P6 coils and measurements from additional coils located around the vessel. Before a shot is performed, the reference waveforms of all plasma parameters are sent to the PCS. This includes the Z_{ref} parameter, which controls the reference for the Z position of the geometric axis and thus determines the level by which β_p is dropped.

The MAST PCS system was therefore modified to permit the state of the Z_{ref} parameter to be controlled using an optical fibre in real-time. The NTM event generator was also modified to generate this optical signal, which would trigger the PCS on a given mode amplitude. When the optical fibre is on, Z_{ref} is shifted by a fixed amount and this is determined by another parameter, Z_{offset}, which can be set to a specific value before the shot begins.

The duration of a vertical shift is controlled by the NTM event generator. Vertical shifts can be triggered on the rising or falling edges of the amplitude of an NTM. If this amplitude is greater than an upper threshold, the vertical shift is triggered and remains on until the amplitude reaches

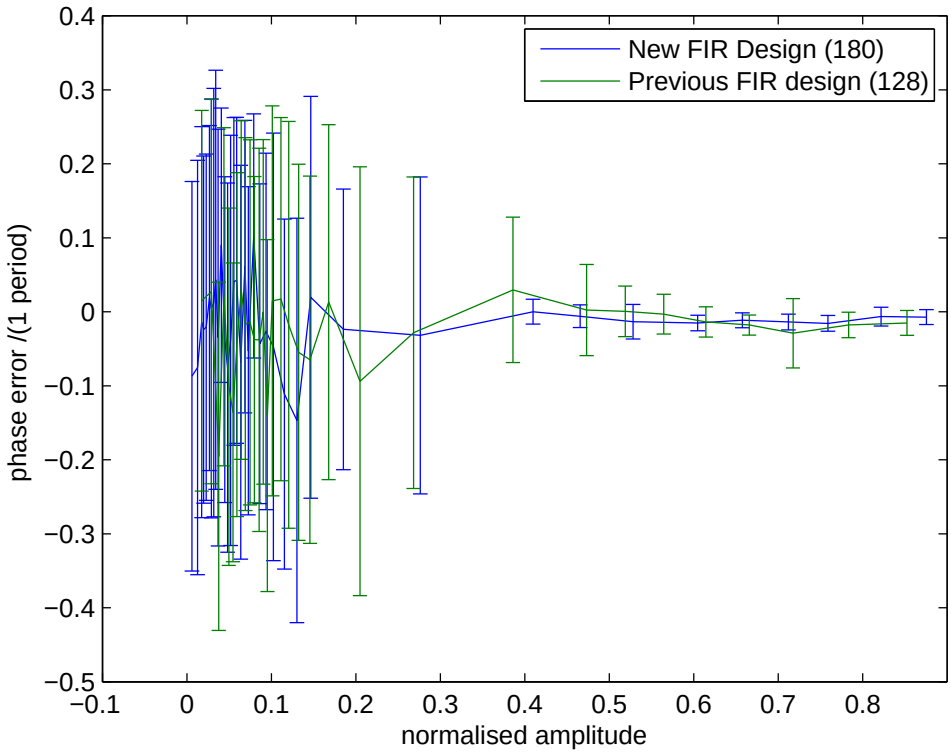

Figure B.7: Error in the phase calculations, resulting from differences in the I and Q filters, as calculated for shot 24503. The new FIR filter design (blue line) reduces the errors in these calculation by an order of 2 compared to the old FIR filter design (green line).

a lower threshold. These thresholds can be set on a shot-by-shot basis. In beta scan experiments vertical shifts will typically be triggered on the falling edge of the NTM amplitude.

Vertical shifts also have the potential to eliminate disruptions that frequently result from 2,1 NTMs. By detecting the growth of an NTM and triggering a vertical shift, this can remove the driving beta poloidal before the mode leads to a disruption. A number of shots are planned for the next experimental campaign to test the effectiveness of this approach to disruption mitigation.

Command	**Description**
$ASYP\,\langle xx\rangle$	Set phase of NTM to trigger YAGS. Xx in range 01 to FF (input in Hex)
$ASAS\,\langle x\rangle$	Select source for archiving, x=0 for raw ADC data, or else NTM amplitude.
$ASNTM\,\langle xx\rangle$	Select NTM mode number. The number indicates the complex value each coil must be multiplied by to describe the mode as 4 sets of binary pairs: 00 equals i 01 equals 1 10 equals -i 11 equals -1 Hence for mode 2 we need 1,i,-1,-i equals 01001110 or 4E in hex - so command is ASNTM4E
$ASNTT\,\langle xx\rangle$	select NTM threshold to arm triggering.
$ASNTF\,\langle xx\rangle$	select NTM threshold for triggering on falling edge (generally less than the value set by ASNTT).
AGS	Get data archived internal to FPGA
SNDT	threshold for d_{amp}/dt
SNDF	threshold for df/dt
SVTT	threshold for start of vertical kick
SVTF	threshold for end of vertical kick
SVTM	enable vertical kicks

Table B.1: Input serial commands used to control the NTM event generator unit.

Appendix C

Publications

The publications in which the author has had an important contribution during this thesis may be divided between diagnostic related work on the TS systems and physics work contributing to transport and stability investigations, principally on NTMs.

Diagnostic related publications

- T. O Gorman, P. J. Mc Carthy, S. Prunty, M. J. Walsh, M. R. Dunstan, R. B. Huxford, G. Naylor, Emmanuel Maguet, R. Scannell, and S. Shibaev. Design and implementation of a full profile sub-cm ruby laser based Thomson scattering system for MAST. *Review of Scientific Instruments*, 81(12):123508, 2010.

- R. Scannell, M. J.Walsh, M. R. Dunstan, J. Figueiredo, G. Naylor, T. O Gorman, S. Shibaev, K. J. Gibson, and H.Wilson. A 130 point Nd:YAG Thomson scattering diagnostic on MAST. *Review of Scientific Instruments*, 81(10):10D520, 2010.

- R. Scannell, M. Beurskens, P. G. Carolan, A. Kirk, M. Walsh, T. O Gorman, and T. H. Osborne. Deconvolution of Thomson scattering temperature profiles. *Review of Scientific Instruments*, 82(5):053501, 2011.

- R. Scannell, M. Beurskens, M. Kempenaars, G. Naylor, M. Walsh, T. O Gorman, and R. Pasqualotto. Absolute calibration of LIDAR Thomson scattering systems by rotational Raman scattering. *Review of Scientific Instruments*, 81(4):045107, 2010.

- S. Shibaev, G. Naylor, R. Scannell, G. McArdle, T. O Gorman, and M.J.Walsh. Control and acquisition for MAST Thomson scattering diagnostics. *Fusion Engineering and Design*, 85(5):683 686, 2010.

- R. Scannell, M. J. Walsh, P. G. Carolan, A. C. Darke, M. R. Dunstan, R. B. Huxford, G. McArdle, D. Morgan, G. Naylor, T. O Gorman, S. Shibaev, N. Barratt, K. J. Gibson, G. J.

Tallents, and H. R. Wilson. Design of a new Nd:YAG Thomson scattering system for MAST. *Review of Scientific Instruments*, 79(10):10E730, 2008.

Physics related publications

- T. O Gorman, P. J. Mc Carthy, D. Howell, K. Gibson, G. Naylor, R. Scannell, J. Snape and H. Wilson. Temperature and density profile measurements of neoclassical tearing modes on MAST. *37^{th} Proceedings of the European Physical Society Conference on Plasma Physics*, 2010, Dublin, Ireland.

- K J Gibson, N Barratt, I Chapman, N Conway, M R Dunstan, A R Field, L Garzotti, A Kirk, B Lloyd, H Meyer, G Naylor, T O Gorman, R Scannell, S Shibaev, J Snape, G J Tallents, D Temple, A Thornton, S Pinches, M Valovic, M J Walsh, H R Wilson, and the MAST team. New physics capabilities from the upgraded Thomson scattering diagnostic on MAST. *Plasma Physics and Controlled Fusion*, 52(12):124041, 2010.

- I.T. Chapman, R.J. Akers, N.C. Barratt, A.R. Field, K.J. Gibson, M.P. Gryaznevich , R.J. Hastie, T.C. Hender, D.F. Howell, M-D. Hua, G. Huysmans, Y.Q. Liu, M. Maraschek, C. Michael, G. Naylor, T. O Gorman, S.D. Pinches, R. Scannell, S.A. Sabbagh, H.R. Wilson and the MAST Team. Macroscopic Stability of High β MAST Plasmas. *ITPA Conference Proceedings*, EXS/P5-04, 2010.

- A Kirk, T O Gorman, S Saarelma, R Scannell, H R Wilson. A comparison of H-mode pedestal characteristics in MAST as a function of magnetic configuration and ELM type. *Plasma Physics and Controlled Fusion*, Volume 51, No 6, 2009.

- L. Garzotti, L. Baylor, F. Kochl, B. Pegourie, M. Valovic, K.B. Axon, J. Dowling, C. Gurl, G.P. Maddison, H. Nehme, T. O Gorman, A. Patel, M. Price, R. Scannell, and M.Walsh. Observation and analysis of pellet material ∇ drift on MAST. *Nuclear Fusion*, 50(10):105002, October 2010.

Bibliography

[1] International Energy Agency. World energy outlook. Technical report, 2010.

[2] J D Lawson. Some criteria for a power producing thermonuclear reactor. *Proc. Phys. Soc.*, B 70,6, 1957.

[3] J Wesson. *Tokamaks, second edition*. Clarendon Press, Oxford, 1997.

[4] F Troyon, R Gruber, H Saurenmann, S Semenzato, and S Succi. MHD-limits to plasma confinement. *Plasma Physics and Controlled Fusion*, 26(1A):209, 1984.

[5] A. Sykes, M. Turner, and S. Patel. Beta limits in tokamaks due to high-n ballooning modes. *Proc. 11th European Conference on Controlled Fusion and Plasma Physics, Aachen*, II:363, 1983.

[6] Jeffrey P. Freidberg. *Plasma Physics and Fusion Energy*. Cambridge University Press, 2007.

[7] Y-K.M. Peng and D.J. Strickler. Features of spherical torus plasmas. *Nuclear Fusion*, 26(6):769, 1986.

[8] A. Sykes, E. Del Bosco, R.J. Colchin, G. Cunningham, R. Duck, T. Edlington, D.H.J. Goodall, M.P. Gryaznevich, J. Holt, J. Hugill, J. Li, S.J. Manhood, B.J. Parham, D.C. Robinson, T.N. Todd, and M.F. Turner. First results from the START experiment. *Nuclear Fusion*, 32(4):694, 1992.

[9] V K Gusev, F Alladio, and A W Morris. The basics of spherical tokamaks and progress in european research. *Plasma Physics and Controlled Fusion*, 45(12A):A59, 2003.

[10] Y.-K. M. Peng. The physics of spherical torus plasmas. 7(5):1681–1692, 2000.

[11] T.C Hender, A Bond, J Edwards, P.J Karditsas, K.G McClements, J Mustoe, D.V Sherwood, G.M Voss, and H.R Wilson. Spherical tokamak power plant design issues. *Fusion Engineering and Design*, 48(3-4):255 – 263, 2000.

[12] H R Wilson, G Voss, J-W Ahn, R J Akers, L Appel, A Bond, A Cairns, J P Christiansen, G Counsell, A Dnestrovskij, M Hole, A Kirk, P Knight, C N Lashmore-Davies, K G McClements, M OBrien, , and S Tsaun. The spherical tokamak fusion power plant. *Proc. 19th IAEA Fusion Energy Conf. (Lyon)*, FT1/5:1, 2003.

[13] G.M. Voss, S. Davis, A. Dnestrovskij, A. Kirk, P.J. Knight, M. Loughlin, M.H. OBrien, D. Sychugov, A. Tabasso, and H.R. Wilson. Conceptual design of a component test facility based on the spherical tokamak. *Fusion Engineering and Design*, 83(10-12):1648 – 1653, 2008.

[14] Y.-K.M. Peng, E.T. Cheng, J.D. Galambos, and R.J. Cerbone. Spherical tokamak (st) transmutation of nuclear wastes. In *Fusion Engineering, 1995. SOFE '95. 'Seeking a New Energy Era'., 16th IEEE/NPSS Symposium*, volume 2, pages 1423 –1429 vol.2, sep-5 oct 1995.

[15] R. J. Bickerton, J. W. Connor, and J. B. Taylor. Diffusion driven plasma currents and bootstrap tokamak. *Nature Physical Science*, 229:110–112, January 1971.

[16] R J Buttery, S Günter, G Giruzzi, T C Hender, D Howell, G Huysmans, R J La Haye, M Maraschek, H Reimerdes, O Sauter, C D Warrick, H R Wilson, and H Zohm. Neoclassical tearing modes. *Plasma Physics and Controlled Fusion*, 42(12B):B61, 2000.

[17] R. J. La Haye. Neoclassical tearing modes and their control. *Physics of Plasmas*, 13(5):055501, 2006.

[18] H. R. Wilson. Neoclassical tearing modes. *Transactions of Fusion Science and Technology*, 49:155, 2006.

[19] R. Carrera, R. D. Hazeltine, and M. Kotschenreuther. Island bootstrap current modification of the nonlinear dynamics of the tearing mode. 29(4):899–902, 1986.

[20] Z. Chang and J.D. Callen. Global energy confinement degradation due to macroscopic phenomena in tokamaks. *Nuclear Fusion*, 30(2):219, 1990.

[21] EFDA ITER. Summary of the ITER Final Design Report. 2001.

[22] K. Ikeda. Progress in the iter physics basis. *Nuclear Fusion*, 47(6), 2007.

[23] T.C. Hender, J.C Wesley, J. Bialek, A. Bondeson, A.H. Boozer, R.J. Buttery, A. Garofalo, T.P Goodman, R.S. Granetz, Y. Gribov, O. Gruber, M. Gryaznevich, G. Giruzzi, S. Gnter, N. Hayashi, P. Helander, C.C. Hegna, D.F. Howell, D.A. Humphreys, G.T.A. Huysmans, A.W. Hyatt, A. Isayama, S.C. Jardin, Y. Kawano, A. Kellman, C. Kessel, H.R. Koslowski, R.J. La Haye, E. Lazzaro, Y.Q. Liu, V. Lukash, J. Manickam, S. Medvedev, V. Mertens, S.V.

Mirnov, Y. Nakamura, G. Navratil, M. Okabayashi, T. Ozeki, R. Paccagnella, G. Pautasso, F. Porcelli, V.D. Pustovitov, V. Riccardo, M. Sato, O. Sauter, M.J. Schaffer, M. Shimada, P. Sonato, E.J. Strait, M. Sugihara, M. Takechi, A.D. Turnbull, E. Westerhof, D.G. Whyte, R. Yoshino, H. Zohm, Disruption the ITPA MHD, and Magnetic Control Topical Group. Chapter 3: Mhd stability, operational limits and disruptions. *Nuclear Fusion*, 47(6):S128, 2007.

[24] O Sauter, M A Henderson, G Ramponi, H Zohm, and C Zucca. On the requirements to control neoclassical tearing modes in burning plasmas. *Plasma Physics and Controlled Fusion*, 52(2):025002, 2010.

[25] R. J. La Haye, A. Isayama, and M. Maraschek. Prospects for stabilization of neoclassical tearing modes by electron cyclotron current drive in ITER. *Nuclear Fusion*, 49(4):045005, 2009.

[26] O. Sauter, R. J. La Haye, Z. Chang, D. A. Gates, Y. Kamada, H. Zohm, A. Bondeson, D. Boucher, J. D. Callen, M. S. Chu, T. A. Gianakon, O. Gruber, R. W. Harvey, C. C. Hegna, L. L. Lao, D. A. Monticello, F. Perkins, A. Pletzer, A. H. Reiman, M. Rosenbluth, E. J. Strait, T. S. Taylor, A. D. Turnbull, F. Waelbroeck, J. C. Wesley, H. R. Wilson, and R. Yoshino. Beta limits in long-pulse tokamak discharges. *Physics of Plasmas*, 4(5):1654–1664, 1997.

[27] J P Meskat, H Zohm, G Gantenbein, S Günter, M Maraschek, W Suttrop, Q Yu, and ASDEX Upgrade Team. Analysis of the structure of neoclassical tearing modes in ASDEX upgrade. *Plasma Physics and Controlled Fusion*, 43(10):1325, 2001.

[28] M Holzl, S Gunter, I G J Classen, Q Yu, the TEXTOR Team, and E Delabie. Determination of the heat diffusion anisotropy by comparing measured and simulated electron temperature profiles across magnetic islands. *Nuclear Fusion*, 49(11):115009 (7pp), 2009.

[29] A C Darke, M Cox, J R Harbar, J H Hay, J B Hicks, J W Hill, D Hurford, J S McKenzie, A W Morris, M P S Nightingale, T N Todd, G M Voss, and J R Watkins. The Mega Amp Spherical Tokamak. 1995.

[30] A R Field, J McCone, N J Conway, M Dunstan, S Newton, and M Wisse. Comparison of measured poloidal rotation in MAST spherical tokamak plasmas with neo-classical predictions. *Plasma Physics and Controlled Fusion*, 51(10):105002, 2009.

[31] H Meyer, R J Akers, F Alladio, L C Appel, K B Axon, N Ben Ayed, P Boerner, R J Buttery, P G Carolan, D Ciric, C D Challis, I T Chapman, G Coyler, J W Connor, N J Conway,

S Cowley, M Cox, G F Counsell, G Cunningham, A Darke, M DeBock, G DeTemmerman, R O Dendy, J Dowling, A Yu Dnestrovskij, Yu.N. Dnestrovskij, B Dudson, D Dunai, M Dunstan, A R Field, A Foster, L Garzotti, K Gibson, M P Gryaznevich, W Guttenfelder, N C Hawkes, J Harrison, P Helander, T C Hender, B Hnat, M J Hole, D F Howell, M Duc Hua, A Hubbard, M Istenic, N Joiner, D Keeling, A Kirk, H R Koslowski, Y Liang, M Lilley, S Lisgo, B Lloyd, G P Maddison, R Maingi, A Mancuso, S J Manhood, R Martin, G J McArdle, J McCone, C Michael, P Micozzi, T Morgan, A W Morris, D G Muir, E Nardon, G Naylor, M R O'Brien, T O'Gorman, A Patel, S D Pinches, J Preinhaelter, M N Price, E Rachlew, D Reiter, C M Roach, V Rozhansky, S Saarelma, A Saveliev, R Scannell, S E Sharapov, V Shevchenko, S Shibaev, H Smith, G E Staebler, D Stork, J Storrs, A Sykes, S Tallents, P Tamain, D Taylor, D Temple, N Thomas-Davies, A Thornton, A Thyagaraja, M R Turnyanskiy, J Urban, M Valovic, R G L Vann, F Volpe, G Voss, M J Walsh, S E V Warder, R Watkins, H R Wilson, M Windridge, M Wisse, A Zabolotski, S Zoletnik, O Zolotukhin, the MAST, and N B I Teams. Overview of physics results from MAST. *Nuclear Fusion*, 49(10):104017 (13pp), 2009.

[32] L. Spitzer, D. J. Grove, W. E. Tonks, and W. R. Westendorp. Problems of the stellarator as a useful power source. *Technical Report NYO 6047, USAEC*, 1954.

[33] B Pgouri. Review: Pellet injection experiments and modelling. *Plasma Physics and Controlled Fusion*, 49(8):R87, 2007.

[34] C Ribeiro, R Akers, F Alladio, K Axon, L Baylor, G.F Counsell, J Dowling, S Fielding, L Garzotti, M Gryaznevich, W.E Han, P Innocente, I Jenkins, J deKloe, R Martin, P Micozzi, B Sass, A Sykes, D Terranova, T.N Todd, P Twynam, M Wakatani, M.J Walsh, and S You. Pellet injection on START and MAST. *Fusion Engineering and Design*, 58-59(0):319 – 324, 2001.

[35] Alan Wootton. *Magnetic Fields and Magnetic Diagnostics for Tokamak Plasmas*.

[36] I H Hutchinson. *Principles of plasma diagnostics*. Cambridge University Press, 2nd edition, 2002.

[37] N. J. Conway, M. F. M. De Bock, C. A. Michael, M. J. Walsh, P. G. Carolan, N. C. Hawkes, E. Rachlew, J. F. G. McCone, S. Shibaev, and G. Wearing. The MAST motional stark effect diagnostic. 81(10):10D738, 2010.

[38] N. J. Conway, P. G. Carolan, J. McCone, M. J. Walsh, and M. Wisse. High-throughput charge exchange recombination spectroscopy system on mast. 77(10):10F131, 2006.

[39] L.L. Lao, H. St. John, R.D. Stambaugh, A.G. Kellman, and W. Pfeiffer. Reconstruction of current profile parameters and plasma shapes in tokamaks. *Nuclear Fusion*, 25(11):1611, 1985.

[40] L.L. Lao, J.R. Ferron, R.J. Groebner, W. Howl, H. St. John, E.J. Strait, and T.S. Taylor. Equilibrium analysis of current profiles in tokamaks. *Nuclear Fusion*, 30(6):1035, 1990.

[41] H. Lütjens, A. Bondeson, and O. Sauter. The CHEASE code for toroidal MHD equilibria. *Computer Physics Communications*, 97(3):219–260, 1996.

[42] O Sauter, R J Buttery, R Felton, T C Hender, D F Howell, and contributors to the EFDA-JET Workprogramme. Marginal beta-limit for neoclassical tearing modes in JET H-mode discharges. *Plasma Physics and Controlled Fusion*, 44(9):1999, 2002.

[43] Oak Ridge National Laboratory NCLASS, Fusion Energy Division. NCLASS module - calculates neoclassical transport properties of a multi-species axisymmetric plasma, 2011.

[44] W. A. Houlberg, K. C. Shaing, S. P. Hirshman, and M. C. Zarnstorff. Bootstrap current and neoclassical transport in tokamaks of arbitrary collisionality and aspect ratio. 4(9):3230–3242, 1997.

[45] Xilinx. Xilinx software development kit., July 2011.

[46] Peacock N.J., Robinson D.C., Forrest M. J., Wilcock P. D., and Sannikov V.V. Measurement of the electron temperature by Thomson scattering in tokamak T3. *Nature (London)*, 224:488–490, 1969.

[47] S L Prunty. Private communications on Thomson scattering theory. 2008.

[48] Richard P. Feynman, Robert B. Leighton, and Matthew Sands. *The Feynman Lectures on Physics*. Addison-Wesley Publishing Company, 1977.

[49] Anne P Thorne, U Litzen, and S Johansson. *Spectrophysics*. Chapman and Hall, 1988.

[50] M Mattioli. Incoherent light scattering from high temperature plasmas. *EUR-CEA-FC-752*, 1974.

[51] A Selden. *Simple analytic form of the relativistic Thomson scattering spectrum*. UKAEA Reports - Culham Laboratory, Abingdon, Oxfordshire, 1982.

[52] A C Selden. Simple analytic form of the relativistic Thomson scattering spectrum. *Physics Letters*, 79A:405–406, 1980.

[53] O Naito, H Yoshida, and T Matoba. Analytic formula for fully relativistic Thomson scattering spectrum. *Physics of fluids B*, 5:4256, 1993.

[54] Rory Scannell. *H-mode edge profile behaviour on MAST*. PhD thesis, University College Cork, November 2006.

[55] J Sheffield. The incoherent scattering of radiation from a high temperature plasma. *Plasma Physics*, 14(8):783, 1972.

[56] D Johnson, N Bretz, D Dimock, B Grek, D Long, R Palladino, and E Tolnas. Multichannel Thomson scattering systems with high spatial resolution (invited). *Review of Scientific Instruments*, 57(8):1856–1861, 1986.

[57] C. J. Barth, H. J. v. d. Meiden, T. Oyevaar, and N. J. Lopes Cardozo. High resolution multiposition Thomson scattering for the TEXTOR tokamak. *Review of Scientific Instruments*, 72(1):1138, 2001.

[58] H. J. van der Meiden, C. J. Barth, T. Oyevaar, S. K. Varshney, A. J. H. Donné, M. Yu. Kantor, D. V. Kouprienko, A. Alexeev, W. Biel, and A. Pospieszczyk. 10 kHz repetitive high-resolution TV Thomson scattering on TEXTOR. *Review of Scientific Instruments*, 75(10):3849–3851, 2004.

[59] R. Scannell, M. J. Walsh, M. R. Dunstan, J. Figueiredo, G. Naylor, T. O'Gorman, S. Shibaev, K. J. Gibson, and H. Wilson. A 130 point Nd:YAG Thomson scattering diagnostic on MAST. *Review of Scientific Instruments*, 81(10):10D520, 2010.

[60] S C McCool, I L McCool, R D Bengston, and P E Phillips. *Calibration of Thomson Scattering Density Measurements*. DOE/ET/53042-7, FRCR 234, University of Texas, 1981.

[61] S. Shibaev, G. Naylor, R. Scannell, G. McArdle, T. O'Gorman, and M.J. Walsh. Control and acquisition for MAST Thomson scattering diagnostics. *Fusion Engineering and Design*, 85(5):683 – 686, 2010.

[62] M Leylandw. Quantifying and removing systematic errors on MAST Thomson scattering profiles of temperature and density. 2010.

[63] R. Scannell, M. Beurskens, M. Kempenaars, G. Naylor, M. Walsh, T. O'Gorman, and R. Pasqualotto. Absolute calibration of LIDAR Thomson scattering systems by rotational Raman scattering. *Review of Scientific Instruments*, 81(4):045107, 2010.

[64] R J Groebner and T N Carlstrom. Critical edge parameters for H-mode transition in DIII-D. *Plasma Phys. Control. Fusion*, 40:673–677, 1998.

[65] R. Scannell, M. Beurskens, P. G. Carolan, A. Kirk, M. Walsh, T. O Gorman, and T. H. Osborne. Deconvolution of Thomson scattering temperature profiles. *Review of Scientific Instruments*, 82(5):053501, 2011.

[66] I. T. Chapman, R. Scannell, W. A. Cooper, J. P. Graves, R. J. Hastie, G. Naylor, and A. Zocco. Magnetic reconnection triggering magnetohydrodynamic instabilities during a sawtooth crash in a tokamak plasma. *Phys. Rev. Lett.*, 105(25):255002, Dec 2010.

[67] A Thornton. *The impact of transient mitigation schemes on the MAST edge plasma*. PhD thesis, University of York, 2011.

[68] Chris Bowman. Application of local-polynomial regression techniques to Thomson scattering data analysis. Technical report, University of York, 2011.

[69] M. N. A. Beurskens, T. H. Osborne, P. A. Schneider, E. Wolfrum, L. Frassinetti, R. Groebner, P. Lomas, I. Nunes, S. Saarelma, R. Scannell, P. B. Snyder, D. Zarzoso, I. Balboa, B. Bray, M. Brix, J. Flanagan, C. Giroud, E. Giovannozzi, M. Kempenaars, A. Loarte, E. de la Luna, G. Maddison, C. F. Maggi, D. McDonald, R. Pasqualotto, G. Saibene, R. Sartori, Emilia R. Solano, M. Walsh, and L. Zabeo. H-mode pedestal scaling in DIII-D, ASDEX Upgrade, and JET. 18(5):056120, 2011.

[70] R. Scannell, M. J. Walsh, P. G. Carolan, A. C. Darke, M. R. Dunstan, R. B. Huxford, G. McArdle, D. Morgan, G. Naylor, T. O'Gorman, S. Shibaev, N. Barratt, K. J. Gibson, G. J. Tallents, and H. R. Wilson. Design of a new Nd:YAG Thomson scattering system for MAST. *Review of Scientific Instruments*, 79(10):10E730, 2008.

[71] M. J. Walsh, E. R. Arends, P. G. Carolan, M. R. Dunstan, M. J. Forrest, S. K. Nielsen, and R. O'Gorman. Combined visible and infrared Thomson scattering on the MAST experiment. *Review of Scientific Instruments*, 74(3):1663–1666, 2003.

[72] M. J. Walsh, N. J. Conway, M Dunstan, M.J. Forrest, and R.B. Huxford. Interactive optical design and realization of an optimized charge coupled device Thomson scattering system for the spherical tokamak START. *Review of Scientific Instruments*, 70:742–746, January 1999.

[73] T. O'Gorman, P. J. Mc Carthy, S. Prunty, M. J. Walsh, M. R. Dunstan, R. B. Huxford, G. Naylor, Emmanuel Maguet, R. Scannell, and S. Shibaev. Design and implementation of a full profile sub-cm ruby laser based Thomson scattering system for MAST. *Review of Scientific Instruments*, 81(12):123508, 2010.

[74] G. H. Sigel, E. J. Friebele, M. E. Gingerich, and L. M.; Hayden. Radiation response of large core polymer clad silica optical fibers. *IEEE Transactions on Nuclear Science*, 26(6):4796–4801, December 1979.

[75] J Flamand. *Diffraction gratings ruled and holographic Handbook*. Horiba Jobin-Yvon, 2003.

[76] Princeton Instruments. Proem, 2011.

[77] S K Park, R a Schowengerdt, and M a Kaczynski. Modulation-transfer-function analysis for sampled image systems. *Applied optics*, 23(15):2572, August 1984.

[78] A D Maidment and M J Yaffe. Analysis of signal propagation in optically coupled detectors for digital mammography: II. Lens and fibre optics. *Phys Med Biol*, 41(3):475–493, March 1996.

[79] Zemax Inc. Getting started using ZEMAX, 2011.

[80] G. Naylor. An FPGA based control unit for synchronization of laser Thomson scattering measurements to plasma events on MAST. *Fusion Engineering and Design*, 85(3-4):280–285, July 2010.

[81] IEEE. VHDL analysis and standardization group, 2011.

[82] M. N. A. Beurskens, C. J. Barth, C. C. Chu, and N. J. Lopes Cardozo. Error analysis of Rijnhuizen tokamak project Thomson scattering data. *Review of Scientific Instruments*, 70(4):1999–2011, 1999.

[83] M Valovic, K Axon, L Garzotti, S Saarelma, A Thyagaraja, R Akers, C Gurl, A Kirk, B Lloyd, G P Maddison, A W Morris, A Patel, S Shibaev, R Scannell, D Taylor, M Walsh, and the MAST team. Particle confinement of pellet-fuelled tokamak plasma. *Nuclear Fusion*, 48(7):075006, 2008.

[84] L. Garzotti, L. Baylor, F. Köchl, B. Pégourié, M. Valovič, K.B. Axon, J. Dowling, C. Gurl, G.P. Maddison, H. Nehme, T. O'Gorman, A. Patel, M. Price, R. Scannell, and M. Walsh. Observation and analysis of pellet material ∇ B drift on MAST. *Nuclear Fusion*, 50(10):105002, October 2010.

[85] T J Martin. Computer programs for electromagnetic fields and charge particle calculation. Technical report, EURATOM/CCFE Fusion Association, 1973.

[86] Richard Fitzpatrick. Helical temperature perturbations associated with tearing modes in tokamak plasmas. *Physics of Plasmas*, 2(3):825–838, 1995.

[87] R. J. Buttery, O. Sauter, R. Akers, M. Gryaznevich, R. Martin, C. D. Warrick, and H. R. Wilson. Neoclassical Tearing Physics in the Spherical Tokamak MAST. *Physical Review Letters*, 88(12):1–4, March 2002.

[88] H. P. Furth, J. Kileen, and M. N. Rosenbluth. Finite-resistivity instabilities of a sheet pinch. *Physics of Fluids*, 6:459, 1963.

[89] Z Chang, J D Callen, E D Fredrickson, R V Budny, C C Hegna, K M McGuire, M C Zarnstorff, and TFTR group. Observation of Nonlinear Neoclassical Pressure-Gradient–Driven Tearing Modes in TFTR. *Phys. Rev. Lett.*, 74(23):4663–4666, June 1995.

[90] E Poli, A G Peeters, A Bergmann, S Günter, and S D Pinches. Reduction of the ion drive and ρ_θ^* scaling of the neoclassical tearing mode. *Phys. Rev. Lett.*, 88(7):75001, February 2002.

[91] O. Sauter, C. Angioni, and Y. R. Lin-Liu. Neoclassical conductivity and bootstrap current formulas for general axisymmetric equilibria and arbitrary collisionality regime. *Physics of Plasmas*, 6(7):2834–2839, 1999.

[92] A. H. Glasser, J. M. Greene, and J. L. Johnson. Resistive instabilities in general toroidal plasma configurations. 18(7):875–888, 1975.

[93] H Lütjens, J F Luciani, and X Garbet. Nonlinear three-dimensional MHD simulations of tearing modes in tokamak plasmas. *Plasma Physics and Controlled Fusion*, 43(12A):A339, 2001.

[94] A B Mikhailovskii, V D Pustovitov, and A I Smolyakov. On collisionality dependence of the neoclassical tearing modes. *Plasma Physics and Controlled Fusion*, 42(3):309, 2000.

[95] H. R. Wilson, J. W. Connor, R. J. Hastie, and C. C. Hegna. Threshold for neoclassical magnetic islands in a low collision frequency tokamak. 3(1):248–265, 1996.

[96] Jack Snape. Experimental studies of NTMs on MAST. 1st year report, September 2010.

[97] K J Gibson, N Barratt, I Chapman, N Conway, M R Dunstan, A R Field, L Garzotti, A Kirk, B Lloyd, H Meyer, G Naylor, T O'Gorman, R Scannell, S Shibaev, J Snape, G J Tallents, D Temple, A Thornton, S Pinches, M Valovic, M J Walsh, H R Wilson, and the MAST team. New physics capabilities from the upgraded Thomson scattering diagnostic on MAST. *Plasma Physics and Controlled Fusion*, 52(12):124041, 2010.

[98] Lyman Spitzer and Richard Härm. Transport phenomena in a completely ionized gas. *Phys. Rev.*, 89:977–981, Mar 1953.

[99] Princeton Plasma Physics Laboratory. Transp: time dependent transport analysis code for tokamak experiments, August 2011.

[100] R J La Haye, C C Petty, E J Strait, F L Waelbroeck, and H R Wilson. Propagation of magnetic islands in the E_r = 0 frame of co-injected neutral beam driven discharges in the DIII-D tokamak. *Physics of Plasmas*, 10(9):3644–3648, 2003.

[101] S P Gerhardt, D P Brennan, R Buttery, R J La Haye, S Sabbagh, E Strait, M Bell, R Bell, E Fredrickson, D Gates, B LeBlanc, J Menard, D Stutman, K Tritz, and H Yuh. Relationship between onset thresholds, trigger types and rotation shear for the m/n = 2/1 neoclassical tearing mode in a high-β spherical torus. *Nuclear Fusion*, 49(3):32003, 2009.

[102] Koki Imada. *Influence of Polarisation Current on Tearing Instabilities in a Tokamak Plasma*. PhD thesis, University of York, September 2010.

[103] J. Schirmer, C.F. Maggi, H. Zohm, G.D. Conway, R. Dux, A. Flaws, M. Maraschek, A. Peeters, K. Sassenberg, A. Scarabosio, L. Urso, and ASDEX Upgrade Team. Rotation frequencies of mhd modes in asdex upgrade. 2007.

[104] Maarten De Bock. *Understanding and controlling plasma rotation in Tokamaks*. PhD thesis, Technische Universiteit Eindhoven, 2007.

[105] A. Scarabosio, A. Bortolon, B.P. Duval, and A. Pochelon. Comparison of mhd-mode and plasma rotation frequencies in tcv ohmic and ech discharges. 2006.

[106] F.L. Waelbroeck. Theory and observations of magnetic islands. *Nuclear Fusion*, 49(10):104025, 2009.

[107] C J Ham, J W Connor, S C Cowley, C G Gimblett, R J Hastie, T C Hender, and T J Martin. Strong toroidal effects on tokamak tearing mode stability in the hybrid and conventional scenarios. *Plasma Physics and Controlled Fusion*, 2011.

[108] D.P. Brennan, S.E. Kruger, T.A. Gianakon, and D.D. Schnack. A categorization of tearing mode onset in tokamaks via nonlinear simulation. *Nuclear Fusion*, 45(9):1178, 2005.

[109] R.J. La Haye, P.A. Politzer, and D.P. Brennan. Beta limit due to m/n = 2/1 tearing mode onset in the DIII-D hybrid scenario. *Nuclear Fusion*, 48(1):015005, 2008.

[110] Mathworks. Simulink: environment for multidomain simulation and model-based design., July 2011.

[111] H. Meyer, A. Kirk, L.C. Appel, E.R. Arends, P.G. Carolan, G.F. Counsell, G. Cunningham, A.R. Field, R. Martin, T.M. Pinfold, A. Tabasso, M.R. Tournianski, M. Valovi, M.J. Walsh, and the MAST Team. The effect of magnetic configurations on H-mode in MAST. *ECA: 29th EPS Conference on Plasma Phys. and Contr. Fusion Montreux, 17-21 June 2002*, 26B:P–1.056, 2002.

[112] T. W. Parks and J .H. McClellan. Chebyshev approximation for nonrecursive digital filters with linear phase. *IEEE Trans. Circuit Theory*, vol. CT-19, no. 2:189194, 1972.

[113] T. W. Parks and C. S. Burrus. *Digital Filter Design*. John Wiley and Sons Inc, 1987.